Experimental, Numerical and Analytical Studies of the MHD-driven plasma jet, instabilities and waves

Thesis by

Xiang Zhai

In Partial Fulfillment of the Requirements

for the Degree of

Doctor of Philosophy

California Institute of Technology

Pasadena, California

2015

(Defended June, 9, 2015)

Acknowledgements

I would like to express my most sincere gratitude to my adviser Prof Paul Bellan. Paul is an intelligent physicist with expertise in and a deep understanding of essentially all aspects of plasma physics and related fields, from theoretical analysis to experiment diagnostics, from circuit design to CAD drawing. He is an outstanding writer and speaker who knows how to use simple examples (like Los Angeles' congested highways or South Park) to explain complex physics models. Paul is such a kind and patient mentor and friend, having a great sense of humor. Moreover, I could not appreciate more the interesting life experiences and adventures and stories Paul shared with the group. I am very fortunate to have Paul as my PhD advisor.

It is also a great pleasure to know Dr. Hui Li and Dr. Shengtai Li in Las Alamos National Lab and have Hui as a co-mentor in my PhD career. Hui is a brilliant astrophysicist and has a humble personality. He gave me a lot of valuable suggestions and guidance in both research topics and general academia career. Shengtai helped me learn how to run the numerical simulation code he and Hui developed. Since I worked primarily at Caltech and have multiple projects simultaneously, I always felt a little bit guilty because of my slow progresses in the Bellan group-Li group joint project. Now I also feel pity that I have to graduate, but there are so many more interesting and important topics we can study by involving both the lab experiment in Caltech and the numerical simulation in LANL. Fortunately we have Pakorn Tung Wongwaitayakornkul, a smart, hard-working, and productive young student who will take over the joint project. I can't wait to see more exciting results.

I would like to thank my candidacy committee, Prof. Sterl Phinney, Prof. Kerry Vahala, Prof. Keith Schwab, and Prof. Paul Bellan, for the helpful advice, and also my thesis committee, Prof. Sterl Phinney, Prof. Christian Ott, Prof. Kerry Vahala, Dr. Bruce Tsurutani, and Prof. Paul Bellan, for reading my thesis and providing valuable feedback.

It has been a very joyful experience to work with and learn from other group members, including Rory Perkins, Auna Moser, Eve Stenson, Mark Kendall, Quoc Bao Ha, Vernon Chaplin, Kil-Byoung Chai, Zach Tobin, Magnus Haw, Pakorn Tung Wongwaitayakornkul (Tung), Ryan Marshall, and Young Dae Yoon. Rory taught me how to run the double-loop experiment and walked me through the basics of the experiment facilities. Auna tutored me on the plasma jet experiment — my PhD projects are essentially a continuation and extension of her major discover of the kink-instability-induced Rayleigh-Taylor instability. I am truly thankful for her guidance and also the experimental facilities she built, including a pulsed forming network, a capacitively coupled probe, and a magnetic probe array. Vernon has always been very helpful in the group. He is very knowledgeable in plasma physics and I have learned a lot from him. Vernon examined the derivation of Chapter 3 and provided valuable feedback. Bao is a wonderful lab-mate and a superb team player who always makes the group cheerful. He maintains the lab server and other computer-related facilities essentially by himself. Bao and Vernon have organized the journal clubs for several years that the entire group benefited from. The group is very lucky to have Kil-Byoung (KB) Chai as our postdoc. KB is amazingly efficient, hardworking, and productive. He introduced many new plasma topics and technologies to the group. We collaborated in plenty of experiments together. There have been many times that I needed to leave earlier and KB helped me shut down the facilities. KB also managed to go through the drafted version of Chapter 4 and 5 of this thesis. I could not be more grateful to KB for everything he did and for the things I learned from him. Magnus and I have been spending a lot of time together in diagnosing HV probes and magnetic probes and fixing the lathe machine. Magus, Bao, and I are all activists in salvaging E-wastes from Caltech and sharing experiences in reusing old electronic parts. I feel quite guilty that Vernon, Bao, and I are graduating at the same time and suddenly forcing Magnus to be the most senior grad student in the lab. However, I am pleased to see that Magnus has already built up the "senior field" with him. Tung was a SURF student in the group for two summers and now a formal member. We worked together in building the first version of the whistler probe. Although the probe itself turned out to be not good enough, I was amazed by Tung's productivity and hard-working altitude. I am very happy that Tung will be taking over my role in the collaboration with LANL Li group. Tung, Ryan, and Young, despite their super busy class schedules, are all surprisingly able to find time to study the experiments and develop new facilities. It is

great to see that the lab will remain in good shape.

Our group are so lucky to have Dave Felt, our professional electric engineering technician, and Connie Rodriguez, our responsible and warm-hearted secretary. Dave helped build plenty of facilities for the lab. I also gained a lot of valuable and helpful advices and suggestions from Dave when I was building the whistler probe and the HV probe. I can't be more grateful to Connie for her patience in organizing the group's office work, especially in handling the purchase orders from the group. Assuming that every group member averagely makes one purchase every week and we have about seven group members, that is one purchase everyday or ~ 400 purchases every year Connie has to take care of. She helps run the whole group smoothly.

I am deeply grateful to my wife Lin Song, my father, and my parents-in-law for the most unselfish and consistent support to me. I am thrilled to have my son Daniel join the family in 2013, and who has been bringing me so much joy and responsibility. I am fortunate to have you all in my life.

Abstract

This thesis describes a series of experimental, numerical, and analytical studies involving the Caltech magnetohydrodynamically (MHD)-driven plasma jet experiment. The plasma jet is created via a capacitor discharge that powers a magnetized coaxial planar electrodes system. The jet is collimated and accelerated by the MHD forces.

We present three-dimensional ideal MHD finite-volume simulations of the plasma jet experiment using an astrophysical magnetic tower as the baseline model. A compact magnetic energy/helicity injection is exploited in the simulation analogous to both the experiment and to astrophysical situations. Detailed analysis provides a comprehensive description of the interplay of magnetic force, pressure, and flow effects. We delineate both the jet structure and the transition process that converts the injected magnetic energy to other forms.

When the experimental jet is sufficiently long, it undergoes a global kink instability and then a secondary local Rayleigh-Taylor instability caused by lateral acceleration of the kink instability. We present an MHD theory of the Rayleigh-Taylor instability on the cylindrical surface of a plasma flux rope in the presence of a lateral external gravity. The Rayleigh-Taylor instability is found to couple to the classic current-driven instability, resulting in a new type of hybrid instability. The coupled instability, produced by combination of helical magnetic field, curvature of the cylindrical geometry, and lateral gravity, is fundamentally different from the classic magnetic Rayleigh-Taylor instability occurring at a two-dimensional planar interface.

In the experiment, this instability cascade from macro-scale to micro-scale eventually leads to the failure of MHD. When the Rayleigh-Taylor instability becomes nonlinear, it compresses and pinches the plasma jet to a scale smaller than the ion skin depth and triggers a fast magnetic reconnection. We built a specially designed high-speed 3D magnetic probe and successfully detected the high frequency magnetic fluctuations of broadband whistler

waves associated with the fast reconnection. The magnetic fluctuations exhibit power-law spectra. The magnetic components of single-frequency whistler waves are found to be circularly polarized regardless of the angle between the wave propagation direction and the background magnetic field.

Contents

Acknowledgements iii

Abstract vi

1 Background and Introduction 1

1.1 Magnetohydrodynamic theory . . . 1

1.1.1 Lorentz force and force-free configuration . . . 4

1.1.2 Ideal MHD magnetic flux frozen-in condition . . . 5

1.1.3 Dimensionless nature of ideal MHD . . . 7

1.1.4 Magnetic helicity and Taylor state . . . 9

1.2 Overview of Caltech plasma jet experiment . . . 11

1.2.1 Experiment setup and jet dynamics . . . 11

1.2.2 Diagnostics and other apparatus . . . 15

1.2.2.1 High-speed IMACON 200 camera . . . 16

1.2.2.2 EUV optical system . . . 16

1.2.2.3 VariSpec liquid crystal tunable filter . . . 17

1.3 Overview of this thesis . . . 17

2 Three-Dimensional MHD Numerical Simulation of Caltech Plasma Jet Experiment 20

2.1 Introduction . . . 21

2.2 Numerical MHD simulations . . . 26

2.2.1 Normalization and equations . . . 26

2.2.2 Initial condition . . . 28

2.2.2.1 Initial global poloidal magnetic field . . . 28

2.2.2.2 Initial mass distribution . . . 30

2.2.3 Helicity and energy injection . . . 31
2.2.3.1 Compact injection near the z=0 plane . . . 31
2.2.3.2 Jet collimation as a result of helicity/energy injection . . . 33
2.3 Simulation results . . . 36
2.3.1 A typical argon jet simulation . . . 36
2.3.1.1 Global energy analysis . . . 36
2.3.1.2 Jet collimation and propagation . . . 40
2.3.1.3 Jet structure and the global magnetic field configuration . . . 46
2.3.1.4 Alfvén velocity and Alfvén surface . . . 52
2.3.2 Bernoulli equation in MHD driven flow . . . 54
2.3.2.1 Jet velocity dependence on the poloidal current . . . 56
2.3.2.2 Jet velocity dependence on the jet density . . . 57
2.3.2.3 A direct illustration of MHD Bernoulli equation . . . 57
2.4 Sensitivity to imposed simulation conditions . . . 59
2.4.1 Background condition . . . 59
2.4.2 Toroidal field injection condition . . . 61
2.4.3 Initial mass distribution . . . 62
2.4.4 Initial poloidal flux . . . 63
2.5 Preliminary results on kink instability . . . 64
2.6 Summary and discussion . . . 66

3 A Hybrid Rayleigh-Taylor-Current-Driven Coupled Instability in an MHD Collimated Cylindrical Plasma with Lateral Gravity 69

3.1 Introduction . . . 70
3.2 Equations and equilibrium state . . . 75
3.3 Perturbation and linearization . . . 77
3.3.1 General solution of magnetic field perturbation . . . 79
3.3.2 Inside plasma . . . 81
3.3.3 Outside plasma . . . 81
3.4 Radial motion jump condition at the interface . . . 81
3.4.1 Preliminary analysis on stability . . . 85
3.4.2 Comments on the matrix equation . . . 87

3.4.3 Short/Long wavelength approximation . . . 88
3.5 Solutions . . . 89
3.5.1 Special cases I: weak gravity or strong toroidal magnetic field . . . 89
3.5.2 Special cases II: strong gravity or weak toroidal magnetic field . . . 90
3.5.3 Lateral Rayleigh-Taylor-Current-Driven coupled instability in cylindrical MHD collimated plasma . . . 91
3.5.3.1 Argon plasma jet . . . 92
3.5.3.2 Hydrogen plasma jet . . . 94
3.5.4 RT-CD coupled instability as a quasi-paramagnetic instability . . . 94
3.5.5 Visualization of the instability . . . 96
3.5.6 Comprehensive view of RT-CD coupled instability . . . 100
3.6 Summary and discussion . . . 102
3.7 Supplementary materials . . . 107
3.7.1 Confined perturbed current . . . 107
3.7.2 Asymptotic behaviors of modified Bessel functions . . . 108
3.7.3 Eigenvalues of matrix G . . . 109

4 Circularly polarized Magnetic Field of Obliquely Propagating Whistler Wave during Fast Magnetic Reconnection 111
4.1 Background . . . 113
4.1.1 Two-fluid theory of whistler wave . . . 113
4.1.2 Fast magnetic reconnection and whistler wave . . . 120
4.2 Whistler waves associated with fast reconnection in the plasma jet experiment 125
4.2.1 High-frequency magnetic fluctuations during fast magnetic reconnection 126
4.2.2 High-frequency magnetic fluctuations as an ensemble of whistler waves 130
4.2.3 Circularly polarized whistler wave . . . 136
4.2.3.1 Polarization recognition algorithm . . . 139
4.3 Summary . . . 144

5 A High-Speed 3D Magnetic Probe with Excellent Capacitive Rejection and Noise Shielding 145
5.1 Theories of B-dot probe . . . 146
5.2 Capacitive coupling and RF ground loop . . . 149

5.3 Design of 3D high-speed magnetic probe . . . 151
5.3.1 Elimination of RF ground loop current by studying dummy probe . 153
5.3.2 Construction of the 3D magnetic probe . . . 158
5.3.3 Calibration and test . . . 162
5.4 Measurements . . . 166
5.5 Summary . . . 168

6 An Earth-Isolated Optically Coupled Wideband High Voltage Probe Powered by Ambient Light 170
6.1 Introduction . . . 170
6.2 Probe design . . . 172
6.2.1 Transmitter . . . 172
6.2.1.1 Capacitive voltage divider . . . 172
6.2.1.2 LED driver . . . 176
6.2.1.3 Power supply . . . 176
6.2.1.4 Trigger system . . . 177
6.2.2 Receiver . . . 177
6.2.3 Calibration . . . 178
6.3 Performance and measurement . . . 178
6.4 HV probes in usage . . . 180
6.5 Some discussion about the solar cells . . . 182

7 Summary 183

A Two-color Imaging of the Plasma Jet Experiment using VariSpec Liquid Crystal Tunable Filter 187
A.1 VariSpec liquid crystal tunable filter . . . 187
A.1.1 Hot mirrors . . . 188
A.2 Two-color imaging of the plasma jet experiment . . . 189

B Useful Signal Processing Algorithms 192
B.1 Fourier transform and discrete Fourier transform . . . 192
B.2 Finite impulse response (FIR) filter . . . 195
B.3 Principal component analysis . . . 198

Bibliography **200**

List of Figures

1.1 Apparatus of the plasma jet experiment . . . 12
1.2 Images of hydrogen jet and argon jet . . . 13
1.3 Overview of diagnostics . . . 16

2.1 Examples of astrophysical jets observations . . . 22
2.2 Accretion disk - plasma gun analogy . . . 24
2.3 Evolution of energy in the simulation . . . 37
2.4 Current-Voltage profile in the experiment and simulation . . . 37
2.5 Time sequence of cross-sectional view of the plasma density and poloidal magnetic field in a typical argon jet simulation . . . 41
2.6 Comparison of images of simulation jet and experimental jet . . . 42
2.7 Axial profiles of the simulation jet . . . 43
2.8 Cross-sectional view of the energy fluxes . . . 46
2.9 Radial profiles of the simulation jet . . . 47
2.10 Cross-sectional view of a set of plasma properties at $t = 29.1$ μs . . . 49
2.11 Magnetic field structure of the experimental jet and the simulation jet . . . 51
2.12 3D magnetic field structure of the simulation jet . . . 53
2.13 Alfvén velocity v_A and velocity to Alfvén velocity ratio v/v_A . . . 55
2.14 Jet velocity dependences in the simulation . . . 56
2.15 Bernoulli property of the jet . . . 58
2.16 Cross-sectional view of density distribution and poloidal flux contours of nine simulations with different conditions . . . 60
2.17 Simulation of a kinked hydrogen jet . . . 65
2.18 Simulation of two kinked hydrogen jets with larger poloidal currents . . . 66

3.1 A graph explanation of Rayleigh-Taylor instability . . . 70

3.2 Images of Rayleigh-Taylor instability in the kinked plasma jet 73
3.3 Sketch of the plasma jet configuration in a lateral gravity 75
3.4 largest eigenvalue of truncated matrix $\mathbf{Q}_p$ as a function of largest allowed mode number p 88
3.5 Instability growth rate as a function of axial perturbation wave number/wavelength for the argon and hydrogen plasma jet 93
3.6 Spectra of the fastest growing eigen-perturbation 95
3.7 Pattern of fastest growing eigen-perturbation of argon and hydrogen jet . . . 97
3.8 yz cross-sectional view of the velocity and magnetic field of the fastest growing eigen-perturbation of argon jet solution 98
3.9 xy cross-sectional view of the fastest growing eigen-perturbation of argon jet 99
3.10 Comprehensive solutions of the RT-CD coupled instability in the (α, Φ^2) parameter space 101
3.11 Sketches of curved flux rope and lateral Rayleigh-Taylor instabilities 104
3.12 SDO/AIA 171 EUV images of a CME in active region NOAA 11163, 02/24/2011 106

4.1 Sketch of 2D X-point type Sweet-Parker reconnection 121
4.2 3D magnetic field measurements of shot 17012 127
4.3 Composite images of EUV emission and visible light of the kinked argon jet undergoing Rayleigh-Taylor instability 129
4.4 IV characteristics of shot 17012 129
4.5 3D magnetic field measurements of shot 16940 131
4.6 IV characteristics of shot 16940 132
4.7 Phases of the high-frequency magnetic fluctuations of shot 16940 133
4.8 Phases of the high-frequency magnetic fluctuations of shot 17012 134
4.9 Spectrograms of the 3D magnetic fluctuations of shot 17012 and 16940 . . . 135
4.10 10 MHz magnetic fluctuations from 29 to 30 μs in shot 17012 exhibits circular polarization in hodogram 137
4.11 Hodograms of 9 MHz and 12 MHz fluctuations in shot 17012 138
4.12 Polarization recognition of shot 16940, 17012, and 17014 141
4.13 Direction of wavevectors of shot 17012 in time-frequency domain 142
4.14 Angles between wavevector and magnetic field of shot 16940 and 17014 . . . 143

5.1 A simple equivalent circuit diagram of B-dot probe. 147
5.2 B-dot probe sensitivity as a function of frequency 149
5.3 Unwanted capacitive coupling and RF ground loop in high-speed diagnostics 150
5.4 Sketches of shielded loop probe and dummy probe 153
5.5 RF Ground loop diverting technique 154
5.6 Effective schematics of the RF Ground loop for signal current and RF ground current 155
5.7 Dummy probe test results with RF ground current diverting technique 156
5.8 Sketch of a pair of magnetic probes facing opposite direction 159
5.9 Sketch of three pairs of dual differential probes enclosed in a quartz tube . . 160
5.10 Drawing of the vacuum assembly of the 3D magnetic probe 161
5.11 Pictures of the shielded loop probe and the 3D magnetic probe 161
5.12 Picture of the ferrite cores and shunt cables 162
5.13 Output of the dual probes in Helmholtz coil 164
5.14 Calibration of the high-speed 3D magnetic probe 165
5.15 Magnetic fluctuations measured in shot 17012 167
5.16 Output of each components of the dual probes in shot 17012 168

6.1 Circuit diagram of the transmitter and receiver of the high voltage probe . . 173
6.2 Three dimensional cross-section drawing of the transmitter without HV capacitor C2. 174
6.3 Sketches of the lab-made cylindrical HV capacitor 174
6.4 HV probe calibration result with C2= 60 pF 179
6.5 Measurement results of shot 9950 using both the optically coupled HV probe and a Tektronix probe 181
6.6 Optically coupled floating HV probes in use in the cross-flux-tube experiment, arched-loop experiment, and RF pre-ionized plasma jet experiment 181

A.1 Peak transmission rate and FWHM of the tunable filter as a function of central wavelength. 188
A.2 Sketches of the plasma initial configuration and two possible configurations after merging 189
A.3 Setup of the two-color imaging of the plasma jet filled by nitrogen and argon. 189

A.4 Two-color imaging of the dual-species plasma jet using the VariSpec tunable filter 190

B.1 Demonstration of the FIR bandpass digital filters 197

B.2 An example of principal component analysis 199

List of Tables

2.1 Normalization units for Experimental H/Ar Jet Simulation and AGN Jet Simulation 27
2.2 Location of return current of simulations with different initial density distribution 63

Chapter 1

Background and Introduction

A plasma is an ionized gas containing freely moving ions and electrons and possibly neutral atoms. The charged particles in the plasma collide with other charged particles via Coulomb interaction. Motion of electrons and ions creates an electric current that further generates a magnetic field. On the other hand, an external magnetic field or self-generated magnetic field exerts a Lorentz force on the plasma when applied on the electric current. The coupling of electromagnetic forces and fluid effects leads to complex behaviors of the plasma.

The majority of the observable matter in the universe is in the plasma state, including stars, planetary nebulae, interstellar media, solar corona, solar wind, magnetosphere, etc. Man-made terrestrial plasmas are found in controllable fusion experiments and other plasma research experiments, plasma display, semi-conductor processing/manufacturing, and so on. Studying plasma is crucially important, not only for improving its existing usages in civilian applications, but also for solving human beings' long-term sustainable energy problem, and for understanding the behaviors of the most abundant state of baryonic matter of our universe.

1.1 Magnetohydrodynamic theory

Magnetohydrodynamic (MHD) theory gives the simplest description of plasma dynamics. The theory couples fluid dynamics and electromagnetism by treating plasma as a single

conductive fluid. The Eulerian form of the MHD equations in SI units are

$$\text{continuity equation} \quad \frac{\partial \rho}{\partial t} + \nabla \cdot (\rho \mathbf{v}) = 0 \tag{1.1}$$

$$\text{equation of motion} \quad \rho \left(\frac{\partial \mathbf{v}}{\partial t} + \mathbf{v} \cdot \nabla \mathbf{v} \right) = \mathbf{J} \times \mathbf{B} - \nabla P \tag{1.2}$$

$$\text{Ohm's law} \quad \mathbf{E} + \mathbf{v} \times \mathbf{B} = \eta \mathbf{J} \tag{1.3}$$

$$\text{Faraday's law} \quad \nabla \times \mathbf{E} = -\frac{\partial \mathbf{B}}{\partial t} \tag{1.4}$$

$$\text{Ampere's law} \quad \nabla \times \mathbf{B} = \mu_0 \mathbf{J} \tag{1.5}$$

$$\text{energy equation} \quad \frac{d}{dt} \left(\frac{P}{\rho^\gamma} \right) = 0, \tag{1.6}$$

where ρ is the plasma density, $\mathbf{v}$ is the bulk plasma velocity (velocity of center of mass of electrons and ions), P is the plasma pressure, $\mathbf{E}$, $\mathbf{B}$, and $\mathbf{J}$ are respectively the electric field, magnetic field, and current density vectors, η is the plasma resistivity, and $\gamma = 5/3$ is the adiabatic index for sufficiently collisional plasma.

The continuity equations, equation of motion, and energy equation are similar to those in hydrodynamics except that the equation of motion contains the Lorentz force. Ampere's law is same as in the Maxwell's equations in the non-relativistic limit.

Plasma that can be described by MHD equations must satisfy the following conditions:

- The plasma is charge-neutral. A charged particle in the plasma attracts oppositely charged particles surround it like a charge shield. It can be shown that the charge-neutrality is true when the characteristic lengths of the plasma dynamics are much longer than Debye length $\lambda_D = \sqrt{\frac{\epsilon_0 \kappa_B T}{nq^2}}$, where n is the particle number density and q is the particle charge [e.g., see § 1.6 in Ref. 5].

- The plasma is sufficiently collisional so that the particle distribution is Maxwellian and the plasma can be treated as a single fluid. This is true for plasma dynamics that are much slower than the particle collision rate.

- The plasma phenomenon is nonrelativistic, so no relativistic effect shows up in the MHD theory. For example, the pre-Maxwell version of Ampere's law is used in MHD, which does not include the displacement current $\mu_0 \epsilon_0 \frac{\partial \mathbf{E}}{\partial t}$ [1]. We assume l_{char} and

[1] In fact, relativistic MHD equations are often used for many astrophysical situations, such as active galactic nucleus (AGN) jets [40]. In this thesis we will only use the non-relativistic version of the MHD equations to study the plasma dynamics in the Caltech Bellan group experiment and relevant topics.

t_{char} as respectively the characteristic length scale and time scale for a given plasma phenomenon. Faraday's law (Eq. 1.4) then gives $E/l_{char} \sim B/t_{char}$. The ratio of the displacement current to the left-hand side of Eq. 1.5 is then

$$\frac{|\mu_0\epsilon_0\frac{\partial \mathbf{E}}{\partial t}|}{|\nabla \times \mathbf{B}|} \sim \frac{E/t_{char}}{c^2 B/l_{char}} \sim \frac{(l_{char}/t_{char})^2}{c^2},$$

where we have used $c = (\mu_0\epsilon_0)^{-1/2}$. Therefore, the displacement current term is ignorable for non-relativistic phenomena having $l_{char}/t_{char} \ll c$.

- The characteristic time scale for a given plasma dynamics is much longer than the electron and ion cyclotron period $1/\omega_{c\sigma} = m_\sigma/(eB)$ where $\sigma = e$ or i. Equation 1.2 shows that when the Lorentz force dominates the plasma dynamics there is $J \sim \omega\rho U/B$. Here ω is the characteristic frequency of the dynamics. Hence $J/(ne) \sim \omega m_i U/(eB) = \omega U/\omega_{ci} \ll U$ if $\omega \ll \omega_{ci}$. Therefore the differential velocity of electrons and ions are much slower than the plasma bulk velocity. Equivalently speaking, the electron and ion motions are well coupled. This condition also leads to the fact that the Hall term in the electron equation of motion can be ignored to give the MHD Ohm's law (see § 4.1.2 for details).

- The pressure and density gradients are parallel, so there is no thermoelectric effect (also see § 4.1.2).

We emphasize here that MHD theory is not a simple combination of fluid dynamics and Maxwell's equations. In fact, MHD equations are derived from two-fluid theory by coupling electrons and ions into a single fluid. Two-fluid theory regards electrons and ions as two individual flows and considers their own dynamics and interactions (Ref. [5] § 2.5). Two-fluid theory is often a more appropriate theory than MHD theory to describe small-scale fast-paced plasma dynamics. We will discuss two-fluid theory in Chapter 4 primarily in the context of whistler wave and fast magnetic reconnection. A more fundamental description of plasma dynamics is the Vlasov equation, which considers the evolution of particle distribution in the space-velocity phase space subject to particle motion, collision, and Lorentz force (Ref. [5] § 2.3). The continuity, momentum, and energy transport equations of two-fluid theory and MHD theory result from the zeroth, first, and second momentum integration of the Vlasov equations.

1.1.1 Lorentz force and force-free configuration

Substitute Ampere's law into the Lorentz force to obtain

$$\begin{aligned} \mathbf{J}\times\mathbf{B} &= \frac{1}{\mu_0}(\nabla\times\mathbf{B})\times\mathbf{B} \\ &= \frac{1}{\mu_0}\mathbf{B}\cdot\nabla\mathbf{B}-\nabla\left(\frac{B^2}{2\mu_0}\right), \end{aligned} \tag{1.7}$$

where we have used the vector calculus identity $\nabla(\mathbf{C}\cdot\mathbf{D})=(\mathbf{C}\cdot\nabla)\mathbf{D}+(\mathbf{D}\cdot\nabla)\mathbf{C}+\mathbf{C}\times(\nabla\times\mathbf{D})+\mathbf{D}\times(\nabla\times\mathbf{C})$. Write $\mathbf{B}=B\hat{B}$ and $\nabla\mathbf{B}=\nabla(B\hat{B})=(\nabla B)\hat{B}+B(\nabla\hat{B})$. Therefore

$$\begin{aligned} \mathbf{J}\times\mathbf{B} &= \frac{1}{\mu_0}\mathbf{B}\cdot\nabla\mathbf{B}-\nabla\left(\frac{B^2}{2\mu_0}\right) \\ &= \frac{B^2}{\mu_0}\hat{B}\cdot\nabla\hat{B}+\hat{B}\cdot\left(\nabla\frac{B^2}{2\mu_0}\right)\hat{B}-\nabla\left(\frac{B^2}{2\mu_0}\right) \\ &= \frac{B^2}{\mu_0}\hat{B}\cdot\nabla\hat{B}-\nabla_\perp\left(\frac{B^2}{2\mu_0}\right), \end{aligned} \tag{1.8}$$

where $\nabla_\perp$ is the gradient perpendicular to the magnetic field direction. It can be shown that $\hat{B}\cdot\nabla\hat{B}=-\hat{R}/R$, where $1/R$ is the local curvature of the field line and $\hat{R}$ goes from the center of curvature to the field line, and hence the first term describes a force that tries to straighten out the curved magnetic field line. This tension-like component $\frac{B^2}{\mu_0}\hat{B}\cdot\nabla\hat{B}$ is called the pinch force. The other pressure-like component of the Lorentz force $\nabla_\perp\left(\frac{B^2}{2\mu_0}\right)$ is called the hoop force. Both components are perpendicular to the magnetic field line.

Force-free configuration is an arrangement of plasma that satisfies

$$\nabla\times\mathbf{B}=\alpha\mathbf{B}, \tag{1.9}$$

where α is a scalar that might be spatially dependent. According to Ampere's law, the force-free configuration has $\mathbf{J}=\frac{1}{\mu_0}\nabla\times\mathbf{B}=\frac{\alpha}{\mu_0}\mathbf{B}\parallel\mathbf{B}$ so $\mathbf{J}\times\mathbf{B}=0$. Therefore no Lorentz force acts on the plasma in the force-free configuration.

Equation 1.9 indicates that a force-free configuration must be three-dimensional because the curl of a two-dimensional $\mathbf{B}$ has component perpendicular to $\mathbf{B}$.

Take the divergence of Eq. 1.9 so the left hand side becomes zero. There is

$$0=\nabla\cdot(\alpha\mathbf{B})=\alpha\nabla\cdot\mathbf{B}+\mathbf{B}\cdot\nabla\alpha=\mathbf{B}\cdot\nabla\alpha. \tag{1.10}$$

Therefore $\mathbf{B} \perp \nabla\alpha$, so α remains constant along magnetic field lines.

1.1.2 Ideal MHD magnetic flux frozen-in condition

Ohm's law can be interpreted in two different aspects. One is to consider the traditional Ohm's law in the plasma frame

$$\mathbf{E}' = \eta \mathbf{J}' \tag{1.11}$$

and then switch to the lab frame using Lorentz transform in the low-speed limit

$$\mathbf{E}' = \mathbf{E} + \mathbf{v} \times \mathbf{B} \tag{1.12}$$

$$\mathbf{J}' = \mathbf{J}. \tag{1.13}$$

Another aspect is to consider the electron equation of motion in two-fluid theory. After dropping the electron inertia term, the Hall term, and the pressure term, the electron equation of motion is reduced to Eq. 1.3. A detailed discussion will be given in § 4.1.2.

In thermal equilibrium, Fokker-Planck theory shows that the resistivity of a fully ionized plasma is [e.g., see § 13.3 in Ref. 5]

$$\eta = \frac{\pi Z e^2 m_e^{1/2} \ln\Lambda}{(4\pi\epsilon)^2 (\kappa_B T)^{3/2}} = 1.03 \times 10^{-4} \frac{Z \ln\Lambda}{T_e^{3/2}} \text{ Ohm} \cdot \text{m}, \tag{1.14}$$

where Z is the ionization of ions, m_e is the electron mass, ϵ_0 is the vacuum electric permittivity, $\ln\Lambda$ is the Coulomb logarithm and is usually taken to be 10[2], κ_B is the Boltzmann constant, T is the plasm temperature in Kelvin, and T_e is the plasma temperature in eV. Equation 1.14 is called Spitzer resistivity [105]. It is seen that $\eta \propto T^{-3/2}$, meaning that higher temperature plasma has lower resistivity. This is because free electrons and ions with larger kinetic energy are less vulnerable to Coulomb interaction (collision) with other charged particles. Most astrophysical plasmas and many experimental plasmas have very high temperature and so very low resistivity.

[2]The parameter Λ is defined as $\Lambda = \lambda_D / b_{\pi/2}$, where λ_D is the Debye length previously defined in § 1.1, and $b_{\pi/2} = Ze^2/(4\pi\epsilon_0 m_e v_0^2)$ is the impact parameter of 90°-angle collisions of a Ze charged ion seen by electrons with velocity v_0. It can be shown that $\Lambda = 6\pi n \lambda_D^3$, where n is the plasma particle number density. Therefore, Λ is a measure of number of particles in a sphere having a radius equal to the Debye length. Dependent on density and temperature, Λ can take value ranged from 10^2 to 10^{11} in different plasmas. However, the logarithm operation makes $\ln\Lambda$ lie in the range $5 - 25$. When an order-of-magnitude estimate suffices, it is usually assumed that $\ln\Lambda \sim 10$. More detailed discussions can be found in § 1.8 and § 1.12 in Ref. [5].

Ideal MHD theory takes the zero resistivity limit $\eta = 0$ so an ideal MHD plasma behaves like a superconductor. One of the most important properties of ideal MHD is that the magnetic flux is "frozen-in" to the plasma frame. To see this, we substitute Ampere's law and the resistive Ohm's law into Faraday's law and obtain the MHD induction equation

$$\frac{\partial \mathbf{B}}{\partial t} = \nabla \times (\mathbf{v} \times \mathbf{B}) + \frac{\eta}{\mu_0} \nabla^2 \mathbf{B}. \tag{1.15}$$

Therefore, changes in magnetic field are caused by plasma motion and resistive diffusion. In ideal MHD there is no magnetic diffusion, so

$$\frac{\partial \mathbf{B}}{\partial t} = \nabla \times (\mathbf{v} \times \mathbf{B}). \tag{1.16}$$

Consider a surface $\mathbf{S}(t)$ in the plasma that moves together with the plasma. The total magnetic flux through the surface is

$$\Psi(t) = \int_{S(t)} \mathbf{B}(\mathbf{x}, t) \cdot d\mathbf{s}, \tag{1.17}$$

where $d\mathbf{s}$ is the elementary surface area vector perpendicular to the surface. Therefore, the changing rate of Ψ is

$$\begin{aligned} \frac{d\Psi(t)}{d} &= \lim_{\delta t \to 0} \frac{\int_{S(t+\delta t)} \mathbf{B}(\mathbf{x}, t+\delta t) \cdot d\mathbf{s} - \int_{S(t)} \mathbf{B}(\mathbf{x}, t) \cdot d\mathbf{s}}{\delta t} \\ &= \lim_{\delta t \to 0} \frac{\int_{S(t+\delta t)} \left(\mathbf{B}(\mathbf{x}, t) + \delta t \frac{\partial \mathbf{B}(\mathbf{x}, t)}{\partial t} \right) \cdot d\mathbf{s} - \int_{S(t)} \mathbf{B}(\mathbf{x}, t) \cdot d\mathbf{s}}{\delta t} \\ &= \lim_{\delta t \to 0} \frac{\int_{S(t+\delta t)} \mathbf{B}(\mathbf{x}, t) \cdot d\mathbf{s} - \int_{S(t)} \mathbf{B}(\mathbf{x}, t) \cdot d\mathbf{s}}{\delta t} + \int_{S(t)} \frac{\partial \mathbf{B}(\mathbf{x}, t)}{\partial t} \cdot d\mathbf{s}. \end{aligned} \tag{1.18}$$

Hence the flux changing rate is contributed by shifting of the surface (first term) and changing of the magnetic field through the surface (second term). Denote $d\mathbf{l}$ as the boundary vector of $\mathbf{S}(t)$, and the differential area due to the shifting of $\mathbf{S}(t)$ at the boundary can be

written as $d\mathbf{s} = \mathbf{v}\delta t \times d\mathbf{l}$. The first term in Eq. 1.18 becomes

$$\begin{aligned}
& \lim_{\delta t \to 0} \frac{\int_{S(t+\delta t)} \mathbf{B}(\mathbf{x}, t) \cdot d\mathbf{s} - \int_{S(t)} \mathbf{B}(\mathbf{x}, t) \cdot d\mathbf{s}}{\delta t} \\
= & \lim_{\delta t \to 0} \frac{\oint_C \mathbf{B}(\mathbf{x}, t) \cdot (\mathbf{v}\delta t \times d\mathbf{l})}{\delta t} \\
= & \oint_C \mathbf{B} \cdot (\mathbf{v} \times d\mathbf{l}) \\
= & -\oint_C (\mathbf{v} \times \mathbf{B}) \cdot d\mathbf{l} \\
= & -\int_S \nabla \times (\mathbf{v} \times \mathbf{B}) \cdot d\mathbf{s}, \qquad (1.19)
\end{aligned}$$

where C is the boundary of S, and we have used the Stoke's theorem to convert the boundary integration to a surface integration. Substitute this equation back to Eq. 1.18 and get

$$\frac{d\Psi(t)}{d} = \int_S \left(\frac{\partial \mathbf{B}}{\partial t} + \nabla \times (\mathbf{v} \times \mathbf{B}) \right) \cdot d\mathbf{s} = 0. \qquad (1.20)$$

Therefore, the magnetic flux enclosed by a closed material line is constant. It is usually stated (though not very rigorously) that the magnetic field line is "frozen-in" the plasma.

1.1.3 Dimensionless nature of ideal MHD

Ideal MHD has a very important property that it does not have any intrinsic scale. Equations 1.1-1.6 are all written with dimensional variables. We define three nominal quantities: length L, magnetic field B_0 and plasma density ρ_0. Then we define several nominal quantities dependent on L, B_0, and ρ_0, which are velocity $v_A = B_0/\sqrt{\mu_0 \rho_0}$, time $t_0 = L/v_A$ and pressure $P_0 = B_0^2/\mu_0 = \rho_0 v_A^2$. After normalizing to these nominal quantities, the dimensionless version of the MHD equations are

$$\begin{aligned}
\frac{\partial \tilde{\rho}}{\partial \tilde{t}} + \tilde{\nabla} \cdot (\tilde{\rho} \tilde{\mathbf{v}}) &= 0 & (1.21) \\
\tilde{\rho} \left(\frac{\partial \tilde{\mathbf{v}}}{\partial \tilde{t}} + \tilde{\mathbf{v}} \cdot \tilde{\nabla} \tilde{\mathbf{v}} \right) &= (\tilde{\nabla} \times \tilde{\mathbf{B}}) \times \tilde{\mathbf{B}} - \tilde{\nabla} \tilde{P} & (1.22) \\
\frac{\partial \tilde{\mathbf{B}}}{\partial \tilde{t}} &= \tilde{\nabla} \times (\tilde{\mathbf{v}} \times \tilde{\mathbf{B}}) + \frac{1}{S} \tilde{\nabla}^2 \tilde{\mathbf{B}}, & (1.23)
\end{aligned}$$

where the tilde ($\tilde{}$) denotes the normalized physical quantities or operations. For example, $\tilde{\rho} = \rho/\rho_0$ and $\tilde{\nabla} = L\nabla$. The nominal v_A is called the Alfvén velocity, which is the velocity of

Alfvén wave propagating along the magnetic field lines. The Lundquist number is introduced as

$$S = \frac{\mu_0 v_A L}{\eta}. \tag{1.24}$$

In the reduced MHD equations, the Lundquist number S is the only scale-dependent parameter. However, S is usually very large for most astrophysical and space plasma ($S > 10^{10}$) and laboratory plasma ($S = 10^2 - 10^8$), especially in fusion research experiments, because these plasma usually have very fast Alfvén velocity and low resistivity, due to the strong magnetic field and high temperature. $S \gg 1$ is equivalent to saying that the magnetic diffusion is ignorable compared to the magnetic convection in the dynamics. In this case the last term in the reduced MHD equations can be dropped. Therefore we obtain a set of dimensionless ideal MHD equations that are independent on the scale of the plasma.

One evidence of the scalability of ideal MHD is that astrophysical jets of vastly different scales and lifetimes are found to have very similar morphology, kinetic behavior, and magnetic field structure [30, 45]. Arched flux rope structures that are found in solar corona can also be created in the lab experiment [107]. These facts indicate that the underlying physics of these plasma phenomena are described by ideal MHD.

The dimensionless nature of ideal MHD suggests that plasma dynamics of very large scales, such as astrophysical plasma, can be studied at a much smaller scale, such as in a terrestrial experiment, as long as the ideal MHD conditions are satisfied. A terrestrial experiment has several advantages over passive astrophysical observation, including the possibility of adjusting plasma parameters (i.e., active experiment) and in-situ diagnostics. Compared to numerical simulation, lab experiment includes real plasma effects. In the past decade there have been a rapidly increasing number of studies of using laboratory experiments to study astrophysics. In 2012, a new division, Division of Laboratory Astrophysics Division (LAD), was established in American Astronomical Society (AAS). "Laboratory astrophysics" has become an important branch in the modern astrophysical research.

In chapter 2, we will normalize a typical Active Galactic Nucleus jet and the Caltech experimental plasma jet individually. We find that after normalization the two plasma jets are very similar to each other, despite the fact that in reality these two objects are dramatically different in scale.

1.1.4 Magnetic helicity and Taylor state

Magnetic helicity is an important concept of MHD plasma, and is defined as

$$K = \int_V \mathbf{A} \cdot \mathbf{B} d^3 r, \tag{1.25}$$

where $\mathbf{A}$ is the vector potential of the magnetic field and the integration is performed over the entire volume V of the plasma. $\mathbf{A}$ is undefined with respect to a gauge, i.e., $\mathbf{A} + \nabla f$ gives the same magnetic field $\mathbf{B}$ as $\mathbf{A}$ with f being an arbitrary analytic scalar function. However, K turns out to be gauge invariant as long as no magnetic field line penetrates the surface S enclosing the volume V [5].

Magnetic helicity is a topological measure of number of linkages of magnetic flux tubes with each other and number of twists of magnetic field. Topologically the linkage and twist are the same concept.

Denote ϕ as the electrostatic potential. Using Faraday's law and $\mathbf{E} = -\nabla\phi - \partial_t \mathbf{A}$, we have

$$\begin{aligned}
\frac{\partial}{\partial t}(\mathbf{A} \cdot \mathbf{B}) &= \frac{\partial \mathbf{A}}{\partial t} \cdot \mathbf{B} + \mathbf{A} \cdot \frac{\partial \mathbf{B}}{\partial t} \\
&= -(\mathbf{E} + \nabla\phi) \cdot \mathbf{B} - \mathbf{A} \cdot (\nabla \times \mathbf{E}) \\
&= -\mathbf{E} \cdot \mathbf{B} - \nabla \cdot (\phi \mathbf{B}) - \nabla \cdot (\mathbf{E} \times \mathbf{A}) - \mathbf{E} \cdot (\nabla \times \mathbf{A}) \\
&= -2\mathbf{E} \cdot \mathbf{B} - \nabla \cdot (\phi \mathbf{B} + \mathbf{E} \times \mathbf{A}).
\end{aligned} \tag{1.26}$$

MHD Ohm's law Eq. 1.3 gives

$$\mathbf{E} \cdot \mathbf{B} = (\eta \mathbf{J} - \mathbf{U} \times \mathbf{B}) \cdot \mathbf{B} = \eta \mathbf{J} \cdot \mathbf{B}. \tag{1.27}$$

Substitute this equation to Eq. 1.26 and obtain

$$\frac{\partial}{\partial t}(\mathbf{A} \cdot \mathbf{B}) + \nabla \cdot (\phi \mathbf{B} + \mathbf{E} \times \mathbf{A}) + 2\eta \mathbf{J} \cdot \mathbf{B} = 0. \tag{1.28}$$

Integrate this equation over the entire volume V and apply Gauss's theorem to have

$$\frac{dK}{dt} + \int_S d\mathbf{s} \cdot (\phi \mathbf{B} + \mathbf{E} \times \mathbf{A}) = -2 \int_V \eta \mathbf{J} \cdot \mathbf{B} d^3 r. \tag{1.29}$$

For ideal MHD plasma the right-hand side of this equation is zero. Furthermore, if the ideal plasma is bounded by a conducting wall so that near the wall the magnetic field only has a tangential component and the electric field only has a normal component, the surface integral in the above equation then vanishes. Therefore, the magnetic helicity K is a conserved quantity in ideal MHD.

If the plasma is driven by a magnetized electrode system that has both electrostatic potential and magnetic field with normal component, the second integration is finite. Moreover, the definition of absolute helicity in Eq. 1.26 is gauge-dependent. However, the relative helicity

$$K_{rel} = \int_V (\mathbf{A} \cdot \mathbf{B} - \mathbf{A}_{vac} \cdot \mathbf{B}_{vac}) d^3 r \tag{1.30}$$

remains gauge invariant. It can be shown that the conservation law for the relative helicity is

$$\frac{dK_{rel}}{dt} + \int_{\partial V} (2V\mathbf{B}) \cdot d\mathbf{s} = -2 \int_V \eta \mathbf{J} \cdot \mathbf{B} d^3 r, \tag{1.31}$$

where ∂V is surface of the electrodes [3, 61]. Therefore, helicity can be injected into a plasma by maintaining an electrostatic potential across two electrodes and having external magnetic field threading into the plasma.

Without external helicity injection, the magnetic helicity of an ideal MHD plasma is conserved. Woltjer-Taylor relaxation is a process where a plasma relaxes to a final state with minimum magnetic energy $W_B = \int_V \frac{B^2}{2\mu_0} d^3 r$ while conserving the magnetic helicity. Variational method shows that for a zero-pressure plasma the minimum-energy state satisfies

$$\nabla \times \mathbf{B} = \lambda \mathbf{B}, \tag{1.32}$$

where λ is a spatially uniform constant [121]. Magnetic reconnection dissipates magnetic energy but conserves helicity and therefore provides a mechanism for this relaxation [114]. The final state is called the Taylor state. Comparing with Eq. 1.9 it is seen that the Taylor state is a special force-free state.

One approach to magnetic confinement fusion is to confine a plasma in its Taylor state in order to achieve long confinement time, because the Taylor state is the lowest energy state and also a force-free state. One famous candidate is the Spheromak, a toroidal-shape 3D plasma that satisfies Eq. 1.32. Compared to the tokamak, the Spheromak requires a

greatly simpler facility. Meanwhile, the Spheromak is not susceptible to many instabilities that exist in Tokamak because of the different confinement concept.

1.2 Overview of Caltech plasma jet experiment

1.2.1 Experiment setup and jet dynamics

The Caltech experimental plasma jet is generated using a planar magnetized coaxial plasma gun mounted at one end of a 1.48 m diameter, 1.58 m long cylindrical vacuum chamber (sketch in Fig. 1.1). The coaxial gun is similar to those used for creating the Spheromak [34]. We define the central axis perpendicular to the electrodes as the z axis of a cylindrical coordinate system. The electrode plane is defined as $z = 0$. The radial and axial directions are called the "poloidal" direction and the azimuthal direction θ is called the "toroidal" direction. The vacuum pressure is $\sim 10^{-7}$ torr, corresponding to a background particle density of 3×10^{15} m^{-3} at room temperature. The plasma gun has a 19.1 cm diameter disk-shaped cathode and a co-planar annulus-shaped anode with inner diameter $d = 20.3$ cm and outer diameter $D = 51$ cm. At time $t = -10$ ms, a circular solenoid coil behind the cathode electrode generates a dipole-like poloidal background magnetic field for ~ 20 ms, referred to as the bias field. The total poloidal field flux is about 1.5 mWb. At $t = -1$ ms to -5 ms, neutral gas is puffed into the vacuum chamber through eight evenly spaced holes at $r = 5$ cm on the cathode and eight holes at $r = 18$ cm on the anode at the same azimuthal angles. At $t = 0$, a 120 μF 5 kV high voltage capacitor is switched across the electrodes. This breaks down the neutral gas into eight arched plasma loops spanning from the anode to the cathode following the bias poloidal field lines, a geometry analogous to "spider legs". At 0.6 μs after breakdown, a 4 kV pulse forming network (PFN) supplies additional energy to the plasma and maintains a total poloidal current at $60 - 80$ kA for ≈ 40 μs. A typical current and voltage measurement is given in Fig. 2.4.

Fast ion gauge measurements show that the neutral particle number density immediately before the plasma breakdown is $10^{19} - 10^{20}$ m^{-3} [79, 81]. When the eight arched plasma loops are initially formed (top frames in Fig. 1.2), the poloidal current and poloidal magnetic field in the loops are parallel to each other. However, the plasma is not a force-free system because of the toroidal magnetic field associated with the poloidal current. The inner segments of the eight arched loops, carrying parallel current from the anode to the cathode,

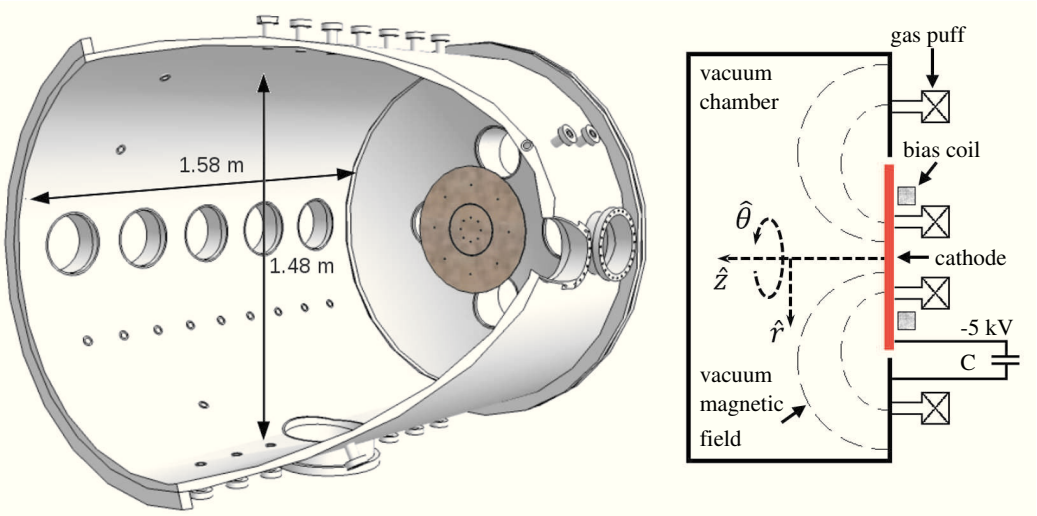

Figure 1.1: Left: 3D cross-sectional view of the vacuum chamber and the coplanar coaxial plasma gun. Right: sketch of the plasma gun and the cylindrical coordinate. The central thick plane is the cathode. The sketch is not to scale.

mutually attract each other by the Lorentz force and merge into a single collimated plasma tube along the z axis. A ten-fold density amplification in the jet due to collimation is observed by Stark broadening and interferometer measurements; these show the typical density of the collimated jet is $10^{22} - 10^{23}$ m^{-3} [63, 126, 127]. The poloidal magnetic field strength in the plasma is also amplified from < 0.05 T to ~ 0.2 T, indicating that the field is frozen into the plasma and is collimated together with the plasma. This amplification of the magnetic field strength has also been observed spectroscopically [102]. The thermal pressure and axial magnetic field pressure $B_z^2/(2\mu_0)$ increase until they balance the radial Lorentz force and lead to a nearly constant jet radius of $2 - 5$ cm (Fig. 1.2) and a toroidal magnetic field $B_\theta \sim 0.1 - 0.5$ T (see experimental measurements in Fig. 2.11). This radial equilibrium is gradually established from small to large z, resulting in an MHD pumping mechanism that accelerates the plasma towards the $+z$ direction to form a jet. The typical jet velocity is $10 - 20$ km s^{-1} for argon, $30 - 40$ km s^{-1} for nitrogen, and ~ 50 km s^{-1} for hydrogen [63].

The plasma jet, as a one-end-free current-conducting plasma tube, undergoes a kink instability to relax to a lower energy state when its length grows long enough to satisfy the classical Kruskal-Shafranov kink threshold [49, 50]. An intuitive approach to understand the kink instability is to consider the current-carrying plasma jet as an inductor. The energy stored in an inductor is $E = \Psi^2/(2L)$, where Ψ is the total magnetic flux and L is

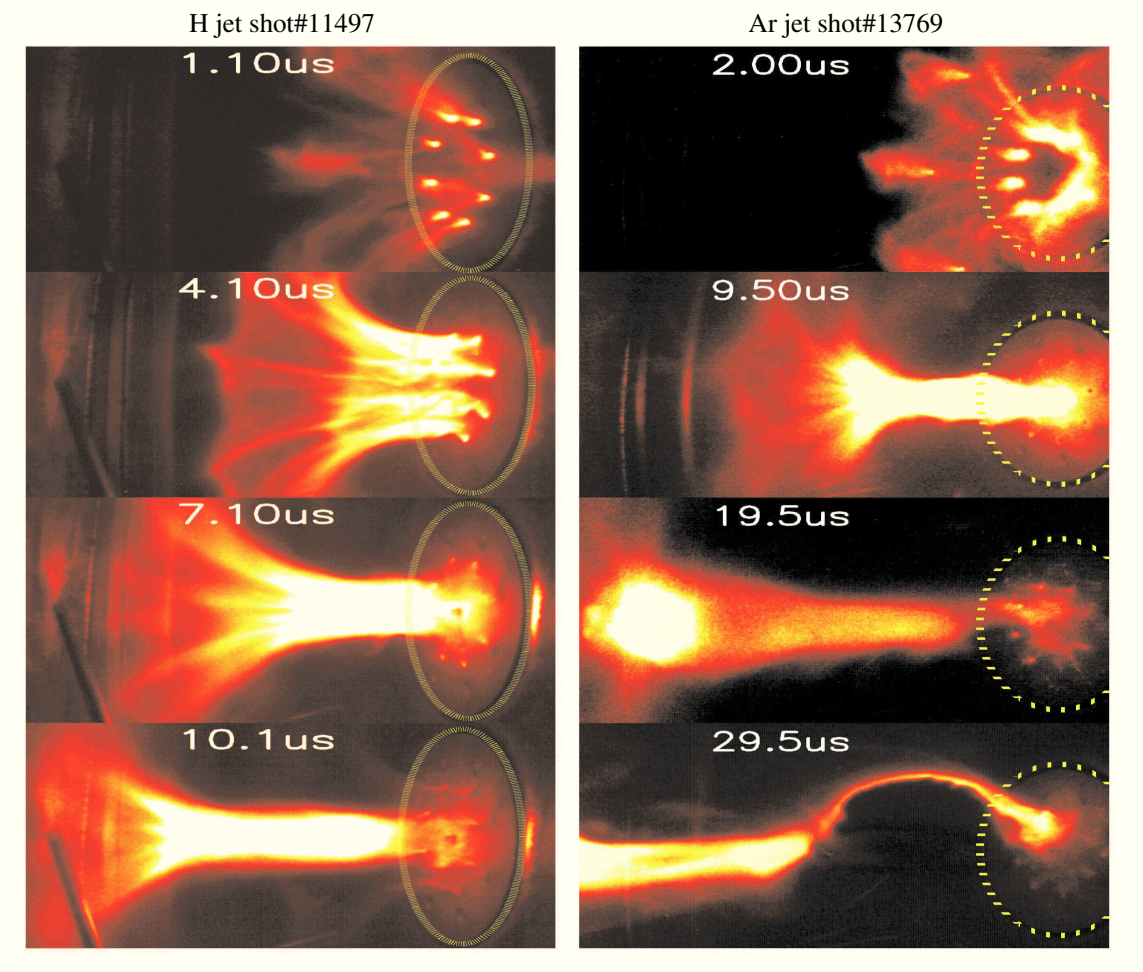

Figure 1.2: False color images showing the formation of a hydrogen plasma jet (left, shot 11497) and an argon plasma jet (right, shot 13769). The hydrogen shot only used the 120 μF 5 kV power supply and the argon one used the PFN in addition to the power supply. The images are taken by a high-speed visible-light IMACON 200 camera at two slightly different angles. The dotted circle at the right of each frame is the 10 cm radius central cathode.

the inductance of the plasma. In the plasma jet case, Ψ is the total toroidal flux. During the kink instability Ψ remains quasi-constant. Hence the plasma changes its shape from a straight column to a spiral solenoid to have a larger inductance and so relaxes to a lower energy state. A detailed theory of kink instability will be given in § 3.5.1, as a special case of a Rayleigh-Taylor-Current-Driven coupled instability. Kink instability is a fundamental current-driven MHD instability that occurs in many other current-driven systems, such as Tokamak, Z-pinch plasma, solar flux ropes, and astrophysical jets.

When the kink grows exponentially fast and accelerates the plasma laterally away from the central axis, an effective gravitational force due to the acceleration is experienced by the plasma jet. At the inner boundary of the kinked jet, where this effective gravity points from the displaced jet (dense plasma) to the z axis (zero-density vacuum), a Rayleigh-Taylor instability occurs [80]. The Rayleigh-Taylor instability eventually leads to a fast magnetic reconnection and destroys the jet structure. In Chapter 3 we will present an MHD theory of the Rayleigh-Taylor instability.

The jet life-time is ~ 10 μs for hydrogen, $20-30$ μs for nitrogen, and $30-40$ μs for argon. Because heating is not important during this short, transient lifetime, the plasma remains at a relatively low temperature, $T_e \sim 2$ eV, inferred from spectroscopic measurements [126]. Under typical experiment plasma conditions, the temperature relaxation time between electrons and ions is about 100 ns, less than 1% of the jet life time. Therefore, $T_i \approx T_e \sim 2$ eV. At this temperature, the plasma is essentially 100% singly ionized according to the Saha-Boltzmann theory, which is also confirmed by spectroscopic measurements [49, 126]. Figure 1.2 shows how the plasma is initially generated as eight arched loops, which then merge into one collimated jet. The jet then undergoes a kink instability when its length exceeds $\sim 30-40$ cm and the Kruskal-Shafranov kink threshold is satisfied [49, 50]. For the current experiment configuration, the radius-length ratio of the jet in the final stage is about $1:10$.

For a typical experimental plasma with $n_e = 10^{22}$ m^{-3}, $T_e = T_i = 2$ eV, $B = 0.2$ T and ion mass $\mu \equiv m_i/m_H$, the Debye length $\lambda_D \approx 10^{-7}$ m, the ion gyroradius $r_i \approx 0.7\sqrt{\mu}$ mm, and the ion skin depth $d_i \approx 2\sqrt{\mu}$ mm are all significantly smaller than the length/radius of the experimental jet. The typical thermal to magnetic energy density ratio is $\beta \approx 0.1-1$, showing that the magnetic field is essential to the jet dynamics. Despite its relatively low temperature, the plasma has sufficiently high conductivity so that the Lundquist (see § 1.1.3)

and magnetic Reynolds numbers $S \sim R_m \gtrsim 10^2 \times (L/0.3\text{ m})/\sqrt{\mu}$ are both much greater than one with $L \sim 0.3$ m being the length of the jet. Therefore, ideal MHD theory can describe jet global dynamics, such as collimation, acceleration, and kinking [49, 50, 61, 63, 126, 127], and magnetic field diffusion is negligible during the jet dynamics. The kinked jet image in Fig. 1.2 shows that the magnetic field is frozen into the plasma, consistent with ideal MHD theory. Therefore, the collimation of the bright plasma shown in Fig. 1.2 also demonstrates the collimation of the magnetic field. The secondary Rayleigh-Taylor instability, on the other hand, involves small-scale dynamics that are smaller than can be described by MHD theory [80].

1.2.2 Diagnostics and other apparatus

The transient experimental plasma jet varies from shot to shot, especially after the jet undergoes the kink instability. Therefore, measurements obtained by averaging over a large number of repeated single shots, which are commonly seen in other laboratory experiments, are not applicable in our experiment. Instead, high-speed diagnostics capable of resolving microsecond-scale plasma dynamics are required.

Diagnostic instrumentation used in the plasma jet experiment includes a high-speed visible-light IMACON 200 camera, a $30 - 60$ eV band extreme ultra-violet (EUV) optical system [17], a 12-channel spectroscopic system [126], a He-Ne interferometer perpendicular to the jet [62], a 20-channel 3D magnetic field probe array (MPA) along the r direction with adjustable z and ~ 1 μs response time [95], a whistler probe with excellent capacitive rejection and noise shielding (see Chapter 5), a Rogowski coil, and a Tektronix P6015A high-voltage probe. Figure. 1.3 gives a sketch of the system.

The data acquisition (DAQ) system contains 12 eight-channel Struck Innovative Systeme SIS3300 data acquisition boards. Each channel has a ± 0.5 V dynamic measurement range with 12-bit resolution and a sampling frequency of 100 MHz. Therefore, the digitization resolution of the DAQ system is $1/2^{12} = 0.244$ mV.

The lab also owns a collection of optical bandpass filters and a VIS-7-35 VariSpec liquid crystal tunable filter. These filters when mounted in front of the IMACON200 camera can turn the camera into a 2D fast framing spectroscopic system.

Detailed descriptions and reviews of most of the experiment diagnostics have already been included in the theses by Auna L. Moser [79], Deepak Kumar [61], and Carlos A.

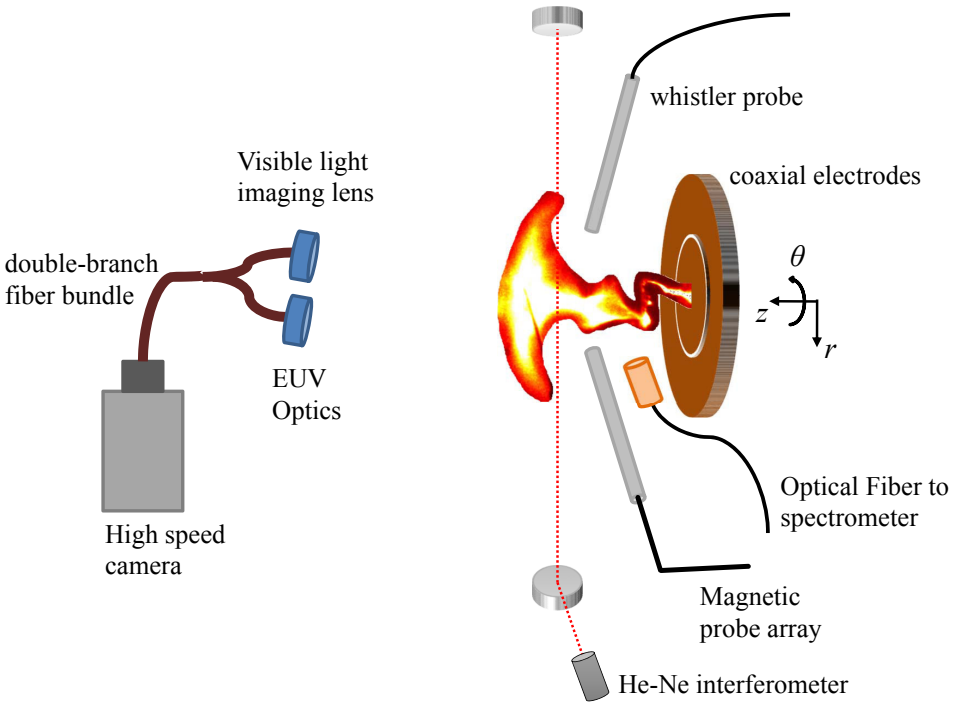

Figure 1.3: An overview of some diagnostics in the plasma jet experiment. Not to scale.

Romero Talamás [113]. In this section we will provide brief reviews of the fast framing IMACON 200 camera, the EUV optics built by Kil-Byoung Chai, and the VariSpec tunable filter. In Appendix A we give a detailed description and some interesting applications using the tunable filter.

1.2.2.1 High-speed IMACON 200 camera

The IMACON 200 camera is an ultra-high-speed camera manufactured by DRS Technologies. The IMACON camera contains an eight-way beam splitter system and seven functional monochrome 1360×1024-pixel 10-bit CCDs. Each of the CCDs records two images to give a movie of 14 frames in one experiment. The minimal inter-frame time between different CCDs is 5 ns and the waiting time between two frames of a single CCD is 200 ns. The IMACON 200 camera is sensitive to visible band and near-infrared band.

1.2.2.2 EUV optical system

Kil-Byoung Chai built an extreme ultra-violet optical system consisting of a Mo:Si multilayer mirror that focuses EUV photons to a P-46 YAG:Ce phosphor screen coated with a 50

nm Al film. The EUV optics converts EUV photons ranging from 30 eV to 60 eV ($20 - 40$ nm) to visible-light photons at an average converting efficiency of 5×10^{-4}. Detailed information about the EUV optics is described in Ref. [17]. The EUV optical system is mounted inside the vacuum chamber with the phosphor screen facing a window. The IMACON 200 camera is focused on the phosphor screen through the window and records the visible images converted from the EUV images. Another configuration is to use a double-branch fiber bundle to convey both the visible and EUV images simultaneously to the IMACON 200 camera, as shown in Fig. 1.3.

1.2.2.3 VariSpec liquid crystal tunable filter

The VariSpec liquid crystal tunable filter is an optical filter with transmitting wavelength electrically controllable from 400 nm to 720 nm. It is claimed that the tunable filter has an integral hot mirror that can reflect infrared photons because the thermal energy carried by the infrared photons can affect performance of the filter or even cause damages. However, we found that the filter can still transmit a significant amount of near-infrared photons that can be recorded by the IMACON 200 camera. Therefore, an external hot mirror is mounted in front of the tunable filter. In Appendix A we provide a detailed description of the tunable filter and show a two-color imaging of the plasma jet experiment using the tunable filter.

1.3 Overview of this thesis

In Chapter 1 we have presented some brief introduction to plasma physics, MHD theory, and the Caltech plasma jet experiment. A more detailed introduction regarding specific topics will be given individually in each chapter.

In Chapter 2 we will give a brief review of astrophysical jets and show the similarity between the plasma jet experiment and astrophysical jets in terms of electromagnetic configurations at the jet boundary and the global magnetic structure. We use an astrophysical magnetic tower model initially proposed by Lynden-Bell [74, 75] as the base model and present three-dimensional ideal MHD simulations of the plasma jet experiment. A localized magnetic energy and helicity injection is implemented in the simulation to mimic both the experimental and astrophysical situations. Detailed analysis to the simulation results and

comparison between the experiment and simulation give a comprehensive description of the jet collimation and acceleration processes. We study numerically the magnetic to kinetic energy conversion and obtain quantitative agreement between the simulation results and the experiment.

As shown in § 1.2.1, the plasma jet undergoes a global kink instability and then a secondary local Rayleigh-Taylor instability due to lateral acceleration of the kink instability. This Rayleigh-Taylor instability is very interesting because it occurs on a cylindrical surface of an MHD-collimated plasma tube and the direction of gravity is not always perpendicular to the interface. We found that the conventional hydrodynamic and magnetic Rayleigh-Taylor theories, which only consider 2D planar interface, give incorrect results when applied to our case. In Chapter 3 we use linear stability analysis to develop an MHD theory of the Rayleigh-Taylor instability on the cylindrical surface of a plasma flux rope in the presence of a lateral external gravity. The Rayleigh-Taylor instability is found to couple to the classic current-driven instability, resulting in a new type of hybrid instability. The coupled instability, produced by combination of helical magnetic field, curvature of the cylindrical geometry, and lateral gravity, is fundamentally different from the classic magnetic Rayleigh-Taylor instability occurring at a two-dimensional planar interface. The theory gives instability wavelengths and growth rates that match with experiments having several different configurations. We also show that this hybrid instability theory can be applied to many situations in solar physics.

Chapter 3 solves the Rayleigh-Taylor instability in the early phase when the linear stability analysis is still valid. In the experiment, however, this instability quickly evolves to a nonlinear phase and eventually leads to the failure of MHD. The Rayleigh-Taylor instability compresses and pinches the plasma jet to a scale smaller than the ion skin depth and then triggers a fast magnetic reconnection. In Chapter 4 we present measurements of high-speed magnetic fluctuations at the time of the reconnection and show that these fluctuations contain broadband right-hand circularly polarized whistler waves associated with the fast reconnection. With the specially designed high-speed 3D magnetic probe (Chapter 5), we are able to resolve the circular polarization of the whistler waves spontaneously generated in the fast magnetic reconnection.

Chapter 5 presents the philosophies and detailed designs of the high-speed 3D magnetic probe (whistler probe) that gives the magnetic fluctuations measurements in Chapter 4.

The whistler probe consists of six shielded loop B-dot probes made of semi-rigid coaxial cables. We implement an RF ground current diverting technique that was first used by Perkins & Bellan (2011) [89]. The whistler probe has a 70 dB rejection to electrostatic interference, making it ideal for high-speed time-dependent magnetic field detection in an extremely noisy environment such as the Caltech plasma jet experiment.

Chapter 6 presents an earth-isolated optically coupled DC-5 MHz wideband high voltage probe powered by solar cells under ambient lab light. The HV probe uses a lab-made 60 pF high-voltage capacitor and a commercial 100 nF low-voltage capacitor to form a $1000 : 0.6$ voltage divider. The divided low voltage is coupled into a LED driver that converts the voltage signal into an amplitude-modulated infrared signal. The AM light signal is conveyed through an optical fiber and then converted back to an electric signal at the data acquisition device. The transmitter is powered by a 30 μF capacitor pre-charged by solar cells under lab ambient light. Therefore, the high voltage probe is electrically isolated from earth ground. The HV probe is being used in the cross-flux-tube experiment and other experiments in the Caltech Bellan group.

Chapter 2

Three-Dimensional MHD Numerical Simulation of Caltech Plasma Jet Experiment

Magnetic fields are believed to play an essential role in astrophysical jets with observations suggesting the presence of helical magnetic fields. Here, we present three-dimensional (3D) ideal MHD simulations of the Caltech plasma jet experiment using a magnetic tower scenario as the baseline model. Magnetic fields consist of an initially localized dipole-like poloidal component and a toroidal component that is continuously being injected into the domain. This flux injection mimics the poloidal currents driven by the anode-cathode voltage drop in the experiment. The injected toroidal field stretches the poloidal fields to large distances, while forming a collimated jet along with several other key features. Detailed comparisons between 3D MHD simulations and experimental measurements provide a comprehensive description of the interplay among magnetic force, pressure, and flow effects. In particular, we delineate both the jet structure and the transition process that converts the injected magnetic energy to other forms. With suitably chosen parameters that are derived from experiments, the jet in the simulation agrees quantitatively with the experimental jet in terms of magnetic/kinetic/inertial energy, total poloidal current, voltage, jet radius, and jet propagation velocity. Specifically, the jet velocity in the simulation is proportional to the poloidal current divided by the square root of the jet density, in agreement with both the experiment and analytical theory. This work provides a new and quantitative method for relating experiments, numerical simulations, and astrophysical observation, and demonstrates the possibility of using terrestrial laboratory experiments to study astrophysical jets.

Primary part of this chapter was published by Xiang Zhai, Hui Li, Paul M. Bellan, and Shengtai Li, in Astrophysical Journal, Volume **791**:40, 2014 [130]. This work is under the collaboration between Bellan group in Caltech and Li group in LANL.

2.1 Introduction

Magnetohydrodynamic (MHD) plasma jets exist in a wide variety of systems, from terrestrial experiments to astrophysical objects, and have attracted substantial attention for decades. For example, energetic and usually relativistic jets are commonly observed, originating from active galactic nuclei (AGNs), which are believed to be powered by supermassive black holes. AGN jets usually remain highly collimated for tens to hundreds of kiloparsecs from the host galaxy core [30]. It is generally accepted that AGN jets are powered by the central black hole accretion disk region. On a much smaller scale, stellar jets are believed to be an integral part of star formation, with an active accretion disk surrounding a young star [45]. See Fig. 2.1.

Despite our limited understanding of how the disks or central objects produce collimated jets, observational evidence has shown that magnetic fields are crucial in collimating and accelerating jets. Highly polarized synchrotron radiation is observed from both AGN jets and stellar jets, implying that jets have a strongly organized magnetic field. For example, the two lobes of T Tauri S, created by the interaction of a bipolar stellar jet with the remote interstellar medium (ISM), exhibit strong circularly polarized radio emission with opposite helicity [93]. Large-scale magnetic fields from bipolar AGN jets also show transverse asymmetries [22]. These observations strongly suggest that a large-scale poloidal magnetic field, centered at the accretion disk or the central object, plays a crucial role in generating and propagating both AGN jets and stellar jets. A close look into the jet origin of M87 has found that the jet at 100 Schwarzschild radii is only weakly collimated (opening angle $\approx 60^\circ$), but becomes very collimated at larger distance (opening angle $< 10^\circ$). This favors a magnetic collimation mechanism at $z > 100$ Schwarzschild radii [56]. The 3C31 jet and several other AGN jets exhibit a global kink-like $m = 1$ instability or helical wiggles [43, 83] (also see Fig. 2.1 panel B), implying the existence of a strong axial current along the jet, or, equivalently, a strong toroidal magnetic field around the jet. Here, we define the central axis along the jet as the z axis of a cylindrical coordinate system. These facts suggest a z-pinch

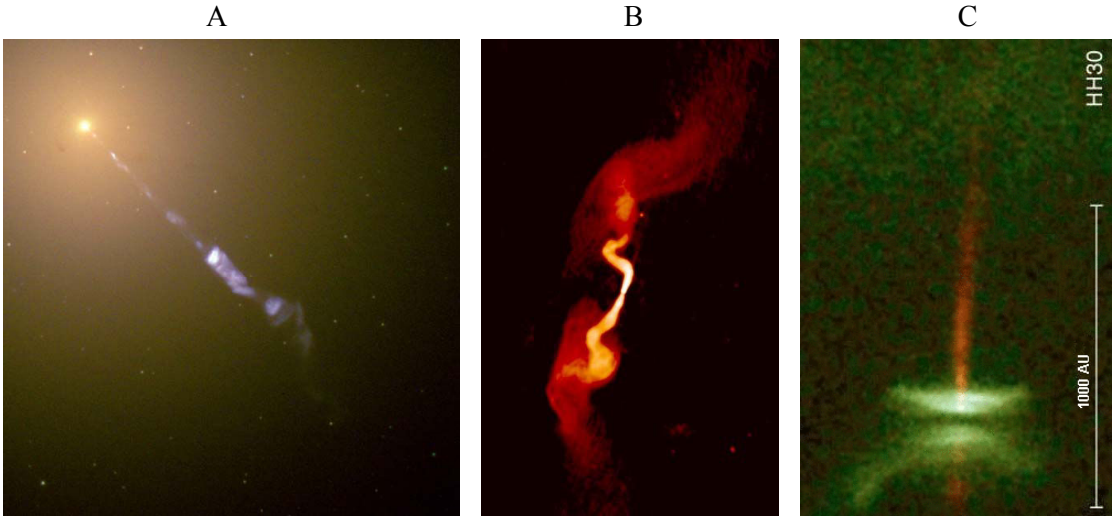

Figure 2.1: Panel A: Composite image of M87 AGN jet by Hubble Space Telescope. The yellow light are emissions from the host elliptical galaxy and the blue light are from synchrotron radiation by cyclotron motions of relativistic electrons. The length of the jet shown in the image is about 5000 light years or 5×10^{19} m. The jet is believed to be driven by a 3×10^9 solar masses supermassive black hole and the surrounding accretion disk [56]. Credit: J. A. Biretta et al., Hubble Heritage Team (STScI /AURA), and NASA. Panel B: False color image of radio galaxy 3C31 (NGC 383) and its jet in 1.4 GHz radial band by VLA. The wiggled jet stretches to a distance of 300 kpc or 10^{22} m. Credit: Laing et al., NRAO. Panel C: HH30 protostellar jet and the accretion disk by Hubble (Burrows, STSci/ESA, WFPC2, NASA). The length of the jet is about 1000 AU or 10^{14} m.

type of collimation mechanism, in which the axial current J_z and the associated azimuthal magnetic field B_θ generate a radial Lorentz force and squeeze the jet plasma against the pressure gradient at the central region of the jet.

The surprising similarities of astrophysical jets in morphology, kinetic behavior, and magnetic field configuration over vastly different scales have inspired many efforts to model these jets using ideal MHD theory. One important feature is that ideal MHD theory has no intrinsic scale (§ 1.1.3). Therefore, an ideal MHD model is highly scalable and capable of describing a range of systems having many orders of magnitude difference in size. Ideal MHD theory assumes that the Lundquist number, a dimensionless measurement of plasma conductivity, to be infinite. This leads to the well-known "frozen-in" condition, wherein magnetic flux is frozen into the plasma and moves together with the plasma [5] (see also § 1.1.2). Hence the evolution of plasma material and magnetic field configuration is unified in ideal MHD. Blandford & Payne (1982) [14] developed a self-similar MHD model, in which

a magnetocentrifugal mechanism accelerates plasma along poloidal field lines threading the accretion disk; the plasma is then collimated by a toroidal dominant magnetic field at larger distance. Lynden-Bell (1996,2003) [74, 75] constructed an analytical magnetostatic MHD model where the upward flux of a dipole magnetic field is twisted relative to the downward flux. The height of the magnetically dominant cylindrical plasma grows in this configuration. The toroidal component of the twisted field is responsible for both collimation and propagation. The Lynden-Bell (1996,2003) [74, 75] model and various following models, (typically numerical simulations with topologically similar magnetic field configurations; e.g., [68, 69, 73, 84, 122]), are called "magnetic tower" models. In these models, the large scale magnetic fields are often assumed to possess "closed" field lines with both footprints residing in the disk. Because plasma at different radii on the accretion disk and in the corona have different angular velocity, the poloidal magnetic field lines threading the disk will become twisted up [14, 69, 73, 74, 75, 100], giving rise to the twist/helicity or the toroidal component of the magnetic fields in the jet. Faraday rotation measurements to 3C 273 show a helical magnetic field structure and an increasing pitch angle between toroidal and poloidal component along the jet [128]. These results favor a magnetic structure suggested by magnetic tower models. Furthermore, it is (often implicitly) assumed that the mass loading onto these magnetic fields is small, so the communication by Alfvén waves is often fast compared to plasma flows.

These models have achieved various degrees of success and have improved understanding of astrophysical jets significantly. However, the limitations of astrophysical observation, e.g., mostly unresolved spatial features, passive observation, and impossibility of in-situ measurement, have imposed a natural limitation to these models. During the last decade, on the other hand, it has been realized that laboratory experiments can provide valuable insights for studying astrophysical jets. Laboratory experiments have the intrinsic value of elucidating key physical processes (especially those involving magnetic fields) in highly nonlinear systems. The relevance of laboratory experiments relies on the scalability of the MHD theory and the equivalence of differential rotation of the astrophysical accretion disk to voltage difference across the laboratory electrodes (at least in the magnetically dominated limit). The latter can be seen by considering Ohm's Law in ideal MHD theory, $\mathbf{E} + \mathbf{v} \times \mathbf{B} = 0$; $\mathbf{E}$ is the electric field and $\mathbf{v}$ is the plasma velocity. The radial component of Ohm's Law is $E_r + v_z B_\theta - v_\theta B_z = 0$. If we ignore the vertical motion v_z of the accretion

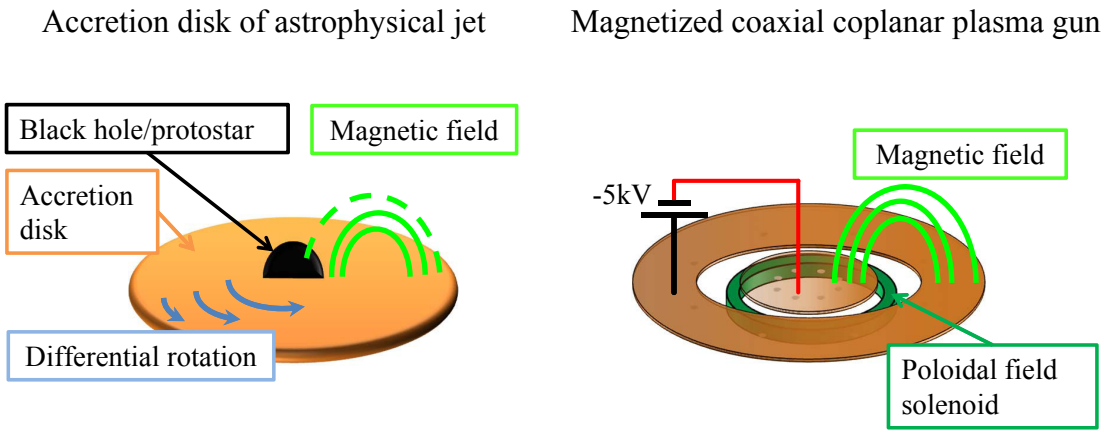

Figure 2.2: Analogy of accretion disk system of astrophysical jet and magnetized coaxial coplanar plasma gun.

disk, it is seen that $E_r = v_\theta B_z$, i.e., an equivalent radial electric field is created by θ motion (rotation), and spatial integration of this electric field gives the voltage difference at different radii. Such a voltage difference is relatively easy to create in lab experiments by applying a voltage across a coaxial electrode pair (See § 2.2.3 for the discussion on the helicity). Figure 2.2 shows the analogy of the magnetized coaxial coplanar plasma gun and the accretion disk system. Experimental jets are reproducible, parameterizable, and in-situ measurable. They automatically "calculate" the MHD equations and also "incorporate" non-ideal MHD plasma effects. Most importantly, the very fact that jets can be produced in the experiments strongly suggests there should be relatively simple unifying MHD concept characterizing AGN jets, stellar jets, and experimental jets [8].

The experiments carried out at Caltech [48, 63] and Imperial College [20, 21, 67] have used pulse-power facilities to simulate "magnetic tower" astrophysical jets. The two experiments have topologically similar toroidal magnetic field configurations and plasma collimation mechanisms. However, in addition to the toroidal field, the Caltech plasma jets also have a poloidal magnetic field threading a co-planar coaxial plasma gun so the global field configuration is possibly more like a real astrophysical situation. Magnetically driven jets are produced by both groups, and the jets are collimated and accelerated in essentially the same manner described by the magnetic tower models. Due to the lack of poloidal magnetic field, the plasma jets in the group at Imperial College undergo violent instability and break into episodic parts (magnetic bubbles). The Caltech jets remain very

collimated and straight and undergo a global kink instability when the jet length satisfies the classic Kruskal-Shafranov threshold [49, 50]. The Alfvénic and supersonic jets created by the Caltech group have relatively low thermal to magnetic pressure ratio $\beta \sim 0.1$ and large Lundquist number $S \sim 10 - 100$. Other features including flux rope merging, magnetic reconnection, Rayleigh-Taylor instability, and jet-ambient gas interaction are also produced [49, 50, 80, 81, 126, 127]. See § 1.2 for a detailed introduction to the Caltech plasma jet experiments.

Observation, analytical modeling, numerical simulation and terrestrial experiments (laboratory astrophysics) are all crucial approaches for a better understanding of astrophysical jets. Compared to observation or analytical models, numerical simulation and terrestrial experiments share certain common features, such as the ability to deal with more complex structures and sophisticated behaviors, larger freedom in the parameter space compared to observation, and more resolution. However, cross-validation between numerical simulations and experiments has been very limited. Lab experiments can provide detailed validation for numerical models, while the numerical models can test the similarity between the terrestrial experimental jets and astrophysical jets.

In this chapter we report 3D ideal MHD numerical studies that simulate the Caltech plasma jet experiment. The numerical model uses a modified version of a computational code [70] previously given by Li et al. (2006) [68] for simulating AGN jets in the intra-cluster medium. Motivated by both observations and experiments, we adopt the approach that the jet has a global magnetic field structure and both poloidal and toroidal magnetic fields in the simulation are totally contained in a bounded volume. Following the approach Li et al. (2006) [68], the MHD equations are normalized to suit the experiment scale. An initial poloidal field configuration is chosen to simulate the experimental bias field configuration and the toroidal magnetic field injection takes a compact form to represent the electrodes. Detailed comparisons between simulation and experiment have been undertaken, addressing the collimation and acceleration mechanism, jet morphology, axial profiles of density and magnetic field, and the 3D magnetic field structure. The simulations have reproduced most salient features of the experimental jet quantitatively, with discrepancies generally less than a factor of three for key quantities. The conversion of magnetic to kinetic energy from jet base to jet head is examined in the simulation and compared to the experiment. As a result, a Bernoulli-like equation, stating that the sum of kinetic and toroidal magnetic field energy

is constant along the axial extent of the jet, is validated by analytical modeling, laboratory experiment, and the numerical simulation.

The chapter is organized as follows: In § 2.2 we describe the approach and configuration of our simulation, and show that the compact toroidal magnetic field injection method used in the simulation is equivalent to the energy and helicity injection through the electrodes used in the experiment. In § 2.3.1, we present the simulation results of a typical run, and compare these results with experimental measurements. In § 2.3.2, we perform multiple simulations with different toroidal injection rates and examine the jet velocity dependence on poloidal current. These results together with experimental measurements confirm the MHD Bernoulli equation and the magnetic to kinetic energy conversion in the MHD driven plasma jet. In § 2.4 we discuss the sensitivity of the simulation results to initial and injection conditions. In § 2.5 we present some preliminary results of the numerical investigation to kink instability. Summary and discussions are given in § 2.6.

2.2 Numerical MHD simulations

Discussion in this chapter is restricted to the global axisymmetric behaviors of the jet, such as collimation and acceleration. In this section, we prescribe appropriate initial and boundary conditions used to solve the ideal MHD equations numerically for the Caltech plasma jet experiment.

2.2.1 Normalization and equations

Number density, length and velocity are scaled to nominal reference values. In particular, density is normalized to $n_0 = 10^{19}$ m^{-3}, lengths are normalized to $R_0 = 0.18$ m (radial position of the outer gas feeding holes of the plasma gun in the experiment), and velocities are normalized to the ion sound speed $C_{s0} = \sqrt{2kT/m_i} = 1.96 \times 10^4 \sqrt{m_H/m_i}$ m s^{-1} (with temperature 2 eV). All other quantities are normalized to reference values derived from these three nominal values and ion mass m_i. Table 2.1 lists the derivation and the normalization values adopted in the experimental hydrogen/argon jet simulation and the AGN jet simulation by Li et al. (2006) [68]. SI units are used for the lab experiment while cgs units are used for the AGN jet in order to facilitate comparison to respective experimental and astrophysical literature.

Table 2.1: Normalization units for Experimental H/Ar Jet Simulation and AGN Jet Simulation

Quantity unit	Quantity symbols	H ($\mu = 1$)	Ar ($\mu = 40$)	AGN jet ($\mu = 1$)
Length	R_0	0.18 m	0.18 m	15 kpc
Number density	n_0	10^{19} m^{-3}	10^{19} m^{-3}	3×10^{-3} cm^{-3}
Speed	C_{s0}	1.96×10^4 m s^{-1}	3.1×10^3 m s^{-1}	1.16×10^8 cm s^{-1}
Ion weight	$\mu = m_i/m_H$	1	40	1
Time	$t_0 = R_0/C_{s0}$	9.2 μs	58.2 μs	1.3×10^7 yr
Mass density	$\rho_0 = n_0 m_i/2$	8.4×10^{-9} kg m^{-3}	3.3×10^{-7} kg m^{-3}	2.5×10^{-30} g cm^{-3}
Pressure	$p_0 = \rho_0 C_{s0}^2$	3.2 pa	3.2 pa	3.4×10^{-11} erg cm^{-3}
Temperature	$k_B T = m_i C_{s0}^2/2$	2eV	2eV	7 keV
Energy	$E_0 = p_0 R_0^3$	0.0187 J	0.0187 J	3.4×10^{57} erg
Power	$P_0 = E_0/t_0$	2.0×10^3 Watt	321 Watt	2.6×10^{50} erg/yr
Magnetic field	$B_0 = \sqrt{\mu_0 p_0}$	0.002 T	0.002 T	2×10^{-5} Gauss
Magnetic flux	$\Psi_0 = B_0 R_0^2$	0.0648 mWB	0.0648 mWB	4.4×10^{40} G cm^2
Current density	$J_0 = B_0/(\mu_0 R_0)$	8.871×10^3 A m^{-2}	8.871×10^3 A m^{-2}	3.5×10^{-28} A cm^{-2}
Current	$I_0 = J_0 R_0^2$	2.874×10^2 A	2.874×10^2 A	7.6×10^{17} A
Voltage	$V_0 = P_0/I_0$	7.07 V	1.118 V	1.1×10^{18} V

The dimensionless ideal MHD equations, normalized to the quantities given in Table 2.1, can be written as

$$\frac{\partial \rho}{\partial t} + \nabla \cdot (\rho \mathbf{v}) = 0 \tag{2.1}$$

$$\frac{\partial (\rho \mathbf{v})}{\partial t} + \nabla \cdot (\rho \mathbf{v}\mathbf{v} + P_g \overleftrightarrow{\mathbf{I}} + P_B \overleftrightarrow{\mathbf{I}} - \mathbf{B}\mathbf{B}) = 0 \tag{2.2}$$

$$\frac{\partial e}{\partial t} + \nabla \cdot [(e + P_g + P_B)\mathbf{v} - \mathbf{B}(\mathbf{v} \cdot \mathbf{B})] = \dot{e}_{\text{inj}} \tag{2.3}$$

$$\frac{\partial \mathbf{B}}{\partial t} - \nabla \times (\mathbf{v} \times \mathbf{B}) = \dot{\mathbf{B}}_{\text{inj}}. \tag{2.4}$$

The momentum equation and the energy equation have been written in the form of conservation laws. We assume the same ion/electron temperature $T = T_i = T_e$. The particle number density $n = 2n_e = 2n_i$ is used assuming singly-ionized plasma. The ionization status is assumed to be time-independent. The equation of state for an ideal gas with adiabatic index $\gamma = 5/3$ is used. The gas pressure $P_g = n_i k_B T_i + n_e k_B T_e = n k_B T$ is then related to the thermal energy density by $e_{\text{thermal}} = P_g/(\gamma - 1)$. The magnetic pressure P_B,

or magnetic energy density e_B, is $P_B = e_B = B^2/(2\mu_0)$ and the total energy density is $e \equiv \rho v^2/2 + P_g/(\gamma - 1) + P_B$. Compared to the MHD equations given in the introduction Chapter, here we use the energy transportation equation 2.3 instead of the adiabatic energy equation 1.6. They are equivalent mathematically but the energy transportation equation is easier to implement in the finite-volume numerical computation algorithm since it is written in the form of a conservation law.

An injection term $\dot{\mathbf{B}}_{\text{inj}}$ is added to the induction equation. The associated dimensionless energy density injection is

$$\dot{e}_{\text{inj}} = \dot{\mathbf{B}}_{\text{inj}} \cdot \mathbf{B}, \tag{2.5}$$

where $\mathbf{B}$ is the magnetic field.

Simulations are performed in a 3D Cartesian coordinate system $\{x, y, z\}$ using the 3D MHD code as part of the Los Alamos COMPutational Astrophysics Simulation Suite [LA-COMPASS, 70]. The solving domain is a cube $[-4R_0, 4R_0]^3 = [-0.72\text{ m}, 0.72\text{ m}]^3$, similar to the vacuum chamber size in the experiment. Each Cartesian axis is discretized into 800 uniformly spaced grids, giving a total of 5.12×10^8 grid points. The spatial resolution $\Delta x = 8R_0/800 = 1.8$ mm in the simulation is significantly greater than the Debye length, and is similar to the ion gyroradius and the ion skin depth of the plasma jet in the experiment. A typical run takes 5 to 24 hr on the Los Alamos National Lab Turquoise Network using 512 processors.

In contrast to the experiment where the jet exists only for positive z, the simulation has a mirrored plasma jet in the negative z direction so as to have a bipolar system centered at $z = 0$ plane. The solving domain contains plasma only and has no plasma-electrode interaction region. Non-reflecting outflow boundary conditions are imposed at the boundaries (large x, y or z). The MHD equations are solved in Cartesian coordinates so that no computational singularity exists at the origin.

2.2.2 Initial condition

2.2.2.1 Initial global poloidal magnetic field

It is generally believed that the poloidal and toroidal magnetic component evolve together under the dynamo processes in accretion disk and surrounding corona. However, when the poloidal component varies slower than the toroidal component, it is possible to treat the

two components separately. In Lynden-Bell (1996, 2003) [74, 75], a poloidal field is assumed to be pre-existing, and the toroidal field is generated by twisting the upward flux relative to downward flux. During this process, the poloidal flux remains constant while toroidal field is enhanced with the increase of number of turns (helicity). These processes are realized equivalently in the lab experiment, where an initial dipole poloidal field is first generated by an external coil, and then helicity is increased by injecting poloidal current. In the simulation, an initial dipole poloidal magnetic field is similarly imposed, given by

$$\Psi_{\rm pol}(r,z) \equiv 2\pi\alpha_p \frac{r^2}{(l^2+a_0^2)^{3/2}} e^{-l^2}, \tag{2.6}$$

where $a_0 \equiv 0.623 R_0 = 11.2$ cm ($R_0 = 0.18$ m, see Table 2.1) and $l \equiv \sqrt{r^2+z^2}$ is the distance from the origin. This configuration is topologically similar to the initial poloidal flux $\Psi_{\rm pol} = r^2 e^{-l^2}$ adopted by Li et al. (2006) [68]. By default, simulation equations/variables will be written in dimensionless form with reference units given in Table 2.1. For example, Eq. 2.6 is the dimensionless version of $\Psi_{\rm pol}(r,z) = 2\pi\alpha_p B_0 R_0^2 (r/R_0)^2/[(l/R_0)^2 + (a_0/R_0)^2]^{3/2} e^{-l^2/R_0^2}$, where B_0 and R_0 are given in Table 2.1. Compared to the ideal infinitesimal magnetic dipole flux $\Psi \propto r^2/l^3$, $\Psi_{\rm pol}$ contains a constant factor a_0 to make the dipole source finite; it also has an exponential decay at large distance so that the initial field vanishes at the solving domain boundaries. At small r and z, $\Psi_{\rm pol} \propto r^2$ hence B_z is nearly constant. a_0 is selected so that $\Psi_{\rm pol}(r = r_1, z = 0) = \Psi_{\rm pol}(r = r_2, z = 0)$, where $r_1 = 0.278 \Rightarrow 5$ cm and $r_2 = 1 \Rightarrow 18$ cm corresponding to the radii of the inner and outer gas lines in the experiment. The dimensionless parameter α_p quantifies the strength of the flux. The vector potential can be selected to be $\mathbf{A} = (\Psi_{\rm pol}/(2\pi r))\hat{\theta}$. The initial poloidal field is

$$\mathbf{B}_{\rm pol} = \nabla \times \mathbf{A} = \frac{1}{2\pi} \nabla\Psi_{\rm pol} \times \nabla\theta \tag{2.7}$$

$$\Rightarrow \begin{cases} B_r = \dfrac{\alpha_p z r e^{-l^2}}{(l^2+a_0^2)^{5/2}} (3 + 2a_0^2 + 2l^2) \\ B_z = \dfrac{\alpha_p e^{-l^2}}{(l^2+a_0^2)^{5/2}} \left[2(1-r^2)(l^2+a_0^2) - 3r^2\right] \end{cases}, \tag{2.8}$$

where $\hat{\theta}$ is the azimuthal unit vector and $\nabla\theta = \hat{\theta}/r$. The total poloidal flux is

$$\Psi_{0,\rm pol} \equiv \Psi_{\rm pol}(r_o, 0) = 2.448\alpha_p \Rightarrow 0.1586\alpha_p \text{ mWb}, \tag{2.9}$$

where $r_o = 0.5667 \Rightarrow 10.20$ cm is the position of the null of the initial poloidal field, i.e., $B_z(r_o, 0) = 0$. The first frame of Fig. 2.5 shows the flux contours of the initial poloidal field in the rz plane.

The toroidal current associated with the poloidal field is

$$J_\theta = \partial_z B_r - \partial_r B_z = -\alpha_p \frac{r e^{-l^2}}{(l^2 + a_0^2)^{7/2}} \cdot g(l), \tag{2.10}$$

where

$$g(l) = 4l^6 + (8a_0^2 + 2)l^4 + 4a_0^2(a_0^2 - 2)l^2 - 5a_0^2(a_0^2 + 3). \tag{2.11}$$

Simple calculation shows that $l_0 = 0.9993 \approx 1$ is the only zero point of $g(l)$ and $g(l) < 0$ for $0 \le l < l_0$ and $g(l) > 0$ for $l > l_0$.

2.2.2.2 Initial mass distribution

In the experiment, plasma is initially created following the path of initial poloidal field lines (see Fig. 1.2 H jet at 1.1 μs and Ar jet at 2.0 μs), i.e., the plasma is distributed around the $\Psi_{\rm pol}(r, z) = \Psi_0$ surface. Here $\Psi_{\rm pol}(r, z)$ is the initial poloidal flux function (Eq. 2.6) and $\Psi_0 \equiv \Psi_{\rm pol}(r_1, 0) = \Psi_{\rm pol}(r_2, 0)$ is the flux contour connecting the inner ($r_1 = 5$ cm) and outer ($r_2 = 18$ cm) gas feeding holes. A possible choice for the initial mass distribution function in the simulation is $n_{\rm init} \sim \exp[-\delta(\Psi_{\rm pol}(r, z) - \Psi_0)^2]$.

Note that this initial distribution has low plasma density on the axis. In the experiment, fast magnetic reconnection occurs as the eight arched loops merge into one. This allows the plasma and magnetic field to fill in the central region. The ideal MHD simulation, however, lacks the capability to simulate the fast magnetic reconnection, and hence cannot accurately describe the merging process. As a compromise, we start the simulation immediately after the merging process but before the collimation and propagation processes. We therefore choose a simple form topologically similar to the contour $\Psi_{\rm pol}(r, z) = \Psi_0$ but without the central hollow region, namely

$$n_{\rm init}(r, z) = 1 + n_{\rm init,0} \cdot e^{-l^2} \cdot e^{-\delta\left[(r-1/2)^2 + z^2 - 1/4\right]^2}. \tag{2.12}$$

The first term 1 corresponds to a background particle number density 10^{19} m^{-3}. This is $\sim 10^3$ times more dense than the background in the experiment, but still $\sim 10^{-3}$ less

dense than the plasma jet. $n_{\rm init,0}$ is the assumed initial plasma number density. The $e^{-\delta\left[(r-1/2)^2+z^2-1/4\right]^2}$ term states that the plasma is initially distributed over a torus surface $(r-1/2)^2+z^2=1/4$, connecting $r=0$ and $r=1=18$ cm at mid plane. The torus surface is roughly parallel to the initial poloidal flux surface $\Psi_{\rm pol}(r,z)=\Psi_0$, but without the central hole. The e^{-l^2} term assures that the initial plasma is localized around the origin. Using this distribution, the central region $r\simeq 0$ in the simulation is initially filled with dense plasma.

2.2.3 Helicity and energy injection

2.2.3.1 Compact injection near the z=0 plane

Toroidal magnetic flux is continuously injected into the simulation system, in order to replicate the energy and magnetic injection through the electrodes in the experiment. The helicity conservation equation in an ideal MHD plasma with volume $\mathcal{V}$ is

$$\frac{dK_{rel}}{dt}=-\int_{\partial\mathcal{V}}(2V\mathbf{B})\cdot d\mathbf{S}=2\Psi_{\rm pol}\cdot\frac{\partial(IL)}{\partial t}, \tag{2.13}$$

where $K_{\rm rel}$ is the relative magnetic helicity, $\partial\mathcal{V}$ is the boundary of the volume and the area $d\mathbf{S}$ is normal to the boundary, V is the electrode voltage, I is the total current through the plasma, and L is the plasma self inductance across the electrodes [3, 9, 31, 61] (also see § 1.1.4). The electrode surface in the experiment is the effective $\partial\mathcal{V}$. When a poloidal magnetic field is present, Eq. 2.13 states that magnetic helicity injection can be realized either by maintaining a non-zero voltage across the electrodes, or by increasing the poloidal current/toroidal field in the plasma. In the experiment, these two methods are essentially equivalent. Meanwhile, magnetic energy is also injected into the plasma by $\dot{E}=P=IV=Id\Psi_{tor}/dt$, where Ψ_{tor} is the toroidal magnetic flux. Since neither electric field nor potential is explicitly used in the simulation, we choose the second method to inject helicity. Thus we inject toroidal magnetic field into the system to increase the poloidal current and the magnetic helicity. The toroidal field injection term in Eq. 2.4 is defined as

$$\dot{\mathbf{B}}_{\rm inj}\equiv\gamma_b(t)\mathbf{B}_{\rm tor}, \tag{2.14}$$

where $\gamma_b(t)$ is the injection rate and

$$\mathbf{B}_{\rm tor} = \frac{f(\Psi_{\rm pol})}{2\pi r} e^{-Az^2}\hat{\theta} = \frac{1}{2\pi} f(\Psi_{\rm pol}) e^{-Az^2}\nabla\theta \tag{2.15}$$

is a pure toroidal field. The localization factor A is a large positive number so that toroidal field injection is localized near the $z = 0$ plane. $f(\Psi_{\rm pol})$ is an analytical function of $\Psi_{\rm pol}$ and following the magnetic tower model used in Li et al. (2006) [68], we choose $f(\Psi_{\rm pol}) = \alpha_t \Psi_{\rm pol}$ so that

$$\mathbf{B}_{\rm tor} = \alpha_t\alpha_p \frac{r}{(l^2 + a_0^2)^{3/2}} e^{-l^2} e^{-Az^2} = \alpha_t\alpha_p \frac{r}{(r^2 + z^2 + a_0^2)^{3/2}} e^{-r^2-(A+1)z^2}. \tag{2.16}$$

The poloidal current associated with this toroidal field is

$$\mathbf{J}_{\rm pol} = \nabla \times \mathbf{B}_{\rm tor} = \frac{1}{2\pi}\nabla\left(\alpha_t \Psi_{\rm pol} e^{-Az^2}\right) \times \nabla\theta = \alpha_t e^{-Az^2}\mathbf{B}_{\rm pol} + \frac{\alpha_t \Psi_{\rm pol}}{\pi r} A z e^{-Az^2}\hat{r}, \tag{2.17}$$

where $\nabla \times \nabla\theta = 0$ and Eq. 2.7 are used.

At $z = 0$, $B_{\rm tor} = \alpha_t \Psi_{\rm pol}/(2\pi r)$. Therefore the net poloidal current within radius r is $2\pi r B_{\rm tor} = \alpha_t \Psi_{\rm pol}$. Using Eq. 2.9, the total positive poloidal current associated with $B_{\rm tor}$ is

$$I_{\rm pol} = 2.488\alpha_t\alpha_p \Rightarrow 0.704\alpha_t\alpha_p \text{ kA}. \tag{2.18}$$

The localization factor A has no impact on the total poloidal current.

It is important to point out that the field injection term in the induction Eq. 2.4 is a compromise used to avoid having a plasma-electrode interaction boundary condition. Theoretically, Eq. 2.4 is not physically correct because of the injection term. However, because the localization factor A is a large positive number, the magnetic energy of $\mathbf{B}_{\rm tor}$ decreases rapidly with z. Therefore the "unphysical" region is very localized to the vicinity of the $z = 0$ plane. In particular, using $A = 9$, the total toroidal magnetic energy at the $z = 0.307 \Rightarrow 5.5$ cm plane is only 10% of the total planar magnetic energy at the $z = 0$ plane. The toroidal magnetic flux within $|z| < 0.307$ contributes 87% of the total toroidal flux, although the volume is only 7.7% of the total simulation domain. We define $z_{\rm foot} \equiv 0.307$, so the region where $|z| < z_{\rm foot}$ is the "engine region" where most of the energy injection is enclosed, and the region outside the engine region ($|z| > z_{\rm foot}$) is the

"jet region" where unphysical toroidal field injection does not occur. In the engine region, the toroidal magnetic field is directly added to the existing configuration by the modified induction equation (Eq. 2.4). The injection also adds magnetic helicity, poloidal current, and magnetic energy. In the jet region, on the other hand, this direct injection is negligible so the ideal MHD laws hold almost perfectly. The helicity, current, and energy enter the jet region with the plasma flow.

In the simulations presented here, we use $A = 9$. Although the choice of A is somewhat arbitrary, in general, A needs to be sufficient large to localize the engine region to the vicinity of the $z = 0$ plane. This compact engine region serves as an effective plasma-electrode interface, and leaves most of the simulation domain described by the correct induction equations (i.e., no artificial injection). If a small A were used, injection would occur globally. There would then be a large amount of energy directly added to remote regions with low density plasma. A magnetized shock would then arise and dissipate injected energy. Using a large A guarantees that the magnetic field is mostly frozen into the dense plasma. However, A should be not too large in our simulation, since otherwise numerical instability and error would occur because of excessive gradients.

The process of helicity/energy injection in the simulation is not exactly the same as in the experiments or the astrophysical case. In the experiment, a non-zero electric potential drop between the electrodes is responsible for the process. In AGN jet or stellar jet cases, the injection process could also be accompanied by electric potential drop in the radial direction as a result of interaction among the central object, wind, magnetic field, and the accretion disk dynamics, such as differential rotation of the disk and corona. However, the artificial injection of a purely toroidal field should produce mathematically equivalent magnetic structure. This injection is also consistent with the asymptotic X-winds solution by Shu et al. (1995) [103] and Shang et al. (2006) [98].

2.2.3.2 Jet collimation as a result of helicity/energy injection

To illustrate how injected toroidal magnetic field impacts the system, we consider a "virtual magnetic field" configuration composed by $\mathbf{B}_{\rm pol}$ (defined in Eq. 2.6-2.8) and $\mathbf{B}_{\rm tor}$ (defined

in Eq. 2.16). The Lorentz force

$$\begin{aligned}\mathbf{F} \equiv \mathbf{J} \times \mathbf{B} &= (\mathbf{J}_{\rm pol} + \mathbf{J}_{\rm tor}) \times (\mathbf{B}_{\rm pol} + \mathbf{B}_{\rm tor}) \\ \mathbf{F}_{\rm pol} &= \mathbf{J}_{\rm pol} \times \mathbf{B}_{\rm tor} + \mathbf{J}_{\rm tor} \times \mathbf{B}_{\rm pol} \\ \mathbf{F}_{\rm tor} &= \mathbf{J}_{\rm pol} \times \mathbf{B}_{\rm pol}\end{aligned} \tag{2.19}$$

has both poloidal and toroidal components.

We first examine the toroidal component of the Lorentz force, or, the twist force. The first component of $\mathbf{J}_{\rm pol}$ in Eq. 2.17 is parallel to $\mathbf{B}_{\rm pol}$, and only the second term contributes to the twist, namely,

$$\mathbf{F}_{\rm tor} = \frac{\alpha_t \Psi_{\rm pol} A z e^{-Az^2}}{\pi r} \hat{r} \times B_z \hat{z} = -2\alpha_t \alpha_p^2 A \frac{rz}{(l^2 + a_0^2)^4} e^{-2l^2 - Az^2} \cdot \left[2(1-r^2)(l^2+a_0^2) - 3r^2\right] \hat{\theta}. \tag{2.20}$$

For small radius, the twist force scales as $F_{\rm tor}/r \sim z e^{-(A+2)z^2}/(z^2+a_0^2)^3$. The twist force is strongest at $z = 0.166 \Rightarrow 3$ cm and weak for very small z and large z. In the simulation, $F_{\rm tor}$ twists the plasma differently at different radii and height, and hence contributes to E_r by increasing $v_\theta B_z$ negatively. This electric field is equivalent to the voltage across the inner cathode and outer anode in the experiment.

In the poloidal component of the Lorentz force, the $\mathbf{J}_{\rm tor} \times \mathbf{B}_{\rm pol}$ term is the hoop force that expands the system resulting from the poloidal magnetic field; while $\mathbf{J}_{\rm pol} \times \mathbf{B}_{\rm tor}$ is the pinch force and is caused solely by the toroidal magnetic field. Insertion of Eq. 2.7, 2.8, 2.10, 2.16 , and 2.17 into Eq. 2.19 yields

$$F_r = -\frac{\alpha_p^2 r e^{-2l^2}}{(l^2+a_0^2)^6} \left[2(1-r^2)(l^2+a_0^2) - 3r^2\right] \cdot \left[g(l) + \alpha_t^2 e^{-2Az^2} (l^2+a_0^2)^2\right] \tag{2.21}$$

$$F_z = \frac{\alpha_p^2 r^2 z e^{-2l^2}}{(l^2+a_0^2)^6} \left[\left(3 + 2l^2 + 2a_0^2\right) g(l) + \alpha_t^2 e^{-2Az^2} (l^2+a_0^2)^2 (3 + 4l^2 + 4a_0^2)\right]. \tag{2.22}$$

The terms containing $g(l)$ result from the poloidal field and the terms proportional to α_t^2 are given by the toroidal field. In the small α_t limit, the pinch applied by the toroidal field is weak, so the $g(l)$ term determines the direction of the Lorentz force. In the region of small r and l, $F_r > 0$ and $F_z/z < 0$, showing that the plasma expands and is made more diffuse by the hoop force. The same argument is true for $l < l_0 \approx 1$ and for finite α_t with

$Az^2 \gg 1$. In the cases where α_t is sufficiently large, i.e., the pinch due to the poloidal current/toroidal field overcomes the hoop force, $F_r < 0$ and $F_z/z > 0$ for small r. This is where the toroidal field squeezes the plasma radially and lengthens it axially. To see this more clearly, if we ignore the poloidal field effect by dropping the terms containing $g(l)$, the radial Lorentz force is $F_r/r \propto e^{-2(A+1)z^2}/(l^2+a_0^2)^3$, which decreases rapidly along the z axis. Hence the plasma is pinched and pressurized more at small z than at large z. The huge pressure gradient along the central axis, due to the huge gradient of collimation force, then accelerates the plasma away from the $z = 0$ plane. Equivalently, the large gradient of the toroidal magnetic pressure $B_\theta^2/(2\mu_0)$ in the z direction is responsible for the collimation and acceleration of the plasma.

It is important to point out that the Lorentz force is primarily poloidal. Since

$$\frac{F_{\rm tor}}{F_r} = \frac{2\alpha_t A z e^{-Az^2}(l^2+a_0^2)^2}{g(l)+\alpha_t^2 e^{-2Az^2}(l^2+a_0^2)^2} \propto \begin{cases} \alpha_t \text{ for small } \alpha_t \\ 1/\alpha_t \text{ for large } \alpha_t \end{cases}, \tag{2.23}$$

F_r is usually much stronger than $F_{\rm tor}$.

The above analyses show the Lorentz force tends to squeeze the plasma radially and accelerate it axially with the presence of $\mathbf{B}_{\rm tor}$. However, in the simulation, only $\mathbf{B}_{\rm pol}$ is initially imposed as the bias poloidal field. The toroidal field is continuously injected into the system at small z. Meanwhile, the existing poloidal and toroidal magnetic field configuration is continuously deformed together with the plasma. Eq. 2.20-2.21 are not exact expressions of the Lorentz force experienced by the plasma. However, Eq. 2.20-2.21 nevertheless gives a semi-quantitative description of how injected toroidal field affects the plasma.

In summary, we have established both the initial condition and the continuous injection condition for simulating the Caltech plasma jet experiment. Only a poloidal field and a dense plasma distributed roughly parallel to the field lines are imposed initially. As the plasma starts to evolve, although the hoop force by the initial toroidal current tries to expand the plasma radially, the injected toroidal magnetic field (poloidal current) applies Lorentz force that overcomes the poloidal field pressure, and squeezes the plasma radially and lengthens it axially to form a jet in both the $+\hat{z}$ and $-\hat{z}$ directions. We only consider the $+z$ part as the $-z$ part is a mirror image.

2.3 Simulation results

In this section, we present some typical simulation results and compare them to the experimental results.

2.3.1 A typical argon jet simulation

First we show a typical argon plasma jet simulation ($\mu = 40$). The initial poloidal flux factor is selected as $\alpha_p = 10$ corresponding to a 1.59 mWb poloidal flux with maximum B_z strength of 0.165 T at the origin. The initial mass distribution is given by Eq. 2.12 with $\delta = 40$ and $n_{\text{init},0} = 4000$, corresponding to a maximum initial electron number density 2×10^{22} m^{-3}.

The dimensionless injection coefficient is

$$\gamma_b(t)\alpha_t = 1000e^{-30t} + 150e^{-20(t-0.5)^2} \tag{2.24}$$

for $0 \leq t \leq 0.6 = 35$ μs, which contains a short exponential decay and then a long-duration Gaussian profile. This corresponds to the fast power input by the main capacitor and then the long-duration power input by the PFN in the experiment. This injection rate is obtained based on the experiment current characteristics. In the experiment, the main capacitor gives rise to a plasma poloidal current at a rate of ≈ 150 kA/3 μs $\times(\pi/2) \sim 10^2$ kA/μs. The PFN supplies current $60 - 80$ kA with a rise time of ~ 10 μs, giving a current injection rate ~ 10 kA/μs. With $\alpha_p = 10$, Eq. 2.18 indicates a dimensionless injection rate $\gamma_b\alpha_t \sim 10^3$ for the main capacitor and $\sim 10^2$ for the PFN.

The localization factor is $A = 9$ so the engine region extends up to $z_{\text{foot}} = 0.307 \Rightarrow 5.5$ cm. The initial plasma temperature is uniformly $T_i = T_e = 2$ eV, and the plasma remains 100% singly ionized through the simulation.

2.3.1.1 Global energy analysis

First, we examine the overall global energetics of the jet. The kinetic energy, magnetic energy and thermal energy in different regions are calculated by integrating dimensional quantities $\rho v^2/2$, $e_B = B^2/(2\mu_0)$ and $P_g/(\gamma - 1)$ over the volume of interest for comparison with experiment. The evolution of these various types of energy are plotted in Fig. 2.3.

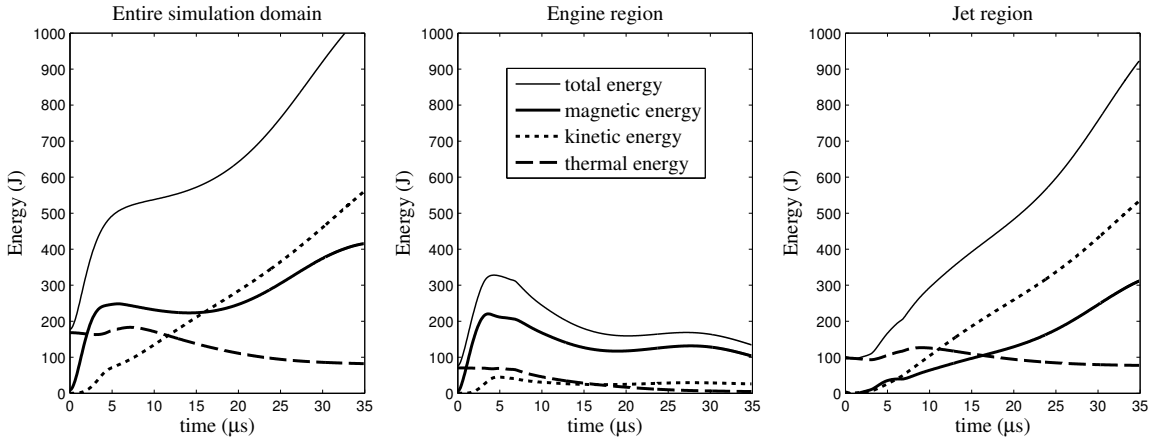

Figure 2.3: Evolution of different energy components in the entire simulation domain (left), engine region $|z| < z_{\text{foot}}$ (middle) and jet region $|z| \geq z_{\text{foot}}$ (right).

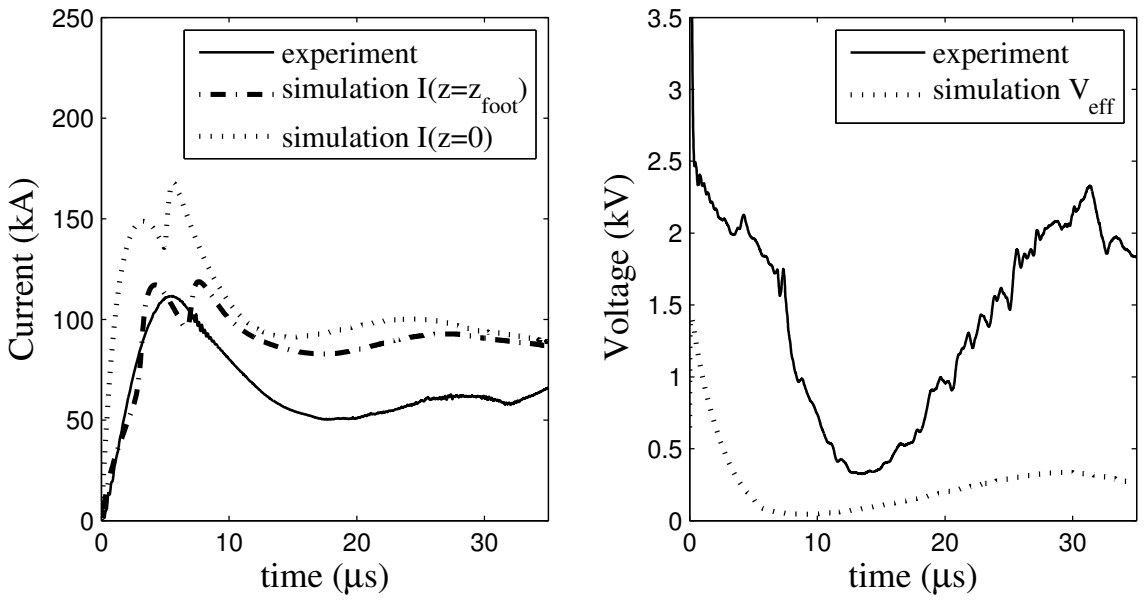

Figure 2.4: Left: evolution of the total positive poloidal current. Right: evolution of the (effective) voltage. The solid curves are measured in a typical argon plasma experiment (shot # 12780, plasma discharged at 5 kV). The dotted curves and dash-dot curves are simulation results calculated at $z = 0$ and $z = z_{\text{foot}}$ by Eq. 2.30.

The simulation starts with a finite thermal energy and a small magnetic energy from the initial poloidal magnetic field. During the first 5 μs, the toroidal field is injected into the engine region at a very fast rate, leading to a rapid rise in total magnetic energy. Meanwhile, the injected toroidal field continuously applies a Lorentz force to the plasma, converting magnetic energy into kinetic energy. At 5 μs, this energy conversion rate exceeds the declining toroidal field injection rate, and the magnetic energy of the entire simulation domain begins to drop. This dropping trend is terminated by the second fast injection occurring at later time. At 10 μs, the relative amounts of magnetic and kinetic energy in the engine region reach a quasi-equilibrium state where magnetic energy dominates and remains roughly constant. However, the magnetic and kinetic energy in the jet region continue growing at constant rates. Therefore magnetic energy injected in the engine region is effectively transferred to the jet region because the energy in the engine region stays saturated. The energy partition and evolution are consistent with estimation for the experiment [see Chapter 3 of Ref. 61].

The thermal energy is insignificant compared to the magnetic and kinetic energies. The thermal energy has a small rise in early time due to the adiabatic heating from the collimation, and then slowly decreases because of the mass loss at the domain boundaries. Heating during the jet evolution is in general also not important in the experiment.

In § 2.2.3.2, we showed that the jet is accelerated by the plasma pressure gradient along the central axis. This pressure gradient is caused by the non-uniform toroidal field pinching. In the jet region, the rate of increase of kinetic energy greatly exceeds the decrease of the thermal energy. Therefore, it is confirmed that the jet gains kinetic energy ultimately from magnetic energy, not from thermal energy, i.e., the jet is magnetically driven.

The total power input into the system is given by

$$P_{\rm tot} \equiv \iiint (\dot{e}_B + \dot{e}_K + \dot{e}_T) dV, \tag{2.25}$$

where e_B, e_K and e_T are the magnetic, kinetic and thermal energy density.

If we ignore the energy loss due to the outflow mass at the solving domain boundaries, the energy conservation law states that the rate of change of total energy equals the energy

injection rate associated with toroidal field injection, i.e.,

$$P_{\rm tot} = P_{\rm inj} \equiv \iiint \dot{e}_{\rm inj} dV \qquad \dot{e}_{\rm inj} \equiv \gamma_b(t) \mathbf{B}_{\rm tor} \cdot \mathbf{B}. \tag{2.26}$$

According to the analysis in § 2.2.3.1, the power injection mainly occurs in the engine region, i.e.,

$$P_{\rm inj} \approx \iiint_{|z|<z_{\rm foot}} \dot{e}_{\rm inj} dV \equiv P_{\rm inj,engine}. \tag{2.27}$$

Due to energy saturation in the engine region, there is also

$$P_{\rm tot} \approx \iiint_{|z|\geq z_{\rm foot}} (\dot{e}_B + \dot{e}_K + \dot{e}_T) dV \equiv P_{\rm jet} \quad \text{at large } t. \tag{2.28}$$

Therefore,

$$P_{\rm inj,engine} \approx P_{\rm jet} \qquad \text{at large } t. \tag{2.29}$$

This shows that the power input at the jet base is mainly used to accelerate the jet, and not for heating.

An effective voltage at the $z = 0$ plane can be defined as

$$V_{\rm eff} \equiv \frac{P_{\rm tot}}{I(z=0)} \qquad I(z) = \iint_{J_z>0} J_z dx dy, \tag{2.30}$$

where $I(z)$ is the total positive poloidal current through the plane z.

Figure 2.4 shows that the poloidal current in the simulation is in good agreement with the experimental measurement. At $t \leq 3$ μs, the current at $z = z_{\rm foot}$ is less than 30% of the current at the $z = 0$ plane. This is because most of the toroidal injection occurs within the engine region. However, for $t > 5$ μs, the current entering the jet region is comparable with the total current in the system, indicating that the engine region is injecting toroidal flux into the jet region.

It is difficult in the experiment to measure the voltage across the plasma precisely because the impedance of the plasma is very low. The voltage measurement given by the solid curve in Fig. 2.4 contains the plasma voltage drop as well as voltage drops on the cables and connectors. The effective voltage in the simulation is expected to be comparable to but lower than the experiment measurement, as is generally the case in Fig. 2.4.

The global energy and electric characteristics comparison between the simulation and

experiment confirm that the simulation captures the essential features. The jet is MHD-driven and gains kinetic energy from magnetic energy. In the following sections, we discuss the detailed process of jet collimation and propagation and various properties of the jet.

2.3.1.2 Jet collimation and propagation

According to the analysis in § 2.2.3.1 the $A = 9$ localized toroidal field injection, quantified by Eq. 2.24, will generate a pinch force that collimates the plasma near the $z = 0$ plane. Meanwhile, the plasma pressure gradient along the axis, caused by the z gradient of collimation force on the jet surfaces, will accelerate the plasma away from the $z = 0$ plane. The evolution of the plasma is given in Fig. 2.5, which presents the time sequence of plasma density in the xz (rz) plane overlaid by azimuthally-averaged poloidal magnetic field contours. Figure 2.5 shows that plasma with frozen-in poloidal field is pinched radially and lengthened axially. Starting from a torus structure around the origin, the plasma eventually forms a dense collimated jet with a radius $r \simeq 0.2 \Rightarrow 3.6$ cm (at $z = 0$) and height $h \simeq 2 \Rightarrow 36$ cm at ~ 30 μs. The radius-length ratio of the plasma decreases from $\approx 1:1$ to $\approx 1:10$. Consequentially, a more than five times amplification of density and poloidal field is observed to be associated with the collimation process in the simulation, consistent with the experimental measurement by Yun et al. (2007) [127]. The jet radius $r \simeq 0.2$ at $z = 0$ in the simulation is found where plasma density drops below 5% of the central density $\rho(r = 0, z)$. An unmagnetized hydrodynamic shock bounding the global structure forms in the numerical simulation and propagates outward, as a result of supersonic jet flow propagating into the finite pressure background; this shock is not observed in the experiment because of the lack of background plasma. Here we define the jet head as the leading edge of dense magnetized plasma along the central axis. This leading edge corresponds to the top of the T-shaped shell in Fig. 2.5 (from $z = 0$ to $z \sim 1.8$ at 27.94 μs, see also in Fig. 2.6). The jet head is the point where all the poloidal flux bends and returns back to the mid-plane. In front of the jet head, plasma is essentially unmagnetized and the density drops from $\sim 10^{22}$ m^{-3} to $< 10^{20}$ m^{-3}. Therefore the hydro shock and its downstream region from the T-shell to the shock front are not considered as part of the jet, but rather the termination of the entire global structure. Figure 2.5 also shows that the entire plasma structure remains axisymmetric in the simulation.

The high speed images of the experiment plasma jets shown in Fig. 1.2 are integration

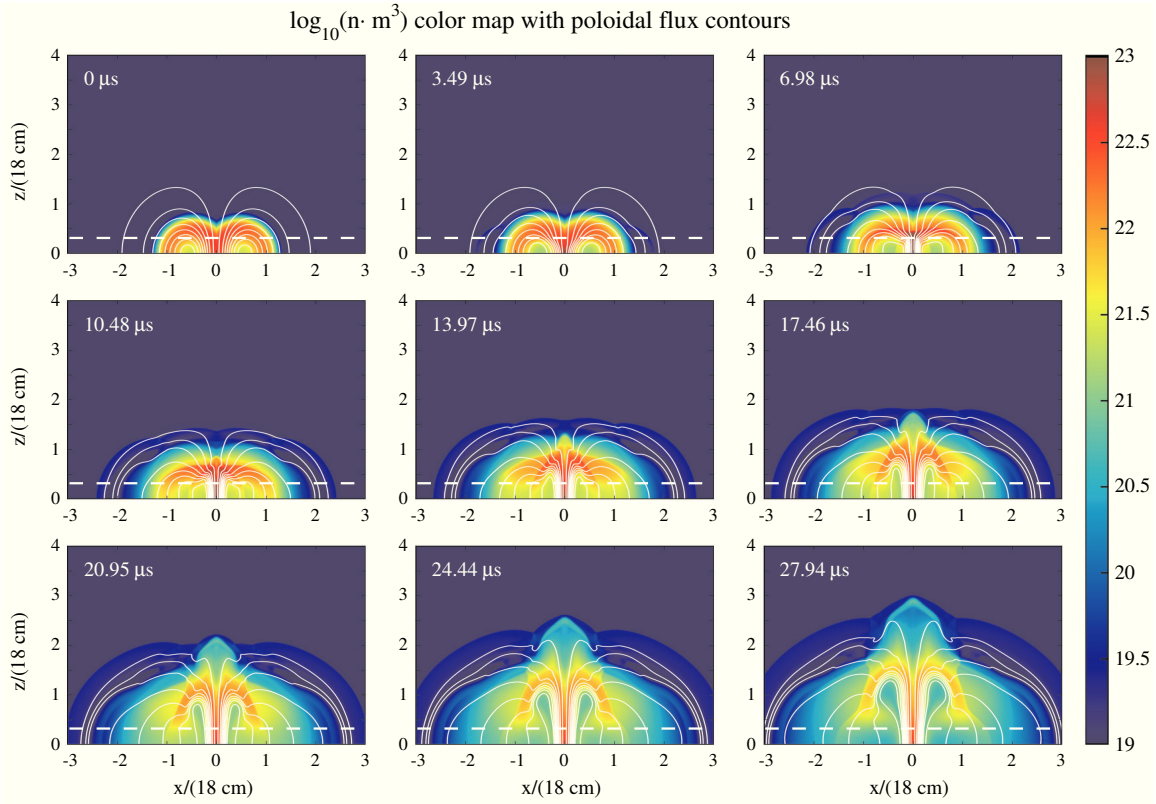

Figure 2.5: Evolution of the density distribution (color map) and azimuthally-averaged poloidal flux surfaces (white contours) in xz plane ($z > 0$) from $t = 0$ to 0.48 with 0.06 interframe time, corresponding to dimensional time from 0 to 27.94 μs with interframe time 3.49 μs. The color represents the common logarithm of the total particle number density $n = n_e + n_i$ in m^{-3}. Each frame contains 13 evenly spaced flux contours from 0.05 mWb to 1.45 mWb every 0.2 mWb. The white horizontal dash lines in each frames mark the position of $z_{\mathrm{foot}} = 0.307 \Rightarrow 5.5$ cm.

of plasma atomic line emission along the line of sight. Generally atomic line emission is proportional to the square of density. Therefore we calculate the line-of-sight integration of density squared of the simulation jet and plot the equivalent "emission" images in Fig. 2.6, along with five experimental plasma images. The plasma is optically thin. Figure 2.6 shows that simulation and experimental jets have similar radius, length/velocity, brightness variation, and the relatively flat and bright plasma at jet head, a T-shaped structure. This T-shaped structure is a signature of return flux (also see the structure at the top of jet in Fig. 2.5). Due to the lack of any background pressure, the experimental jet has a much flatter return flux structure, compared to the T-shaped structure shown in simulation images at later times. This structure is much dimmer in Fig. 1.2 because for those figures the camera was not placed perpendicular to the jet so the line of sight does not lie entirely

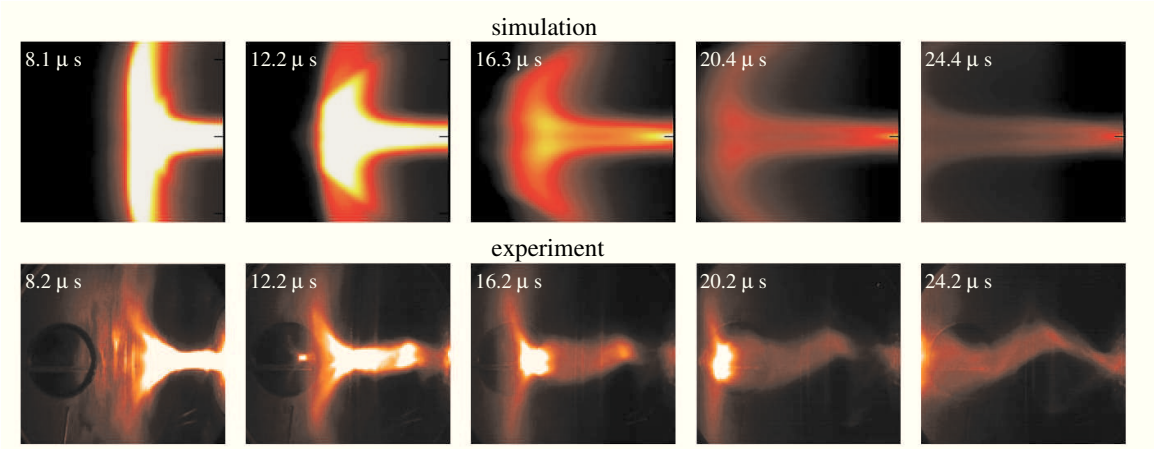

Figure 2.6: Top panels: distribution of line-of-sight integration of square of density in simulation, i.e., $\int n^2(x, y, z)dy$. Lower panels: false color images of a typical Argon jet experiment in visible band taken by IMACON 200 camera placed almost perpendicular to the jet axis (along r direction). Shot # 11082. The second frame also shows a reflected jet image on a glass window behind the jet. The plots are rotated 90° about $(x = 0, z = 0)$, and are scaled to be 26 cm in z (horizontal) direction by 22 cm in x (vertical) direction. The respective color tables for both the simulation and experimental images do not change with time.

in the T-shell structure. Note that the experimental jet starts to kink at 20 μs but the jet still propagates in a similar manner and remains attached to the center electrode.

Although the localized toroidal field (poloidal current) injection is confined to the engine region ($|z| < z_{\rm foot}$, below the dashed lines in Fig. 2.5), the plasma nevertheless collimates in the jet region. This is because the poloidal current, pre-injected in the engine region, propagates into the jet region along with the plasma motion and so provides a pinch force to collimate the plasma there (Fig. 2.4, also see Fig. 2.10). Hence the toroidal field injection actually occurs in both the engine region and jet region. The injection in the engine region is realized artificially by Eq. 2.4, a non-ideal process; the injection in the jet region is achieved through the $z = z_{\rm foot}$ plane associated with the plasma dynamics.

The detailed axial profile of the collimated jet is given in Fig. 2.7, which plots density, kinetic and magnetic profiles along the central z axis spanning from 11.6 μs to 30.2 μs. Although the experimental jet already undergoes a kink instability as early as ~ 20 μs, the simulation results at late times can still be used to study the expansion of the length of the axis of the kinked experimental jet according to Fig. 2.6.

The left four panels A-D in Fig. 2.7 show the evolution of jet's kinetic properties. The number density plots (panels A and B) show that mass is rearranged to become more

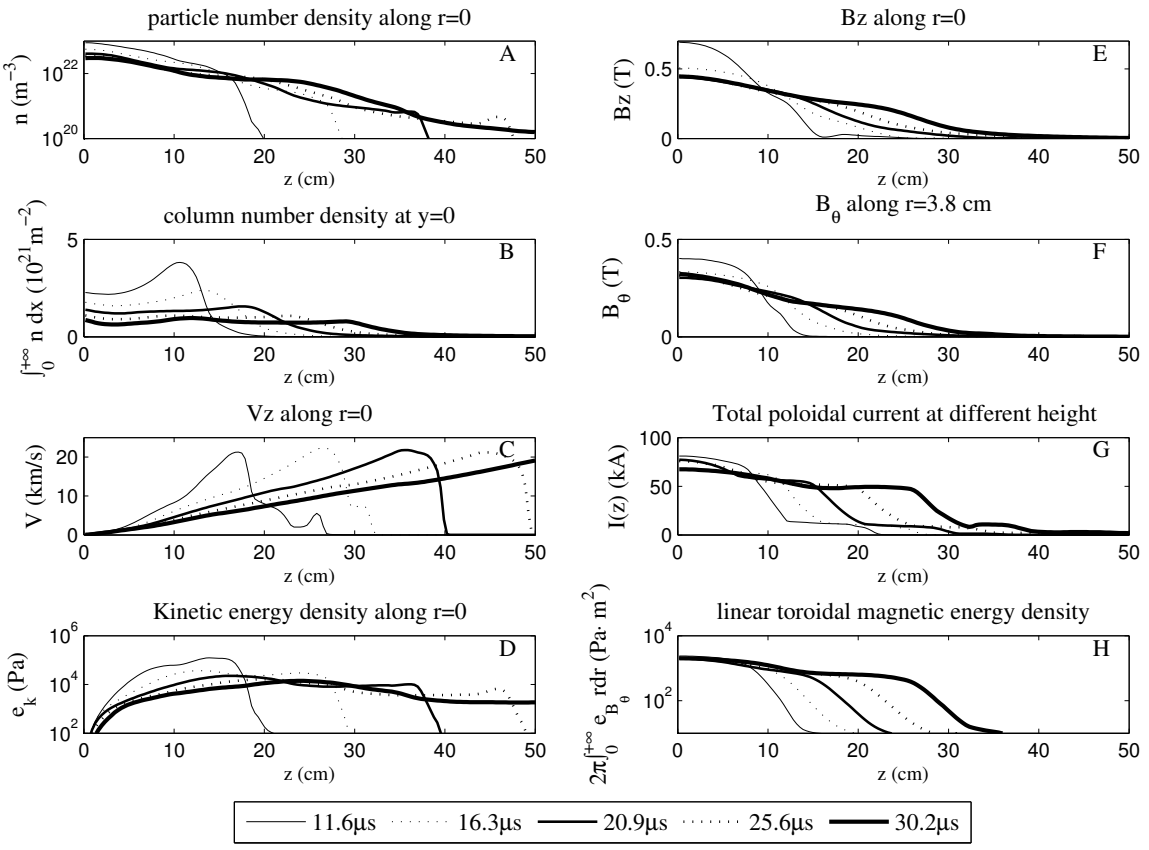

Figure 2.7: Particle number density along central axis $n(r = 0, z)$ (panel A), column particle number density $\int n dx$ along $y = 0$ (panel B), axial velocity v_z along $r = 0$ (panel C), axial kinetic energy density $e_k = \rho v_z^2/2$ along $r = 0$ (panel D), axial magnetic field B_z along $r = 0$ (panel E), toroidal magnetic field $B_\theta(r, z)$ at $r = 0.21$ (3.8 cm) (panel F), total poloidal current $I(z) \equiv \max_r I(r, z)$, where $\mu_0(r, z) = B_\theta(r, z)/2\pi r$ (panel G), and total toroidal field energy at each height $\int_0^\infty e_{B_\theta} d\theta r dr$ (panel H) where $e_{B_\theta} = B_\theta^2/2\,u_0$.

elongated and more evenly distributed along the jet. Since the total mass is conserved in the solving domain, consequentially, the density or column density decreases along the jet body when the jet gets longer. Panels C and D show the axial velocity and kinetic energy are gradually developed along the jet. The plasma axial velocity decreases in the lab frame because of the jet elongation. In fact, panel C indicates that the axial velocity approximately follows a self-similar profile $v_z(t, z) \propto z/t$. Detailed calculation finds that tv_z/z approaches 1 for $z > z_{\rm foot}$ at later time, i.e., $v_z \to z/t$. Therefore, the acceleration in the frame of jet is $dv_z/dt = \partial_t v_z + v_z \partial_z v_z = 0$. This means that the jet has reached a dynamic steady state and the entire jet is elongating as a whole. However, it is crucial to point out that the $v_z \propto z/t$ behavior is only true at later times, when the injection rate varies very slowly. At

early times when injection rate has a large variation, the jet velocity profile is expected to be very different from self-similar behavior, with density accumulation/attenuation in some parts of the jet and even internal shocks. At the jet head, plasma flow slows down in the moving frame of plasma, density accumulation always occurs (see panel B), which is also observed in experiments [126]. This accumulation can be regarded as an indicator of jet head, e.g., $z \approx 16$ cm at $t = 16.3$ μs and $z \approx 28$ cm at $t = 25.6$ μs. This gives a jet speed of $v_z \approx 13$ km s^{-1}, consistent with the experiment (Fig. 2.6).

The jet speed is faster than the background plasma sound speed $c_s = 3.1$ km s^{-1}. The supersonic jet flow is expected to excite a hydro shock with speed $v_s = [(3\gamma-1)/(6\gamma-4) + \sqrt{(3\gamma-1)^2/(6\gamma-4)^2 + c_s^2/v_z^2}]\cdot v_z \approx 18$ km s^{-1} where the adiabatic constant is $\gamma = 5/3$ [60]. This is consistent with the simulation results in panel C. Under the strong shock approximation $v_z \gg c_s$, the shock speed is $v_s \approx [(3\gamma-1)/(3\gamma-2)]\cdot v_z$. In the experiment, although a hydro shock is also expected, it is not feasible to measure it because the background density is too low. Moser & Bellan (2012) [81] had a $v_z \approx 16$ km s^{-1} argon experiment jet collide with a pre-injected hydrogen neutral cloud with density $n \sim 10^{19} - 10^{20}$ m^{-3}, and observed a hydro shock in the cloud with a speed of $v_s \sim 25$ km/s. This satisfied the strong shock solution with $\gamma = 7/5$ for neutral diatomic gas.

Yun (2010) [126] measure the density and velocity profiles of a typical nitrogen jet using Stark broadening and Doppler effect (Fig. 15, 17 of Ref. [126]). It is found that the experimental jet has a typical density $(0.5 - 1.0) \times 10^{23}$ m^{-3}, and the density profiles behave very similarly to the argon simulation jet in aspects like mass distribution, time-dependent profile evolution, and density accumulation at the jet head, especially for the column number density (Fig. 2.7 panel B). The velocity profiles of the experiment nitrogen jet also show similar trends as Fig. 2.7 panel C, e.g., velocity behind the jet head slows down in lab frame and the jet head travels at a roughly constant speed. In the experiment, because there is negligible background density, the measurable plasma velocity reaches zero at the jet head. In the simulation, however, the axial velocity profiles are terminated by the hydro shock in front of the jet head. Yun & Bellan (2010) [126] show a smaller density decrease of the jet in the experiment than in the simulation, due to the continuous mass injection into the plasma through the gas feeding holes on the electrodes [107]. Continuous mass injection is not included in the simulation in order to reduce complexity. This results in a larger density attenuation in the simulation as the jet propagates (panel A and B). It

is important to point out that the experimental nitrogen jets and argon jets do not have exactly the same conditions, so the discussion here on nitrogen jet, while identifying similar trends, is not quantitative.

As the jet lengthens, axial magnetic field embedded in the plasma is also stretched out, resulting in a quasi-uniform magnetic density along the jet axis. This is clearly evident by noticing the B_z evolution in Fig. 2.7 panel E. At 11.6 μs, B_z attenuates from 0.7 T to 0.35 T in 9.5 cm, while at 30.2 μs this 2-fold decay occurs in a distance of 25 cm $\approx$ 6 jet radius. Hence the axial magnetic field is becoming more uniform. Panel F, G, and H demonstrate that toroidal magnetic field and poloidal current propagate along the jet body and reach the same distance as does the plasma density, despite the fact that toroidal field/poloidal current is injected in the engine region at small z. The jet is thus still being collimated by the toroidal field/poloidal current even though the jet is already far from the engine region. The total positive poloidal current (panel G) and total toroidal magnetic energy density (panel H) become quite uniform along the jet in later time. Panel G also clearly indicates the jet head location, where all poloidal current turn back and results in a sharp decrease in total positive poloidal current at the jet head. The locations of this sharp decrease is consistent with the location of density accumulation shown in panel B.

According to Fig. 2.7 here and Fig. 17 in Yun & Bellan (2010) [126], there is no distinct jet head in either simulation or experiment. After the main jet body, plasma density and other characteristics, such as poloidal flux and current, take significant distance to reach zero. The reason is again the lack of background pressure. In the jet-neutral cloud collision experiment [79, 81], a sharper jet head with significant amplified density and magnetic field is observed.

Although panels E & F show B_z along the axis remains comparable with B_θ at the jet boundary, we will show in § 2.3.1.3 that this result does not conflict with Lynden-Bell models [74, 75, 100] or Zavala & Taylor (2005) [128], in which an increasing pitch angle B_θ/B_z is expected tracing magnetic field lines along the jet.

Figure 2.8 shows the distribution of Poynting flux $B_\theta^2 v_z$, kinetic flux ρv_z^3 and enthalpy flux $\gamma p/(\gamma-1)v_z$ at $t = 29.1$ μs. The figure shows that Poynting flux has successfully reached the height of jet head $z \approx 1.8$, even though the toroidal field is injected at $z < 0.307$. Poynting flux is generally $2-10$ times larger than kinetic flux, and two to three orders of magnitude larger than thermal flux, showing that the jet is MHD driven and magnetically

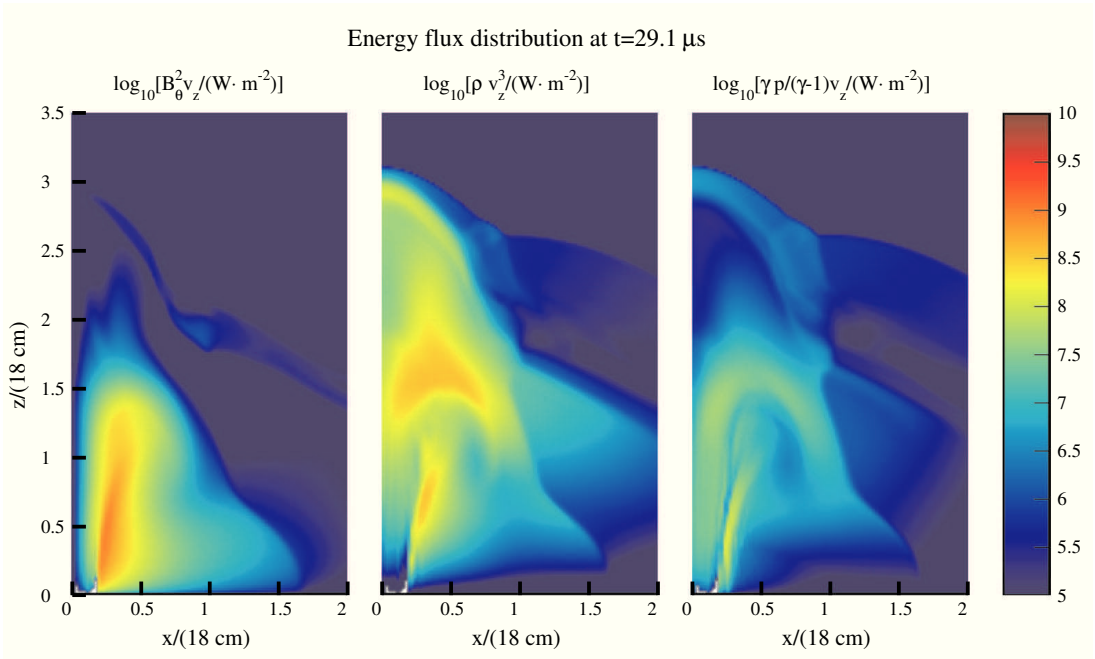

Figure 2.8: From left to right: distribution of logarithm of Poynting flux $\log_{10}(v_z B_\theta^2)$, kinetic flux $\log_{10}(\rho v_z^3)$, and enthalpy flux $\log_{10}(\gamma p/(\gamma-1)v_z)$ at $t = 29.1$ μs. At this time, the jet head is at $z \approx 1.8$ or 32 cm and jet radius is about $r = 0.2$ or 3.6 cm. The SI unit for energy flux is W m^{-2}.

dominated. However, at small radius where B_θ is small, kinetic and thermal flux are larger than Poynting flux. The hydro shock in front of the jet carries a notable amount of kinetic energy due to the fast expansion velocity.

2.3.1.3 Jet structure and the global magnetic field configuration

We have shown that a collimated jet automatically forms in the jet region when toroidal field is injected into the engine region. We now examine the jet structure in the jet region.

Figure 2.9 plots the radial profiles of the plasma density, pressure, velocity and magnetic field at $z = 1.14 \Rightarrow 20.5$ cm (15 cm above the $z_{\rm foot}$ plane) at different times. At 5.8 μs, according to Fig. 2.5, a collimated jet structure has not yet formed, and the injection in the engine region has caused little impact at $z = 20.5$ cm. As expected, the left three panels of Fig. 2.9 reveal a low density ($\sim 10^{19}$ m^{-3}), low velocity, and very weakly magnetized plasma structure. (Note that vertical scales for 5.82 μs and 29.1 μs are different in Fig. 2.9). However, the negative radial velocity between 1 and 10 cm shows that the collimation has already started at this time. At 29.1 μs, a collimated jet in steady-state is expected at

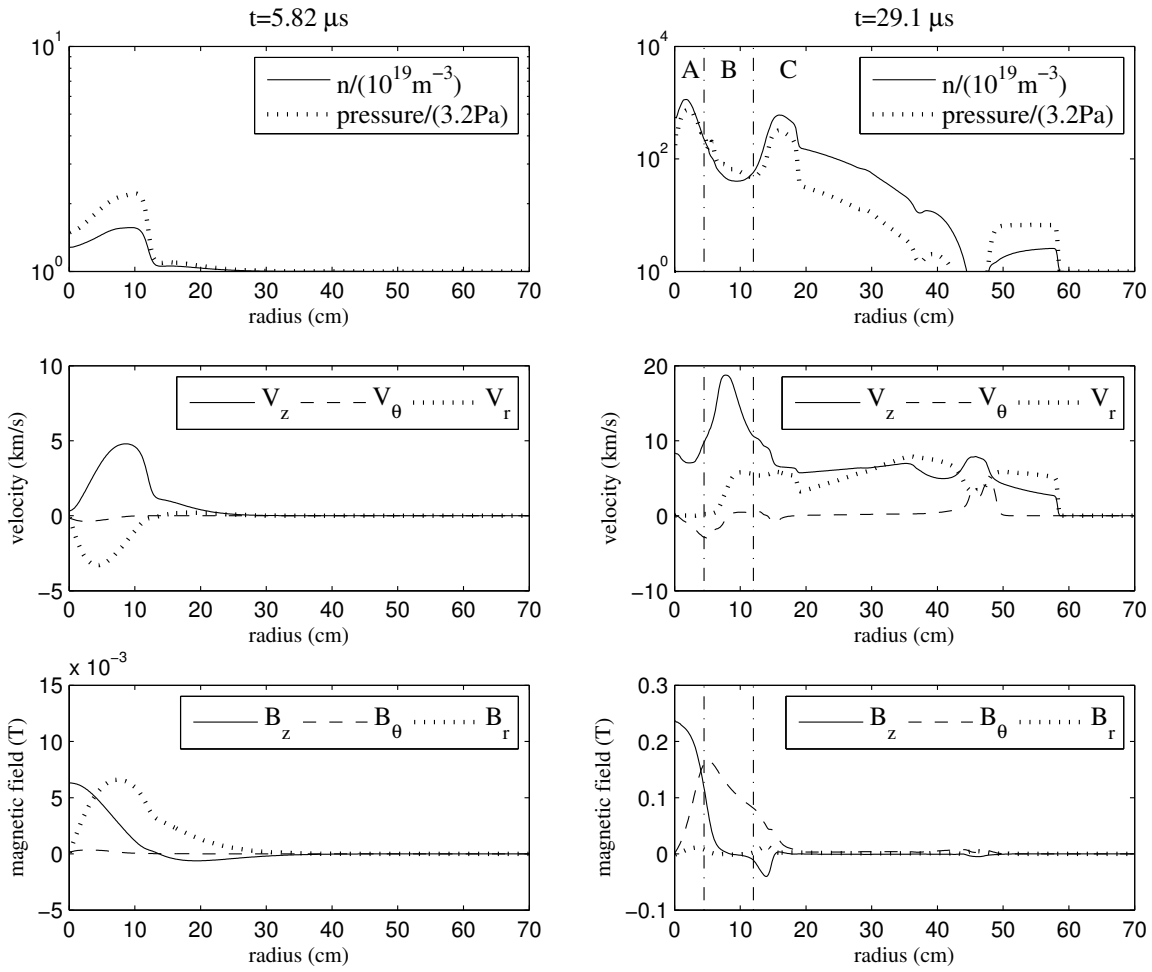

Figure 2.9: Radial profiles of the jet at $z = 20.5$ cm (15 cm above z_{foot} at $t = 0.1$ or 5.82 μs (left three panels) and $t = 0.5$ or 29.1 μs (right three panels). Top two panels: particle number density $n(r)$ (in 10^{19} m^{-3}, solid curves) and thermal pressure $p(r)$ (in 3.2 Pa, dotted curves). Middle two panels: velocity profiles in km s^{-1}. $v_z(r)$ (solid curves), $v_\theta(r)$ (dashed curves) and $v_r(r)$ (dotted curves). Bottom two panels: magnetic field profiles in Tesla. $B_z(r)$ (solid curves), $B_\theta(r)$ (dashed curves), and $B_r(r)$ (dotted curves). Each of the right three panels (29.1 μs) is divided into three regions A, B, and C, separated by two vertical dot-dash lines at $r = 4.5$ cm and $r = 12$ cm. See § 2.3.1.3 for details.

$z = 20.5$ cm because the jet head has travelled beyond 20.5 cm according to Fig. 2.5. The right three panels of Fig. 2.9 show that the entire radial profile can be divided into three regions from small to large radii, namely the central column (jet, region A), the diffuse pinch region (region B) and the return flux region (region C) (see also discussions of these structures in Nakamura et al. (2006) [82] and Colgate et al. (2014) [23]).

Central column For $r \lesssim 4-5$ cm, the central jet is characterized by a $\sim 10^{22}$ m^{-3} high density, a ~ 10 km s^{-1} quasi-uniform axial velocity and a ~ 0.24 T axial magnetic field. The radial velocity is zero, indicating that collimation is complete and a radially balanced z-pinch configuration is maintained. The toroidal magnetic field gradually increases from $r = 0$ to $r \approx 5$ cm at a roughly constant slope, suggesting that the central jet is filled by a roughly uniform current J_z. The zero B_r additionally demonstrates that the magnetic field is well confined inside the jet. At the jet boundary, density, pressure, axial magnetic field, and current density drop rapidly and connect to the diffuse pinch region. Specifically, at $r = 5$ cm, the plasma density is already less than 15% of the maximal density 1.14×10^{23} m^{-3} at $r = 1.7$ cm. The density dip at $r = 0$ results from the initial torus-shaped mass distribution.

Diffuse pinch region For 5 cm$\lesssim r \lesssim 12$ cm, there is a relatively large region filled by low density plasma ($\sim 5 \times 10^{20}$ m^{-3}) surrounding the central dense jet. The toroidal magnetic field B_θ scales as $r^{-0.96} \approx 1/r$ in this region, showing that the poloidal current is almost zero. Detailed calculation shows that 87% of total axial current I_Z flows inside the central column $r < 5$ cm, and another 13% of I_Z exists in the 5 cm$\lesssim r \lesssim 10$ cm region. The axial magnetic field B_z drops to zero with a steep scaling $B_z \sim r^{-5.5}$ from 5 cm to 8 cm, and reverses polarity at $r = 8.5$ cm. The radial magnetic field B_r is $\lesssim 10^{-2}$ times weaker than B_z and B_θ. This region has a relatively fast axial velocity and finite radial velocity. However, because of the low density, the kinetic energy in this region is only 15% of the toroidal magnetic energy in the same region, and is less than 10% of the central column kinetic energy. Thus the diffuse pinch region is a toroidal magnetic field dominant region with low J_z.

Return flux region Since the simulation starts with a complete global dipole magnetic field, the poloidal flux, carried by the central jet, must return to the central plane at some

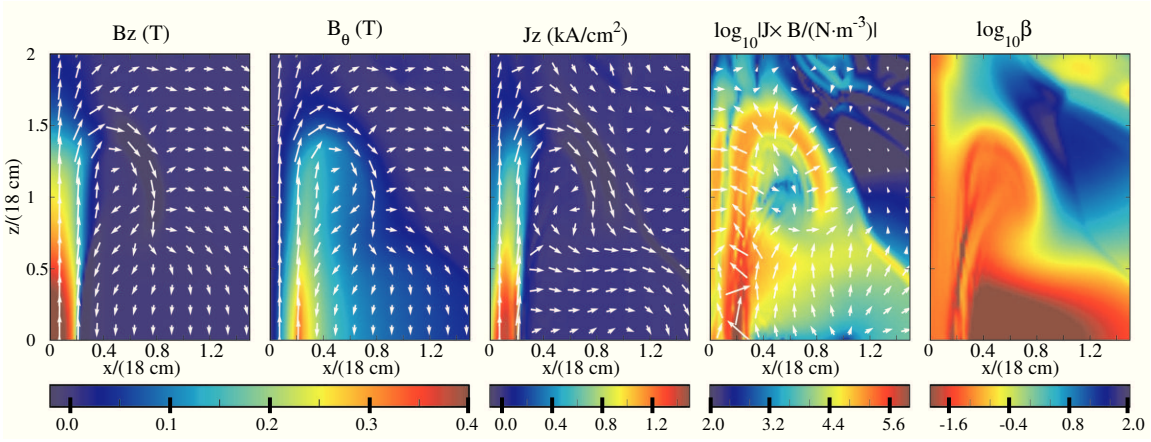

Figure 2.10: Cross-sectional view of plasma properties at $t = 0.5$ or 29.1 μs. From left to right: axial magnetic field B_z with poloidal field arrows, toroidal magnetic field B_θ with poloidal field arrows, axial current J_z with poloidal current arrows, logarithm of Lorentz force density with poloidal $\mathbf{J} \times \mathbf{B}$ arrows, logarithm of plasma β (ratio of thermal energy density to magnetic energy density) distribution. In all panels, the length of each arrow is proportional to the 1/5 power of the corresponding quantity at the location of arrow center. For example, an arrow I with a half length of an arrow II means that the represented quantity at arrow I is only $1/2^5 \sim 3\%$ of arrow II.

point. According to Fig. 2.5 and Fig. 2.7, all the upward flux frozen into the dense plasma starts to return at the jet head. The return flux at $z = 20.5$ cm is found in the narrow 12 cm$\lesssim r \lesssim$ 15 cm region and has a ~ 0.04 T negative strength. The toroidal field sharply decays to zero in this region as well, indicating the existence of a narrow return poloidal current sheet. The Lorentz force acting on this current sheet repels this region away from the central axis at a fast speed ($v_r \approx 6$ km s^{-1}), and piles up and compress plasma in 15 cm$\lesssim r \lesssim$ 18 cm and forms the T-shell shown in Fig. 2.5.

The return flux region transitions to the background plasma configuration through a hydrodynamic shock at $r \approx 50-60$ cm. At $t = 29.2$ μs, since the return flux region still has higher density and pressure compared to the background, the unmagnetized shock expands radially at a supersonic velocity of $v_s \approx 6$ km s^{-1} (sound speed $C_{s0} = 3.1$ km s^{-1}, see Table 2.1). At very late time, when there is sufficient radial expansion, the density and pressure in the return flux region are expected to be low enough so that the expansion will become sonic. The entire jet structure is expected to transit to pressure confinement from inertial confinement [82].

These radial profiles of the central jet confirm that the jet is highly magnetized and is MHD-collimated. The cross-sectional view of various plasma properties in Fig. 2.10 further

validate this point. By comparing Fig. 2.10 with Fig. 2.5, we find that the strong poloidal field and current are both confined in the dense plasma region (central jet region and the outer boundary of the return flux region). Poloidal field, current, and toroidal field have been established from $z = 0$ to $z = 1.8$, same as the density and Poynting flux (Fig. 2.5 and 2.8).

Figure 2.10 shows that the poloidal current is approximately parallel to the poloidal magnetic field in most of the region, especially in the central column, suggesting that the Lorentz force is dominantly poloidal, because the toroidal Lorentz force $\mathbf{F}_{\rm tor} = \mathbf{J}_{\rm pol} \times \mathbf{B}_{\rm pol} \approx 0$. This is consistent with the analysis given by Eq. 2.23. Detailed calculation finds that $F_{\rm tor}$ in the simulation is generally one to three orders of magnitude smaller than $F_{\rm pol}$. The Lorentz force distribution panel shows that $\mathbf{J} \times \mathbf{B}$ is extremely strong at the jet boundary especially at relatively low height. The Lorentz force at the jet boundary is radially inwards due to the self-pinch of the poloidal current, and is responsible for the collimation. The very large gradient of this pinching force along z direction $\partial_z[(\mathbf{J} \times \mathbf{B})_r]$, equivalent to the gradient of toroidal magnetic energy $\partial_z(B_\theta^2)_r$, collimates the plasma gradually from lower z to higher z, and ultimately accelerates the plasma. This demonstrates the MHD pumping mechanism in the current-driven plasma tube proposed by Bellan (2003) [4] and verified in the Caltech plasma jet experiment [63, 126, 127]. Figure 2.10 also shows that the return flux/current are expanding outwards under a relatively strong Lorentz force. It is notable that at $z > 0.7$, where the jet has not been fully collimated, the poloidal field is being compressed at very small radius, resulting in a radial outward Lorentz force.

The plasma β panel shows that the central jet has a typical $\beta \approx 10^{-1.5} - 10^{-1}$ $(0.03-0.1)$, consistent with the experiment (§ 1.2). Hence the jet is magnetically dominated. The β value is even smaller in the diffuse pinch region, due to the low plasma density and relatively strong toroidal magnetic field. The hydro shock has a very high β value since it is essentially unmagnetized.

Figure 2.11 compares the magnetic structure of the simulation jet with the experimental jet. The experimental measurements are obtained using the 1 MHz 20-channel MPA at $z = 15$ cm from the electrode plane [95] in a typical argon jet experiment. The top panel shows poloidal flux contours calculated from the MPA measurement from $t = 15$ μs to $t = 25$ μs, during which times the MPA has effectively "scanned" approximately 15 cm distance along the z direction in the moving frame of jet, although the MPA is fixed in the

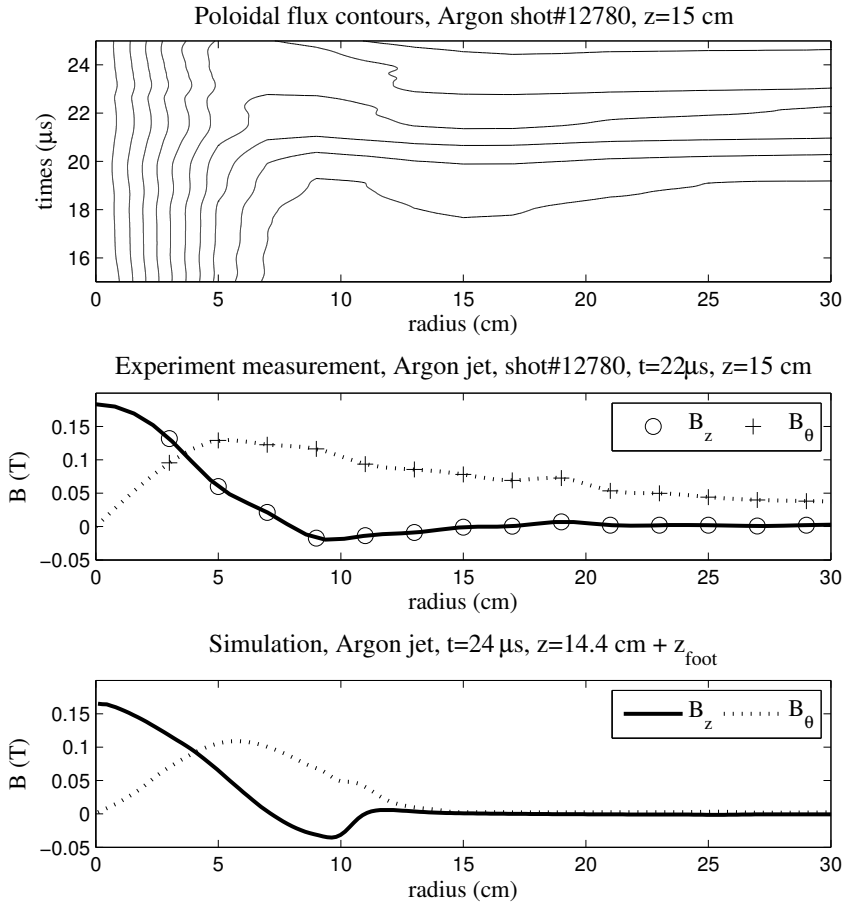

Figure 2.11: Top panel: poloidal magnetic field contours inferred from the MPA measurements from $t = 15$ μs to $t = 25$ μs. Mid and Bottom panels: magnetic field in axial (heavy solid curves) and azimuthal (dotted curves) direction measured in the experiment (mid panel) and in the simulation (bottom panel). The experimental measurements (top two panels) are obtained in argon jet experiment shot # 12780. This experiment jet remains quasi-axisymmetric at $t = 22$ μs.

lab frame. The contours show that the magnetic field lines inside the jet ($r \lesssim 5$ cm) are quite collimated. The middle panel plots the radial profiles of B_z and B_θ at $t = 22$ μs in the experiment. The bottom panel gives the magnetic profiles in the simulation at $z = 14.4$ cm$+z_{\rm foot}$ at $t = 24$ μs. In both simulation and experiment, B_z is $\simeq 0.2$ T at the central axis and reverses direction at $r \approx 7$ cm; B_θ rises quasi-linearly for small r and peaks at $r = 5$ cm. Hence J_z is approximately constant within the central jet. Despite the excellent agreement in the central column region, it should be noted that the return current in the experiment extends to a much larger radius, leaving the entire 5 cm$< r <$ 30 cm region devoid of current ($B_\theta \propto 1/r$). The return current in the simulation is at $\approx 8-15$ cm, where

B_θ deviates from the $1/r$ behavior and quickly becomes zero. The return magnetic flux in the experiment, on the other hand, is located at $\approx 9-10$ cm, very similar to the simulation.

The B_θ due to the axial current in the jet produces a radially outward Lorentz force at the location of the return current. The expansion speed of the return current is determined by the density of the return flux region (T-shell in Fig. 2.5) and the background pressure. The density of the return flux region $n \sim 10^{21}$ m^{-3} (Fig. 2.5 and 2.9) is possibly too high compared to the experiment, although the experiment does not have accurate measurements of the low density plasma in the return current region. Also, the background pressure in the experiment (10^{-7} torr $\sim 10^{-5}$ Pa for $n \sim 10^{15}$ m^{-3} and $T = 300$ K) is also much lower than the simulation background pressure ($p_0 = 3.2$ Pa for $n = 10^{19}$ m^{-3} and $T = 2$ eV). Numerical investigation has found that the return current extends to a larger radius for a less dense T-shell or background. More discussion is given in § 2.4.3 and 2.6.

Figure 2.12 plots the 3D global magnetic field structure at $t = 29.1$ μs, which shows a typical magnetic tower structure with upward flux along the jet and return flux surrounding the jet. The upward flux is twisted relative to the return flux. Tracing each field line from mid plane, the ratio B_θ/B_z is roughly constant along the central jet, and increases rapidly near the jet head because B_z becomes zero at the turning point. Combining this figure with Fig. 2.7 panel E & F, we find that at the jet head the poloidal field along the axis can remain comparable to the toroidal field at the jet boundary, although for each field line B_θ/B_z always increases. This is because the poloidal field and current do not bend over and return to mid plane at exactly the same height and same radius, i.e., there is no distinct jet head (also see § 2.3.1.2). Both B_z along the axis and B_θ at the jet boundary decrease gradually in the jet head region, giving a relatively constant ratio between them. The opening angles of the field lines shown in Fig. 2.12 are $5-6°$. Calculation shows that a field line starting from $r \sim 0.2$, essentially the boundary of the jet, has an opening angle of 11°; a field line from $r = 0.1$ has an opening angle of 4°. It is found in the simulation that the opening angles become smaller as the toroidal field injection continuously accelerates and collimates the jet.

2.3.1.4 Alfvén velocity and Alfvén surface

Spruit (2010) [106] categorizes the standard magnetocentrifugal acceleration model [14] into three distinct regions: accretion disk, magnetic dominant region surrounding the central

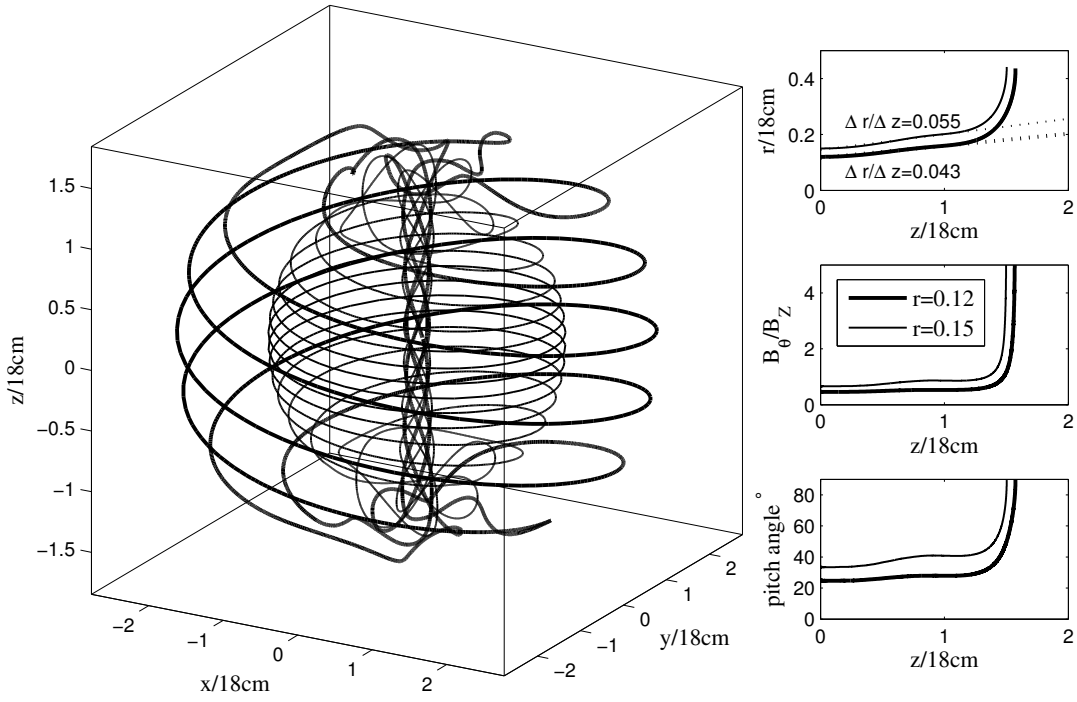

Figure 2.12: Left: 3D magnetic field structure of the simulation jet. The structure is composed by two groups of field lines starting from mid plane at $r = 0.12$ (2.16 cm) and $r = 0.15$ (2.7 cm). Each group contains four field lines azimuthally equally spaced starting at same radius. Upper right: radial location of each fieldline at different height. Linear regression within $0 \leq z \leq 1.2$ gives $\Delta r/\Delta z = 0.043$ with $R^2 = 0.981$ for field lines starting from $r = 0.12$, and $\Delta r/\Delta z = 0.055$ with $R^2 = 0.980$ for field lines starting from $r = 0.15$. These correspond to opening angles $\theta = 2\arctan(\Delta r/\Delta z) = 4.9°$ and $6.3°$ for the two groups of field lines, respectively. Mid right: B_θ/B_z along the field line from mid plane to jet head. Lower right: the pitch of the magnetic field $\theta \equiv \arctan(B_\theta/B_z)$ in degree. In all three subplots, the thick curves represent fieldlines starting from $(r = 0.12, z = 0)$ and the thin curves represent fieldlines from $(r = 0.18, z = 0)$. The fieldlines are obtained at $t = 0.5$ or 29.1μs.

objects, and a distant kinetic dominant region. An Alfvén surface, on which the plasma velocity equals the Alfvén velocity $v_A \equiv B/\sqrt{\mu_0\rho}$, separates the magnetic dominant region and kinetic dominant region, since the ratio of plasma velocity to Alfvén velocity, $v/v_A = [(\rho v^2)/(B^2/\mu_0)]^{1/2}$, is the square root of the ratio of kinetic energy to magnetic energy.

Figure 2.13 plots the distribution of dimensionless Alfvén velocity (top four panels) and v/v_A ratio (bottom four panels) in the rz plane at different times. The boundaries of the central jet region and the diffuse pinch region are overlaid on the lower right panel. The figure shows that v_A is always high in the diffuse pinch region due to the low density and strong toroidal field. In the central jet, v_A remains roughly constant because of the quasi-

constant density and magnetic field configuration. The high Alfvén velocity region increases in volume together with the jet propagation.

The v/v_A distribution plots show that the Alfvén surface, denoted by the innermost $v = v_A$ contour curve, is also expanding. In the $+z$ direction, the Alfvén surface propagates from $0.5R_0 = 9$ cm at $t = 11.6$ μs to $1.5R_0 = 27$ cm at $t = 29.1$ μs at a speed of ≈ 10 km s^{-1}, similar to the jet propagation speed. Along the central axis, the v/v_A ratio gradually increases from $\ll 1$ at jet base to ~ 1 at jet head, and becomes $\gg 1$ at the hydro shock which has no magnetic field. According to Fig. 2.5, 2.7 and 2.10, the magnetic tower, wherein dense plasma encloses strong axial magnetic field B_z and axial current J_z, is inside the Alfvén surface. We point out here that the entire jet collimation and propagation dynamics is an integrated process. It is inappropriate to characterize the jet as a hydrodynamic jet or magnetized jet simply based on the local v/v_A ratio, because the Alfvén surface is also expanding. Although the kinetic energy of the global system extends beyond the Alfvén surface in Fig. 2.13, the magnetic tower is still an MHD driven jet. Outside the Alfvén surface, according to Fig. 2.7, both the poloidal and toroidal components of the magnetic field decrease rapidly. The entire diffuse pinch region always has a relatively low v/v_A ratio. Outside the Alfvén surface, there is another $v_A = v$ contour expanding outwards, which indicates the hydrodynamic shock. This is essentially the boundary of the entire large-scale jet structure. Outside this structure, both v and v_A are zero.

2.3.2 Bernoulli equation in MHD driven flow

We have shown in detail the process of jet collimation and propagation resulting from the MHD mechanism. In § 2.3.1.2, we have demonstrated that the jet gains its kinetic energy from magnetic energy; kinetic energy dominates near the jet head while magnetic energy dominates near the jet base. This has been quantitatively verified in the experiment.

Assuming that the Lorentz force balances the thermal pressure gradient in the radial direction, an axisymmetric model was proposed by Kumar & Bellan (2009) [61, 63] to study the non-equilibrium steady-state flow along the axial direction. The model claims that a Bernoulli-like quantity involving the toroidal magnetic energy remains constant along the jet, i.e.,

$$\frac{\partial}{\partial z}\left[\rho v_z^2 + \frac{B_{\theta,a}^2}{\mu_0}\left(1 - \frac{r^2}{2a^2}\right)\right] = 0, \tag{2.31}$$

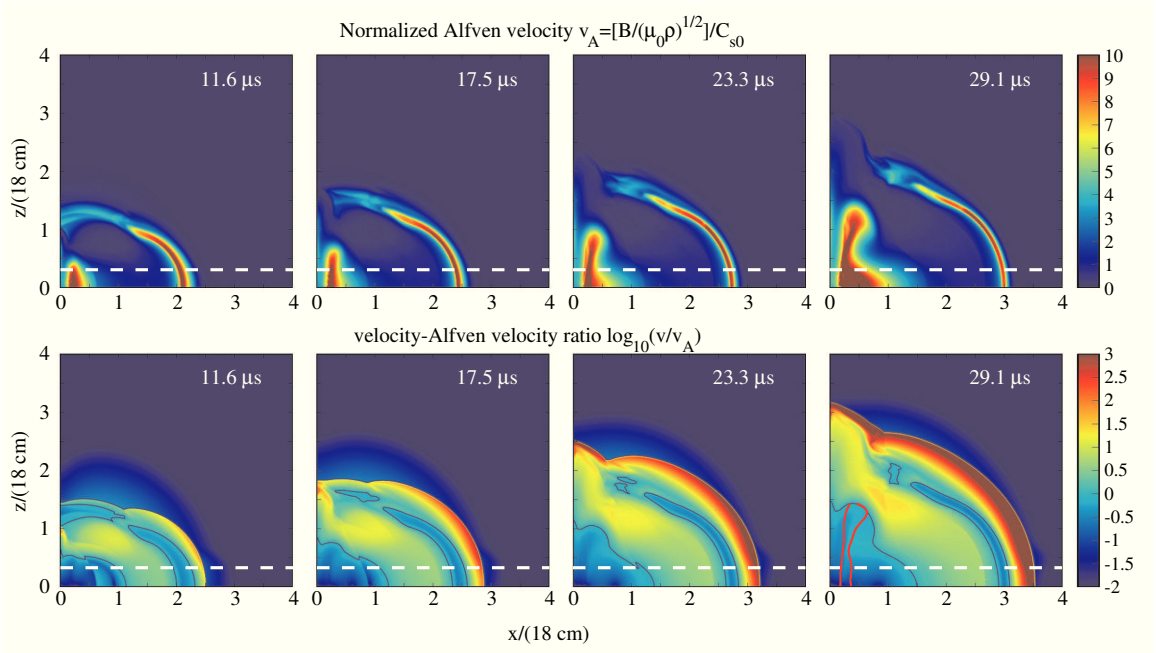

Figure 2.13: Alfvén velocity v_A and velocity to Alfvén velocity ratio v/v_A in rz plane at different times. Top four panels: the color map of dimensionless Alfvén velocity $v_A/C_{s0} = [B/\sqrt{\mu_0\rho}]/C_{s0}$ (C_{s0} given in Table 2.1). Bottom four panels: the color map of $\log_{10}(v/v_A)$ with $v = v_A$ contours (blue curves). The lower right panel is overlaid by two red curves. The one at smaller radius from $z = 0$ to $z = 1.6$ represents the contour of maximum B_θ at each height, and is the boundary between the central jet region and diffuse pinch region. The red curve at larger radius is the $J_z = 0$ contour, that separates the diffuse pinch region and the return flux region.

where a is the jet radius and $B_{\theta,a} = \mu_0 I/(2\pi a)$ is the toroidal field strength at the jet boundary. Evaluating the expression at $r = 0$ gives

$$\rho v_z^2 + \frac{B_{\theta,a}^2}{\mu_0} = \rho v_z^2 + \frac{\mu_0 I^2}{4\pi a^2} = \text{const}, \tag{2.32}$$

which is a Bernoulli-like equation. At $z \sim 0$, the axial velocity $v_z \approx 0$ so the magnetic energy dominates. At the jet head, $B_{\theta,a} \approx 0$ so the kinetic energy dominates. This is consistent with the analysis in § 2.3.1.2. Evaluating Eq. 2.32 at $z = 0$ and at the jet head yields

$$v_z|_{\text{jet head}} \simeq \frac{I}{2\pi a}\sqrt{\frac{\mu_0}{\rho}}\bigg|_{z=0} \propto \frac{I}{\sqrt{\rho}}. \tag{2.33}$$

Kumar & Bellan (2009) [61, 63] reported quantitative experimental measurements and showed that the axial velocity of the MHD driven plasma jet is linearly proportional to the poloidal current, and inversely proportional to the square root of the jet density. Therefore

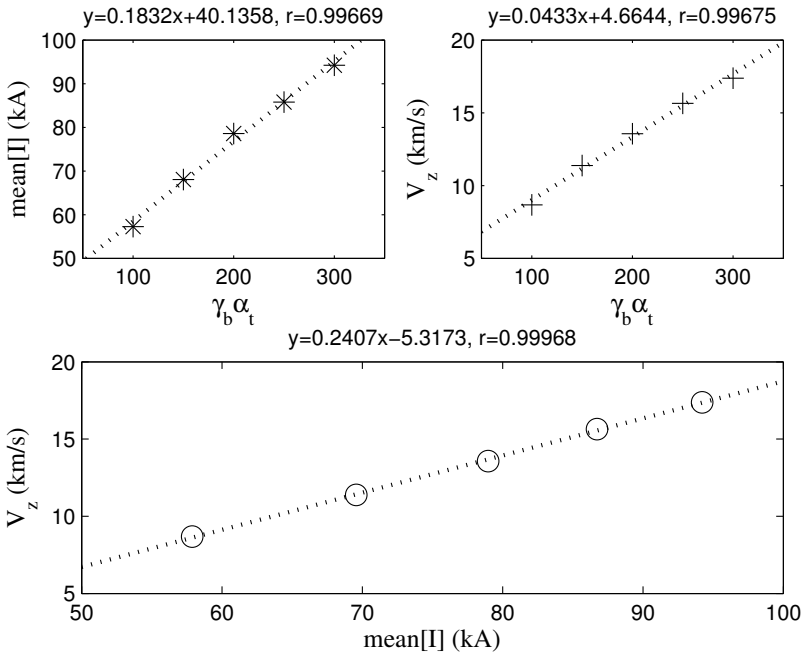

Figure 2.14: Jet velocity dependence in the simulation. Upper left: time-averaged total poloidal current for different injection rate $\gamma_b\alpha_t$ (asterisk symbols). Upper right: the averaged jet velocity at different injection rate $\gamma_b\alpha_t$ (plus symbols). Bottom: jet velocity vs. total poloidal current (open circle symbols). The averaging period is the time the jet head spends traveling from $z = 30$ cm to 60 cm. For each subplot, linear regression is performed (dotted lines) and the results are presented as the title.

Eq. 2.33, a direct corollary of Eq. 2.31, has been verified by the experiment.

Equation 2.33 can be understood from a semi-quantitative analysis. Since the injected Poynting flux or toroidal magnetic field energy will ultimately be used to accelerate the jet, an energy equal-partition gives $B_\theta^2 \sim \rho v_z^2$. Hence $v_z \sim B_\theta/\sqrt{\rho} \sim I/\sqrt{\rho}$. Similar analysis and scaling can also be found in [46, 74, 75, 118].

We now use the simulation to investigate this relation.

2.3.2.1 Jet velocity dependence on the poloidal current

We use the same initial conditions as in § 2.3.1, and the same localized toroidal field injection with the localization factor $A = 9$. However, in order to control the total poloidal current, we use constant injection rates $\gamma_b\alpha_t$ throughout the simulation. Five simulations are performed with different time-independent injection rates over a wide range: $\gamma_b\alpha_t = 100$, 150, 200, 250, and 300. The average jet velocity is computed using the time the jet head takes to travel from $z = 30$ cm to 60 cm ($z = 1.67$ to 3.33 in reduced units). Here we define the location

of the jet head as being where the plasma density drops below 10^{21} m^{-3} along the z axis. According to Fig. 2.5 and Fig. 2.7, this definition gives a sufficiently consistent estimation of the jet head location. The total poloidal current is also averaged over the same period. Figure 2.14 shows that both the jet velocity and the time-averaged total poloidal current are proportional to the toroidal field injection rate $\gamma_b \alpha_t$. Thus the jet velocity is indeed proportional to the poloidal current.

2.3.2.2 Jet velocity dependence on the jet density

Kumar & Bellan (2009) [61, 63] found that under the same experimental configuration, a deuterium plasma jet always propagates at a speed $= 0.73 \approx 1/\sqrt{2}$ times the speed of a hydrogen plasma jet. Therefore $v_z \propto 1/\sqrt{\mu} \sim 1/\sqrt{\rho}$ is verified. In the simulation, this dependence is already incorporated by the normalization process in § 2.2.1. Note that the simulation time unit is defined as

$$t_0 \equiv \frac{R_0}{C_{s0}} \propto \frac{1}{C_{s0}} \tag{2.34}$$

and

$$C_{s0}^2 \propto \frac{1}{m_i} \propto \frac{1}{\mu}, \qquad \mu \equiv \frac{m_i}{m_H}, \tag{2.35}$$

so the simulation time unit is proportional to $\sqrt{\mu}$. Therefore the simulation velocity unit is proportional to $1/\sqrt{\rho}$.

Given that $n \approx 10^{22}$ m^{-3} and $a \approx 4$ cm, Eq. 2.33 predicts $v_z/I \simeq \sqrt{\mu_0/\rho_0}/(2\pi a) = 0.244$ m/(s·A) $= 0.244$ km·s^{-1}/kA, which is consistent with the linear regression results given in the bottom panel of Fig. 2.14.

2.3.2.3 A direct illustration of MHD Bernoulli equation

In fact, Eq. 2.31 can be easily verified directly by the simulation. Evaluating the equation at the jet radius $r = a$ gives

$$\frac{\partial}{\partial z}\left(\rho v_z^2 + \frac{B_{\theta,a}^2}{2\mu_0}\right) = 0 \Rightarrow \quad (e_k + e_{B_{\rm tor}}/2)|_{\rm jet\ radius} = \text{const}, \tag{2.36}$$

where the kinetic energy density is $e_k \equiv \rho v_z^2/2$ and the toroidal magnetic field energy density is $e_{B_{tor}} \equiv B_\theta^2/2\mu_0$.

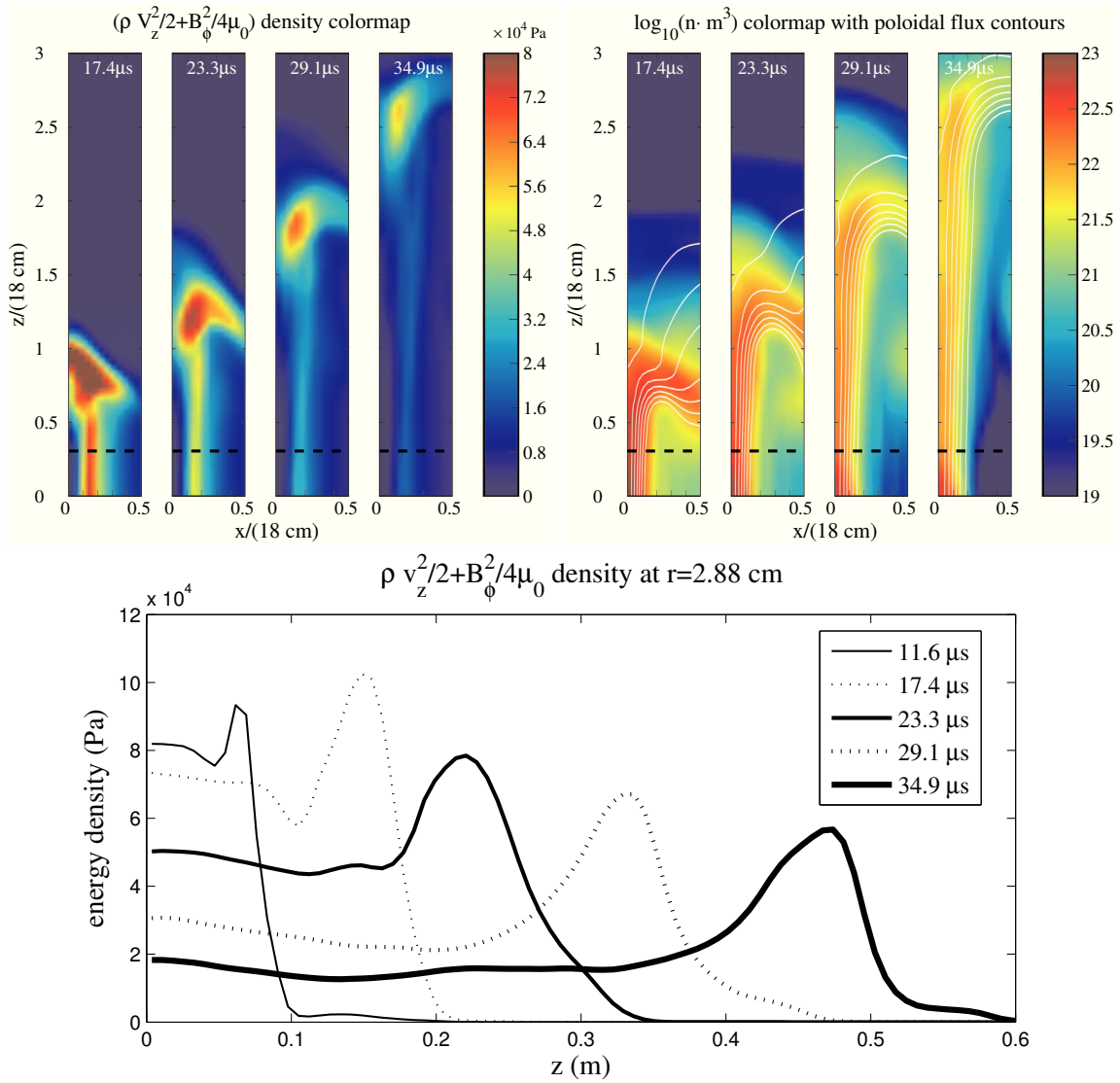

Figure 2.15: Top left panel: cross-sectional view of $(e_k + e_{B_{\rm tor}}/2)$ energy density on the xz plane ($y = 0$) from 17.4 μs to 34.9 μs. Top right panel: cross-sectional view of density distribution (log scale) at the same times as used for the plots in the top panel. Azimuthally averaged poloidal flux contours are overlaid. Note that the jet radius to length ratio has dropped to $\sim 1:20$ at $t = 34.9$ μs. Bottom panel: $(e_k + e_{B_{\rm tor}}/2)$ at $r = 2.88$ cm along the z direction at different times. The plots are generated from the $\gamma_b\alpha_t = 200$ simulation in § 2.3.2.1.

We choose the $\gamma_b \alpha_t = 200$ simulation presented in § 2.3.2.1 and plot the 1D profile of $(e_k + e_{B_{\rm tor}}/2)$ along the jet radius and the cross-sectional 2D view of $(e_k + e_{B_{\rm tor}}/2)$ and density/flux in Fig. 2.15. The three plots directly illustrate that at any given time after jet collimation is completed, $(e_k + e_{B_{\rm tor}}/2)$ is constant on the boundary of a magnetic tower jet through the entire jet body.

Having cross-checked the jet velocity dependence on poloidal current and density using experiments, simulation, and analytical theory, and also demonstrated that Eq. 2.36 holds along the jet in the simulation, we conclude that Eq. 2.33, and more generally, the MHD Bernoulli Eq. 2.31 are true for magnetic tower jets, such as the Caltech experimental plasma jet and possibly actual astrophysical jets.

2.4 Sensitivity to imposed simulation conditions

The numerical simulations presented in § 2.3.1 are based on a number of imposed conditions, including initial mass distribution, background pressure, initial poloidal field, toroidal field injection rate and toroidal field injection volume (factor A). As discussed in § 2.2, the initial poloidal field flux and toroidal field injection rate are selected strictly on the experiment properties. The initial mass distribution in simulation is similar to the real experiment case. We now examine how our key conclusions depend on these imposed conditions.

We perform another eight simulations with exactly the same conditions as the simulation presented in § 2.3.1 (referred as the "original" simulation or simulation A in the following discussion), except for one different condition. The density distribution and poloidal field configuration at $t = 29.1$ μs of these eight simulations are plotted in Fig. 2.16 together with the original simulation.

2.4.1 Background condition

The original simulation has a background plasma particle number density $n_{\rm background} = 1$, or 10^{19} m^{-3}, about $10^3 - 10^4$ times less dense than the central jet (Fig. 2.16A). In the experiment, this number is $10^7 - 10^8$. However, as long as the background density is significantly lower than the plasma of interest, the dynamics of the central jet should not be affected.

This is verified by simulation B and C, which have $n_{\rm background} = 0.1$ and 10, respectively.

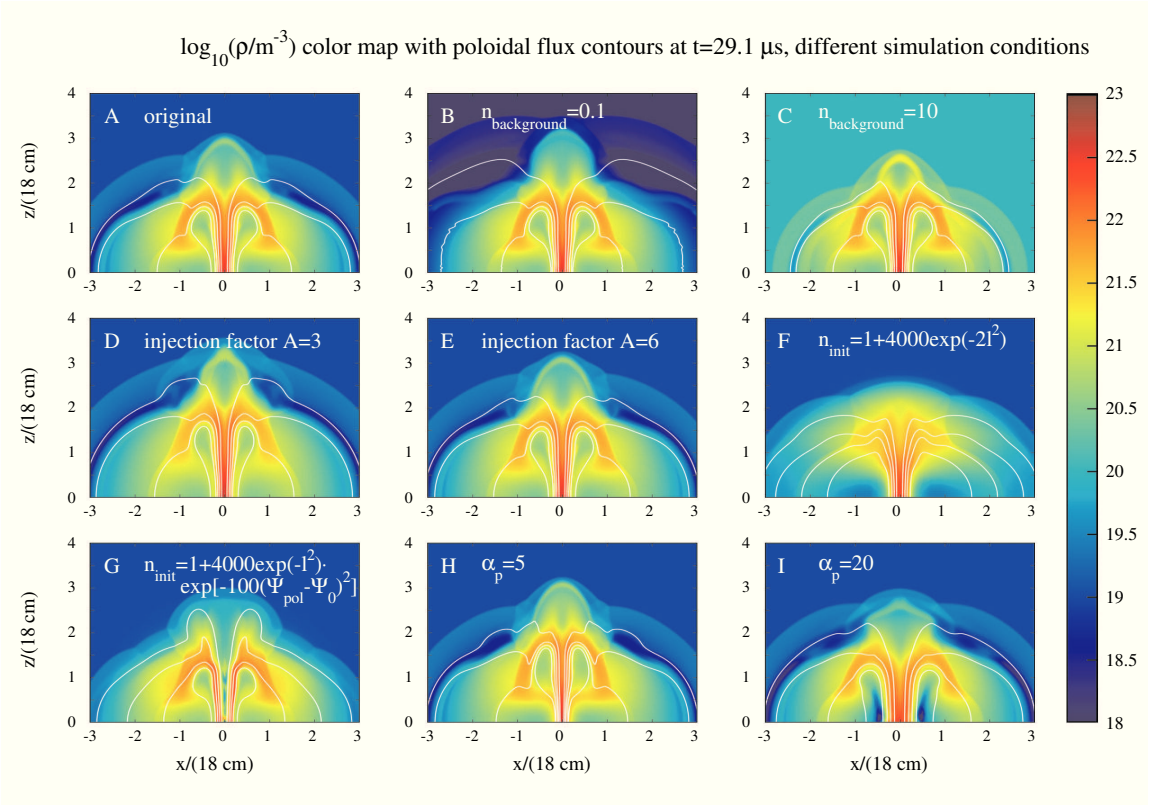

Figure 2.16: Cross-sectional view of density distribution (color map) and azimuthally-averaged poloidal flux contours (white curves) in xz plane ($z > 0$) at $t = 0.5$ (29.1 μs) of nine simulations with different conditions. Each plot is formatted the same way as Fig. 2.5 except the density range is from 10^{18} m^{-3} to 10^{23} m^{-3}. A: the original simulation described in § 2.3.1 with initial mass distribution $n_{\rm init} = n_{\rm background} + 4000e^{-l^2}e^{-40[(r-1/2)^2+z^2-1/4]^2}$, background density $n_{\rm background} = 1$ (corresponding to 10^{19} m^{-3}), injection factor $A = 9$, and total poloidal flux factor $\alpha_p = 10$ (corresponding to a total flux 1.59 mWb). Panel B-I show simulations with same conditions as simulation A except with only **one** different condition. B: simulation with initial background density $n_{\rm background} = 0.1$ (10^{18} m^{-3}), 10 times lower than simulation A. C: simulation with initial background density $n_{\rm background} = 10$ (10^{20} m^{-3}), 10 times denser than simulation A. D: simulation with injection factor $A = 3$. E: simulation with injection factor $A = 6$. F: simulation with initial mass distribution $n_{\rm init} = 1 + 4000e^{-2l^2}$. G: simulation with initial mass distribution $n_{\rm init} = 1+4000e^{-l^2}e^{-100(\Psi_{\rm pol}(r,z)-\Psi_0)^2}$. H: simulation with initial poloidal flux factor $\alpha_p = 5$ (corresponding to a total flux 0.79 mWb, 50% of simulation A). I: simulation with initial poloidal flux factor $\alpha_p = 20$ (corresponding to a total flux 3.17 mWb, twice of simulation A). The injection rates $\gamma_b\alpha_t$ of simulation H and I are adjusted correspondingly so that the effective toroidal injection rate $\gamma_b\alpha_t\alpha_p$ of these two simulations are the same with simulation A. Panel A-G are overlaid by poloidal flux contours from 0.2 mWb to 1.4 mWb every 0.4 mWb. Panel H has contours from 0.1 to 0.7 mWb every 0.2 mWb; Panel I has contours from 0.4 mWb to 2.8 mWb every 0.8 mWb.

Comparing A, B and C, they show no difference in the central jet and the vicinity. The hydro shock and return flux at very large radii, however, are indeed affected by the different background conditions. Consistent with the discussion in § 2.2.2.2, § 2.3.1.2, and § 2.3.1.3, a lower background pressure imposes a weaker restriction to the expansion of the system.

In an astrophysics situation, the density difference between the central jet and ambient environment (ISM/IGM) is expected to be less than in the experiment and the shock structure and the return flux are expected to be somewhat different. With a significant background pressure, the expansion of return flux and current can be highly constrained. If the return flux and current are sufficiently near the center jet, they can influence the jet stability properties. This is similar to how a conducting wall surrounding a current-carrying plasma tube can prevent the plasma against from developing a kink instability.

2.4.2 Toroidal field injection condition

The toroidal field injection condition is subjected to two major possible variations: injection rate and injection volume.

The injection rate affects the total poloidal current and therefore affects the jet velocity according to Eq. 2.33. In § 2.3.2, we have addressed this issue by performing five simulations with different injection rates. Figure 2.14 shows that jet velocity is proportional to the toroidal injection rate.

Injection volume is determined by the injection factor A (§ 2.2.3.1). We already pointed out that the factor A does not alter the total poloidal current associated with the toroidal field. Simulation D and E shown in Fig. 2.16 are performed with $A = 3$ and $A = 6$, respectively. At $z = 1$, the factor $e^{-Az^2} = 0.05$, 2.5×10^{-3}, and 1.2×10^{-4} for $A = 3$ (D), 6 (E), and 9 (A), respectively. Even with such enormous differences, the plasmas in simulation A, D, and E evolve in very similar ways. This is because the injected toroidal field is able to emerge into the propagating jet rapidly, no matter where the field is initially injected (see also in Fig. 2.7, 2.8 and 2.10).

A notable difference for different A factors is the behavior of the hydro shock and remote return flux. This is because toroidal injection with a smaller A gives larger direct field injection at larger distance and low density region, and therefore gives rise to a faster expanding shock and return flux.

The A factor determines the thickness of the effective engine region. In the experiment

and astrophysics cases, the engine region is expected to be limited to the electrodes or the vicinity of central objects. Ideally, a toroidal injection with a larger A factor provides better approximation to the real cases. However, the A factor has little effect on the dynamics of the central jet.

2.4.3 Initial mass distribution

As shown in § 2.3.1 and § 2.3.2, the jet is created as a result of a gradient along the z direction of the pressure associated with the toroidal magnetic field. Therefore the initial mass distribution should not be crucial in the jet dynamics.

Simulation F adopts a very different initial mass distribution $n_{\rm init} = 1 + 4000e^{-2l^2}$, where $l^2 = r^2 + z^2$. A central jet is created with a similar radius and slower speed. Further investigation shows that the well-collimated portion extends from $z \approx 0.8$ to 1.1 in the next 6 μs. The return flux manages to expand further because of the relative low density at large radii initially. The general jet behaviors are consistent with simulation A.

Simulation G takes an initial mass distribution very similar to the real experiment case, $n_{\rm init} = 1 + 4000e^{-l^2}e^{-\delta(\Psi_{\rm pol}(r,z)-\Psi_0)^2}$ with $\delta = 100$ (see § 2.2.2.2). The central region is initially filled with low density plasma. In the experiment, fast magnetic reconnection allows the magnetic field to diffuse into the center along with the plasma. However, in ideal MHD theory, reconnection is forbidden. As shown in panel G of Fig. 2.16, a hollow jet is eventually formed. The axis magnetic field is stronger along the axis than simulation A, because there is no dense plasma in the center helping the poloidal flux against compression of the toroidal pinch. Because the plasma is initially distributed parallel to the poloidal field, simulation G shows a better alignment between plasma and poloidal flux compared to simulation A.

Although the detailed form of initial mass distribution does not significantly affect the formation of the central magnetic tower jet, it can at later times impact the density distribution at larger radius, such as return flux region, and therefore can potentially influence the expansion of the return current. Three additional simulations A2, A3, and A4 are performed which are the same as simulation A (original one) except that there is less dense plasma at either larger radius or larger height. Table 2.2 lists the detailed function of initial mass distribution and the location of return current at $z = 20$ cm for each simulation. Max B_θ in Table 2.2 is the toroidal field strength at the central jet surface. The return flux region

Table 2.2: Location of return current of simulations with different initial density distribution at $z = 20$ cm at $t = 24.4$ μs for simulation A, B A2-A4 and $t = 27.9$ μ for simulation F. Function $f(r,z) = e^{-40[(r-1/2)^2+z^2-1/4]^2}$. $R_{J_z=0}$ is the radius where axial current changes sign and $\bar{R}_{J_z<0}$ is the averaged location of the return current, defined as $\bar{R}_{J_z<0} \equiv (\sum r|J_z|^2)/(\sum |J_z|^2)$ for all negative J_z. The numbers for simulation F are obtained at $t = 27.9$ μs when the jet has a similar height as other simulation jet at $t = 24.4$ μs (see Fig. 15 panel A and F).

Simulation	initial mass distribution	max B_θ (T)	$R_{J_z=0}$ (cm)	$\bar{R}_{J_z<0}$ (cm)
A	$1 + 4000 f(r,z) e^{-r^2-z^2}$	0.119	7.3	11.7
B	$0.1 + 4000 f(r,z) e^{-r^2-z^2}$	0.107	8.3	11.9
F	$1 + 4000 e^{-2r^2-2z^2}$	0.083	9.8	22.6
A2	$1 + 4000 f(r,z) e^{-r^2-4z^2}$	0.123	9.2	16.5
A3	$1 + 4000 f(r,z) e^{-2r^2-z^2}$	0.091	9.0	14.5
A4	$1 + 4000 f(r,z) e^{-2r^2-4z^2}$	0.100	10.5	21.6

(T-shell) of A2-A4 is less dense than that of simulation A. This is because initially there was less dense plasma at larger radius or height. As expected, the return current of A2-A4 expands faster than does simulation A. With a lower background pressure, simulation B also has a faster expanding return current than A does.

It is found that all these simulations produce similar magnetic/kinetic profiles in the central region, although their return current profiles differ significantly. This is because, according to Ampere's Law, there is no magnetic field generated by the return current at the central jet location. In both the simulation and experiment, there is no boundary condition constraining the radius of zero net current and hence the return current radius can expand from the MHD force. The return flux region of simulation A expands at speed $v_r \approx v_z \approx 6$ km s^{-1} at $t = 29.1$ μs (Fig. 2.9). This is comparable with the Alfvén velocity $V_A \sim 15$ km s^{-1} in the diffuse pinch region between the central jet and the return flux/current.

2.4.4 Initial poloidal flux

Compression of the poloidal flux tends to oppose the pinching force of the toroidal field. Simulation H and I verify this with 50% and 200% initial poloidal flux compared to simulation A. Panel H and I of Fig. 2.16 show that with less poloidal flux, the jet has a smaller

radius and propagates faster; with doubled poloidal flux, on the other hand, the plasma struggles to compress the poloidal field, resulting in a much wider and slower jet.

In non-axisymmetric situations, the poloidal flux is expected to impact the stability properties of the current-conducting jet. Experiment investigation involving changing the ratio between poloidal current and poloidal flux, known as "gun parameter", shows that the jet undergoes MHD kink instability when the classical Kruskal-Shafranov threshold is satisfied [49, 50].

In summary, we have shown here how different conditions affect the simulation results. The conditions that directly determine the jet dynamics, such as initial poloidal flux and toroidal injection rate, are selected strictly from the actual experiment conditions. Those conditions that only affect the dynamics of return flux and the hydro shock, such as background pressure, initial mass distribution and toroidal injection volume, can be subject to relatively large variations without significantly influencing the jet dynamics.

2.5 Preliminary results on kink instability

The numerical studies so far in this chapter are only focused on the axisymmetric behaviors of the plasma jet including collimation and propagation. The 3D numerical simulation, however, is capable of studying non-axisymmetric behavior.

In the experiment, due to the inevitably imperfect laboratory condition, the plasma gains enough non-axisymmetric perturbations as seeds that later lead to kink instability. On the other hand, an artificial perturbation must be introduced in the simulation in order to excite non-axisymmetric behaviors. In addition to the initial mass distribution Eq. 2.12, we add a small and localized perturbation

$$n_{perturb} \propto e^{-16r^2} \cdot e^{-5[\mathbf{r}-\mathbf{r}_{pert}(z)]^2} \cdot e^{-2z^2}, \tag{2.37}$$

where $\mathbf{r}_{pert}(z) = 0.15[\cos(15z)\hat{x} + \sin(15z)\hat{y}]$. Figure 2.17 presents the results of a hydrogen jet simulation (see Table 2.1) with the perturbed mass distribution. It is seen that the perturbation is small at $t = 0$ and $t = 6$ μs. However, a notable $m = -1$ kink instability is developed at $t = 10$ μs with a jet-center displacement ≈ 4 cm at $z \approx 9$ cm. The frozen-in poloidal magnetic field and current are also kinked.

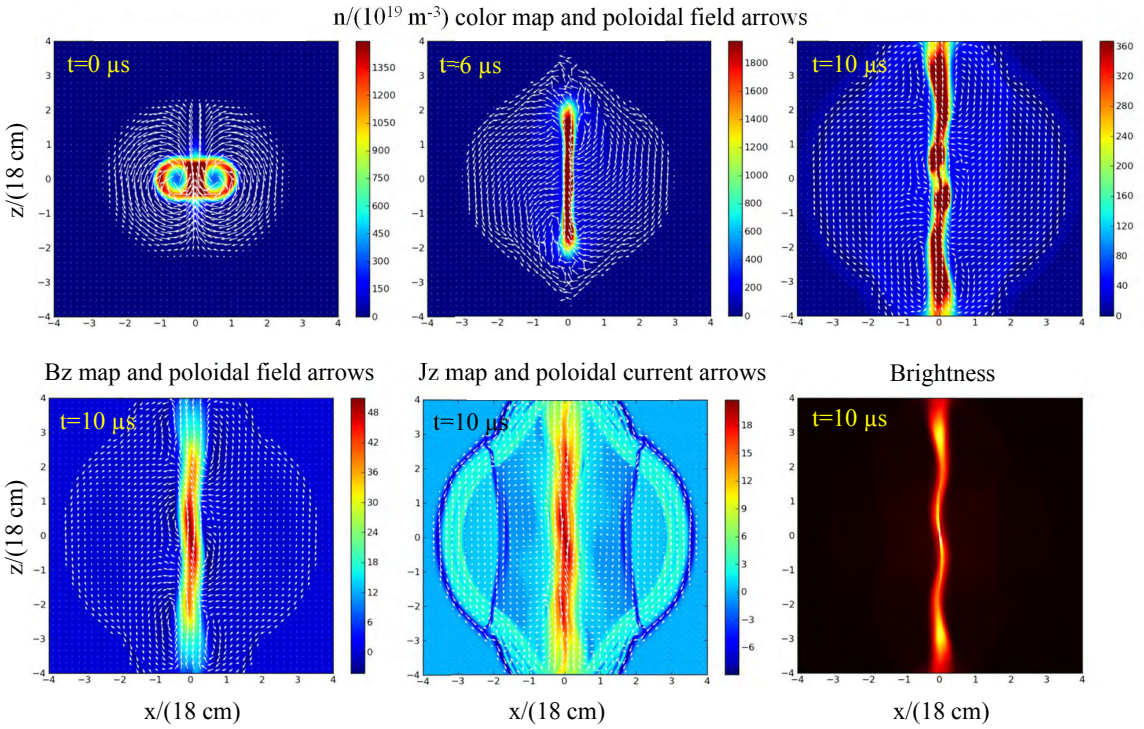

Figure 2.17: A hydrogen jet simulation with perturbed initial mass distribution (Eq. 2.37). Top three panels: three snapshots of the cross-sectional view of plasma density (in unit of 10^{19} m^{-3}) overlaid by poloidal magnetic field arrows. Lower left panel: B_z distribution (in unit of 0.002 T) overlaid by poloidal magnetic field arrows at $t = 10$ μs. Lower middle panel: J_z distribution (in unit of 8.87 kA/m^2) overlaid by poloidal current arrows at $t = 10$ μs. Lower right panel: brightness of the jet obtained by line-of-sight integration of density squares (see Fig. 2.6). Simulation run# 163.

The simulation shown in Fig. 2.17 (run#163) has a total poloidal current $I = 66$ kA at $t = 6$ μs. In a different simulation (run#164), we choose a larger toroidal field injection rate so that the total poloidal current is $I = 80$ kA at $t = 6$ μs. The simulation jet undergoes a faster growing kink instability with the lateral jet-center displacement ≈ 6 cm at $t = 6$ μs (left panel of Fig. 2.18). In simulation run #165, an even larger toroidal field injection rate is selected to give a total poloidal current $I = 150$ kA and a jet-center displacement ≈ 15 cm at $t = 6$ μs (right panel of Fig. 2.18). The fact that larger polodial current gives faster growing kink instability is consistent with theory (see Eq. 3.69 in Chapter 3).

Preliminary analysis of the simulation kink instability shows that the kink amplitude (jet-center displacement) grows linearly with time. This is different from the lab experiment where kink instability grows exponentially fast and gives an equivalent gravity that drives a secondary Rayleigh-Taylor instability. The simulation, on the other hand, shows no sign of

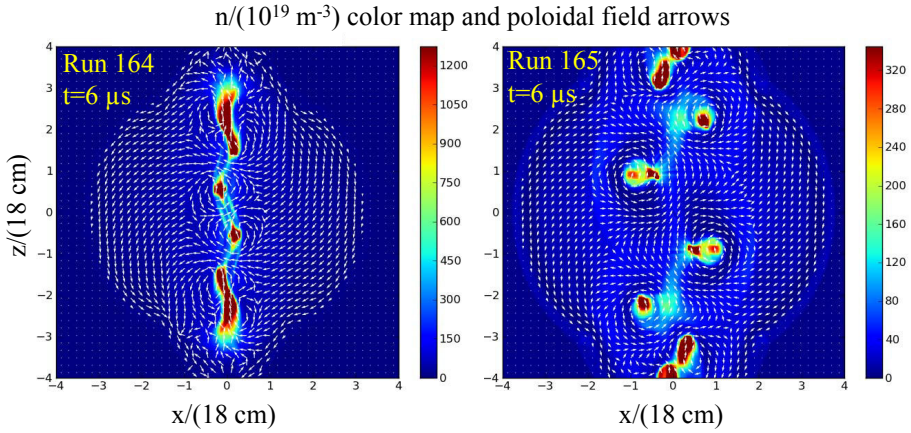

Figure 2.18: Cross-sectional view of plasma density (in unit of 10^{19} m^{-3}) at $t = 6$ μs of two hydrogen simulation runs #164 (left) and #165 (right). The two simulations have different toroidal flux injection rates so that the total poloidal currents at $t = 6$ μs are $I = 80$ kA (left) and $I = 150$ kA (right), respectively.

Rayleigh-Taylor instability. A possible explanation to the discrepancy is the different background condition of the simulation jet compared to the experiment jet. In the experiment, the background is a 10^{15} m^{-3} room-temperature neutral gas (or very weakly ionized gas). In the simulation, however, due to the limitation of numerical computation, we choose a $n_e = 10^{19}$ m^{-3}, fully ionized 2 eV plasma as the background. As discussed in § 2.4 and Fig. 2.16, the relatively high-pressure background in the simulation significantly slows down the expansion of the return current. Meanwhile, the expansion of the kink instability is also expected to be restricted by the dense background plasma.

2.6 Summary and discussion

We have presented MHD numerical simulations of the Caltech plasma jet experiment using a magnetic tower model similar to Li et al. (2006) [68]. By having a purely toroidal magnetic injection localized around the $z = 0$ plane, the simulation jet gains energy and helicity in a manner analogous to the electrode-driven experimental jet, or to astrophysical jets driven by accretion disks. In the simulation, the injected toroidal field near $z = 0$ is efficiently carried through the jet and is responsible for generating the pinch force that collimates both the plasma and the embedded poloidal magnetic field. The gradient of the collimation force along the jet boundary, or equivalently, the gradient of toroidal magnetic field energy in the z direction, is responsible for accelerating the jet. Magnetic to kinetic energy conversion is

verified in the simulation along with the experiment.

The simulation jet agrees quantitatively with the experimental jet in numerous ways, including the energy partition/evolution, current/voltage, jet radius, axial profile, magnetic field structure, and jet velocity scaling. Furthermore, by using the unit systems given in Table 2.1, the simulation results can easily be made dimensionless and then converted to astrophysical scales.

One of the most significant outcomes of this simulation work is the validation of using terrestrial laboratory experiments to study astrophysical jets. Although it is not feasible to experimentally reproduce every single aspect of an astrophysical jet, by careful experiment design it is possible to replicate many of the most important mechanisms that govern the jet dynamics. Also, the experimental investigation shares common advantages with the numerical simulation such as reproducibility, freedom in parameter space and possibility of in-situ measurement. This chapter suggests that combining observation, theoretical modeling, and laboratory experiments helps understand the nature of magnetically driven plasma flows.

We emphasize here that the simulation does not prove that the experimental jets are exactly the same as astrophysical jets. Neither the simulation nor the experiment is expected to reproduce every detail of a theoretical model or an astrophysical jet. However, the fact that an astrophysical magnetic tower model can be used to simulate laboratory experiments suggests that the experiment shares several important similarities with astrophysical jets, such as the collimation and propagation mechanisms. Furthermore consideration of any discrepancies between experiment and simulation help understand the underlying physics.

In both the experiment and simulation, there is no boundary condition or other restriction on the expansion of the return current/flux. The return current/flux expands at a velocity comparable to Alfvénic velocity but the dynamics of the central magnetic tower jet is not influenced by the return current/flux. In astrophysical situations where the background pressure is important [69, 74], free expansion of the return current/flux can be inhibited, resulting in a small or null diffuse pinch region, i.e., the return current/flux could be snugly on the surface of the central jet [83, 100]. In this situation, most of the toroidal field energy is inside the central jet so the jet is expected to be more efficiently collimated and accelerated for a fixed amount of toroidal energy. Meanwhile, an extremely dense return flux region closed to the jet could act like a wall that would stabilize the central jet.

The simulation presented in this chapter mainly addresses jet launching and accelera-

tion mechanisms, i.e., jet collimation, propagation and energy conversion, and considers only axisymmetric dynamics. No asymmetric perturbation is introduced initially or during the simulation. The simulation jets, theoretically vulnerable to kink instability, remain quasi-axisymmetric and stable. However, preliminary investigation has been able to produce slow rising kink instability in the simulation, by using a perturbed initial mass distribution. In the experiment, due to the inevitable imperfectly symmetric laboratory conditions, the jet always undergoes kink instability when the classic Kruskal-Shafranov condition is satisfied [49, 50]. In some cases when the kinked plasma grows exponentially fast and accelerates away from the central axis, a lateral Rayleigh-Taylor instability is induced on the inner boundary of the jet. The Rayleigh-Taylor instability further induces a fast magnetic reconnection that breaks the jet in the middle, and removes some magnetized jet segment from the electrode-attached jet segment [80]. Astrophysical jets in a similar situation, e.g., kink instability or other lateral acceleration, might also be susceptible to this secondary instability. An analytical theory of this Rayleigh-Taylor instability is given in Chapter 3.

The experimental program at Caltech is supported by the NSF/DOE Partnership in Plasma Science. Co-author H. L. is grateful to Stirling Colgate, Ken Fowler, and Ellen Zweibel for discussions. Co-authors H. L. and S. L. are supported by the LANL/LDRD and Institutional Computing Programs at LANL and by DOE/Office of Fusion Energy Science through CMSO.

Chapter 3

A Hybrid Rayleigh-Taylor-Current-Driven Coupled Instability in an MHD Collimated Cylindrical Plasma with Lateral Gravity

We present an MHD theory of Rayleigh-Taylor instability on the surface of a magnetically confined cylindrical plasma flux rope in a lateral external gravity field. The Rayleigh-Taylor instability is found to couple to the classic current-driven instability, resulting in a new type of hybrid instability that grows faster than either of the two instabilities individually. The lateral gravity breaks the axisymmetry of the system and couples all azimuthal modes together. The coupled instability, produced by combination of helical magnetic field, curvature of the cylindrical geometry, and lateral gravity, is fundamentally different from the classic magnetic Rayleigh-Taylor instability occurring at a two-dimensional planar interface. The theory successfully explains the lateral Rayleigh-Taylor instability observed in the Caltech plasma jet experiment [80]. Potential applications of the theory include magnetic controlled fusion, solar emerging flux, solar prominences, coronal mass ejections, and other space and astrophysical plasma processes.

Primary part of this chapter has been submitted to Physics of plasmas.

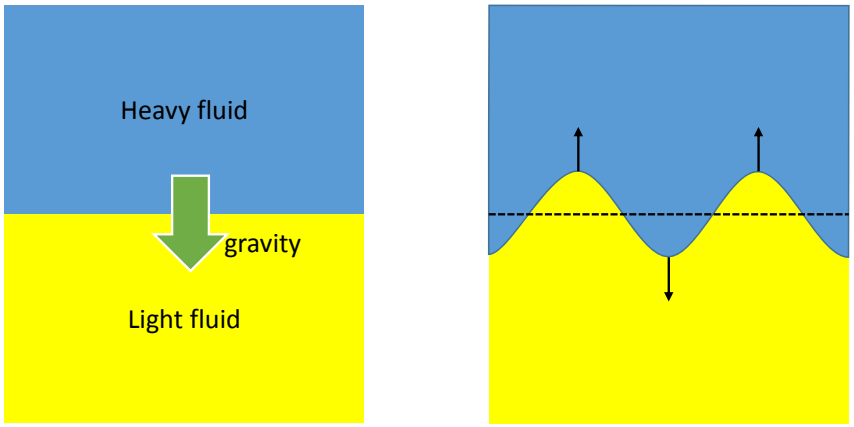

Figure 3.1: Sketch of Rayleigh-Taylor instability. Left: equilibrium state where a heavier fluid is above a lighter fluid. Right: once ripples are developed on the interface, the total gravitational potential energy of the system decreases, and the disturbance to the system is unstable. The black arrows indicate the moving direction of the perturbed surface.

3.1 Introduction

Rayleigh-Taylor (RT) instability is a well-known hydrodynamic instability occurring when a gravitational field points from a high density fluid to a low density fluid [5, 18, 99]. A simple graph explanation of the Rayleigh-Taylor instability is given in Figure 3.1.

In the case that the low density fluid is vacuum and the interface is planar, the growth rate of the one-dimensional (1D) RT instability is

$$\gamma = \sqrt{gk}, \tag{3.1}$$

where g is the gravity and k is the spatial wavenumber of the perturbation on the interface. The instability grows as $\exp(\gamma t)$ in early time when the disturbance caused by the instability is small so that linear stability analysis is valid. The RT instability prefers small scale perturbations because larger k gives faster growth rate. Equation 3.1 results from assuming incompressible fluid with no surface tension. It is known that finite compressibility can stabilize long wavelength perturbations (small k) while surface tension suppresses short wavelength (large k) perturbations [99]. At later times the RT instability is well known to develop bubble and finger-like structures that further undergo Kevin-Helmholtz instability.

The RT instability in a magnetized plasma was first considered by Kruskal and Schwarzschild [59]. For a plasma 'sitting' above vacuum with a magnetic field parallel to

the planar interface, magnetohydrodynamic (MHD) theory shows that the growth rate of this two-dimensional (2D) magnetic Rayleigh-Taylor (MRT) instability is

$$\gamma^2 = gk - \frac{(\mathbf{k}\cdot\mathbf{B_0})^2}{\mu_0\rho}, \tag{3.2}$$

where $\mathbf{B_0}$ is the unperturbed magnetic field, $\mathbf{k}$ is the perturbation wavevector, and ρ is the density of the plasma [5, 18, 59]. It is seen that finite $\mathbf{k}\cdot\mathbf{B}_0$ reduces the growth rate. Because the instability phase is $i\mathbf{k}\cdot\mathbf{x}$, the wavevector $\mathbf{k}$ is perpendicular to the direction of constant phase. This means that for perturbations that try to bend magnetic field lines, i.e., $\mathbf{k}$ not perpendicular to $\mathbf{B_0}$, the magnetic field has a stabilizing effect. Moreover, along the magnetic field, perturbations with $k > \mu_0\rho g/B_0^2$ are completely suppressed, as a result of tension along the magnetic field lines (see § 1.1.1). Such a perturbation, especially for $\mathbf{k} \parallel \mathbf{B}_0$, is usually called an undular mode. For a perturbation with $\mathbf{k} \perp \mathbf{B_0}$, sometimes called the interchange mode, the instability is identical to the hydrodynamic case. However, finite shear in the magnetic field can make a perturbation impossible to align with magnetic field at all depths, and thus helps to stabilize the system [5]. The highly anisotropic nature of the MRT instability has motivated efforts to study its nonlinear behavior using three-dimensional (3D) numerical simulations. It is found that at later times a strong magnetic field may even enhance the growth of bubbles and fingers in comparison to a purely hydrodynamic instability [110].

The RT and MRT instabilities occur in various situations and the 'gravity' $\mathbf{g}$ can originate from different sources. In astrophysical situations such as accretion processes and supernovae remnants, the RT instability happens due to the centripetal gravity from the central object [110]. The interfaces are cylindrical or spherical surfaces. Magnetic implosion of metal liner or Z-pinch plasmas are subject to the MRT instability on the cylindrical interface with the effective gravity caused by radial acceleration of the interface [44, 78, 90, 92]. In laser-based inertial confinement fusion and laser-produced plasma experiments, the RT instability happens when the ablation fronts are accelerated by laser irradiation [11, 112]. The Parker instability or magnetic buoyancy instability can occur when a horizontal magnetic field increasing with depth supports heavier gas on top [2, 51, 88]. This instability shares the same physics as the MRT instability. In space plasmas and magnetic confinement, a concept of "bad" curvature or "good" curvature of magnetic field is also related to

the MRT instability. This is because curved magnetic field lines can introduce an effective gravity to the plasma, as a result of centrifugal force resulting from guiding center motion along curved field lines [5]. In magnetic confinement devices and space plasma, when a pressure gradient exists at a location where the magnetic field has an unfavored curvature, the configuration is RT unstable, and gives rise to the ballooning mode [25, 41, 120]. These RT and MRT processes, despite their diverse geometries and causes, share a common feature that the (effective) gravity $\mathbf{g}$ is perpendicular to the interface. In this sense, the interfaces can be approximately treated as planar.

A recently lab experiment by Moser & Bellan showed a Rayleigh-Taylor instability developed on one side of an argon plasma jet [80]. In the experiment, a plasma jet is created and collimated to uniform radius of $3-5$ cm by MHD forces. The cylindrical jet carries a strong axial magnetic field of 0.2 T and a large axial current of $50-80$ kA, so the magnetic field is in a typical flux rope configuration [63, 126, 130]. When the jet is sufficiently long, it undergoes an $m=-1$ kink instability [49]. The kinked plasma grows exponentially fast and accelerates laterally away from the original central jet axis. In the plasma frame, an equivalent gravity is created due to the acceleration, pointing laterally from the plasma, which is a heavy gas, to the center axis, which is now vacuum. The lateral acceleration of the argon jet is measured to be $g=4\times10^{10}$ m/s^2. See the left panel of Fig. 3.2 for a typical RT instability of a kinked argon jet. A Rayleigh-Taylor instability is induced on the inner boundary of the kinked jet, with an axial wavelength $\lambda_z\sim1-2$ cm and an initial growth rate $\gamma\sim10^6$ s^{-1}. The RT instability quickly erodes and breaks the jet structure, leading to fast magnetic reconnection [80]. Hydrogen plasmas are found to develop kink instability in a very similar manner, but no distinct RT instability has been observed for hydrogen jets with $g\sim10^{10}$ m/s^2; RT instabilities with axial wavelength $\lambda_z=3-5$ cm are observed only in some rare shots with strong lateral acceleration $g=10^{11}-3\times10^{11}$ m/s^2. We name the two cases as type I and type II hydrogen jets, respectively. The right two panels of Fig. 3.2 display the two types of hydrogen jets.

These RT instabilities on one side of a magnetized cylindrical flux rope is interesting because it involves a complicated magnetic structure, a curved interface, and a lateral gravity that is not aways perpendicular to the interface. A sketch of the configuration is given in Fig. 3.3. In a naive attempt we can assume locally the interface is a flat 2D plane. At the bottom of the rope the interface is susceptible to the interchange mode

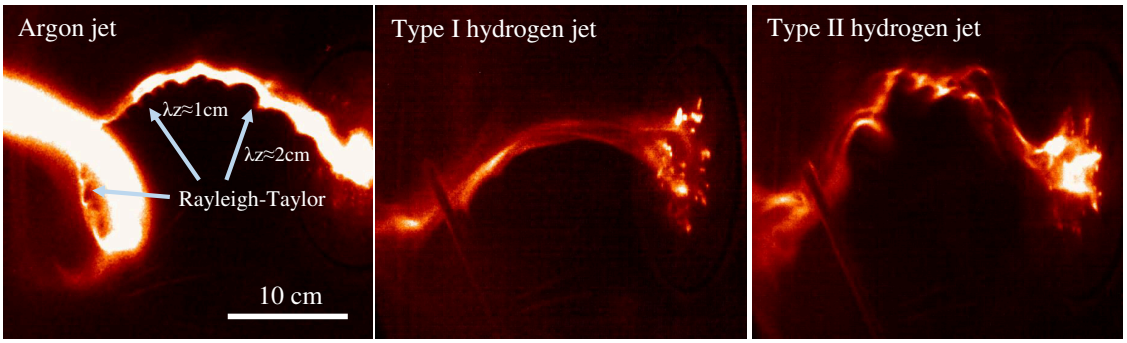

Figure 3.2: Left: a kinked argon jet developing RT instability on the inner side of the surface with lateral acceleration $g = 4 \times 10^{10}$ m/s^2 (shot#13247, $t = 32$ μs). Middle: a type I hydrogen jet with $g = 3 \times 10^{10}$ m/s^2 but no RT, (shot#11596, $t = 11$ μs). Right: a type II hydrogen jet with $g = 1.5 \times 10^{11}$ m/s^2 having $\lambda_z = 4$ cm RT instability (shot#11754, $t = 9.7$ μs). Images are taken by an IMACON 200 high speed camera in visible light (§ 1.2.2.1). Magnetic field measurements show that actual radii of the jets (flux ropes) are 3-5 cm, larger than shown in the visible images [130].

of RT instability, analogous to 2D magnetic RT theory. The growth rate of such mode is $\gamma = \sqrt{2\pi g/\lambda_z} = 5 \times 10^6$ s^{-1}, which is very close to the observation. However, it is questionable whether this interchange mode can exist at other parts of the interface. At the top, the gravity is pointing from vacuum to plasma and hence stabilizes the perturbation; at other locations the gravity is oblique to the interface. The oversimplified local 2D theory is therefore mathematically incompatible with the real case where lateral gravity is applied to cylindrical interface. Moreover, it is also not clear why $\lambda_z = 1$ cm is selected by the instability in argon plasma and why RT does not occur in type I hydrogen jets under the same lateral gravity.

Lateral RT instability in cylindrical geometry was previously considered in geophysics applications of diapir formation and spacing on a rising cylinder of buoyant hydrodynamic fluid [57]. References [71, 72] show theoretically that the RT instability in cylindrical geometry differs significantly from the stability results for 1D or 2D planar interfaces, and that it is fundamentally incorrect to assume that results from planar geometry may be applied to cylindrical configurations.

It is therefore necessary to theoretically consider the lateral RT problem in a more rigorous way. In this chapter we use linear stability analysis to develop an ideal MHD theory of Rayleigh-Taylor instability occurring on the surface of a magnetically collimated plasma-filled flux rope in vacuum with the presence of a gravity perpendicular to the plasma axis.

We linearly perturb an equilibrium flux rope and decompose the perturbation into a summation over all azimuthal modes. The perturbation is assumed to be incompressible. It is found that the lateral gravity breaks the axisymmetry of the system, and consequentially couples all the azimuthal modes to each other. This mutual coupling of all the modes is converted to an eigenvalue problem where an eigenvector gives the amplitude of each azimuthal mode of an 'eigen-perturbation' and the corresponding eigenvalue gives the growth rate of this eigen-perturbation. A parameter $\Phi^2 = gR/v_{A\theta}^2$ quantifies the relative importance of gravity versus azimuthal (toroidal) magnetic field, where R is the flux rope radius and $v_{A\theta} = B_\theta/\sqrt{\mu_0\rho}$ is the toroidal Alfvén speed on the plasma surface. In the weak gravity limit, i.e., $\Phi^2 \ll 1$, different azimuthal modes are decoupled and the theory reduces to the classic current-driven instability ($m = -1$ kink instability). In the weak magnetic field limit, i.e., $\Phi^2 \gg 1$, the theory reduces to the 1D hydrodynamic RT instability (Eq. 3.1) or MRT instability (Eq. 3.2). When both gravity and magnetic field are important, i.e, Φ^2 is of order of unity, the traditional Rayleigh-Taylor instability is coupled to the current-driven instability. This new hybrid instability, denoted as lateral Rayleigh-Taylor-Current-Driven (RT-CD) coupled instability, exhibits interesting features such as an intrinsic 3D geometry and quasi-paramagnetic properties that cannot be fully explained solely by either of the traditional instabilities. It is found that extremely small scale perturbations are suppressed and an optimal axial wavelength exists that gives the fastest growth rate. The theory successfully explains the Caltech experiments: in the argon plasma jet configuration, the theory predicts a coupled RT-CD instability with a $\lambda_z = 1.2$ cm and growth rate $\gamma = 3.6 \times 10^6$ s^{-1}; for the type I hydrogen jets, the theory shows only kink instability; for the type II hydrogen jets, the theory shows some RT effect with a $\lambda_z \sim 5$ cm.

This chapter is arranged as follows. In § 3.2 we state the basic MHD equations and provide an equilibrium solution before perturbation. In § 3.3 we linearly perturb the equilibrium state and use the ideal MHD frozen-in flux condition to connect perturbations inside and outside the plasma. § 3.4 converts the partial differential equations to an eigenvalue problem of infinitely large matrices. In § 3.5 we solve the eigenvalue problem analytically and numerically and compare the results with the lab experiments. § 3.6 summarizes the results and discusses other potential applications. In § 3.7 we provide some supportive materials.

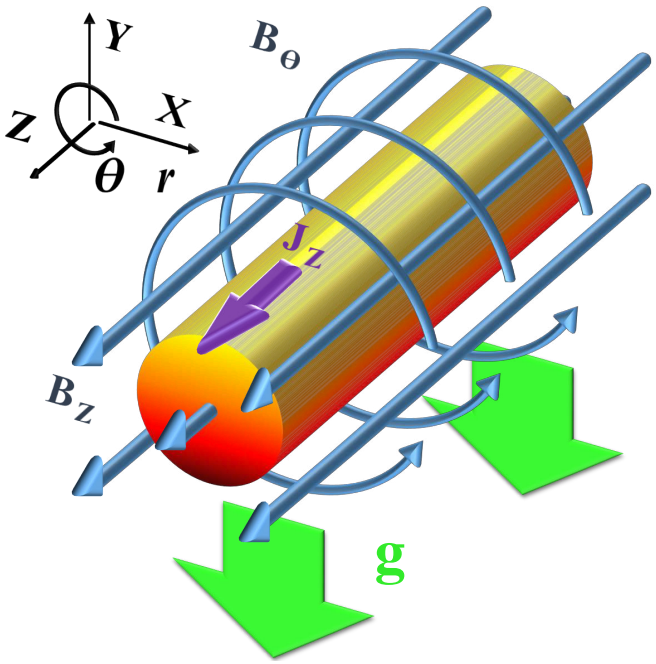

Figure 3.3: A sketch of the plasma jet before RT instability. The jet axis is the z axis and the effective gravity is in $-\hat{y}$ direction ($\theta = 3\pi/2$).

3.2 Equations and equilibrium state

In this chapter we will primarily use cylindrical coordinates but will also use Cartesian coordinates from time to time. The two coordinate systems share a common z axis; the x and y axes of the Cartesian coordinates have respective azimuthal angles $\theta = 0$ and $\pi/2$ in the cylindrical coordinates. See Fig. 3.3 for a sketch of the configuration.

Consider an ideal MHD plasma in the presence of a lateral gravity field in the $-y$ direction. The MHD equations are

$$\frac{\partial \rho}{\partial t} + \nabla \cdot (\rho \mathbf{U}) = 0 \tag{3.3}$$

$$\rho \left(\frac{\partial \mathbf{U}}{\partial t} + \mathbf{U} \cdot \nabla \mathbf{U} \right) = \frac{1}{\mu_0} \mathbf{B} \cdot \nabla \mathbf{B} - \nabla \frac{B^2}{2\mu_0} - \nabla P - \rho g \hat{y} \tag{3.4}$$

$$\frac{\partial \mathbf{B}}{\partial t} = \nabla \times (\mathbf{U} \times \mathbf{B}), \tag{3.5}$$

where all variables have their conventional meaning. The induction equation Eq. 3.5 is equivalent to the ideal MHD frozen-in flux condition, i.e., the magnetic field is frozen into the plasma frame and moves together with the plasma (see § 1.1.2). In Eq. 3.4 the Lorentz

force $\mathbf{J} \times \mathbf{B}$ has been split into a tension-like term and a pressure-like term (see § 1.1.1).

We consider an infinitely long cylindrical plasma which in equilibrium has radius R and uniform B_{0z} inside and outside. The plasma density is uniformly ρ_P inside the cylinder. To reduce complexity, we assume all current is confined to the surface of the cylinder. Therefore $B_{0\theta} = 0$ inside the plasma. B_{0z} is continuous across the surface, hence $J_{0\theta} = 0$. Here the subscript 0 refers to equilibrium quantities. Outside the plasma is vacuum. Therefore the density profile in equilibrium is $\rho_0 = \rho_p \cdot H(r-R)$, where $H(x)$ is the Heaviside step function: $H(x) = 0$ for $x < 0$ and $H(x) = 1$ for $x > 0$.

In equilibrium, $\mathbf{U}_0 = 0$ and so Eqs. 3.3-3.5 reduce to

$$-\nabla\left(P_0 + \frac{B_0^2}{2\mu_0} + \rho_0 g y\right) + \frac{1}{\mu_0}\mathbf{B}_0 \cdot \nabla \mathbf{B}_0 = 0. \tag{3.6}$$

The equilibrium magnetic field is assumed to be azimuthally uniform. The equilibrium magnetic field and current are $B_{0r} = 0$, $\mathbf{B}_0 = B_{0z}\hat{z} + B_{0\theta}\hat{\theta}$, and $\mathbf{J}_0 = J_{0z}\hat{z}$. Since B_{0z} is spatially uniform and θ, z are ignorable coordinates,

$$\mathbf{B}_0 \cdot \nabla \mathbf{B}_0 = B_{0\theta}\hat{\theta} \cdot \nabla(B_{0\theta}\hat{\theta}) = B_{0\theta}^2 \hat{\theta} \cdot \nabla\hat{\theta} = -\frac{B_{0\theta}^2}{r}\hat{r}. \tag{3.7}$$

Equation 3.6 then becomes

$$-\nabla\left(P_0 + \frac{B_{0\theta}^2 + B_{0z}^2}{2\mu_0} + \rho_0 g y\right) - \frac{B_{0\theta}^2}{\mu_0 r}\hat{r} = 0. \tag{3.8}$$

The radial component is

$$-\frac{\partial}{\partial r}\left(P_0 + \frac{B_{0\theta}^2}{2\mu_0} + \rho_0 g y\right) - \frac{B_{0\theta}^2}{\mu_0 r} = 0. \tag{3.9}$$

Because the current is confined to the surface $B_{0\theta}^2 = 0$ inside the plasma and the plasma equilibrium has

$$P_0 + \rho_p g y = const. \tag{3.10}$$

We defined the constants

$$b_z \equiv B_{0z} \qquad b_\theta = B_{0\theta}(R+). \tag{3.11}$$

The total axial current is denoted as I_0 so $b_\theta = \mu_0 I_0 / 2\pi R$ and $B_{0\theta} = (b_\theta R/r) \cdot H(r-R)$.

Without loss of generality, we assume $b_z > 0$ and $I_0 > 0$ and hence $b_\theta > 0$. This gives a right-hand helical magnetic field.

Integration of Eq. 3.9 across the interface gives

$$P_0 + \rho_p g y = \frac{b_\theta^2}{2\mu_0} = \frac{\mu_0 I_0^2}{8\pi R}. \tag{3.12}$$

The equilibrium solution is a simple Bennett pinch configuration with a lateral gravity $\mathbf{g} = -g\hat{y}$ and an axial current confined to the surface.

3.3 Perturbation and linearization

We now perturb the equilibrium state and use the subscript "1" to indicate the first order perturbed quantities. Assume that all the perturbed quantities have dependence $\sim f(r)e^{\gamma t + im\theta + ikz}$, where γ is a complex number and m is an integer. Without loss of generality, we assume $k > 0$. We consider an incompressible perturbation so that

$$\nabla \cdot \mathbf{U}_1 = 0. \tag{3.13}$$

The linearized versions of Eqs. 3.3-3.5 are

$$\gamma\rho_1 + \mathbf{U}_1 \cdot \nabla\rho_0 = 0 \tag{3.14}$$

$$\gamma\rho_0\mathbf{U}_1 = -\nabla\left(P_1 + \frac{\mathbf{B}_0 \cdot \mathbf{B}_1}{\mu_0}\right) + \frac{\mathbf{B}_0 \cdot \nabla\mathbf{B}_1}{\mu_0} + \frac{\mathbf{B}_1 \cdot \nabla\mathbf{B}_0}{\mu_0} - \rho_1 g\hat{y} \tag{3.15}$$

$$\gamma\mathbf{B}_1 = \nabla \times (\mathbf{U}_1 \times \mathbf{B}_0). \tag{3.16}$$

We normalize the magnetic field terms to $b_\theta = B_{0\theta}(R+)$, i.e., $\bar{\mathbf{B}}_0 = \mathbf{B}_0/b_\theta$ and $\bar{\mathbf{B}}_1 = \mathbf{B}_1/b_\theta$. There are

$$\rho_1 = -\frac{1}{\gamma}\mathbf{U}_1 \cdot \nabla\rho_0 = -\frac{1}{\gamma}U_{1r}\frac{\partial\rho_0}{\partial r} \tag{3.17}$$

$$\gamma\frac{\rho_0}{\rho_p}\mathbf{U}_1 = -\nabla\left(\frac{P_1}{\rho_p} + \frac{b_\theta^2}{\rho_p}\frac{\bar{\mathbf{B}}_0 \cdot \bar{\mathbf{B}}_1}{\mu_0}\right) + \frac{b_\theta^2}{\rho_p}\frac{\bar{\mathbf{B}}_0 \cdot \nabla\bar{\mathbf{B}}_1}{\mu_0} + \frac{b_\theta^2}{\rho_p}\frac{\bar{\mathbf{B}}_1 \cdot \nabla\bar{\mathbf{B}}_0}{\mu_0} + \frac{g}{\gamma\rho_p}U_{1r}\frac{\partial\rho_0}{\partial r}\hat{y} \tag{3.18}$$

$$\gamma\bar{\mathbf{B}}_1 = \nabla \times (\mathbf{U}_1 \times \bar{\mathbf{B}}_0). \tag{3.19}$$

The continuity Eq. 3.17 has been used to eliminate ρ_1 in the momentum Eq. 3.18. The constant $1/\rho_p$ has been multiplied on both sides of Eq. 3.18 where ρ_p is the density of unperturbed plasma.

We define the toroidal Alfvén speed

$$v_{A\theta} = \frac{b_\theta}{\sqrt{\mu_0 \rho_p}} \tag{3.20}$$

and dimensionless parameters

$$\Phi^2 = \frac{gR}{v_{A\theta}^2} \qquad \alpha = \frac{b_z}{b_\theta} \qquad \Gamma = \frac{\gamma^2 R^2}{v_{A\theta}^2} \qquad x = kR \qquad q = \alpha x. \tag{3.21}$$

The Alfvén speed $v_{A\theta}$, the parameter Φ^2 and α are all determined by the equilibrium state. α is the pitch angle of the helical magnetic field on the interface. Γ is the dimensionless growth rate. $q = \alpha x = kRb_z/b_\theta$ is the safety factor of the perturbation with $x = kR$.

We divide Eq. 3.18 by $v_{A\theta}^2$ to obtain

$$\frac{\gamma}{v_{A\theta}^2}\frac{\rho_0}{\rho_p}\mathbf{U}_1 = -\nabla \bar{P}_1 + \bar{\mathbf{B}}_0 \cdot \nabla \bar{\mathbf{B}}_1 + \bar{\mathbf{B}}_1 \cdot \nabla \bar{\mathbf{B}}_0 + \frac{\Phi^2}{\gamma \rho_p R} U_{1r} \frac{\partial \rho_0}{\partial r} \hat{y}, \tag{3.22}$$

where we have defined an effective pressure perturbation

$$\bar{P}_1 = \frac{P_1}{\rho_p v_{A\theta}^2} + \bar{\mathbf{B}}_0 \cdot \bar{\mathbf{B}}_1. \tag{3.23}$$

The three components of the equation of motion are

$$\frac{\gamma}{v_{A\theta}^2}\frac{\rho_0}{\rho_p}U_{1r} = -\frac{\partial \bar{P}_1}{\partial r} + (\bar{\mathbf{B}}_0 \cdot \nabla \bar{\mathbf{B}}_1 + \bar{\mathbf{B}}_1 \cdot \nabla \bar{\mathbf{B}}_0)_r + \frac{\Phi^2}{\gamma \rho_p R} U_{1r} \frac{\partial \rho_0}{\partial r} \sin\theta \tag{3.24}$$

$$\frac{\gamma}{v_{A\theta}^2}\frac{\rho_0}{\rho_p}U_{1\theta} = -\frac{1}{r}\frac{\partial \bar{P}_1}{\partial \theta} + (\bar{\mathbf{B}}_0 \cdot \nabla \bar{\mathbf{B}}_1 + \bar{\mathbf{B}}_1 \cdot \nabla \bar{\mathbf{B}}_0)_\theta + \frac{\Phi^2}{\gamma \rho_p R} U_{1r} \frac{\partial \rho_0}{\partial r} \cos\theta \tag{3.25}$$

$$\frac{\gamma}{v_{A\theta}^2}\frac{\rho_0}{\rho_p}U_{1z} = -\frac{\partial \bar{P}_1}{\partial z} + (\bar{\mathbf{B}}_0 \cdot \nabla \bar{\mathbf{B}}_1 + \bar{\mathbf{B}}_1 \cdot \nabla \bar{\mathbf{B}}_0)_z. \tag{3.26}$$

To compute $\bar{\mathbf{B}}_1$, Eq. 3.19 is dotted with ∇h where h is an arbitrary analytic function.

This gives

$$\begin{aligned}
\gamma\nabla h\cdot\bar{\mathbf{B}}_1 &= \nabla h\cdot\nabla\times(\mathbf{U}_1\times\bar{\mathbf{B}}_0)\\
&\overset{*}{=} \nabla\cdot((\mathbf{U}_1\times\bar{\mathbf{B}}_0)\times\nabla h)+(\mathbf{U}_1\times\bar{\mathbf{B}}_0)\cdot\nabla\times\nabla h\\
&\overset{**}{=} \nabla\cdot(\bar{\mathbf{B}}_0\mathbf{U}_1\cdot\nabla h-\mathbf{U}_1\bar{\mathbf{B}}_0\cdot\nabla h)\\
&\overset{***}{=} \bar{\mathbf{B}}_0\cdot\nabla\left(\mathbf{U}_1\cdot\nabla h\right)-\mathbf{U}_1\cdot\nabla\left(\bar{\mathbf{B}}_0\cdot\nabla h\right), \qquad (3.27)
\end{aligned}$$

where identities * $\mathbf{F}\cdot\nabla\times\mathbf{G}=\nabla\cdot(\mathbf{G}\times\mathbf{F})+\mathbf{G}\cdot\nabla\times\mathbf{F}$, ** $(\mathbf{F}\times\mathbf{G})\times\mathbf{H}=\mathbf{G}(\mathbf{F}\cdot\mathbf{H})-\mathbf{F}(\mathbf{G}\cdot\mathbf{H})$, $\nabla\times\nabla h=0$ and *** $\nabla\cdot\bar{\mathbf{B}}_0=0$, $\nabla\cdot\mathbf{U}_1=0$ have been used to simplify the derivation. Taking $h=r$, $h=\theta$, and $h=z$ in the equation, respectively, and noting that $\bar{\mathbf{B}}_0\cdot\hat{r}=\bar{B}_{0r}=0$ and $\bar{\mathbf{B}}_0\cdot\hat{z}=\bar{B}_{0z}$ are constant, we obtain the three components of $\bar{\mathbf{B}}_1$

$$\bar{B}_{1r} = \frac{1}{\gamma}\bar{\mathbf{B}}_0\cdot\nabla U_{1r} \qquad (3.28)$$

$$\bar{B}_{1\theta} = \frac{r}{\gamma}\left[\bar{\mathbf{B}}_0\cdot\nabla\left(\frac{U_{1\theta}}{r}\right)-\mathbf{U}_1\cdot\nabla\left(\frac{\bar{B}_{0\theta}}{r}\right)\right] \qquad (3.29)$$

$$\bar{B}_{1z} = \frac{1}{\gamma}\bar{\mathbf{B}}_0\cdot\nabla U_{1z}. \qquad (3.30)$$

The magnetic field perturbation is therefore expressed in terms of the equilibrium magnetic field subject to small motion of plasma, as a direct result of the ideal MHD frozen-in flux condition.

3.3.1 General solution of magnetic field perturbation

In the equilibrium state, $\mathbf{J}_0=J_{0z}\hat{z}$ is non-zero only on the plasma surface. It can be proved that the perturbed current $\mathbf{J}_1$ is also confined on the surface (See § 3.7.1). Therefore $\nabla\times\mathbf{B}_1=0$ both inside and outside the plasma. This means that there exists a scalar "potential" χ where $\bar{\mathbf{B}}_1=\nabla\chi$ and

$$\nabla^2\chi=\nabla\cdot\bar{\mathbf{B}}_1=0. \qquad (3.31)$$

Because χ is a perturbation term, it has the form of $\chi \sim e^{\gamma t+im\theta+ikz}$. Solving the equation in cylindrical coordinates and requiring regularity at $r=0$ and $r\to+\infty$ gives

$$\chi=\begin{cases}\sum_m a_m I_m(kr)e^{\gamma t+im\theta+ikz} & r<R \text{ (in plasma)}\\ \sum_m b_m K_m(kr)e^{\gamma t+im\theta+ikz} & r>R \text{ (in vacuum)}\end{cases}, \tag{3.32}$$

where the summations are over all integers m, $I_m(x)$ and $K_m(x)$ are the modified Bessel functions of the first kind and the second kind, respectively [1].

Coefficients a_m and b_m are related by the fact that the perturbed magnetic field cannot penetrate the surface of plasma according to the ideal MHD frozen-in flux condition. This is satisfied by the MHD induction equation (Eq. 3.28-3.30) plus continuity at the plasma interface. The latter condition requires that the velocity component orthogonal to the interface must be continuous across the interface, i.e.,

$$U_{1r}(R-)=U_{1r}(R+). \tag{3.33}$$

Notice that since $\bar{B}_0=\alpha\hat{z}$ inside plasma and $\bar{B}_0=\alpha\hat{z}+(R/r)\hat{\theta}$ outside plasma, Eq. 3.28 can be written explicitly as

$$\bar{B}_{1r}=\begin{cases}\frac{1}{\gamma}ik\alpha U_{1r} & r<R\\ \frac{1}{\gamma}(imR/r^2+ik\alpha)U_{1r} & r>R\end{cases}, \tag{3.34}$$

where we have used $\hat{z}\cdot\nabla=\partial_z=ik$ and $\hat{\theta}\cdot\nabla=(1/r)\partial_\theta=im/r$.

On the other hand, 3.32 gives $\bar{B}_{1r}(R-)=a_m kI'_m$ and $\bar{B}_{1r}(R+)=b_m kK'_m$. Hence

$$a_m kI'_m = \frac{1}{\gamma}ik\alpha U_{1r}(R-) \tag{3.35}$$

$$b_m kK'_m = \frac{1}{\gamma}\left(\frac{im}{R}+ik\alpha\right)U_{1r}(R+). \tag{3.36}$$

Applying Eq. 3.33 to Eqs. 3.35 and 3.36 gives

$$b_m=\frac{m+q}{q}\frac{I'_m}{K'_m}a_m. \tag{3.37}$$

The vacuum field is now expressed in terms of the plasma field.

3.3.2 Inside plasma

Inside the plasma, $\bar{\mathbf{B}}_0 = \alpha\hat{z}$ is uniform so Eqs. 3.28-3.30 reduce to $\mathbf{B}_1 = (1/\gamma)\bar{\mathbf{B}}_0 \cdot \nabla\mathbf{U}_1 = (ik\alpha/\gamma)\mathbf{U}_1$ and

$$\mathbf{U}_1 = \frac{\gamma}{ik\alpha}\bar{\mathbf{B}}_1. \tag{3.38}$$

Equation 3.26 and the z component of Eq. 3.38 give

$$\bar{P}_1(R-) = \left(\alpha + \frac{\gamma^2}{\alpha k^2 v_{A\theta}^2}\right)\bar{B}_{1z}(R-) = ik\alpha\left(1 + \frac{\Gamma}{q^2}\right)a_m I_m, \tag{3.39}$$

where Γ and q are defined in Eq. 3.21.

3.3.3 Outside plasma

Outside the plasma, $\bar{\mathbf{B}}_0(R+) = \alpha\hat{z} + \hat{\theta}$. Hence

$$\begin{aligned}
\bar{P}_1(R+) &= \bar{\mathbf{B}}_0(R+) \cdot \bar{\mathbf{B}}_1(R+) \\
&= \bar{B}_{1\theta}(R+) + \alpha\bar{B}_{1z}(R+) \\
&= \frac{im}{R}b_m K_m + ik\alpha b_m K_m \\
&= \frac{i}{R}\frac{(m+q)^2}{q}\frac{I'_m K_m}{K'_m I_m}a_m I_m,
\end{aligned} \tag{3.40}$$

where Eq. 3.37 has been used.

3.4 Radial motion jump condition at the interface

The interface region where the current flows is part of the plasma and so is governed by the MHD equations, i.e., the momentum equation and the induction equation.

We integrate the radial motion Eq. 3.24 across the interface from $r = R-$ to $R+$ to obtain

$$0 = -\bar{P}_1\big|_{R_-}^{R_+} + \int_{R_-}^{R_+}(\bar{\mathbf{B}}_0 \cdot \nabla\bar{\mathbf{B}}_1 + \bar{\mathbf{B}}_1 \cdot \nabla\bar{\mathbf{B}}_0)_r dr - \frac{\Phi^2}{\gamma R}U_{1r}(R-)\sin\theta. \tag{3.41}$$

For general cylindrical vectors

$$(\mathbf{F} \cdot \nabla\mathbf{G})_r = F_r\frac{\partial G_r}{\partial r} + \frac{F_\theta}{r}\frac{\partial G_r}{\partial\theta} + F_z\frac{\partial G_r}{\partial z} - \frac{F_\theta G_\theta}{r}, \tag{3.42}$$

and therefore

$$(\bar{\mathbf{B}}_0 \cdot \nabla \bar{\mathbf{B}}_1)_r = \bar{B}_{0r}\frac{\partial \bar{B}_{1r}}{\partial r} + \frac{\bar{B}_{0\theta}}{r}\frac{\partial \bar{B}_{1r}}{\partial \theta} + \bar{B}_{0z}\frac{\partial \bar{B}_{1r}}{\partial z} - \frac{\bar{B}_{0\theta}\bar{B}_{1\theta}}{r}, \tag{3.43}$$

$$(\bar{\mathbf{B}}_1 \cdot \nabla \bar{\mathbf{B}}_0)_r = \bar{B}_{1r}\frac{\partial \bar{B}_{0r}}{\partial r} + \frac{\bar{B}_{1\theta}}{r}\frac{\partial \bar{B}_{0r}}{\partial \theta} + \bar{B}_{1z}\frac{\partial \bar{B}_{0r}}{\partial z} - \frac{\bar{B}_{1\theta}\bar{B}_{0\theta}}{r}. \tag{3.44}$$

Because $\bar{B}_{0r} = 0$ and $\bar{B}_{0z} = \alpha$,

$$(\bar{\mathbf{B}}_0 \cdot \nabla \bar{\mathbf{B}}_1 + \bar{\mathbf{B}}_1 \cdot \nabla \bar{\mathbf{B}}_0)_r = \frac{im}{r}\bar{B}_{0\theta}\bar{B}_{1r} + ik\alpha\bar{B}_{1r} - \frac{2\bar{B}_{0\theta}\bar{B}_{1\theta}}{r}. \tag{3.45}$$

The second term of Eq. 3.41 involves an integration across an infinitesimally thin layer. Only terms behaving like a delta-function at $r = R$ contribute to this integration. These terms must contain a partial derivative at $r = R$ in the radial direction. On examination of Eqs. 3.28-3.29 it is seen that only $\bar{B}_{1\theta}$ is a delta-function type term. To see this, rewrite Eq. 3.29 and only keep the term with ∂_r to obtain

$$\bar{B}_{1\theta} = -\frac{r}{\gamma}U_{1r}\frac{\partial}{\partial r}\left(\frac{\bar{B}_{0\theta}}{r}\right) + \text{non-delta}. \tag{3.46}$$

Therefore,

$$\begin{aligned}(\bar{\mathbf{B}}_0 \cdot \nabla \bar{\mathbf{B}}_1 + \bar{\mathbf{B}}_1 \cdot \nabla \bar{\mathbf{B}}_0)_r &= \frac{2}{\gamma}U_{1r}\bar{B}_{0\theta}\frac{\partial}{\partial r}\left(\frac{\bar{B}_{0\theta}}{r}\right) + \text{non-delta} \\ &= \frac{U_{1r}}{\gamma r}\frac{\partial \bar{B}_{0\theta}^2}{\partial r} + \text{non-delta}. \end{aligned} \tag{3.47}$$

Integration across the interface gives

$$\begin{aligned}\int_{R-}^{R+}(\bar{\mathbf{B}}_0 \cdot \nabla \bar{\mathbf{B}}_1 + \bar{\mathbf{B}}_1 \cdot \nabla \bar{\mathbf{B}}_0)_r dr &= \frac{U_{1r}(R+)}{\gamma R}\bar{B}_{0\theta}(R+)^2 = \frac{U_{1r}(R+)}{\gamma R} \\ &= \frac{U_{1r}(R-)}{\gamma R} = \frac{k}{iq}a_m I'_m, \end{aligned} \tag{3.48}$$

where Eqs. 3.33 and 3.35 have been used.

The last term in Eq. 3.41 is given by the lateral gravity. We write $\sin\theta = (e^{i\theta} - e^{-i\theta})/2i$

and expand U_{1r} using Eq. 3.35 to obtain

$$\begin{aligned}\frac{\Phi^2}{\gamma R}U_{1r}(R-)\sin\theta &= \frac{\Phi^2}{i\alpha k R}\frac{e^{i\theta}-e^{-i\theta}}{2i}\sum_m a_m k I'_m e^{im\theta} \\ &= -\frac{\Phi^2 k}{2q}\sum_m a_m I'_m (e^{i(m+1)\theta}-e^{i(m-1)\theta}) \\ &\overset{m^{th}}{=} -\frac{\Phi^2 k}{2q}(a_{m-1}I'_{m-1}-a_{m+1}I'_{m+1}). \end{aligned} \tag{3.49}$$

This equation shows that the lateral gravity breaks the axisymmetry of the cylindrical system and links the m^{th} mode to the $(m\pm1)^{th}$ modes.

Substitution of Eqs. 3.39, 3.40, 3.48 and 3.49 into Eq. 3.41 gives

$$0 = ik\alpha\left(1+\frac{\Gamma}{q^2}\right)a_m I_m - \frac{i}{R}\frac{(m+q)^2}{q}\frac{I'_m K_m}{K'_m I_m}a_m I_m + \frac{k}{iq}a_m I'_m + \frac{\Phi^2 k}{2q}(a_{m-1}I'_{m-1}-a_{m+1}I'_{m+1}). \tag{3.50}$$

We multiply by iRq to obtain

$$(m+q)^2\frac{I'_m K_m}{K'_m I_m}a_m I_m + x a_m I'_m + \frac{i}{2}x\Phi^2(a_{m-1}I'_{m-1}-a_{m+1}I'_{m+1}) = (\Gamma+q^2)a_m I_m. \tag{3.51}$$

Equation 3.51 is a very strong condition because it holds for all integers m. However, this equation is not to be considered as a coefficient recurrence relation because one should not expect an arbitrary perturbation to precisely satisfy the condition for all azimuthal modes. Instead, Eq. 3.51 should be considered as an eigenvalue problem. We define new coefficients

$$w_m \equiv a_m I_m \qquad \text{for all integer } m, \tag{3.52}$$

an infinitely long column vector

$$\mathbf{w} \equiv [\cdots, w_{-2}, w_{-1}, w_0, w_1, w_2, \cdots]^T, \tag{3.53}$$

an infinitely large zero-diagonal-entry tridiagonal matrix

$$\mathbf{G} = (G_{mn})_{m,n\in\mathbf{Z}}, \quad G_{m,m}=0, \quad G_{m,m-1} = x\frac{I'_{m-1}}{I_{m-1}}, \quad G_{m,m+1} = -x\frac{I'_{m+1}}{I_{m+1}}, \tag{3.54}$$

two infinitely large diagonal matrices

$$\mathbf{M} = (M_{mn})_{m,n\in\mathbf{Z}} \qquad M_{m,m} = (m+q)^2 \frac{I'_m}{I_m}\frac{K_m}{K'_m} \tag{3.55}$$

$$\mathbf{N} = (N_{mn})_{m,n\in\mathbf{Z}} \qquad N_{m,m} = x\frac{I'_m}{I_m}, \tag{3.56}$$

and an infinitely large tridiagonal matrix

$$\mathbf{Q} \equiv \mathbf{M} + \mathbf{N} + \frac{i}{2}\Phi^2\mathbf{G}. \tag{3.57}$$

Equation 3.51 becomes

$$\begin{aligned}\left[\mathbf{M} + \mathbf{N} + \frac{i}{2}\Phi^2\mathbf{G}\right]\mathbf{w} &= (\Gamma + q^2)\mathbf{w}, \\ \mathbf{Q}\mathbf{w} &= (\Gamma + q^2)\mathbf{w}.\end{aligned} \tag{3.58}$$

The procedure to find the growth rate γ of a perturbation is equivalent to finding the eigenvalues of the matrix $\mathbf{Q}$. The infinite matrix $\mathbf{Q}$ has an infinite and countable number of eigenvalues $\{\sigma^m\}_{m\in\mathbf{Z}}$ and eigenvectors $\{\mathbf{w}^m\}_{m\in\mathbf{Z}}$. Each eigenvector gives the coefficients $\{a_m\}$ of an eigen-perturbation. The growth rate of this eigen-perturbation is given by the corresponding eigenvalue. All of the eigenvectors form a complete basis in the coefficient space. Any arbitrary perturbation can always be decomposed into a linear combination of those eigen-perturbations, and the fastest growing mode is given by the available eigen-perturbation with the largest positive Γ. A similar treatment but for the situations of diapir formation can be found in Refs. [71, 72]. Note that because of the lateral gravity and the cylindrical geometry, an eigen-perturbation contains all azimuthal modes because the matrix $\mathbf{Q}$ is non-diagonal.

Here we briefly review the process of deriving Eq. 3.51. First, the linearization of the continuity equation expresses the density perturbation ρ_1 as a function of the velocity perturbation U_{1r}. The linearized induction equation gives the magnetic field perturbation $\bar{\mathbf{B}}_1$ in terms of the velocity perturbation $\mathbf{U}_1$, as a consequence of frozen-in flux condition. Equivalently, velocity perturbation $\mathbf{U}_1$ is also expressed as function of $\bar{\mathbf{B}}_1$. In the system, current is always confined within the interface, so the magnetic field perturbation $\bar{\mathbf{B}}_1$ is a vacuum-type field both inside and outside plasma. As a general vacuum field, $\bar{\mathbf{B}}_1$ is written

as two different Fourier series inside and outside the plasma. The coefficients of the two Fourier series are related by the continuity of radial velocity across the interface, given $\bar{\mathbf{B}}_1$ as a function of $\mathbf{U}_1$. The linearization of momentum equation gives three equations of motion involving the three velocity components, the effective pressure $\bar{P}_1$, the magnetic field perturbation $\bar{\mathbf{B}}_1$ and the gravity term due to density perturbation. However, only two of the motion equations are linearly independent because the perturbation is incompressible. The z motion is used to express $\bar{P}_1$ inside the plasma in terms of $\bar{B}_{1z}$. $\bar{P}_1$ outside plasma is naturally a function of $\bar{\mathbf{B}}_1$ due to the lack of plasma pressure. The r motion is integrated across the interface to link $\bar{P}_1$, the magnetic field and gravity term inside and outside plasma. Because all terms have already been written as functions of $\bar{\mathbf{B}}_1$ or $\mathbf{U}_1$, and $\mathbf{U}_1$ is also expressed in terms of $\bar{\mathbf{B}}_1$ by the induction equation, the integrated r motion becomes a self-consistent equation for $\bar{\mathbf{B}}_1$. Fourier expansion of the equation determines the relation of all Fourier coefficients, i.e., Eq. 3.51.

3.4.1 Preliminary analysis on stability

We multiply the pre-matrix equation Eq. 3.51 by $v_{A\theta}^2/R^2$ and divide by $a_m I_m$ to get

$$\frac{v_{A\theta}^2}{R^2}(m+q)^2\frac{I'_m K_m}{I_m K'_m}+\frac{v_{A\theta}^2}{R}k\frac{I'_m}{I_m}+\frac{i}{2}gk\frac{a_{m-1}I'_{m-1}-a_{m+1}I'_{m+1}}{a_m I_m}=\gamma^2+\alpha^2k^2v_{A\theta}^2. \tag{3.59}$$

This equation has a one-to-one correspondence with Eq. 3.58 and provides more physical intuition than the matrix equation.

Both $I_m(x)$ and $K_m(x)$ are positive for $x>0$. $I_m(x)$ is a monotonically increasing function and $K_m(x)$ is a monotonically decreasing function. Therefore, $I'_m>0$, $K'_m<0$ and hence $M_{mm}<0$, $N_{mm}>0$, $G_{m,m-1}>0$ and $G_{m,m+1}<0$.

All diagonal entries of the diagonal matrix $\mathbf{M}$ are negative. Larger $|M_{mm}|$ results in smaller Γ and so more stable system. The dimensioned version of $\mathbf{M}$ is given by the first term of Eq. 3.59, hence

$$\mathbf{M}_{mm}\propto\frac{v_{A\theta}^2}{R^2}(m+q)^2\propto\frac{b_\theta^2}{R^2}\left(m+\frac{kRb_z}{b_\theta}\right)^2=\left(\frac{m}{R}b_\theta+kb_z\right)^2=(\mathbf{k}\cdot\mathbf{B})^2, \tag{3.60}$$

where $\mathbf{k}=k\hat{z}+(m/R)\hat{\theta}$ and $\mathbf{B}=b_z\hat{z}+b_\theta\hat{\theta}$ are the instability wavevector and magnetic field on the plasma surface, respectively. Therefore $\mathbf{M}$ represents the stabilizing effect due

to the tension along the magnetic field.

$\mathbf{N}$ is a positive-definite matrix and hence destabilizes the system. The second term of Eq. 3.59 shows that $\mathbf{N}$ is proportional to $v_{A\theta}^2/R$, which has a dimension of an acceleration. $v_{A\theta}^2/R$ can be understood as the centrifugal acceleration a test particle experiences when traveling around the $r = R$ interface at the Alfvén speed $v_{A\theta}$. Therefore the destabilizing effect is a result of 'bad' curvature of the azimuthal magnetic field on the circular plasma-vacuum interface. The destabilizing effect leads to a traditional current-driven instability such as kink instability. Similar mechanism exists in toroidal magnetic confinement devices and space plasmas as ballooning mode and resistive ballooning mode [25, 41, 120].

The gravity term $i\mathbf{G}$ does not have a simple stabilizing or destabilizing effect. Because $\mathbf{G}$ is similar to a skew-symmetric matrix and $i\mathbf{G}$ is similar to a Hermitian matrix, all the eigenvalues of $i\mathbf{G}$ are pure real. Moreover, the eigenvalues of $i\mathbf{G}$ come in positive-negative pairs, i.e., if $\lambda > 0$ is an eigenvalue then $-\lambda$ is also an eigenvalue. A mathematical proof is given in § 3.7.3. Positive eigenvalues correspond to destabilizing effect, and negative ones stabilize the system. This can be understood intuitively by considering a perturbation occurring around the cylindrical plasma: the perturbation on the 'top' of the surface (i.e., $y > 0$) undergoes a stable oscillation, and a perturbation on the 'bottom' of the surface ($y < 0$) undergoes a Rayleigh-Taylor instability. Another important feature of $i\mathbf{G}$ is that it is the only non-diagonal matrix in Eq. 3.58. Specifically, the first sub-diagonal and super-diagonal entries of $i\mathbf{G}$ are nonzero. Therefore any azimuthal mode m is coupled with neighboring modes $m - 1$ and $m + 1$ due to $i\mathbf{G}$, and therefore all azimuthal modes are coupled together.

The second term of the RHS of Eq. 3.59, $\alpha^2 k^2 v_{A\theta}^2$, is proportional to $k^2 b_z^2$ and hence corresponds to tension along the axial magnetic field. This term helps to reduce γ^2 for fixed Γ and therefore stabilizes the system.

As a short summary, B_z and B_θ help stabilize the system because of magnetic tension. However the "bad" curvature of B_θ destabilizes the system. The gravity term has a dual effect which stabilizes some perturbations and destabilizes others. The gravity term also breaks the azimuthal symmetry and couples all azimuthal modes together.

3.4.2 Comments on the matrix equation

Equation 3.58 involves infinitely large matrices that cannot be solved directly. However in practice, approximate solutions can be obtained by truncating the matrices. We define a series of finite matrices

$$\mathbf{Q}_p \equiv (Q_{mn})_{-p\le m,n\le p}, \qquad p = 1, 2, 3, .. \tag{3.61}$$

For each integer p, $\mathbf{Q}_p$ is a $(2p+1)$ by $(2p+1)$ square tridiagonal matrix. We solve the eigenvalue problems $\mathbf{Q}_p\mathbf{w}_p^q = \sigma_p^q\mathbf{w}_p^q$ in a complex space, where $q \in \{1, 2, \ldots, 2p+1\}$ is the index of the eigenvalues and eigenvectors of $\mathbf{Q}_p$. We sort the eigenvalues in descending order by their real parts, i.e., $\text{real}(\sigma_p^1) \ge \cdots \ge \text{real}(\sigma_p^{2p+1})$. We solve the above systems with successively increasing p and look for limits

$$\lim_{p\to+\infty} \sigma_p^1 \to \sigma^1, \qquad \lim_{p\to+\infty} \mathbf{w}_p^1 \to \mathbf{w}^1. \tag{3.62}$$

For a well-defined problem, we expect the above limits converge to $\{\sigma^q\}$ and $\{\mathbf{w}^q\}$, which are the eigenvalues and eigenvectors of the infinitely large linear system Eq. 3.58. The largest eigenvalue σ^1 gives the growth rate of the fastest growing mode using $\Gamma = \sigma^1 - q^2$, while $\mathbf{w}^1$ gives the coefficients of each azimuthal mode of the fastest growing mode. If there exists some mechanism inhibiting high-order azimuthal modes, p can be chosen to be the highest permitted azimuthal mode number.

Along the azimuthal direction, B_θ is expected to suppress high order azimuthal modes. The 1D MHD Rayleigh-Taylor theory shows that the undular mode with wavenumber $k > g\mu_0\rho_0/B^2$ is prohibited. We apply this result to the azimuthal direction of the cylindrical system and we find that modes with $m > g\mu_0\rho_0 R/B_\theta^2 = \Phi^2$ are expected to be prohibited. On the other hand, for a system with axial perturbation wavenumber k, fluctuation with typical length scale $2\pi/k$ is allowed. Hence azimuthal mode $m \sim kR$ should be permitted.

Fig. 3.4 shows numerically that the limit in Eq. 3.62 always converges for magnetized plasma (finite Φ) but diverges for unmagnetized plasma ($\Phi^2 \to \infty$). The figure also shows that empirically $\sigma_p^1 \approx \sigma^1$ is generally acceptable for $p > \max(\Phi^2, kR)$.

The three matrices $\mathbf{M}$, $\mathbf{N}$ and $\mathbf{G}$ contain the derivatives of modified Bessel functions. The recurrent relations $2I'_m(x) = I_{m-1}(x) + I_{m+1}(x)$ and $-2K'_m(x) = K_{m-1}(x) + K_{m+1}(x)$

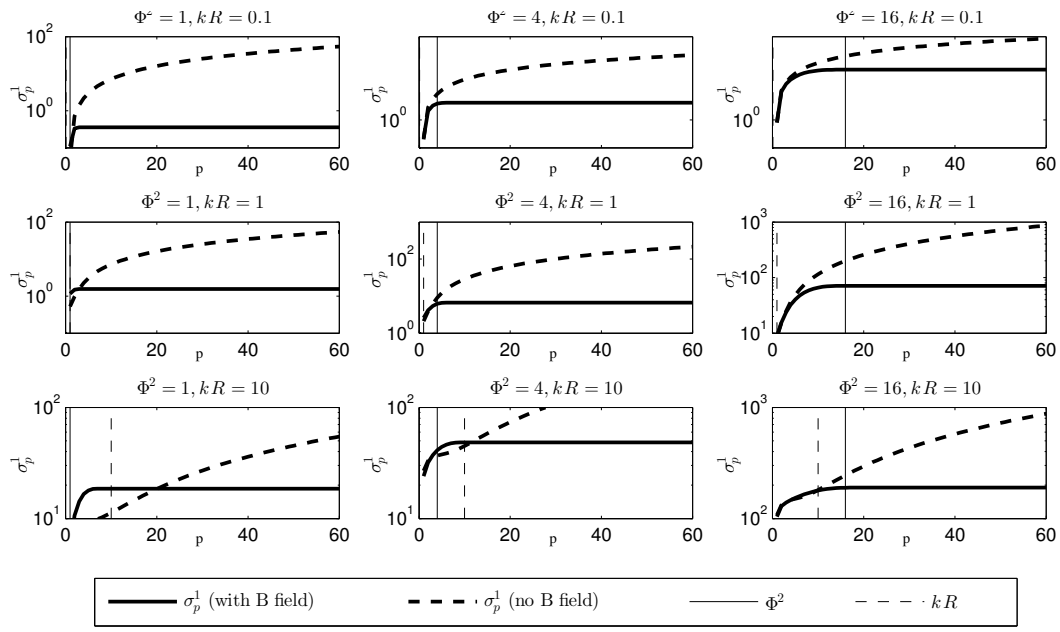

Figure 3.4: Eigenvalue σ_p^1 of truncated matrix $\mathbf{Q}_p$ (defined in Eq. 3.61) as a function of largest allowed mode number p for magnetized plasma cylinder(finite Φ, solid curves) and unmagnetized plasma ($\mathbf{N}$ and $\mathbf{M}$ are omitted, dashed curves) at different axial wavelength. The solid vertical lines label the position of $p = \Phi^2$ and the dotted vertical lines label $p = kR$. Pitch angle $\alpha = 1$ is used.

can be used to avoid calculating the complicated derivatives when computing the matrices.

3.4.3 Short/Long wavelength approximation

Truncating the matrix $\mathbf{Q}$ at $\pm p$ is an artificial way to inhibit the perturbations with azimuthal wavelength smaller than $\lambda_\theta = 2\pi R/p$ or wavenumber larger than $k_\theta = p/R$ along the azimuthal direction. Along its orthogonal direction on the plasma-vacuum interface, i.e., the z direction, the scale of perturbations is characterized by kR and wavelength $\lambda_z = 2\pi/k$.

Mathematically, the modified Bessel functions $I_m(x)$ and $K_m(x)$ have different asymptotic behaviors under different limits. § 3.7.2 shows that the large x approximation of modified Bessel functions is valid if $x \gg m^2/2$. This is approximately equivalent to $kR \gg m^2$ or $\sqrt{R\lambda_z} \ll \lambda_\theta$. The small x approximation is valid if $x \ll \sqrt{m+1}$. This is equivalent to $k^2R^2 \ll m$ or $\lambda_z \gg \sqrt{R\lambda_\theta}$.

We therefore formalize the terms "short wavelength approximation" as $kR \gg m^2$ or $\sqrt{R\lambda_z} \ll \lambda_\theta$, and "long wavelength approximation" as $k^2R^2 \ll m$ or $\lambda_z \gg \sqrt{R\lambda_\theta}$. The two approximations correspond to the large and small argument approximations of modified

Bessel functions, respectively (§ 3.7.2). Physically speaking, the short (long) wavelength approximation is equivalent to saying that the axial (azimuthal) perturbation dominates.

3.5 Solutions

We now solve Eq. 3.58. First we consider several special cases where either gravity or the magnetic field is weak. In these cases some analytical solutions can be obtained using short or long wavelength approximations. Then we numerically solve the truncated matrix equation for general cases.

3.5.1 Special cases I: weak gravity or strong toroidal magnetic field

The limit of weak gravity or strong toroidal magnetic field is defined by $\Phi^2 = gR/v_{A\theta}^2 \ll 1$, or equivalently $g \ll v_{A\theta}^2/R$. In this limit, Eq. 3.58 becomes

$$(\mathbf{M}+\mathbf{N})\mathbf{w} = (\Gamma + q^2)\mathbf{w}. \tag{3.63}$$

Since both $\mathbf{M}$ and $\mathbf{N}$ are diagonal matrices, each $e^{im\theta}$ mode is now an eigen mode of the system because there is no gravity breaking the axisymmetry. The growth rate of the m^{th} mode simply is

$$\Gamma = M_{mm} + N_{mm} - q^2 \tag{3.64}$$

$$\gamma^2 = \frac{v_{A\theta}^2}{R^2}\left((m+q)^2\frac{I'_m K_m}{I_m K'_m} + x\frac{I'_m}{I_m} - q^2\right). \tag{3.65}$$

The marginal stability is given by

$$(m+q)^2\frac{I'_m K_m}{I_m K'_m} + x\frac{I'_m}{I_m} - q^2 < 0. \tag{3.66}$$

At this point, we have returned to the textbook current-driven MHD instability. Equation 10.171 in Ref. [5] shows for such system marginal stability is given by

$$kR\frac{b_z^2}{b_\theta^2}\frac{I_m}{I'_m} - \frac{(m+q)^2}{kR}\left[\frac{I_m\hat{K}'_m - \hat{I}'_m K_m}{I'_m\hat{K}'_m - \hat{I}'_m K'_m}\right] > 1, \tag{3.67}$$

where I_m or I'_m and K_m or K'_m are evaluated at kR and $\hat{I}_m$ or $\hat{I}'_m$ and $\hat{K}_m$ or $\hat{K}'_m$ are

evaluated at the finite-distanced wall. In the limit of infinitely far wall, there are $\hat{I}'_m \to \infty$ and $\hat{K}'_m \to 0$. Hence the marginal stability inequality reduces to

$$x\alpha^2 \frac{I_m}{I'_m} - \frac{(m+q)^2}{x}\frac{K_m}{K'_m} > 1 \tag{3.68}$$

After multiplied $x(I'_m/I_m)$ on both sides the inequality becomes identical to Eq. 3.66. Therefore we have verified that the theory reduces to classic current-driven MHD instability in the weak gravity limit.

In the long wavelength approximation $k^2R^2 \ll m$, the modified Bessel functions give $I'_m/I_m \approx |m|/x$ and $K'_m/K_m \approx -|m|/x$ (§ 3.7.2). Equation 3.65 becomes

$$\gamma^2 = \frac{v_{A\theta}^2}{R^2}(-(m+q)^2 + |m| - q^2), \tag{3.69}$$

which is positive for $m = -1$ when $q < 1$. This is the classic $m = -1$ kink instability.

3.5.2 Special cases II: strong gravity or weak toroidal magnetic field

In the limit of $\Phi^2 \gg 1$ or equivalently $g \gg v_{A\theta}^2/R$, Eq. 3.58 becomes

$$\frac{i}{2}\Phi^2 \mathbf{G}\mathbf{w} = (\Gamma + q^2)\mathbf{w}. \tag{3.70}$$

Consider the short wavelength approximation $kR \gg p^2$ with the matrix $\mathbf{G}$ intentionally truncated at $\pm p$. In this limit $I'_m/I_m \approx 1$ for $|m| \le p$ (§ 3.7.2). Hence all sub-diagonal entries of $\mathbf{G}_p$ are x and all the super-diagonal entries are $-x$. $\mathbf{G}_p$ is then also a Toeplitz matrix. It can be shown mathematically that eigenvalues of $i\mathbf{G}_p$ are $2x\cos(k\pi/(2p+2))$, where $k = 1, 2, 3, \cdots 2p+1$ (e.g., see Ref. [85]). The largest positive eigenvalue of $i\mathbf{G}$ is $2x$. Hence

$$\Gamma = x\Phi^2 - q^2 = x\Phi^2 - \alpha^2 x^2, \tag{3.71}$$

$$\gamma^2 = gk - \frac{b_z^2 k^2}{\mu_0 \rho_0} = gk - v_{Az}^2 k^2, \tag{3.72}$$

where $v_{Az} = b_z/\sqrt{\mu_0\rho_p} = \alpha v_{A\theta}$. This is the 1D MRT theory for the undular mode along the axial direction. In the zero field limit, $b_z = 0$ and $q = 0$, the short wavelength approximation gives $\Gamma = x\Phi^2$ or $\gamma^2 = gk$, which is the 1D hydrodynamic Rayleigh-Taylor instability.

Note that the short wavelength approximation emphasizes axial perturbation and ignores azimuthal perturbation. This explains why under short wavelength approximation the theory is identical to 1D MRT.

The maximum of Γ or γ^2 occurs for x that satisfies $d\Gamma/dx = 0$. From Eq. 3.72 this maximum is at

$$\begin{aligned} x &= \frac{\Phi^2}{2\alpha^2} & \max\Gamma &= \tfrac{\Phi^4}{4\alpha^2} \\ k &= \frac{g}{2v_{Az}^2} & \max\gamma^2 &= \tfrac{g^2}{4v_{Az}^2}. \end{aligned} \tag{3.73}$$

It is notable that Eq. 3.70 is an ill-posed problem unless $\mathbf{G}$ is truncated. Otherwise there are always sufficiently large integers p so that the short wavelength approximation fails. The extreme case is when the long wavelength approximation is valid, i.e., $kR \ll \sqrt{p}$, $G_{p+1,p} = xI_p'/I_p \approx |p|$ (see § 3.7.2). Therefore the non-zero elements of $\mathbf{G}$ diverge as $p \to +\infty$, and so do the eigenvalues. This is also seen in Fig. 3.4.

3.5.3 Lateral Rayleigh-Taylor-Current-Driven coupled instability in cylindrical MHD collimated plasma

We have shown that the solution reduces to the conventional current-driven MHD instability and the 1D hydrodynamic/magnetic Rayleigh-Taylor instability when either gravity or (toroidal) magnetic field are neglected. When both gravity and magnetic field are present, the two instabilities are expected to couple together and give a Rayleigh-Taylor-Current-Driven (RT-CD) coupled instability.

In the Caltech plasma jet experiment, a typical argon jet has $n_e = n_i = 10^{22}$ m^{-3}, $I_z = 60$ kA, $R = 3.5$ cm, $B_z = 0.2$ T, and so $B_\theta = 0.34$ T. Hence $\alpha = 0.583$. A typical effective gravity has $g = 4 \times 10^{10}$ m/s^2 (See Ref. [80]) hence $\sqrt{gR} = 34.6$ km/s. The system parameters are

$$v_{Az} = 6.9 \text{ km/s} \qquad v_{A\theta} = 11.8 \text{ km/s} \qquad \Phi^2 = 10.0 \qquad \alpha = 0.583. \tag{3.74}$$

For a type I hydrogen jet with the same g and R, there are

$$v_{Az} = 43.6 \text{ km/s} \qquad v_{A\theta} = 74.8 \text{ km/s} \qquad \Phi^2 = 0.25 \qquad \alpha = 0.583. \tag{3.75}$$

Based on these parameters, it is seen that due to the different ion weight the gravity effect is strong in the argon jet while the current-driven effect is strong in the type I hydrogen jet.

Despite the complexity of the theory, Eq. 3.58 has only three free parameters. Given x, Φ^2 and α (or kR, $gR/v_{A\theta}^2$ and b_z/b_θ), the three matrices $\mathbf{M}$, $\mathbf{N}$, and $\mathbf{G}$ are uniquely determined. Therefore for a given equilibrium, the growth rate of the RT-CD coupled instability is determined solely by the axial perturbation scale kR.

Using the parameters given in Eq. 3.74 and 3.75, we vary kR to calculate the corresponding growth rate Γ and γ. Figure 3.5 shows the instability growth rate for argon and hydrogen plasmas as a function of kR (thick solid curve). Also plotted are the instability growth rate in the weak gravity limit, strong gravity limit and zero field limit ($\mathbf{N}$ and $\mathbf{M}$ omitted, $\alpha = 0$, thick dotted-dashed curve). For further comparison, 1D MHD Rayleigh-Taylor growth rate $\gamma^2 = gk - v_{Az}^2 k^2$ (light dashed curve) and 1D hydrodynamic Rayleigh-Taylor growth rate $\gamma^2 = gk$ (light solid curve) are also plotted.

In both argon and hydrogen jet configurations, very small wavelength perturbations are always suppressed and the peak growth rate occurs at a finite axial wavelength. This is fundamentally different from the 1D hydrodynamic RT instability and the interchange mode of 2D MRT instability.

3.5.3.1 Argon plasma jet

In the argon plasma jet configuration, $\Phi^2 = 10.0$ and the instability shows strong coupling between RT instability and CD instability, especially for long wavelength perturbation. The growth rate of this RT-CD coupled instability is faster than either 1D MHD RT or CD instability, as a result of the destabilizing effect from the cylindrical geometry and effective gravity. On the other hand, the RT-CD instability grows slower than the strong gravity (zero toroidal field) limit or zero field limit, showing the stabilizing effect due to magnetic field B_z and B_θ.

The fastest growth rate of RT-CD instability for argon plasma jet is $\Gamma = 115.6$ at $kR = 18.0$, corresponding to a dimensioned growth rate $\gamma = (v_{A\theta}/R)\sqrt{\Gamma} = 3.6 \times 10^6$ s^{-1} at $\lambda_z = 1.22$ cm. This is very close to the experimental measurement that $\gamma \sim 10^6$ s^{-1} and $\lambda_z \approx 1 \sim 2$ cm.

The 1D MHD RT theory predicts the maximal growth rate is $\Gamma = \Phi^2/(4\alpha^2) = 73.4$

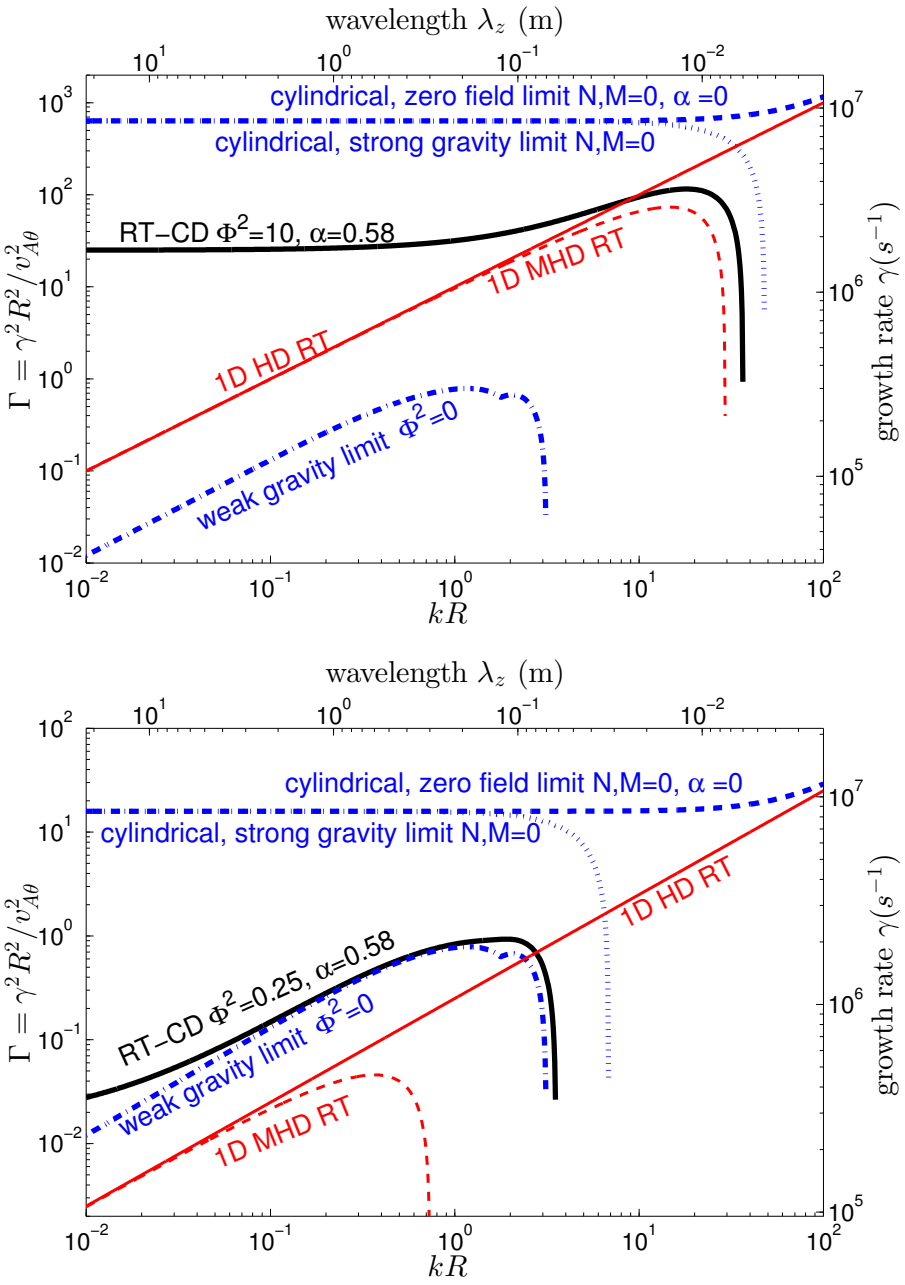

Figure 3.5: Instability growth rate as a function of axial perturbation wave number/wavelength for Caltech argon plasma jet with $\Phi^2 = 10$ (top panel) and hydrogen plasma jet with $\Phi^2 = 0.25$ (bottom panel). $\alpha = 0.58$ for both cases. The growth rates are computed using: **(1)** RT-CD coupled theory for cylindrical plasma (Eq. 3.58, thick solid curve); **(2)** weak gravity limit ($\Phi^2 = 0$, Eq. 3.65, thick dotted-dashed curve); **(3)** strong gravity limit (**N** and **M** omitted, Eq. 3.70, thick dotted curve); **(4)** zero field limit (Eq. 3.70 with $q = 0$, thick dashed curve); **(5)** 1D MHD RT theory in axial direction (Eq. 3.72, light dashed curve); **(6)** 1D hydrodynamic RT theory $\gamma^2 = gk$ (light solid curve). The bottom abscissa is the dimensionless variable kR and the top abscissa gives the dimensioned wavelength $\lambda_z = 2\pi/k$ with $R = 3.5$ cm. The left ordinate is the dimensionless growth rate $\Gamma = \gamma^2 R^2/v_{A\theta}^2$ and the right one is the dimensioned rate γ. Matrix $\mathbf{Q}$ is truncated at $p = 70$ in the calculation.

at $kR = \Phi^2/(2\alpha^2) = 14.7$ or $\gamma = 2.9 \times 10^6$ s^{-1} at $\lambda_z = 1.5$ cm. It is seen that the 1D MHD RT theory does provide a reasonable approximation to RT-CD theory, despite the big discrepancy between the two at small kR (long wavelength).

The weak gravity limit describes current-driven MHD instabilities such as $m = -1$ kink instabilities. As shown in Fig. 3.5, the CD instability growth rate is $10 - 100$ times slower than the RT-CD coupled instability. The fastest growth rate of the weak gravity limit is $\gamma = 3 \times 10^5$ s^{-1} at $kR = 4.0$ or $\lambda_z = 18.7$ cm, in excellent agreement with the experiment measurement.

3.5.3.2 Hydrogen plasma jet

In hydrogen plasma jet configuration with $g = 4 \times 10^{10}$ m/s^2, $\Phi^2 < 1$ due to the low ion mass of hydrogen. Figure 3.5 confirms that the RT-CD instability in hydrogen jet is essentially reduced to weak gravity limit. This explains why distinct Rayleigh-Taylor-like ripple is not observed in most hydrogen jet experiments with $g < 10^{11}$ m/s^2. The fastest growth rate is $\Gamma = 0.931$ at $kR = 1.92$ or $\gamma = 2.1 \times 10^6$ s^{-1} at $\lambda_z = 11.5$ cm. Unlike the argon plasma jet case, the 1D MHD RT theory does not apply to the hydrogen jet system at all.

3.5.4 RT-CD coupled instability as a quasi-paramagnetic instability

The classic current-driven instability is paramagnetic in the long wavelength approximation. The surface wavevector $\mathbf{k} = k\hat{z} + m\hat{\theta}/R$ is perpendicular to magnetic field $\mathbf{B} = b_z\hat{z} + b_\theta\hat{\theta}$ on plasma surface, i.e., $\mathbf{k} \cdot \mathbf{B} = kb_z + mb_\theta/R = 0$. This requires a negative m and thus a right handed perturbation. The surface current after perturbation has an additional right handed part, which enhances the equilibrium axial field [49]. The 2D MRT instability allow wavevectors in random direction. However the interchange mode having wavevector perpendicular to the magnetic field grows fastest because it is not suppressed by the field line tension. Hence for interchange mode there is $\mathbf{k} \cdot \mathbf{B} = 0$. The interchange mode does not modulate the equilibrium magnetic field. The hydrodynamic 1D Rayleigh-Taylor instability does not involve a magnetic field. In an MHD collimated cylindrical plasma configuration, it is of interest to study the paramagnetic property of RT-CD coupled instability on the

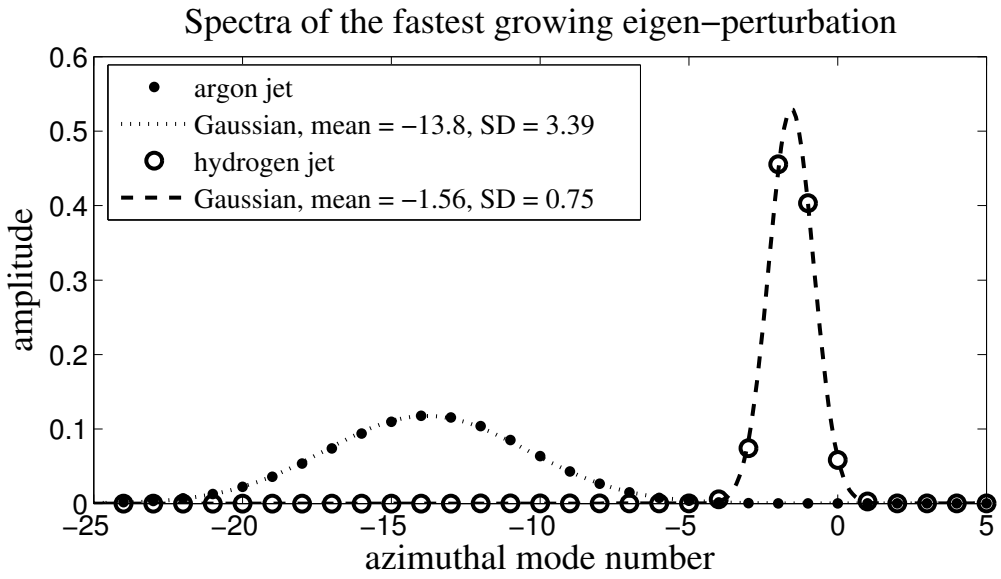

Figure 3.6: Spectra of the fastest growing eigen-perturbation for argon jet configuration (solid dots) and hydrogen jet configuration (open circles). The spectrum is defined by Eq. 3.76. Two Gaussian functions with means and standard deviations calculated using the spectra are also plotted for comparison. Matrix $\mathbf{Q}$ is truncated at $p = 70$.

curved interface. To see this, we define the spectrum of the fastest eigen-perturbation as

$$f(m) = \frac{|w_m^1|}{\sum_{j\in\mathbb{Z}} |w_j^1|} \qquad m = 0, \pm 1, \pm 2, \cdots, \tag{3.76}$$

where $\mathbf{w}^1$ is the eigenvector of $\mathbf{Q}$ corresponding to σ^1, the eigenvalue with the largest real part. Because $\chi(R) = \sum_m a_m I_m(kR) e^{\gamma t + im\theta + ikz} = \sum_m w_m e^{\gamma t + im\theta + ikz}$, $f(m) \sim |w_m^1|$ is the amplitude of the m^{th} azimuthal mode on the plasma surface. We also define the average azimuthal mode number

$$\bar{m} = \sum_m m f(m) \tag{3.77}$$

and spectral width (standard deviation)

$$SD = \sqrt{\sum_{m\in\mathbb{Z}} (m - \bar{m})^2 f(m)} \tag{3.78}$$

to quantify how concentrated the spectrum is.

Figure 3.6 shows the spectra of the fastest growing RT-CD eigen-perturbation in argon and type I hydrogen plasma jet configuration (Eq. 3.74, 3.75). The spectrum of argon jet reveals a Gaussian profile centered at $\bar{m} = -13.8$ with width $SD = 3.39$, and hydrogen

jet spectrum is centered at $\bar{m} = -1.56$ with narrow width $SD = 0.75$. This is consistent with previous discussion that gravity breaks the axisymmetry and links different m modes together. In a relatively strong gravity case like the argon jet, $\Phi^2 = 10$, gravity is able to create a wide spectrum from $m \sim -23$ to $m \sim -5$. In a weak gravity case like the hydrogen jet, $\Phi^2 \ll 1$, the current-driven instability dominates and gives a sharp spectrum centered around $m = -1$ (kink) and $m = -2$. These spectra also demonstrate the validity of truncating the matrix $\mathbf{Q}$ at $p = 70$ because the spectrum is essentially zero below $m = -25$ or above $m = 1$.

The average mode number $\bar{m}$ is negative for both argon and hydrogen jet so the instability is paramagnetic. The inner product of averaged surface wavevector $\mathbf{k} = k\hat{z} + \bar{m}\hat{\theta}/R$ and magnetic field $\mathbf{B} = b_z\hat{z} + b_\theta\hat{\theta}$ is

$$\mathbf{k}\cdot\mathbf{B} = k_z b_z + \frac{\bar{m}}{R} b_\theta = b_\theta(q+\bar{m})/R \tag{3.79}$$

$$\frac{\mathbf{k}\cdot\mathbf{B}}{|\mathbf{k}||\mathbf{B}|} = \frac{q+\bar{m}}{(x^2+\bar{m}^2)^{1/2}(1+\alpha^2)^{1/2}}, \tag{3.80}$$

where $x = kR$, $\alpha = b_z/b_\theta$ and $q = \alpha x$. Calculation in previous section gives $q = 10.5$ for argon jet and $q = 1.12$ for hydrogen jet. For both jets the safety factor q does not completely cancel $\bar{m}$ so $\mathbf{k}\cdot\mathbf{B} \neq 0$, different from the conventional CD instability or the interchange mode of 2D MRT instability. Further calculation shows that $\mathbf{k}\cdot\mathbf{B}/|\mathbf{k}||\mathbf{B}| = -0.126$ for argon jet and -0.154 for hydrogen jet, corresponding to an angle of 97.2° and 98.9° between $\mathbf{k}$ and $\mathbf{B}$ on the plasma surface. We call this property quasi-paramagnetic because it is slightly different from the paramagnetic behavior of the CD instability. There is a small but finite angle between the magnetic field and the direction of constant instability phase on the plasma surface. This imperfect alignment is a result of the curved interface because on a planar interface the fastest growing modes (interchange modes) always have $\mathbf{k}\cdot\mathbf{B} = 0$.

3.5.5 Visualization of the instability

Figure 3.7 shows in both 2D and 3D the perturbed surface of argon and hydrogen jets given by $U_{1r} \sim \partial\chi/\partial r \sim \sum_m w_m(I'_m/I_m)e^{ikz+im\theta}$. The instability disturbs the argon jet surface primarily around $\theta = 3\pi/2$ because gravity is in the $-\hat{y}$ direction. The instability on the hydrogen jet surface occurs at all θ because it is a current-driven dominant instability. The gravity nevertheless enhances the perturbation around $\theta = 3\pi/2$ as well. The surface

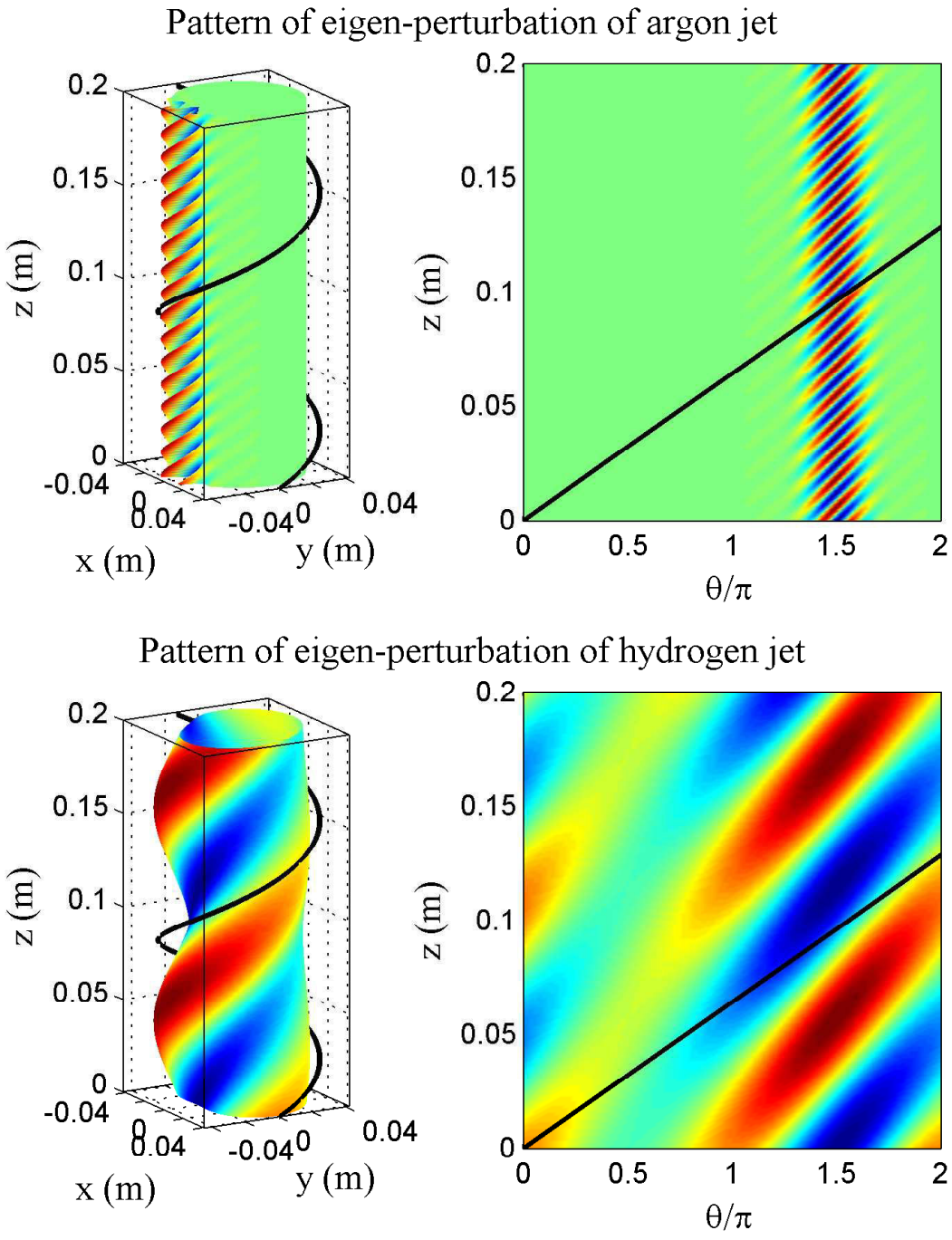

Figure 3.7: Pattern of fastest growing eigen-perturbation of argon jet (top) and hydrogen jet (bottom) from $z = 0$ to $z = 0.2$ m. The 2D images are $U_{1r}(\theta, z)$ evaluated at plasma surface. The 3D surfaces show the plasma boundary under the fastest growing eigen-perturbation. The black curves illustrate the magnetic field line at the plasma boundary.

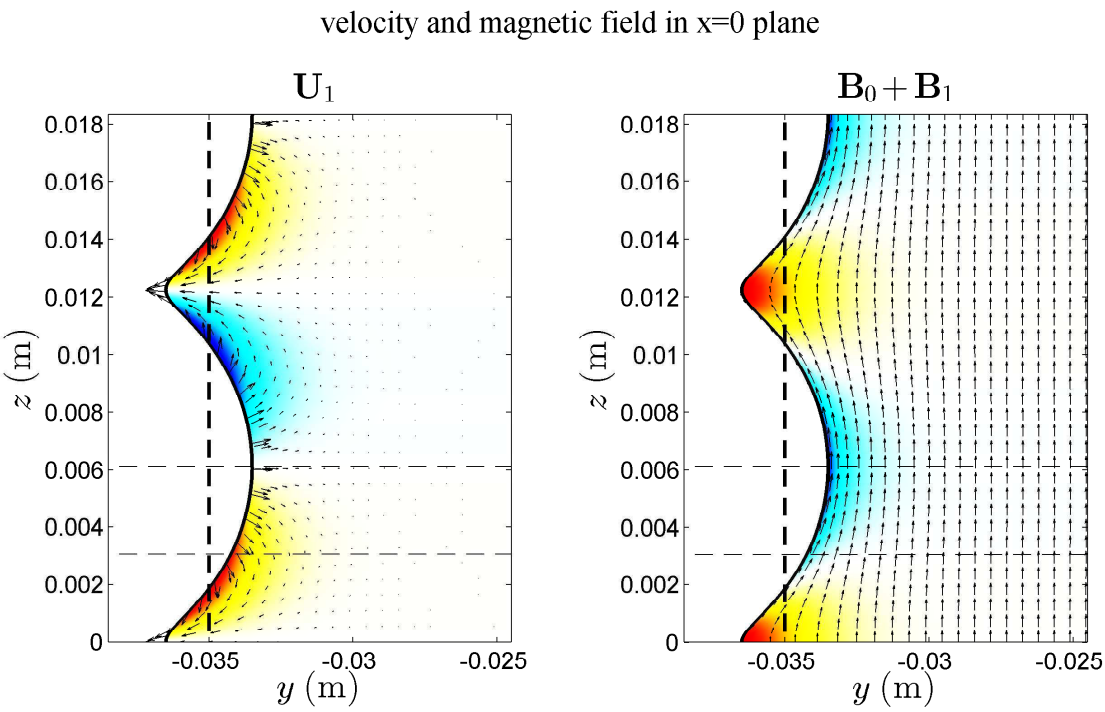

Figure 3.8: Cross-sectional view of velocity and magnetic field of the fastest growing eigen-perturbation of argon jet solution on $y-z$ plane at $x=0$: The background color illustrates azimuthal component ($U_{1\theta}$ or $B_{1\theta}$) and arrows on top represent radial and axial components of $\mathbf{U}_1$ or $\mathbf{B}_0+\mathbf{B}_1$. The thick dash line/curves in each plot are unperturbed surface and the thick solid curves are perturbed surface. Blue/cyan color represents component into the paper and red/yellow color represents component out of the paper. Arrow length is proportional to field strength.

magnetic field (thick black curves) is approximately parallel to the phase of the instability. The argon jet instability shows strong coupling between Rayleigh-Taylor and current-driven effect. The hydrogen jet case is very similar to a pure $m=-2$ CD instability.

Figure 3.8 and 3.9 give the cross-sectional view of velocity and magnetic field under the fastest growing eigen-perturbation inside argon plasma. The figures demonstrate an intrinsic 3D geometry of RT-CD coupled instability. Unstable deformation occurs along both axial and azimuthal direction. The right panel of Fig. 3.8 clearly shows that the poloidal (radial and axial) components of magnetic field remain parallel to plasma surface under perturbation, because of the frozen-in flux requirement. Consequently, the xy-cross-sectional view (Fig. 3.9) shows amplification in B_z when there is an inward velocity ($U_{1r}<0$) and vice versa. Finite azimuthal magnetic field is created inside the plasma because of deformation of the surface current.

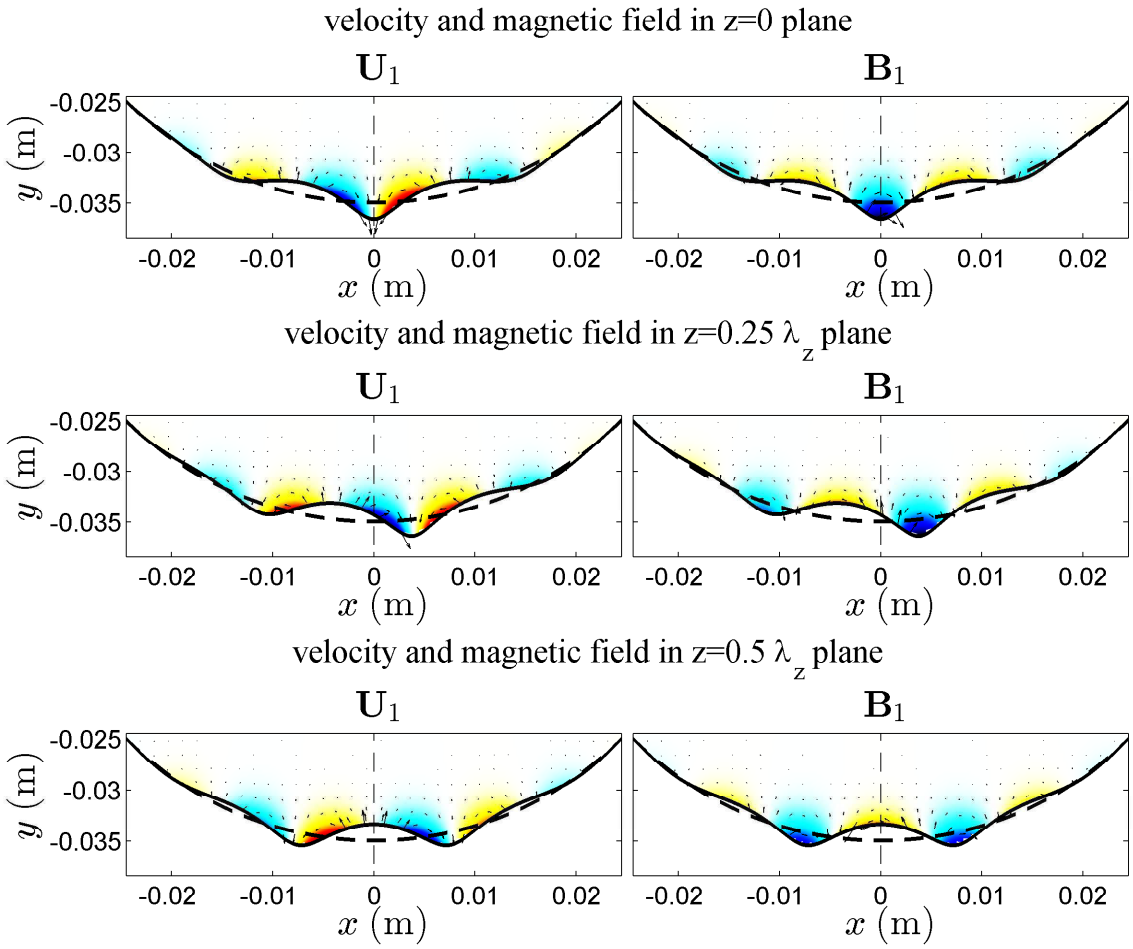

Figure 3.9: Cross-sectional view of velocity and magnetic field of the fastest growing eigen-perturbation of argon jet solution on $x-y$ plane at $z=0$, $z=\lambda_z/4$, and $z=\lambda_z/2$, where $\lambda_z = 1.14$ cm is the axial wavelength of the instability. The locations of these three slices are also marked in Fig. 3.8. The color images are U_{1z} or B_{1z} and arrows represent radial and azimuthal components of $\mathbf{U}_1$ or $\mathbf{B}_1$. The thick dash line/curves in each plot are unperturbed surface and the thick solid curves are perturbed surface. Blue/cyan color represents component into the paper and red/yellow color represents component out of the paper. Arrow length is proportional to field strength.

3.5.6 Comprehensive view of RT-CD coupled instability

As this point we have shown two special cases with $\Phi^2 = 0.25$ and $\Phi^2 = 10$ and $\alpha = 0.583$. For a plasma filled flux rope, Φ and α are fully determined by the equilibrium. The instability growth rate is further determined by the axial perturbation $x = kR$. In general case, we define $\Gamma(\Phi^2, \alpha, x)$ as the fastest growing solution of Eq. 3.58 for given Φ^2, α and x, i.e., $\Gamma(\Phi^2, \alpha, x) = \sigma^1 - \alpha^2 x^2$ where σ^1 is the largest eigenvalue of matrix $\mathbf{Q}$.

Now consider a system with Φ^2 and α subject to a random perturbation that contains all possible $x = kR$ components. Those components that give $\Gamma(\Phi^2, \alpha, x) > 0$ are unstable and grow exponentially fast. The component x that gives the largest positive $\Gamma(\Phi^2, \alpha, x)$, denoted as x^*, grows faster than all other components, and is therefore the dominant component. Hence

$$x^*(\Phi, \alpha) = x \text{ that maximizes } \Gamma(\Phi^2, \alpha, x). \tag{3.81}$$

We further define

$$\Gamma^*(\Phi^2, \alpha) = \max_{x \geq 0} \Gamma(\Phi^2, \alpha, x) = \Gamma(\Phi^2, \alpha, x^*) \tag{3.82}$$

$$\bar{m}^*(\Phi^2, \alpha) = \bar{m} \text{ of } x^* \text{ eigen-perturbation} \tag{3.83}$$

$$SD^*(\Phi^2, \alpha) = SD \text{ of } x^* \text{ eigen-perturbation.} \tag{3.84}$$

We now solve for Γ^*, x^*, $\bar{m}^*$ and SD^* over a wide range of Φ and α and show the results in Fig. 3.10. The argon jet configuration ($\Phi^2 = 10$, $\alpha = 0.585$) and type I hydrogen jet configuration ($\Phi^2 = 0.25$, $\alpha = 0.583$) are marked in the plots. Also marked is the type II hydrogen jet configuration (as "H(2)") with $g = 3 \times 10^{11}$ m/s^2. Unlike the type I hydrogen jet, this type II hydrogen jet has $\Phi^2 = 1.89$ and is observed to develop $\lambda_z = 3 \sim 5$ cm RT-type ripple in the experiment.

There are two domains in the parameter space that have already been solved by existing theories.

Classic current-driven instability dominated domain The lower half portion of each plots in Fig. 3.10 has $\Phi^2 \ll 1$ and is the current-driven instability dominated domain. The impact from gravity is much weaker than that from toroidal field, hence the instability is weakly dependent on Φ^2 in this domain. The type I hydrogen jet experiment is located

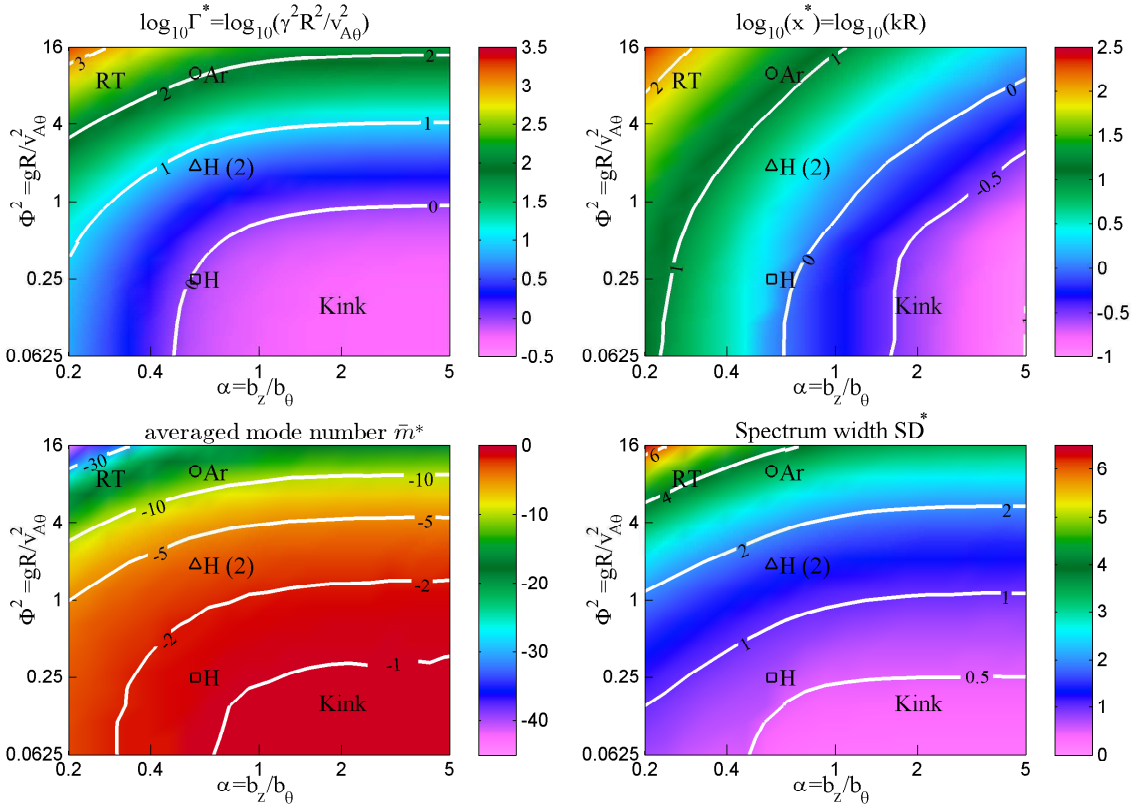

Figure 3.10: Solution of $\log_{10}\Gamma^*$ (upper left), $\log_{10} x^*$ (upper right), $\bar{m}^*$ (lower left), and SD^* (lower right) in the $0.0625 \le \Phi^2 \le 16$ and $0.2 \le \alpha \le 5$ domain. For each (Φ^2, α), we scan x from from 10^{-2} to 10^3 and find x^* that maximizes $\Gamma(\Phi^2, \alpha, x)$. The xy axes are both in log scale. Matrix $\mathbf{Q}$ is truncated at $p = 70$ in the calculation. Since $p = 70$ is about 4 times the maximal standard deviation away from the maximal mean mode number (max $SD^* = 6.5$ and max $|\bar{m}^*| = 45$), the truncation is valid. The $\circ$ and $\square$ symbols mark the location of argon and hydrogen plasma jet configuration with $g = 4 \times 10^{10}$ m/s^2 in the (Φ^2, α) parameter space. The $\triangle$ symbols marks the hydrogen configuration with $g = 3 \times 10^{11}$ m/s^2.

in this domain ($\square$ symbol). For cases with relatively strong axial field, e.g., $\alpha > 0.6$, the instability occurs with a long axial wavelength (small x^*), and the instability is the standard $m = -1$ kink instability with very sharp spectra. For weak axial field cases (small α), large k and high m modes can develop, but the spectrum remains sharply distributed around the peak mode, because weak gravity cannot efficiently couple different azimuthal modes.

Classic Rayleigh-Taylor instability dominated domain The upper left corner of each subplot (large Φ^2 and small α, or weak B_z and B_θ) of Fig. 3.10 is the Rayleigh-Taylor instability dominated domain. The instability occurs with large x^* (small axial wavelength),

as well as large and broad azimuthal spectrum (small scaled azimuthal perturbations). These results are consistent with the classic Rayleigh-Taylor instability theory where small scale perturbations have larger growth rates. Equation 3.73 shows that under strong gravity limit and short wavelength approximation, the maximum of Γ is obtained at $x^* = \Phi^2/(2\alpha^2)$ as $\Gamma^* = \Phi^4/(4\alpha^2)$. Hence $\log\Gamma^* = 2\log\Phi^2 - 2\log\alpha - \log 4$ and $\log x^* = \log\Phi^2 - 2\log\alpha - \log 2$. These matches with the behaviors of Γ^* and x^* for large Φ and small α. More specifically, in the upper left corner of the subplots, contours of Γ^* have slope $d(\log\Phi^2)/d(\log\alpha) = 1$ and contours of x^* have slope $d(\log\Phi^2)/d(\log\alpha) = 2$, consistent with the 1D MHD RT theory.

Figure 3.10 shows continuous transition from $m = -1$ long wavelength kink instability (lower right portion) to 1D hydrodynamic/magnetic Rayleigh-Taylor instability (upper left corner). The argon jet configuration ($\Phi^2 = 10$) and the type II hydrogen jet ($\Phi^2 = 1.89$) are located in the transition region. The former case has been discussed in § 3.5.3. For the latter case, the theory gives $x^* = 4.3$ or $\lambda_z = 5$ cm, consistent with the experiment. In general, when a lateral gravity field is applied to an MHD confined flux rope, the Rayleigh-Taylor and current-driven instability are intrinsically coupled and a unified theory of RT-CD instability on cylindrical geometry should be considered.

3.6 Summary and discussion

By using linear stability analysis, we have established an analytic theory of a hybrid lateral Rayleigh-Taylor-Current-Driven coupled instability of an incompressible MHD collimated cylindrical plasma (flux rope) in the present of a lateral gravitational field. This RT-CD coupled instability is affected by magnetic field tension, curvature, and gravity. The coexistence of lateral gravity and cylindrical geometry leads to a complex coupling of all azimuthal modes of the cylinder, a fundamentally different situation compared to results from a 1D or 2D planar interface. The coupled instability reduces to the classic current-driven instability in the weak gravity limit and to the conventional hydrodynamic or magnetic RT instability in the strong gravity limit. In the general case, the RT and current-driven instabilities are coupled and result in a new hybrid instability.

A useful parameter $\Phi^2 = \mu_0\rho_0 gR/b_\theta^2$ is defined to quantify the relative importance of gravity versus toroidal magnetic field. This parameter is interesting because it includes magnetic field, curvature, plasma density, and gravity, and is completely determined by

the equilibrium state. Φ^2 can be written as $\Phi^2 = (\rho_0 g R)/(b_\theta^2/\mu_0)$, which is the ratio of gravitational energy density to toroidal magnetic energy; or it can be written as $\Phi^2 = g/(v_{A\theta}^2/R)$, the ratio between real gravity and effective gravity due to the curvature of the toroidal magnetic field. g is responsible for the RT instability and $v_{A\theta}^2/R$ is responsible for the current-driven instability. Φ^2 describes whether a flux rope is more susceptible to the RT instability (if $\Phi^2 \gg 1$) or the current-driven instability (if $\Phi^2 \ll 1$), or coupled instability ($\Phi^2 \sim 1$).

The RT-CD instability is quasi-paramagnetic since $\bar{m}$ is negative. The instability wavevector $\mathbf{k}$ is nearly perpendicular to the surface magnetic field $\mathbf{B}$ so the instability phase is roughly constant along the magnetic field. Note that on a 2D planar interface $\mathbf{k} \cdot \mathbf{B} = 0$ corresponds to the interchange mode and the instability is essentially identical to the hydrodynamic situation. In cylindrical geometry, the magnetic field prefers a perpendicular $\mathbf{k}$ at the bottom of the flux rope, but as the perturbation extends to other parts of the cylinder, gravity is no longer perpendicular to the interface or can become stabilizing. The combination of magnetic field, cylindrical geometry and gravity can suppress high k modes even when $\mathbf{k}$ is nearly perpendicular to $\mathbf{B}$.

The RT-CD coupled instability theory successfully explains the experimental observation (Fig. 3.2). For the argon jet, the theory predicts $\lambda_z = 1.22$ cm with growth rate $\gamma = 3.6 \times 10^6$ s^{-1}; for the type I hydrogen jet the theory shows that the RT effect is not important and the instability is dominantly current-driven; for the type II of hydrogen jet with much larger lateral acceleration, the theory shows RT-CD coupled instability with $\lambda_z \sim 5$ cm. Conventional MRT instability theory that only considers axial magnetic field and axial perturbation is able to explain the argon jet, but fails to consider interchange mode or explain hydrogen jets.

Figure 3.10 shows comprehensive results of RT-CD coupled instability in a large parameter space, and illustrates a smooth transition from CD to RT. This figure can be used as function tables for $\gamma^*(\Phi^2, \alpha)$, $x^*(\Phi^2, \alpha)$, $\bar{m}^*(\Phi^2, \alpha)$, and $SD^*(\Phi^2, \alpha)$, because it is difficult to obtain relatively simple explicit functions to approximate the results from the large matrix equations.

One major simplification in the theory is to assume that current is confined to the plasma surface. With this assumption, the perturbed magnetic field is a vacuum field both inside and outside the plasma. This greatly simplifies the mathematical analysis. In a

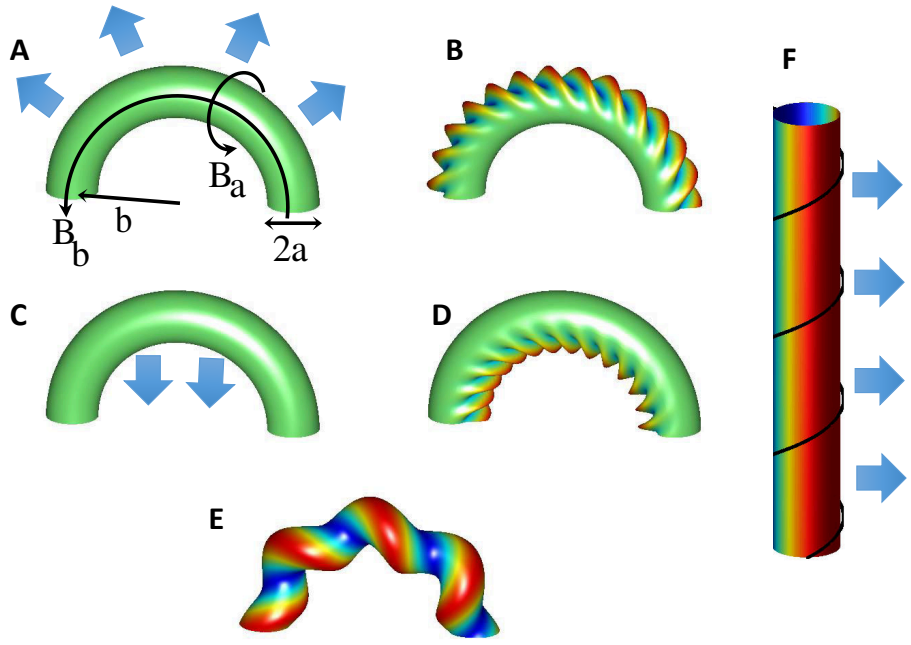

Figure 3.11: Configuration of a curved flux rope with minor radius a, major radius b, axial magnetic field B_b and azimuthal field B_a. Lateral gravity can be caused by magnetic field curvature (panel A), real gravity or lateral acceleration (panel C). Configuration A and C are analogous to a straight flux rope (panel F) with lateral gravity. Flux rope A can develop RT instability similar to panel B and flux rope C can have RT instability similar to panel D. If the gravity effect is weak, the flux rope can undergo kink instability like shown in panel E.

more realistic configuration where axial current density J_z is finite inside the plasma, the perturbed magnetic field is no longer curl-free, and Eq. 3.32 is no longer valid for $r < R$. Finite J_z for $r < R$ gives a shear of the magnetic field along the radial direction because $B_{0\theta}(r) = \mu I(r)/(2\pi r)$ depends on r as does the pitch angle $\alpha = B_{0z}/B_{0\theta}$. This shear provides extra stabilizing effect because a paramagnetic perturbation on plasma surface will not be aligned with magnetic field inside the plasma [5].

This lateral RT-CD coupled instability could be applicable for many situations where there is a flux rope presented in a lateral (effective) gravity. Consider a stationary curved flux rope with minor radius a and major radius b. Assume the axial magnetic field is B_b and azimuthal magnetic field around the plasma axis is B_a (Fig. 3.11A). The curvature of the plasma axis is $1/b$. We define Alfvén speeds $v_{Aa} = B_a/\sqrt{\mu_0\rho}$ and $v_{Ab} = B_b/\sqrt{\mu_0\rho}$. An effective lateral gravity $g_b = v_{Ab}^2/b$ is applied perpendicular to the flux rope axis, pointing in the direction from the curvature center to the flux rope, as indicated by the big arrows

in Fig. 3.11A. This configuration is analogous to a straight flux rope subject to a lateral gravity as shown in Fig. 3.11F. Therefore the outer surface of the curved flux rope can develop curvature-driven RT instability (Fig. 3.11B). The characteristic parameter Φ^2 in this configuration is $\Phi^2 = g_b/(v_{Aa}^2/a) = aB_b^2/(bB_a^2)$ or $\Phi^2 = B_b/(TB_a) = b/(T^2a)$, where $T = bB_a/(aB_b)$ is number of twists of the surface helical magnetic field around the axis. If $B_b \sim TB_a$ then a RT-CD coupled instability is expected. If $B_b \ll TB_a$, the flux rope is subject to kink instability (Fig. 3.11E). In the process of flux emergence in the solar corona, a flux rope with a curved axis exists. A typical configuration has $b \sim 2a$ and $T \sim 2$ (e.g., see Ref. [36]). Hence $\Phi^2 \sim 0.5$ and $\alpha \sim 1$. Figure 3.10 shows that for this configuration the fastest growing mode has $ka = 0.7$ and averaged mode number $\bar{m}^* = -1.2$ with spectrum width $SD^* = 0.75$. Hence the RT effect is weak and the instability is essentially an $m = -1$ kink instability. In a configuration with larger b and fewer twists, our theory predicts that the RT-CD hybrid instability can develop on the outer edge of the flux ropes. For example, curvature-driven Rayleigh-Taylor instability on the top of solar prominence is studied in theory and is proposed as cause of prominence destabilization and fast magnetic reconnection [91, 101]. In Ref. [101] an effective gravity due to the curvature of high-beta prominence $g = V_{\|}^2/R$ is considered, where $V_{\|}$ is the thermal velocity along the magnetic field. The resulted RT instability is also called ballooning instability [91, 101], in analogous to the ballooning mode in magnetic controlled fusion devices. However, in Ref. [91, 101] concepts of RT and MRT instability of planar interface were used for qualitative or quasi-quantitative analysis. We suggest that the cylindrical geometry is crucial.

Quiescent prominence, believed to be supported by magnetic curvature, can also develop Rayleigh-Taylor instability due to solar gravity [10, 47]. This configuration, illustrated in Fig. 3.11C, is susceptible to RT-CD coupled instability at the bottom of the flux rope as shown in Fig. 3.11D. So far only planar interface has been considered. Our theory shows that in cylindrical geometry this type of planar approximation might be inappropriate.

Another potential application is coronal mass ejection (CME) where flux rope is erupting due to some MHD instability like torus instability [58]. As the flux rope is expanding exponentially fast, a lateral effective gravity due to the acceleration is applied on the flux rope pointing opposite to the direction of expansion (Fig. 3.11C). This configuration is very similar to the Caltech plasma jet experiment. A high resolution observation from SDO shows a bright helical brightening with $3-4$ turns occurs at 7:24:12 UT below the apex

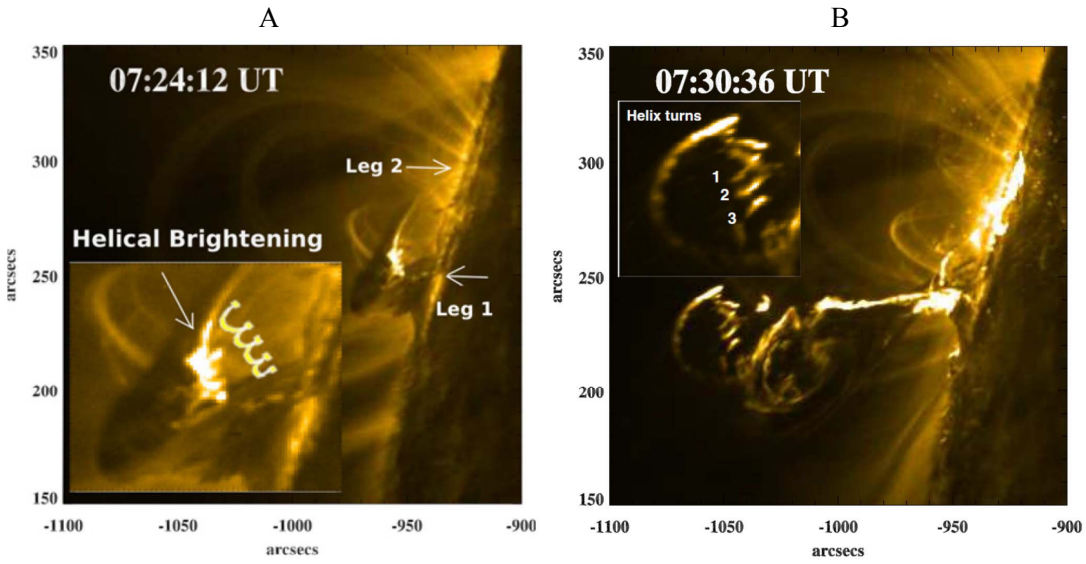

Figure 3.12: SDO/AIA 171 EUV images of a coronal mass ejection occurring in active region NOAA 11163 on 2011 February 24. These two images are from Fig. 1 of Kumar et al. (2012) [65].

of the prominence of the 2011 Feb 24 CME in active region NOAA 11163 (Fig. 3.12A). In Ref. [65] this helical brightening is attributed to helical kink instability and is believed to trigger formation of two blobs that later on erupt to give the CME. At 7:30:36 UT some ripple-like fine structures and several helix turns can be seen at inner edge of blob "B" (Fig. 3.12B). The facts that the helical brightening occurs on the inner edge of the apex of the prominence and helix turns exists at inner edge of blob "B" suggest that there could be some RT effect (Fig. 3.11D) coupled in the phenomena. Precise estimation of Φ^2 is not applicable due to lack of detailed measurement, especially in magnetic field. But a rough estimation gives

$$\Phi^2 = 2.2 \times \left(\frac{g}{500\text{km/s/min}}\right) \cdot \left(\frac{n_e}{10^{11}\text{cm}^{-3}}\right) \cdot \left(\frac{R}{5\text{Mm}}\right) \cdot \left(\frac{20\text{G}}{B_\theta}\right)^2 . \tag{3.85}$$

For nominal quantities given in the equation, $\Phi^2 \sim 2$. Therefore it is likely that the lateral Rayleigh-Taylor-Current-Driven instability exists. Figure 3.10 shows that for $\Phi^2 = 2$ and $\alpha = 0.4$, the averaged mode number of the RT-CD instability is $\bar{m}^* \approx -4.5$ with $kR = 10$ and the growth rate is $\gamma^* \approx 13$. This corresponds to an axial perturbation scale $\lambda_z = 2\pi R/(kR) = 0.64R = 3.2$ Mm (or 4.4 arcsec) and growth rate $\gamma = 0.1$ s^{-1} for $n_e = 10^{11}$ cm^{-3}, $R = 5$ Mm and $B_\theta = 20$ gauss. The growth rate is consistent with the

life time of the helix turns observed in "blob" B, which is on the order of 20 sec. Higher resolution observation is nevertheless necessary to identify whether the phenomena is indeed RT-CD coupled instability, or just purely kink. This is because RT-CD coupled instability is also paramagnetic and could be confused with current-driven instability. However, if high resolution observation is indeed able to distinguish the two instabilities, it can be used to estimate magnetic field configuration of the system using the RT-CD theory.

Numerical simulation of buoyant magnetic flux tube in solar convection zone has found mushroom-shaped RT-type disturbance at bottom of the flux tube [26, 27], and this RT-type disturbance is significantly stabilized by adding more toroidal magnetic field. This is consistent with the RT-CD theory because larger toroidal magnetic field gives smaller Φ^2 and hence the RT effect is weaker. As the flux tube emerges from the convection zone to the solar corona, a filamentary structure can form at the top of the emerging flux tube as a result of MRT instability [52, 53] under solar gravity. The filamentary structure is found to be parallel to the surface magnetic field, consistent with the interchange mode of MRT instability. We suggest that the geometry of the cylindrical emerging flux may also be important and could modulate the behavior of the RT instability. However, we admit that the RT-CD theory presented in this chapter should not be directly used in situations like buoyant and emerging flux tube, because in these cases the flux tube is surrounded by dense plasma that can be denser than the flux tube. Nevertheless the theory suggests that in cylindrical geometry the RT could be fundamentally different from 2D planar case.

This work is supported by the U.S. Department of Energy Office of Science, Office of Fusion Energy Sciences under Award Numbers DE-FG02-04ER54755 and DE-SC0010471, by the National Science Foundation under Award Number 1059519, and by the Air Force Office of Scientific Research under Award Number FA9550-11-1-0184.

3.7 Supplementary materials

In this section we provide some supportive materials.

3.7.1 Confined perturbed current

We have assumed that in equilibrium the current $\mathbf{J}_0$ is confined to the surface of the flux rope. However, it is not obvious that the perturbed current $\mathbf{J}_1$ is still confined to the surface.

Here we prove that $\mathbf{J}_1$ is zero in side the plasma.

Consider the momentum equation Eq. 3.18 inside plasma, where $\rho_1 = 0$, $\mathbf{B}_0 = b_z\hat{z}$ so $\mathbf{B}_0 \cdot \nabla = b_z\partial_z = ikb_z$. Hence

$$\gamma\rho_p\mathbf{U}_1 = -\nabla\left(P_1 + \frac{\mathbf{B}_0 \cdot \mathbf{B}_1}{\mu_0}\right) + \frac{ikb_z}{\mu_0}\mathbf{B}_1. \tag{3.86}$$

The dimensioned version of Eq. 3.38 gives

$$\mathbf{U}_1 = \frac{\gamma}{ik\alpha b_\theta}\mathbf{B}_1 = \frac{\gamma}{ikb_z}\mathbf{B}_1. \tag{3.87}$$

Use this equation to eliminate $\mathbf{U}_1$ in Eq. 3.86 and get

$$\frac{\gamma^2\rho_p}{ikb_z}\mathbf{B}_1 = -\nabla\left(P_1 + \frac{\mathbf{B}_0 \cdot \mathbf{B}_1}{\mu_0}\right) + \frac{ikb_z}{\mu_0}\mathbf{B}_1. \tag{3.88}$$

Take the curl of this equation and the first term on the right hand side vanishes. There is

$$\left(\frac{\gamma^2\rho_p}{ikb_z} - \frac{ikb_z}{\mu_0}\right)\nabla \times \mathbf{B}_1 = 0. \tag{3.89}$$

In general, $\gamma^2\rho_0/ikb_z \neq ikb_z/\mu_0$. Therefore $\mu_0\mathbf{J}_1 = \nabla \times \mathbf{B}_1 = 0$ inside plasma. Hence $\mathbf{J}_1$ is also confined in the interface.

3.7.2 Asymptotic behaviors of modified Bessel functions

Asymptotic behaviors of modified Bessel functions are very useful for semi-quantitative analysis in different limits. Here we relist some results from Ref. [1].

In large argument approximation, $x \gg m^2/2$ and

$$\begin{aligned} I_m(x) &= \frac{e^x}{\sqrt{2\pi x}}\left(1 - \frac{4m^2-1}{8x} + O(x^{-2})\right) \\ K_m(x) &= \sqrt{\frac{\pi}{2x}}e^{-x}\left(1 + \frac{4m^2-1}{8x} + O(x^{-2})\right) \end{aligned}$$

for $|\arg x| < \pi/2$. Therefore $I_m(x)$ and $K_m(x)$ are weakly dependent in the limit of $x \gg m^2/2$ and hence

$$\frac{I_m'}{I_m} \approx 1 - \frac{1}{2x} \approx 1 \qquad \frac{K_m'}{K_m} \approx -1 - \frac{1}{2x} \approx -1.$$

In small x approximation, $0 < x \ll \sqrt{m+1}$,

$$\begin{aligned} I_m(x) &\approx \frac{1}{|m|!}\left(\frac{x}{2}\right)^{|m|} \\ K_m(x) &\approx \frac{(|m|-1)!}{2}\left(\frac{2}{x}\right)^{|m|} \quad m \neq 0, \end{aligned}$$

so that

$$\frac{I'_m}{I_m} \approx \frac{|m|}{x} \quad \text{and} \quad \frac{K'_m}{K_m} \approx -\frac{|m|}{x} \quad m \neq 0.$$

3.7.3 Eigenvalues of matrix G

In this section we show that the eigenvalues of $i\mathbf{G}$ are purely real and are in positive-negative pairs.

In the following derivation we will always use a finite symmetrically truncated matrix $\mathbf{G}_p$ (see Eq. 3.61) instead of the original infinitely large matrix $\mathbf{G}$ defined in Eq. 3.54.

Matrix $\mathbf{G}$ is a tridiagonal matrix with zero diagonal, negative super-diagonaland positive sub-diagonal entries. A finite truncated $\mathbf{G}_p$ has the form of

$$G_{m,m+1} = \omega_m < 0, \quad G_{m,m} = 0, \quad G_{m+1,m} = \beta_m > 0.$$

Define a real diagonal matrix $\mathbf{D}$ with

$$D_{1,1} = 1, \quad D_{m,m} = \sqrt{\frac{\beta_{m-1}}{-\omega_{m-1}} \cdots \frac{\beta_1}{-\omega_1}}$$

and real matrix $\mathbf{H}$

$$\mathbf{H} = \mathbf{D}^{-1}\mathbf{G}_p\mathbf{D}.$$

$\mathbf{H}$ is also a tridiagonal matrix with zero diagonal elements and the off-diagonal elements are

$$\begin{aligned} H_{m,m+1} &= D^{-1}_{m,m} G_{m,m+1} D_{m+1,m+1} = -\sqrt{\omega_m \beta_m} \\ H_{m+1,m} &= D^{-1}_{m+1,m+1} G_{m+1,m} D_{m,m} = \sqrt{\omega_m \beta_m}. \end{aligned}$$

Therefore $\mathbf{H}^T = -\mathbf{H}$, where ^{T} is the transpose operation. Hence $\mathbf{H}$ is a real skew-symmetric matrix. Furthermore, $(i\mathbf{H})^\dagger = -i\mathbf{H}^T = i\mathbf{H}$, where † is complex conjugate

transpose operation. Therefore $i\mathbf{H}$ is a Hermitian matrix. Since matrix $i\mathbf{G}_p$ is similar to a Hermitian matrix, all eigenvalues of $i\mathbf{G}_p$ are pure real.

A matrix is similar to its transpose, so $\mathbf{H}$ and $\mathbf{H}^T = -\mathbf{H}$ must have same eigenvalues. This immediately leads to the results that the eigenvalues of $\mathbf{H}$ always come in pairs $\pm\lambda$, where λ are imaginary. Therefore the eigenvalues of $i\mathbf{G}_p$ always come in real positive and negative pairs. Since $i\mathbf{G}_p$ is a $(2p+1)$ by $(2p+1)$ matrix, by symmetry, 0 must also be an eigenvalue of $i\mathbf{G}_p$. Therefore $i\mathbf{G}$ has p positive eigenvalues and p negative eigenvalues (in pairs) and one zero eigenvalue. This is also consistent with the fact that the summation of all eigenvalues of a matrix, which is zero for $i\mathbf{G}$, equals to the trace of the matrix, which is also zero because $i\mathbf{G}$ has zero diagonal entries.

Chapter 4

Circularly polarized Magnetic Field of Obliquely Propagating Whistler Wave during Fast Magnetic Reconnection

The whistler wave is a cold electromagnetic plasma wave ubiquitous in collisionless magnetic reconnection [29, 32, 54], Earth's magnetosphere [24, 108, 116, 117], and laboratory antenna excitation experiments [108, 109]. Whistler waves can be excited in a magnetized plasma when the frequency is much higher than the ion cyclotron frequency but much lower than the electron cyclotron frequency, i.e., $\omega_{ci} \ll \omega \ll |\omega_{ce}|$ [5, 6, 54]. The conventional derivation of whistler waves shows that both the electric component and the magnetic component of the wave are right-hand circularly polarized when the wavevector is parallel to the background magnetic field. Tsurutani et al. [117] discovered that the magnetic component of a magnetospheric whistler wave is circularly polarized even when the wavevector is oblique to the background magnetic field. Theoretical analyses [6, 119] confirm that the whistler wave always has a circularly polarized magnetic component regardless of the wave propagation direction, but the wave electric component is circularly polarized only when the wavevector is parallel to the background magnetic field.

Lab experiments [54, 80], electron magnetohydrodynamic (EMHD) simulations and particle-in-cell (PIC) simulations [28, 29, 32], and space observations [24, 117] suggest that the whistler wave is an integral component of fast magnetic reconnection. However it is still unclear what role the whistler wave plays in the reconnection processes. Theoretical modeling shows that the equations that govern the fast reconnection process may involve

whistler waves [7].

In the Caltech plasma jet experiment, a current-carrying collimated jet is created from the merging of eight plasma-filled flux ropes. When the current-carrying jet undergoes a kink instability, a lateral Rayleigh-Taylor instability occurs on the jet surface. A linear theory of this Rayleigh-Taylor instability has been presented in Chapter 3. The Rayleigh-Taylor instability quickly evolves to a nonlinear phase, and the plasma jet is eroded by the instability to have a width smaller than the ion skin depth. At the ion skin depth scale, MHD is no longer valid because ion and electron motion are decoupled. A fast magnetic reconnection induced by the Rayleigh-Taylor instability then occurs and eventually breaks the plasma jet structure [80]. A capacitively coupled probe placed near the jet measured fast electric field fluctuations with frequencies in the whistler regime [79, 80].

In this chapter, we present the measurements and analyses of the magnetic components of the whistler waves associated with the fast magnetic reconnection in the Caltech plasma jet experiment. A 3D high speed magnetic probe with excellent electrostatic rejection has been specifically designed and constructed to perform the measurement (see Chapter 5 for details about the magnetic probe). High-frequency magnetic fluctuations in the whistler regime are detected by the probe at the time of Rayleigh-Taylor instability and reconnection. The magnetic fluctuations span a wide frequency range and have a very steep power spectrum. Circularly polarized magnetic components of obliquely propagating whistler waves are identified. The detection of whistler waves is important evidence indicating that the reconnection process is in the two-fluid, not MHD regime.

This chapter is arranged as follows. First we briefly review the theories of whistler wave and its association with fast reconnection. Then we analyze the measurements from the high-speed 3D magnetic probe and show that the high-frequency magnetic fluctuations are an ensemble of whistler waves generated during the reconnection. We use a hodogram technique to resolve the circularly polarized magnetic components of the whistler waves. A polarization recognition algorithm was developed to automatically identify the type of polarization. Useful signal processing algorithms are listed and briefly reviewed in Appendix B, such as Fourier transform, finite impulse response digital filters and principal component analysis.

4.1 Background

4.1.1 Two-fluid theory of whistler wave

The whistler wave is a cold electromagnetic plasma wave with frequency much higher than the ion cyclotron frequency but much lower than the electron cyclotron frequency. Therefore ions can be assumed to be unmagnetized and the electron motion and the ion motion are decoupled. This is different from MHD theory which treats ions and electrons as a single bulk fluid. Two-fluid theory is required to explain the physics of whistler waves. Linear perturbation to the two-fluid theory shows that electromagnetic fluctuations in a cold plasma satisfy

$$\nabla \times \mathbf{B} = \frac{1}{c^2}\frac{\partial}{\partial t}(\mathbb{K}\cdot\mathbf{E}) \tag{4.1}$$

$$\nabla \times \mathbf{E} = -\frac{\partial \mathbf{B}}{\partial t}, \tag{4.2}$$

where the dielectric tensor is

$$\mathbb{K} = \begin{bmatrix} S & -iD & 0 \\ iD & S & 0 \\ 0 & 0 & P \end{bmatrix}, \tag{4.3}$$

and the elements of the dielectric tensor are

$$S = 1 - \sum_{\sigma=i,e} \frac{\omega_{p\sigma}^2}{\omega^2 - \omega_{c\sigma}^2} \tag{4.4}$$

$$D = \sum_{\sigma=i,e} \frac{\omega_{c\sigma}}{\omega} \frac{\omega_{p\sigma}^2}{\omega^2 - \omega_{c\sigma}^2} \tag{4.5}$$

$$P = 1 - \sum_{\sigma=i,e} \frac{\omega_{p\sigma}^2}{\omega^2}. \tag{4.6}$$

The z axis of the coordinate system has been defined parallel to the equilibrium magnetic field. See Bellan (2006) [5] for details.

Assuming the perturbation terms have a spatial and time dependence as $\exp(i\mathbf{k}\cdot\mathbf{x} - i\omega t)$,

Eq. 4.1 and 4.2 becomes

$$\mathbf{k} \times (\mathbf{k} \times \mathbf{E}) = -\frac{\omega^2}{c^2} \mathbb{K} \cdot \mathbf{E} \tag{4.7}$$

$$\mathbf{nn} \cdot \mathbf{E} - n^2 \mathbf{E} + \mathbb{K} \cdot \mathbf{E} = 0, \tag{4.8}$$

where we have defined the refractive index $\mathbf{n} = c\mathbf{k}/\omega$. Without loss of generality, the x axis of the coordinate system is defined to lie along the perpendicular component of $\mathbf{n}$ so that $n_y = 0$. We further define θ to be the angle between $\mathbf{n}$ and $\hat{z}$ (the direction of equilibrium magnetic field) so that $n_x = n \sin\theta$ and $n_z = n \cos\theta$. The above equation becomes

$$\begin{bmatrix} S - n^2 \cos^2\theta & -iD & n^2 \sin\theta \cos\theta \\ iD & S - n^2 & 0 \\ n^2 \sin\theta \cos\theta & 0 & P - n^2 \sin^2\theta \end{bmatrix} \cdot \begin{bmatrix} E_x \\ E_y \\ E_z \end{bmatrix} = 0. \tag{4.9}$$

Existence of non-trivial solutions to Eq. 4.9 requires that the determinant of the matrix must vanish. This leads to a very complicated dispersion relation between ω and n (or k).

Consider the special case where $\theta = 0$. Equation 4.9 becomes

$$\begin{bmatrix} S - n^2 & -iD & 0 \\ iD & S - n^2 & 0 \\ 0 & 0 & P \end{bmatrix} \cdot \begin{bmatrix} E_x \\ E_y \\ E_z \end{bmatrix} = 0. \tag{4.10}$$

Equating the determinant of the matrix to zero gives

$$[(S - n^2)^2 - D^2]P = 0, \tag{4.11}$$

which has roots

$$P = 0, \qquad n^2 = R \equiv S + D, \qquad n^2 = L \equiv S - D. \tag{4.12}$$

$P = 0$ corresponds to the cold plasma limit of unmagnetized electrostatic plasma wave. $n^2 = R$ or L are the dispersion relations of magnetized cold plasma waves propagating along the background magnetic field. Consider the solution $n^2 = R = S + D$. Equation 4.10

becomes

$$\begin{bmatrix} -D & -iD & 0 \\ iD & -D & 0 \\ 0 & 0 & P \end{bmatrix} \cdot \begin{bmatrix} E_x \\ E_y \\ E_z \end{bmatrix} = 0. \tag{4.13}$$

Hence the $n^2 = R$ solution has

$$\frac{E_x}{E_y} = -i. \tag{4.14}$$

This corresponds to a right-hand circularly polarized electric component of an electromagnetic wave propagating in the positive z direction. Because Faraday's law gives $i\omega\mathbf{B} = i\mathbf{k} \times \mathbf{E}$, the magnetic component is also right-hand circularly polarized. Similarly, the $n^2 = L$ solution gives a left-hand circularly polarized plasma wave.

Now we consider a special high-frequency limit so that the ion terms in S, D, and P are all small compared to unity or the electron terms, i.e.,

$$\begin{aligned} S &\approx 1 - \frac{\omega_{pe}^2}{\omega^2 - \omega_{ce}^2} \\ D &\approx \frac{\omega_{ce}}{\omega} \frac{\omega_{pe}^2}{\omega^2 - \omega_{ce}^2} \\ P &\approx 1 - \frac{\omega_{pe}^2}{\omega^2}. \end{aligned} \tag{4.15}$$

It can be shown that the approximations give the famous Altar-Appleton-Hartree dispersion relation

$$n^2 = 1 - \left[\frac{2\frac{\omega_{pe}^2}{\omega^2}\left(1 - \frac{\omega_{pe}^2}{\omega^2}\right)}{2\left(1 - \frac{\omega_{pe}^2}{\omega^2}\right) - \frac{\omega_{ce}^2}{\omega^2}\left(1 - \frac{\omega_{pe}^2}{\omega^2}\right)^2 \pm \Gamma} \right], \tag{4.16}$$

where

$$\Gamma = \sqrt{\frac{\omega_{ce}^4}{\omega^4}\sin^4\theta + 4\frac{\omega_{ce}^2}{\omega^2}\left(1 - \frac{\omega_{pe}^2}{\omega^2}\right)^2 \cos^2\theta}. \tag{4.17}$$

The + sign in the dispersion relation corresponds to the $n^2 = R$ solution in the $\theta = 0$ case and the $-$ sign corresponds to the $n^2 = L$ solution.

We further take the limit

$$\frac{\omega_{ce}^4}{\omega^4}\sin^4\theta \ll 4\frac{\omega_{ce}^2}{\omega^2}\left(1 - \frac{\omega_{pe}^2}{\omega^2}\right)^2 \cos^2\theta \tag{4.18}$$

so that

$$\Gamma \approx -2\left(1-\frac{\omega_{pe}^2}{\omega^2}\right)^2 \cos^2\theta. \tag{4.19}$$

In most literature, this approximation is made under the quasi-longitudinal (QL) approximation $\theta \approx 0$. However, a simplification to Eq. 4.18 gives

$$\sin^2\theta \ll \frac{2\omega}{|\omega_{ce}|}\left|1-\frac{\omega_{pe}^2}{\omega^2}\right|\cos\theta \tag{4.20}$$

$$\text{or} \qquad \frac{\sin^2\theta}{\cos\theta} \ll \frac{2\omega_{pe}^2}{\omega|\omega_{ce}|}, \qquad \text{if } \omega \ll \omega_{pe}. \tag{4.21}$$

Therefore the quasi-longitudinal approximation $\theta \approx 0$ can be relaxed to Eq. 4.21. We will see later that in the Caltech plasma jet experiment the RHS of Eq. 4.21 is of order of 10^7. Hence Eq. 4.21 is valid for essentially all θ except for $\theta = \pi/2$.

Upon substitution of Eq. 4.19, the dispersion relation Eq. 4.16 becomes

$$n_\pm^2 = 1 - \frac{\omega_{pe}^2/\omega^2}{1 \mp \left|\frac{\omega_{ce}}{\omega}\cos\theta\right|}. \tag{4.22}$$

The mode with upper sign is the quasi-longitudinal right-hand (QLR) mode and has a right-hand circularly polarized magnetic component. When $\omega \ll |\omega_{ce}\cos\theta|$, the QLR mode is called the whistler or helicon wave and the dispersion relation becomes

$$\frac{c^2k^2}{\omega^2} = n_+^2 = \frac{\omega_{pe}^2}{\omega|\omega_{ce}\cos\theta|}. \tag{4.23}$$

or

$$\omega = \frac{c^2|\omega_{ce}\cos\theta|}{\omega_{pe}^2}k^2 = \frac{c^2|\omega_{ce}\cos\theta|}{\omega_{pe}^2}\mathbf{k}^2 \qquad , \qquad k = \frac{\omega_{pe}}{c}\sqrt{\frac{\omega}{|\omega_{ce}\cos\theta|}}. \tag{4.24}$$

The phase velocity of the whistler wave is

$$\mathbf{v}_p = \frac{\omega}{k}\hat{k} = \frac{c}{\omega_{pe}}\sqrt{\omega|\omega_{ce}\cos\theta|}\cdot\hat{k} = \frac{c}{n}\hat{k}. \tag{4.25}$$

The group velocity associated with the dispersion relation is

$$\mathbf{v}_g = \frac{\partial\omega}{\partial\mathbf{k}} = \frac{2c}{\omega_{pe}}\sqrt{\omega|\omega_{ce}\cos\theta|}\cdot\hat{k} = \frac{2c}{n}\hat{k} = 2\mathbf{v}_p. \tag{4.26}$$

The whistler wave has an interesting quadratic dispersion relation $\omega \propto k^2$. Consequentially,

low-frequency models travel slower than high-frequency modes. In the magnetosphere when a burst of broadband whistler waves is excited by lightning or magnetic reconnection, a distant observer always sees the high-frequency modes first and then low-frequency modes, analogous to a descending whistler tone.

Verkhoglyadova et al. (2010) [119] and Bellan (2013) [6] showed theoretically that the magnetic component of an obliquely propagating whistler wave is also right-hand circularly polarized. The electric field oscillation has a finite component along the wave propagation direction if the latter is not aligned with the background magnetic field, but the perpendicular component remains right-hand circularly polarized. Therefore when the wave vector is oblique to the background magnetic field, the electric field is not exactly circularly polarized.

In the Caltech plasma jet experiment, at the location of the 3D whistler probe ($z = 29$ cm, $r = 6$ cm), the electron number density is about $n_e \approx 10^{21}$ m^{-3}, and the magnetic field strength is $B \sim 0.15$ T. The electron/ion plasma frequencies and cyclotron frequencies are

$$\begin{aligned} & \omega_{pe} = 1.8 \times 10^{12} Hz \qquad && \omega_{pi} = 6.6 \times 10^{9} Hz \\ & |\omega_{ce}| = 2.6 \times 10^{10} Hz \qquad && \omega_{ci} = 3.6 \times 10^{5} Hz \\ \text{or} \quad & f_{pe} = 2.9 \times 10^{11} Hz \qquad && f_{pi} = 1.1 \times 10^{9} Hz \\ & |f_{ce}| = 4.1 \times 10^{9} Hz \qquad && f_{ci} = 5.7 \times 10^{4} Hz. \end{aligned}$$

The typical frequency of the magnetic fluctuations measured by the 3D magnetic probe is in the range of $2 - 20$ Mhz, corresponding to an angular frequency $\omega = 0.13 \times 10^8$ Hz to 1.3×10^8 Hz. Hence $\omega_{ci} \ll \omega \ll \omega_{pi} \ll |\omega_{ce}| \ll \omega_{pe}$. It can be shown that $2\omega_{pe}^2/(\omega|\omega_{ce}|) = 2 \times 10^6 - 2 \times 10^7$. Therefore the approximation made in Eq. 4.21 is valid except for θ

extremely close to $\pi/2$. It can also be shown that

$$\begin{aligned}
\left|\frac{\omega_{pe}^2}{\omega^2-\omega_{ce}^2}\right| &\approx \frac{\omega_{pe}^2}{\omega_{ce}^2} = 4.6\times10^3 \\
\left|\frac{\omega_{pi}^2}{\omega^2-\omega_{ci}^2}\right| &\approx \frac{\omega_{pi}^2}{\omega^2} = 2.7\times10^3 - 2.7\times10^5 \\
\left|\frac{\omega_{ce}}{\omega}\frac{\omega_{pe}^2}{\omega^2-\omega_{ce}^2}\right| &\approx \frac{\omega_{pe}^2}{\omega|\omega_{ce}|} = 10^6 - 10^7 \\
\left|\frac{\omega_{ci}}{\omega}\frac{\omega_{pi}^2}{\omega^2-\omega_{ci}^2}\right| &\approx \frac{\omega_{ci}\omega_{pi}^2}{\omega^3} = 8 - 8\times10^3 \\
\frac{\omega_{pe}^2}{\omega^2} &= 2\times10^8 - 2\times10^{10} \\
\frac{\omega_{pi}^2}{\omega^2} &= 2.7\times10^3 - 2.7\times10^5.
\end{aligned}$$

Therefore the approximations in Eq. 4.15 for D and P are valid. For S, according to the above estimation, the ion term is comparable or even larger than the electron term, so it is inappropriate to drop the ion term. However, calculation shows that the dispersion relation Eq. 4.23 is still valid even though it was derived by assuming the ion term in S is ignorable.

To see this, we consider a different approach to derive the whistler wave dispersion relation. According to the calculation above, there are $|P|\approx10^9$, $|D|\approx10^6$ and $|S|\approx10^4$. Moreover, the whistler dispersion relation gives $n^2\sim\omega_{pe}^2/(\omega|\omega_{ce}|)\sim10^6$. Therefore $|P|\gg n^2\sim|D|\gg S$. Revisit Eq. 4.9 and write the determinant of the matrix as

$$(P-n^2\sin^2\theta)\begin{vmatrix} S-n^2\cos^2\theta & -iD \\ iD & S-n^2 \end{vmatrix} + n^2\sin\theta\cos\theta\begin{vmatrix} -iD & n^2\sin\theta\cos\theta \\ S-n^2 & 0 \end{vmatrix} = 0. \quad (4.27)$$

Because $|P-n^2\sin^2\theta|$ is much larger than other terms in the equation, the balance of this equation requires that

$$\begin{vmatrix} S-n^2\cos^2\theta & -iD \\ iD & S-n^2 \end{vmatrix} \approx 0 \qquad \text{if } |P|\gg|D|,n^2,|S|. \quad (4.28)$$

Expansion of the above equation gives

$$n^4 \cos^2\theta - Sn^2(1+\cos^2\theta) + S^2 - D^2 = 0. \tag{4.29}$$

$$n^2 = \frac{S(1+\cos^2\theta) + \sqrt{4D^2\cos^2\theta + S^2\sin^4\theta}}{2\cos^2\theta}. \tag{4.30}$$

With quasi-longitudinal approximation $4D^2\cos^2\theta \gg S^2\sin^4\theta$ and also $|D| \gg |S|$, the above equation becomes

$$\begin{aligned} n^2 &\approx \frac{D}{\cos\theta} \\ &\approx \frac{\omega_{ce}}{\omega}\frac{\omega_{pe}^2}{\omega^2-\omega_{ce}^2}\frac{1}{\cos\theta} \qquad (4.31) \\ &\approx \frac{\omega_{ce}}{\omega}\frac{\omega_{pe}^2}{-\omega_{ce}^2\cos\theta} \\ &= \frac{\omega_{pe}^2}{\omega|\omega_{ce}|\cos\theta}. \qquad (4.32) \end{aligned}$$

Equation 4.32 is identical to the whistler dispersion relation obtained in Eq. 4.23. The approximations we have made to derive Eq. 4.32 are $|P| \gg |D| \gg |S|$, $|D| \gg |S|\sin^2\theta/\cos\theta$ and that the ion term is ignorable in D. In the Caltech plasma jet experiment configuration, the above two conditions are satisfied as long as $\omega_{ci} \ll \omega \ll |\omega_{ce}|$.

It is important to note that the above derivation of the whistler wave dispersion does not rely on the sign of S. S can be positive or negative as long as $|D| \gg |S|$ is satisfied. $S = 0$ corresponds to the lower hybrid resonance, an electrostatic resonance occurring perpendicular to the magnetic field. The frequency of the lower hybrid resonance is

$$\omega_{lh}^2 = \omega_{ci}^2 + \frac{\omega_{pi}^2}{1+\frac{\omega_{pe}^2}{\omega_{ce}^2}}. \tag{4.33}$$

In our plasma $\omega_{pe} \gg |\omega_{ce}|$, and the above expression can be simplified as

$$\begin{aligned} \omega_{lh}^2 &\approx \omega_{ci}^2 + \frac{\omega_{pi}^2\omega_{ce}^2}{\omega_{pe}^2} = \omega_{ci}^2 + \frac{m_e}{m_i}\omega_{ce}^2 = \frac{m_e^2}{m_i^2}\omega_{ce}^2 + \frac{m_e}{m_i}\omega_{ce}^2 \\ &\approx \frac{m_e}{m_i}\omega_{ce}^2 = \frac{m_i}{m_e}\omega_{ci}^2 = \omega_{ci}\omega_{ce}. \qquad (4.34) \end{aligned}$$

Therefore $\omega_{ci} \ll \omega_{lh} \ll |\omega_{ce}|$. Because the derivation of the whistler wave does not depend on the sign of S, the whistler wave can exist with $S > 0$, $S < 0$ or $S = 0$, i.e., the whistler

frequency can be higher, lower, or even equal to the lower hybrid resonance frequency.

We have reviewed the basic theory of whistler waves and verified that the $2-20$ MHz magnetic fluctuation measured by the high speed 3D magnetic probe is in the whistler regime.

4.1.2 Fast magnetic reconnection and whistler wave

Consider the two-fluid electron equation of motion

$$m_e \frac{d\mathbf{u}_e}{dt} = -e(\mathbf{E} + \mathbf{u}_e \times \mathbf{B}) - \frac{1}{n_e}\nabla(n_e \kappa T_e) - \nu_{ei} m_e (\mathbf{u}_e - \mathbf{u}_i), \tag{4.35}$$

where ν_{ei} is the collision rate between electrons and ions. Because $\mathbf{u}_i - \mathbf{u}_e = \mathbf{J}/(n_e e)$ and $\mathbf{u}_i = (1 + m_e/m_i)\mathbf{U} + (m_e/m_i)\mathbf{u}_e \approx \mathbf{U}$, the electron velocity can be written as $\mathbf{u}_e \approx -\mathbf{J}/(n_e e) + \mathbf{U}$. Here $\mathbf{U}$ is the center of mass velocity of electrons and ions. The electron equation of motion, or generalized Ohm's law becomes

$$\underbrace{\frac{m_e}{e}\frac{d\mathbf{u}_e}{dt}}_{\text{electron inertia}} + \mathbf{E} + \mathbf{U} \times \mathbf{B} - \underbrace{\frac{1}{n_e e}\mathbf{J} \times \mathbf{B}}_{\text{Hall}} + \underbrace{\frac{1}{n_e e}\nabla(n_e \kappa T_e)}_{\text{electron pressure}} = \underbrace{\eta \mathbf{J}}_{\text{resistive term}}, \tag{4.36}$$

where $\eta = \nu_{ei} m_e/(n_e e^2)$ is the plasma resistivity. The electron inertia term on the LHS of the equation may be ignored for low speed plasma motion. The third term on the LHS of the equation, $-\mathbf{J} \times \mathbf{B}/(n_e e)$, is call the Hall term, and is ignored in MHD theory. Equation 4.36 is usually used in Ampere's law $-\partial_t \mathbf{B} = \nabla \times \mathbf{E}$. After taken curl, the electron pressure term becomes

$$\begin{aligned} \nabla \times \left(\frac{1}{n_e e}\nabla(n_e \kappa T_e)\right) &= \nabla \frac{1}{n_e e} \times \nabla(n_e \kappa T_e) = -\frac{1}{n_e^2 e}\nabla n_e \times (\kappa T_e \nabla n_e + n_e \nabla(\kappa T_e)) \\ &= -\frac{1}{n_e e}\nabla n_e \times \nabla(\kappa T_e). \end{aligned} \tag{4.37}$$

Since the gradient of density is usually parallel to the gradient of temperature (or pressure), the above equation is close to zero.

Upon dropping the electron inertia term, the Hall term and the pressure term, the equation of electron motion is reduced to the well-known MHD Ohm's law

$$\mathbf{E} + \mathbf{U} \times \mathbf{B} = \eta \mathbf{J}. \tag{4.38}$$

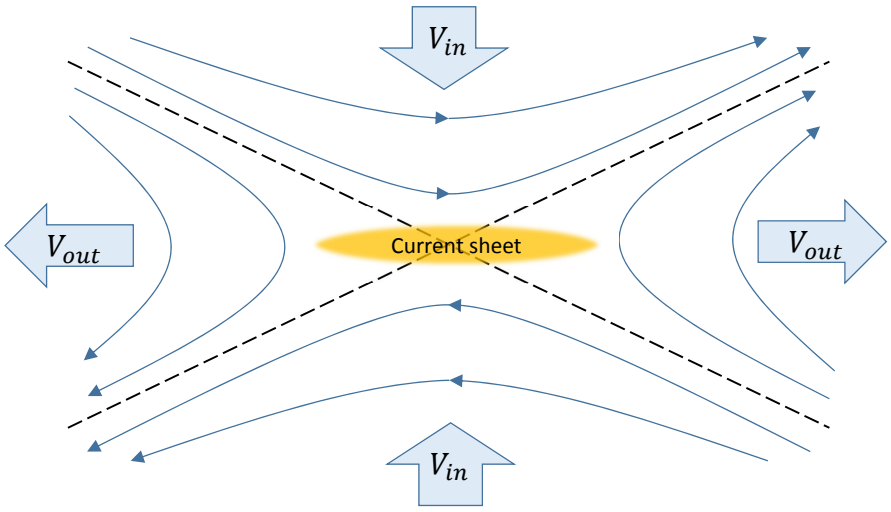

Figure 4.1: Sketch of 2D X-point type Sweet-Parker reconnection. The solid curves with arrows are the magnetic field lines. A current sheet is formed in the center of this X-point configuration.

Ideal MHD theory further takes the zero resistivity limit, i.e., $\eta = 0$. We have shown in the introduction chapter that this leads to the famous frozen-in flux condition in which the magnetic flux enclosed by any closed material line is constant.

Magnetic reconnection, a process wherein magnetic field lines break and reconnect to form a different topological configuration, is forbidden in ideal MHD because the magnetic flux in the reconnection region must change in the reconnection process. With finite electric resistivity, the Sweet-Parker model [13, 87, 111] shows that magnetic reconnection occurs in a stationary, steady-state fashion due to magnetic diffusion. Magnetic reconnection can also be described as a growing instability called tearing instability in the context of resistive MHD [33]. Figure 4.1 shows a sketch of two-dimensional Sweet-Parker magnetic reconnection. Plasmas that carry horizontal magnetic field lines of opposite directions are pinched towards each other at velocity V_{in} by some external force. In the central plane an electric current is generated flowing into the board because of the oppositely oriented magnetic field lines above and beneath the central plane. Because of the finite resistivity, the current sheet region dissipates magnetic energy. Consequentially the horizontal magnetic field lines break (diffuse) in the center, become vertical field lines and move outwards horizontally. The center region is called the X-point.

The reconnection rate of Sweet-Parker model can be quantified by $V_{in}/V_A \sim 1/\sqrt{S}$,

where V_A is the Alfvén velocity and S is the Lundquist number corresponding to the size of the current sheet [13, 123]. This rate, however, is usually too slow compared to actual reconnection processes. For example, in the solar corona the plasma resistivity is very low due to the high temperature and the low density, so the Lundquist number is very large. Coronal mass ejection (CME) events last for seconds to minutes, whereas the Sweet-Parker model would predict weeks to months for the reconnection involved in these events [79]. In the Magnetic Reconnection eXperiment (MRX) in Princeton Plasma Physics Lab, an anomalous resistivity as high as 10 times larger than the Spitzer resistivity has to be assumed to explain the experimental reconnection rate [55, 66, 115, 123].

These discrepancies have motivated efforts to consider non-MHD effects in the plasma dynamics. One of the assumptions of MHD theory is that the ion dynamics and the electron dynamics are coupled and the bulk plasma dynamics is considered. This is usually not correct in the processes involving small-scale fast-paced dynamics like reconnection. On a length scale that is smaller than the ion skin depth $d_i = c/\omega_{pi}$, where c is the speed of light and ω_{pi} is the ion plasma frequency, the plasma should not be considered as a single bulk fluid. Theories of fast magnetic reconnection, sometimes called Hall magnetic reconnection, use the generalized Ohm's law by including the electron inertia term and the Hall term[1]. The generalized Ohm's law can also be written as

$$\mathbf{E} + \mathbf{u}_e \times \mathbf{B} = -\frac{m_e}{e}\frac{d\mathbf{u}_e}{dt} - \frac{\nabla P_e}{n_e e} + \eta \mathbf{J}. \tag{4.39}$$

In the cases that the electron inertia term or the hall term are more important than the resistive term, for example, when the current sheet is thinner than the electron mean free path, the reconnection is also called collisionless reconnection.

Note that if the electron inertia term and the pressure term are dropped, Eq. 4.39 then becomes very similar to Eq. 4.38 except that the velocity involved in Eq. 4.39 is the electron velocity instead of the bulk plasma velocity. In the zero resistivity limit this leads to the result that the magnetic field is frozen into the electron fluid and ions are somewhat "unmagnetized". Sometimes this regime is also called the electron magnetohydrodynamics (EMHD) regime, in contrast to the conventional MHD regime. In general cases when the electron inertia term and resistive term are included it is not correct to assume that the

[1] Sometimes the electron pressure term is also included, such as in Ref. [7]

magnetic field is frozen to the electron motion.

In the Caltech plasma jet experiment, the current density though the cross-section of the pre-kink jet is estimated to be

$$J = \frac{I}{\pi R^2} \sim \frac{50 \text{ kA}}{\pi (5 \text{ cm})^2} = 6.4 \times 10^6 \text{ A/m}^2,$$

where $I = 50$ kA is the total poloidal current and $R = 5$ cm is the radius of the central plasma that carries the current. With $n_e = 10^{22}$ m^{-3}, the relative drift velocity between ions and electrons is

$$U_i - U_e = \frac{J}{n_e e} \sim 4 \text{ km/s}.$$

This drift velocity is about $20 - 30\%$ times the bulk plasma velocity. Hence the for the pre-kink jet the Hall term $\mathbf{J} \times \mathbf{B}/n_e e$ is ignorable comparing to the $\mathbf{U} \times \mathbf{B}$ term. However as the plasma is pinched to a thickness smaller than 5 mm by the Rayleigh-Taylor instability, the local current density increases to

$$J \sim \frac{50 \text{ kA}}{5 \text{ mm} \times 5 \text{ cm}} = 2 \times 10^8 \text{ A/m}^2.$$

Use the electron number density inferred from Stark broadening measurement $n_e = 3.5 \times 10^{22}$ m^{-3}, the relative drift velocity of ions and electrons becomes

$$U_i - U_e = \frac{J}{n_e e} \sim 36 \text{ km/s}.$$

This relative drift velocity is faster than the typical argon jet velocity $v \sim 10 - 20$ km/s, indicating that the ion and electron motion are decoupled. It is therefore inappropriate to drop the Hall term in Ohm's law.

Fast magnetic reconnection has been studied in theoretical modeling [7], lab experiments [54, 55, 66, 115, 123], space observation [24, 86], two-fluid, hybrid, and full-particle numerical simulations [12, 28, 29, 32, 77, 94]. These studies find that the rates of fast magnetic reconnection significantly exceed those obtained from resistive MHD reconnection models [12, 123]. For example, Bellan (2014) [7] showed that when using the full version of the generalized Ohm's law (Eq. 4.36), the systems of equations of the fast magnetic reconnection is inherently fourth-order, and is fundamentally different from the resistive MHD

theory. The latter one is intrinsically second order. The eigen solution of the fourth order equation systems gives a fast and purely growing magnetic reconnection with the growth rate on the order of the whistler frequency.

By including the Hall term and the electron inertia term in the generalized Ohm's law, we have essentially separated the electron motion from the ion motion. Equivalently speaking, Hall magnetic reconnection is in the context of two-fluid theory, not MHD theory. Due to the large ion to electron mass ratio, ion motion is much slower than electron motion. If plasma dynamics occurs with a velocity much faster than the ion motion but much slower than the electron motion, the ions can be assumed to be stationary and the electrons are fast moving particles. We have shown in section 4.1.1 that the characteristic wave in this regime is the whistler wave.

Various studies have revealed a strong relation between fast magnetic reconnection and whistler wave [7, 24, 29, 32, 35, 54, 77, 94]. The role of whistler wave in the fast magnetic reconnection, however, remains strongly debated.

Mandt et al. (1994) [77] studied fast magnetic reconnection using hybrid numerical simulation. It is suggested that in the EMHD regime the whistler wave take over the role of the Alfvén wave in driving magnetic reconnection. More specifically, whistler wave helps develop an out-of-plane magnetic field components and drives fast reconnection as the bent magnetic field straightens out, which pumps the magnetic energy into whistler wave energy. Roger et al. (2001) [94] proposed that collisionless reconnection is controlled by standing whistler waves in the vicinity of the X-point. The quadratic dispersion relation of the whistler wave is necessary to maintain stable whistler waves near the X-point. Drake et al. (2008) [29] used large-scale, particles-in-cell simulation and found that whistler wave plays the key role in driving the electrons away from the magnetic X-line and essentially drives the reconnection. These results prefer a whistler-wave driven fast reconnection mechanism.

Space observation detects whistler-mode waves at the times of Hall magnetic reconnection between the magnetic field of the Earth's magnetosphere and the magnetic field of the Solar wind [24**?**]. Deng & Matsumoto (2001) [24] claimed that the reconnection is mediated by whistler waves. Ji et al. (2004) [54] investigated fast reconnection experimentally and found high-frequency magnetic fluctuations near the current sheet center. The magnetic fluctuations have frequencies comparable to or below the lower hybrid resonance frequency

and the wavevectors are obliquely to the background magnetic field, corresponding to the right-hand polarized whistler wave. These space observations and terrestrial experiments demonstrate positive correlations between the whistler wave and the fast magnetic reconnection. However, they cannot prove that the fast magnetic reconnection is driven by the whistler wave.

By contrast, Bellan (2014) [7] showed in theory that in Hall MHD plasma fast magnetic reconnection is a purely growing instability that does not necessarily involve a whistler wave, although the same equations do give a whistler wave if the perturbation is wavelike. Bellan (2014) [7] also pointed out that the standing whistler wave scenario proposed by Roger et al. (2001) [94] can lead to unphysical behaviors such as fast oscillating electron flow and diverging frequency at the X-point. Fujimoto et al. (2008) [32] showed that whistler wave is driven by electron temperature anisotropy caused by fast magnetic reconnection in the downstream region of the electron flow. The whistler wave does not control the energy dissipation process but instead scatters the electrons and relaxes the temperature anisotropy. These results suggest that whistler waves are associated with fast reconnection, but is not the cause of fast reconnection.

4.2 Whistler waves associated with fast reconnection in the plasma jet experiment

At the location of the lateral Rayleigh-Taylor instability, spectroscopic measurement of Stark broadening shows that the electron density of the compressed plasma is $(3.5 \pm 0.9) \times 10^{22}$ m^{-3}. Assuming $n_i = n_e$, the electron and ion plasma frequency are respectively $\omega_{pi} = 36$ GHz and $\omega_{pe} = 10$ THz. The ion skin depth or ion inertia depth is $d_i = c/\omega_{pi} = 8$ mm and the electron skin depth is $d_e = c/\omega_{pe} = 0.03$ mm. Visible images show that the Rayleigh-Taylor instability rapidly chokes the plasma filament down to less than 5 mm, smaller than the ion skin depth [79, 80]. Therefore the ion motion is decoupled from the electron motion and the plasma dynamics is in the two-fluid regime.

As the Rayleigh-Taylor instability grows, the plasma jet eventually breaks at the location of the instability. As a consequence, the helical magnetic field that was frozen into the jet must have undergone a reconnection process, mostly likely a fast magnetic reconnection process because small-scale dynamics was involved. High-frequency whistler waves are

expected to be associated with this process.

A high-speed 3D magnetic probe (we hereafter use "whistler probe") has been specially designed and built to measure the magnetic component of the whistler waves generated in the Caltech plasma jet experiment. The whistler probe is composed of three orthogonal pairs of oppositely oriented B-dot coils. Each B-dot coil is a single turn shielded loop probe made out of a 0.047 inch semi-rigid coaxial cable. An RF ground loop diverting technique invented by Perkins & Bellan [89] is implemented. The probe has an overall 70 dB rejection to electrostatic interference. The whistler probe is placed at $z = 29$ cm away from the electrode ($z = 0$) and its radial location can be adjusted.

The whistler probe is connected via a 20 dB attenuator to a 100 MHz VME data acquisition system and is sensitive to magnetic fluctuations $\dot{B} > 100$T/sec (or 1 Gauss/μs) up to 20 MHz. The measurement range is $\pm 10^6$T/sec, given the 20 dB attenuation, the ± 0.5 V dynamic range of the data acquisition system and the the calibration factor of the whistler probe 0.5×10^{-4} V/(T/sec). Detailed information about the whistler probe is given in Chapter 5.

4.2.1 High-frequency magnetic fluctuations during fast magnetic reconnection

First we placed the whistler probe at $r = 6$ cm so that the probe is immersed in a relatively low density plasma surrounding the central dense plasma jet. Typical direct measurements of magnetic fluctuations $\dot{B}$ are given in the first row of Fig. 4.2 (shot 17012). The signals are integrated over time to give the magnetic field measurement as shown in the third row of Fig. 4.2. The first and the third rows of the figure show that the magnetized plasma reached the probe as early as 12 μs.

The velocity of the argon plasma jet is $10 - 20$ km/s, hence the motion of the plasma across a 1 cm size probe may cause magnetic field fluctuations up to 2 MHz. To eliminate this effect, we apply a digital 2 MHz highpass filter to the measurements (see § B.2 for details about the digital filter). The filtered high-frequency magnetic fluctuations measurements are shown in the second row of Fig. 4.2. The filtered signals clearly show that the high-frequency magnetic fluctuations in all three components arise at 28 μs and become very violent after 30 μs. The profiles of the high-frequency fluctuations are somewhat stochastic and are similar in all three directions, indicating that the fluctuations contain an ensemble

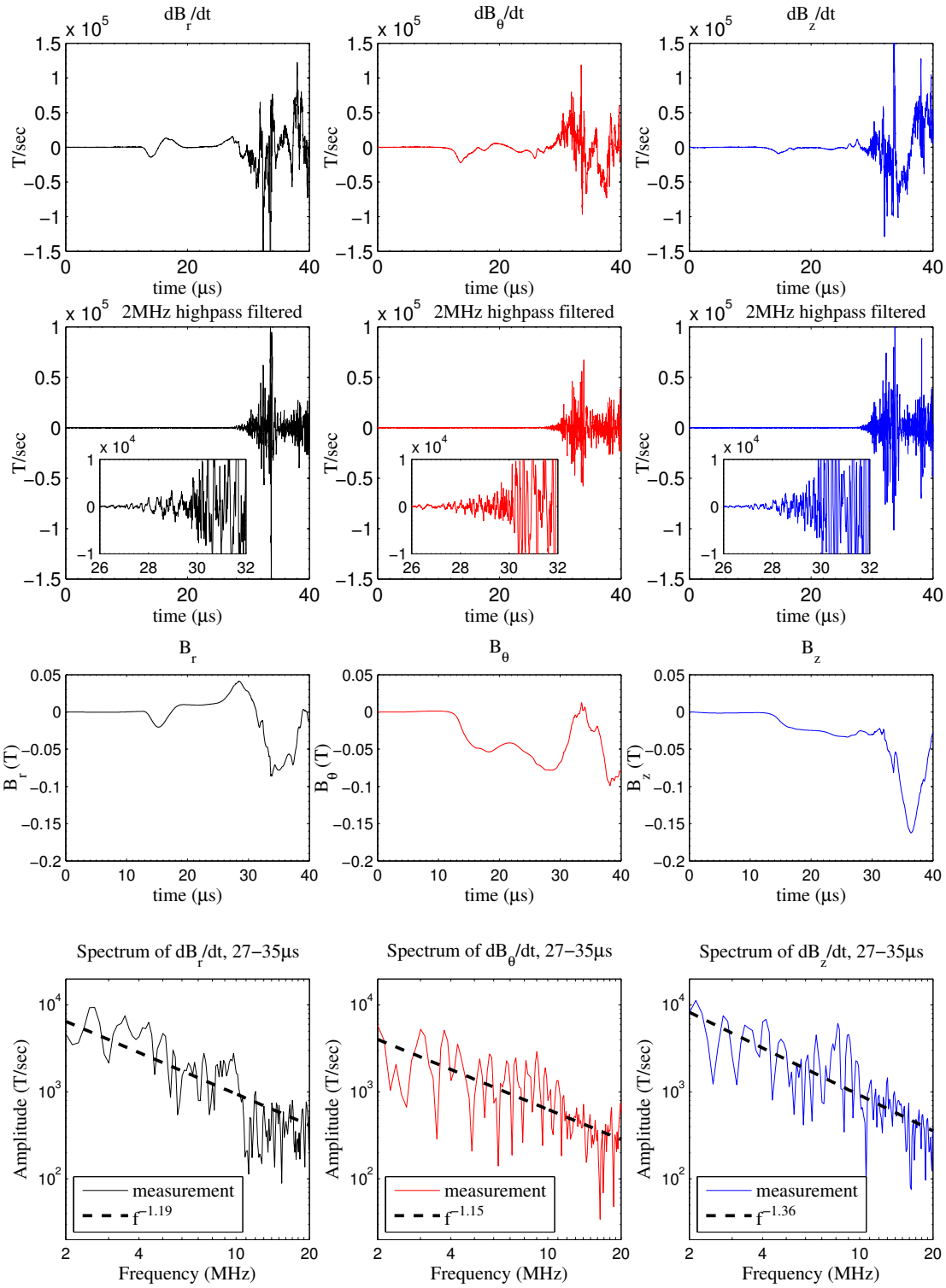

Figure 4.2: 3D magnetic field measurements of shot 17012 from 0 to 40 μs. First row: magnetic fluctuation dB/dt measurements. Second row: Signals in the top row filtered by a 4-th order Butterworth 2 MHz highpass digital filter. The insets show the signals in detail from 26 to 32 μs. Third row: magnetic field measurements obtained by integrating the dB/dt signals over time. Fourth row: Spectra of the magnetic fluctuations $\dot{B}$ from 27 to 35 μs obtained using fast Fourier transform. The dashed lines are the best fitted power-law function. In shot 17012, the probe is located at $z = 29$ cm, $r = 6$ cm.

of modes. The fourth row of the figure shows that the broadband magnetic fluctuations have continuous spectra following f^{-1} power-law from 2 MHz to 20 MHz. As shown in § 4.1.1 these high-frequency magnetic fluctuations measured by the magnetic probe correspond to the whistler regime.

At $t = 28$ μs, a Rayleigh-Taylor instability that eventually leads to magnetic reconnection starts to develop on the kinked plasma jet. Figure 4.3 shows a sequence of false color images created by superimposing extreme ultraviolet (EUV) emissions in $30 - 60$ eV band [17] and visible light emissions (see § 1.2.2 for detailed description about the diagnostics). As the Rayleigh-Taylor instability begins, the top part of the kinked jet becomes extremely bright in EUV while it dims in visible light, indicating a sudden increase in the electron temperature of the top part of the jet. The $30 - 60$ eV ($20 - 40$ nm wavelength) EUV emissions are believed from Ar^{5+}–Ar^{7+} ions. Assuming local thermal equilibrium, the existence of significant amounts of Ar^{5+}–Ar^{7+} ions reveals that the local electron temperature is $5 - 10$ eV. Spectroscopic measurements show that the local ion temperature also rose from ~ 3 eV to ~ 16 eV. This efficient particle heating occurring in microsecond scales is believed to be a consequence of fast magnetic reconnection, where magnetic energy is rapidly dissipated and converted to particle kinetic energy. Similar particle heating is also observed in the Princeton reconnection experiment MRX [123, 124, 125].

Figure. 4.4 shows the voltage and current profiles measured at the electrodes. It is seen that large voltage spikes of $500 - 800$ V occur starting at 29.5 μs, indicating temporal changes of the magnetic flux associated with the electric current through the electrodes. The current profile does not have notable spikes but instead undergoes a non-smooth change at 31.5 μs, coincident with the end of the voltage spikes. This implies that the current has a different path after 31.5 μs.

The fast particle heating and the IV profiles suggest that a magnetic reconnection occurs around 28 μs, triggered by the Rayleigh-Taylor instability. The detection of high-frequency magnetic fluctuations coincident with the Rayleigh-Taylor instability shows that the process is a fast magnetic reconnection.

Figure 4.5 gives the typical measurements of magnetic fluctuations when the probe was placed at $r = 1$ cm so that at later times the probe was immersed in the central dense plasma jet (shot 16940). The results are in general very similar to those of shot 17012. The timing of high-frequency modes is again consistent with the large voltage spike shown in

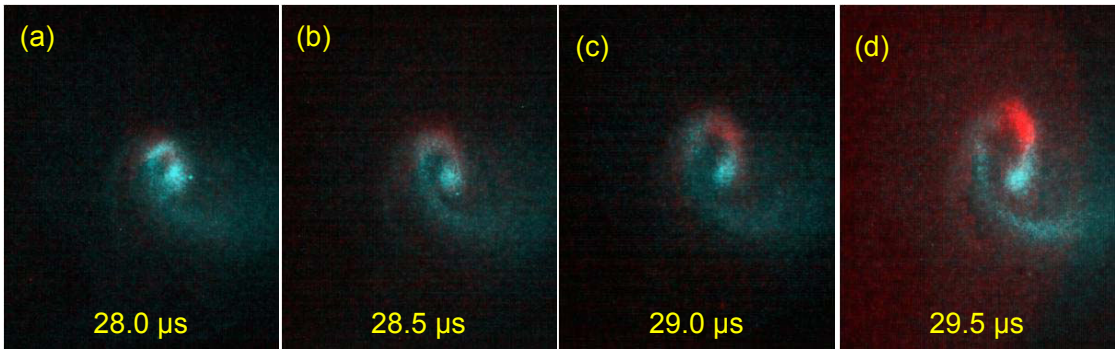

Figure 4.3: Front view of composite images of EUV emission and visible light emission of the kinked argon plasma jet (shot 17012). The EUV emissions are displayed in red and the visible light emissions are depicted in blue. The total power of the EUV burst is estimated to be 50 kW [17]. Figure from Kil-Byoung Chai, personal communication.

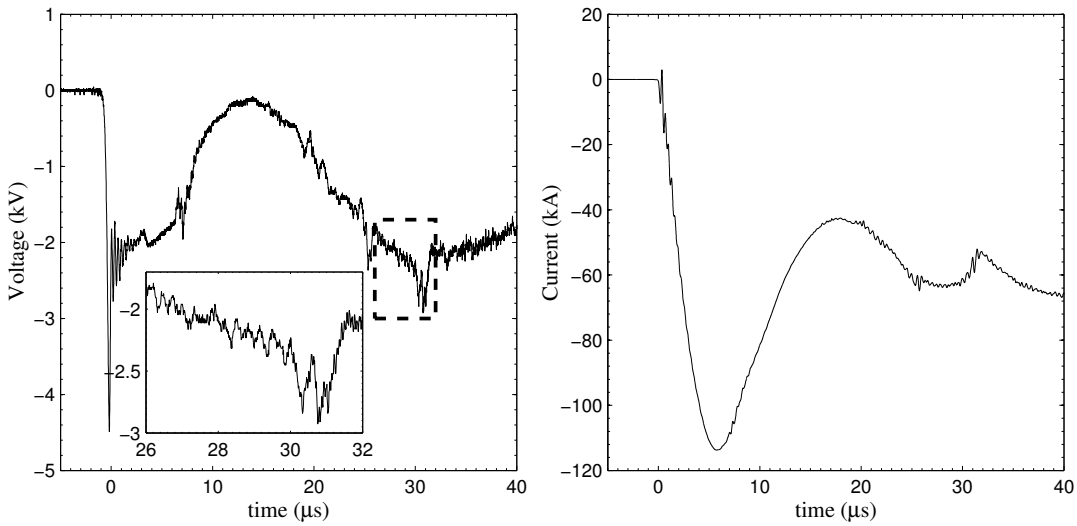

Figure 4.4: IV characteristics of shot 17012. Left: Voltage across the electrodes. Right: Current flowing through the electrodes.

Fig. 4.6.

We have detected high-frequency magnetic fluctuations in the whistler frequency range simultaneously with a Rayleigh-Taylor instability induced magnetic reconnection. This indicates that the whistler wave is associated with the reconnection and that the reconnection is a fast reconnection. The instability occurs at $z \approx 10$ cm, $r \approx 5-10$ cm. Hence the probe is about 15 cm away from the location of the reconnection. We believe that there is no magnetic field line that connects the reconnection point to the probe. Hence the whistler waves generated in the reconnection region need to propagate obliquely to the magnetic field to be picked up by the whistler probe. Assuming an average plasma density $n_e = 10^{21}$ m^{-3} and a magnetic field $B = 0.15$ T, at 10 MHz Eq. 4.23-4.26 give the refractive index $n = ck/\omega \approx 1400$ and $v_g = 2c/n = 430$ km/s. Therefore it only takes 0.35 μs for the whistler waves to travel from the location of magnetic reconnection to the probe.

4.2.2 High-frequency magnetic fluctuations as an ensemble of whistler waves

We have already shown in the third rows of Fig. 4.2 and 4.5 that the high frequency fluctuations have continuous spectra scales as $\dot{B} \propto f^{-1}$. Because $\dot{B} \sim \omega B \sim fB$ and whistler waves have $f \sim k^2$, there are

$$\dot{B} \propto f^{-1} \propto k^{-2} \tag{4.40}$$

$$B \propto f^{-2} \propto k^{-4} \tag{4.41}$$

$$B^2/f \propto f^{-5} \propto k^{-10} \tag{4.42}$$

$$B^2/k \propto f^{-4.5} \propto k^{-9}. \tag{4.43}$$

The magnetic fluctuations measured by the whistler probe have very steep power spectra in comparison to the Alfvénic MHD turbulence observed in the solar wind. The latter ones have $B^2/k \propto k^{-5/3}$ in the inertial range [37]. Chang et al. (2013) [19] performed 3D particle-in-cell simulations and found that in a collisionless magnetized plasma the whistler turbulence, with frequencies much higher than the Alfvén wave, follows power laws between $B^2/k \propto f^{-3}$ and $B^2/k \propto f^{-4}$ for $0.1|\omega_{ce}| < \omega < |\omega_{ce}|$. For $\omega < 0.1|\omega_{ce}|$ the power spectra are much less steep. However, our measurements reveal much steeper power spectra for

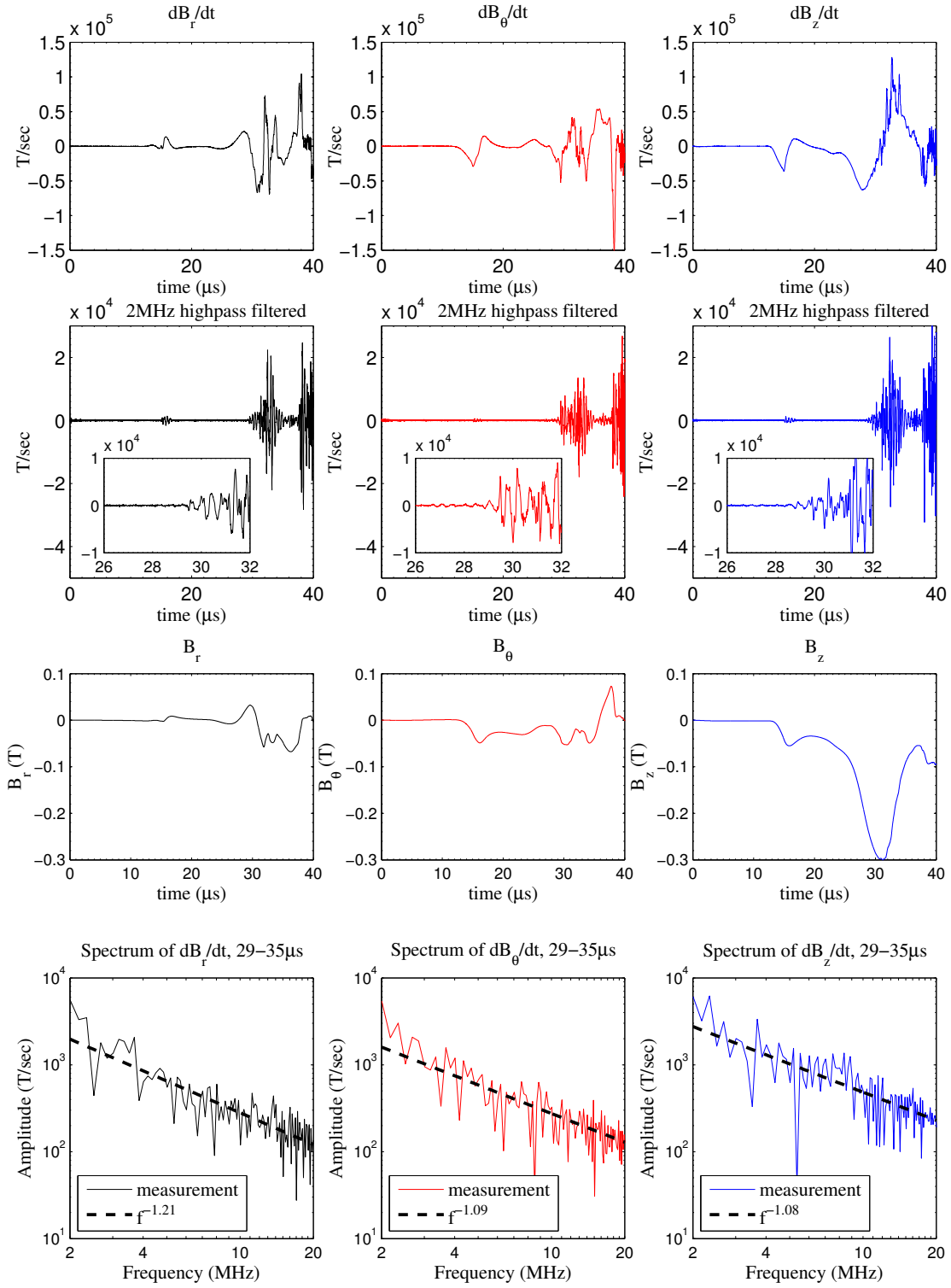

Figure 4.5: 3D magnetic field measurements of shot 16940 from 0 to 40 μs. Location of the probe: $z = 29$ cm, $r = 1$ cm.

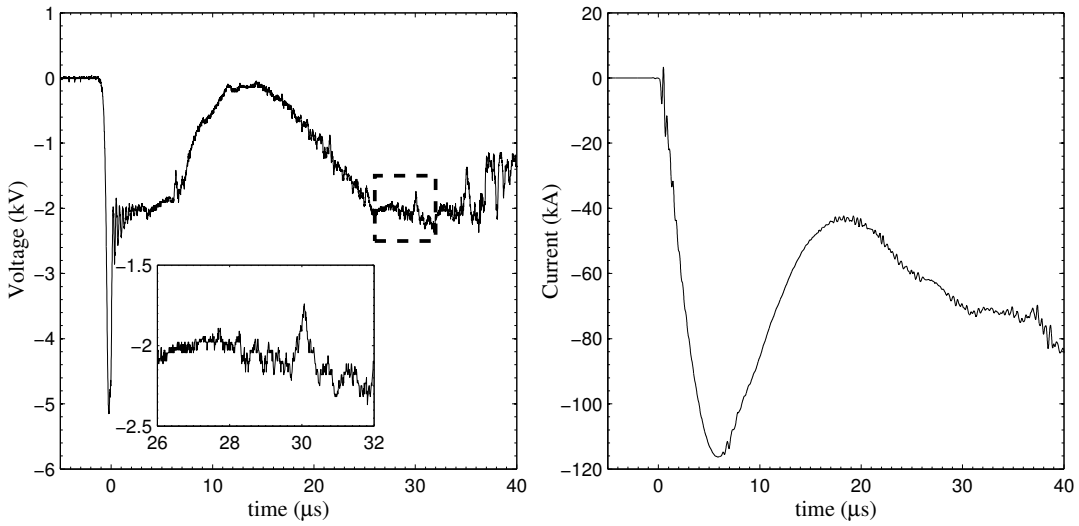

Figure 4.6: IV characteristics of shot 16940. Left: Voltage across the electrodes. Right: Current flowing through the electrodes.

$\omega \ll 0.1|\omega_{ce}|$. The underlying physics of such steep power spectra is not clear. One plausible explanation is that the dissipation of high frequency whistler waves may be more efficient as they travel through the plasma than that of low frequency waves. However the whistler wave is an electromagnetic wave and the particle-wave interaction is normally very weak. Another potential contributing factor is the nature of the in-situ plasma magnetic field measurement. The magnetic probe, enclosed in a quartz tube, is isolated from the plasma. Therefore the magnetic field in the plasma needs to diffuse out of the plasma into the tube to be picked up by the probe. High-frequency modes are more attenuated than the low-frequency modes in the diffusion process. Hence the magnetic power spectra measured by the probe is expected to be steeper than the actual spectra in the plasma.

One major question is whether the magnetic fluctuations detected by the whistler probe are indeed turbulence. Plasma turbulence is a broadband ensemble of incoherent field fluctuations. The stochastic behavior of the detected fluctuations shown in Fig. 4.2 and 4.5 seems to be consistent with the definition. To answer this question, we consider the Fourier transform of the magnetic fluctuations in complex domain. The absolute value of a complex Fourier coefficient gives the amplitude of the corresponding Fourier mode and the argument (complex angle) of the complex Fourier coefficient gives the phase of the corresponding mode. Mathematical details can be found in § B.1. Figure 4.7 and Figure 4.8 present the phases of different modes computed from the Fourier transforms. In shot 16940, where the

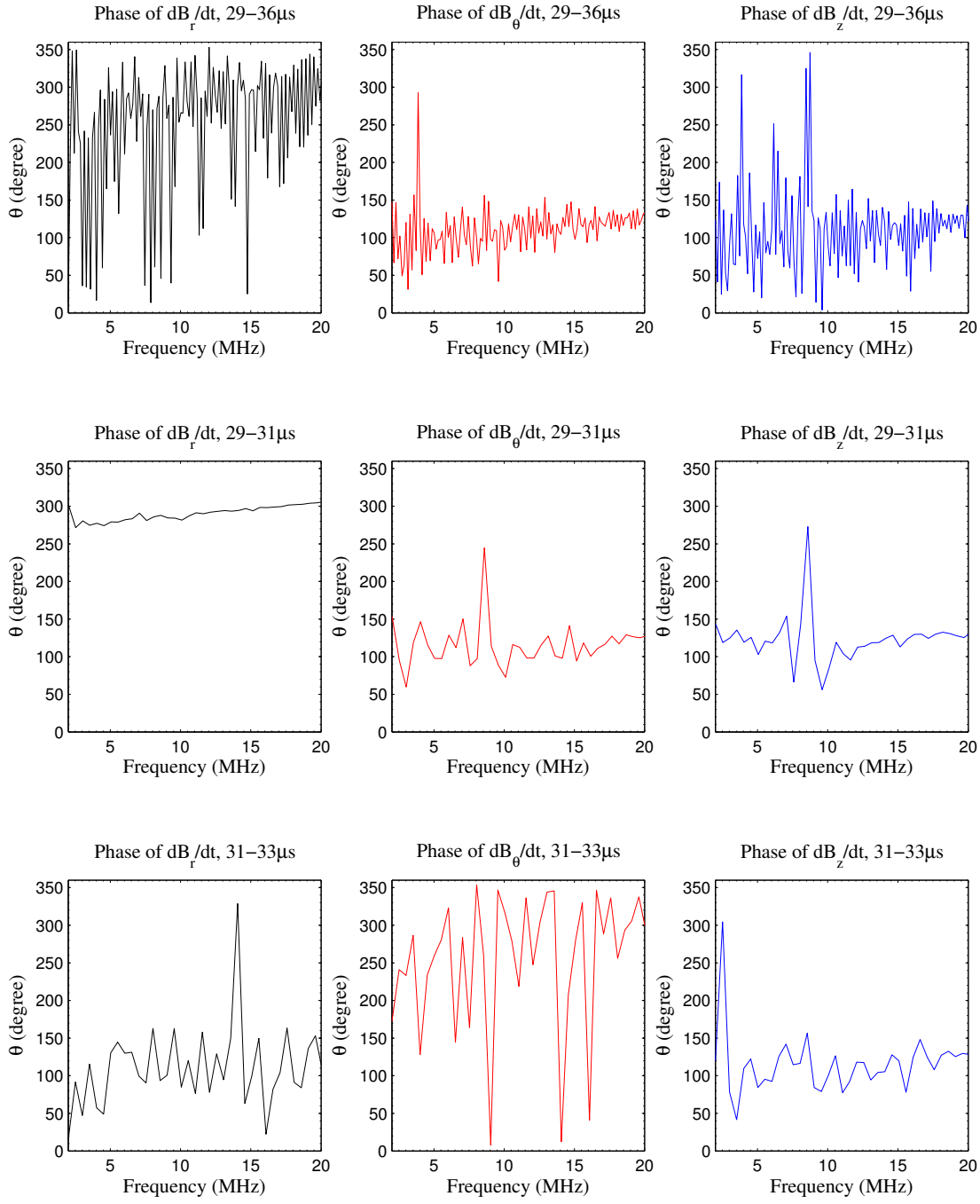

Figure 4.7: Phases of different Fourier modes obtained from the Fourier transform of magnetic fluctuations measurements in different time periods. Shot 16940 (probe at $z = 29$ cm, $r = 1$ cm).

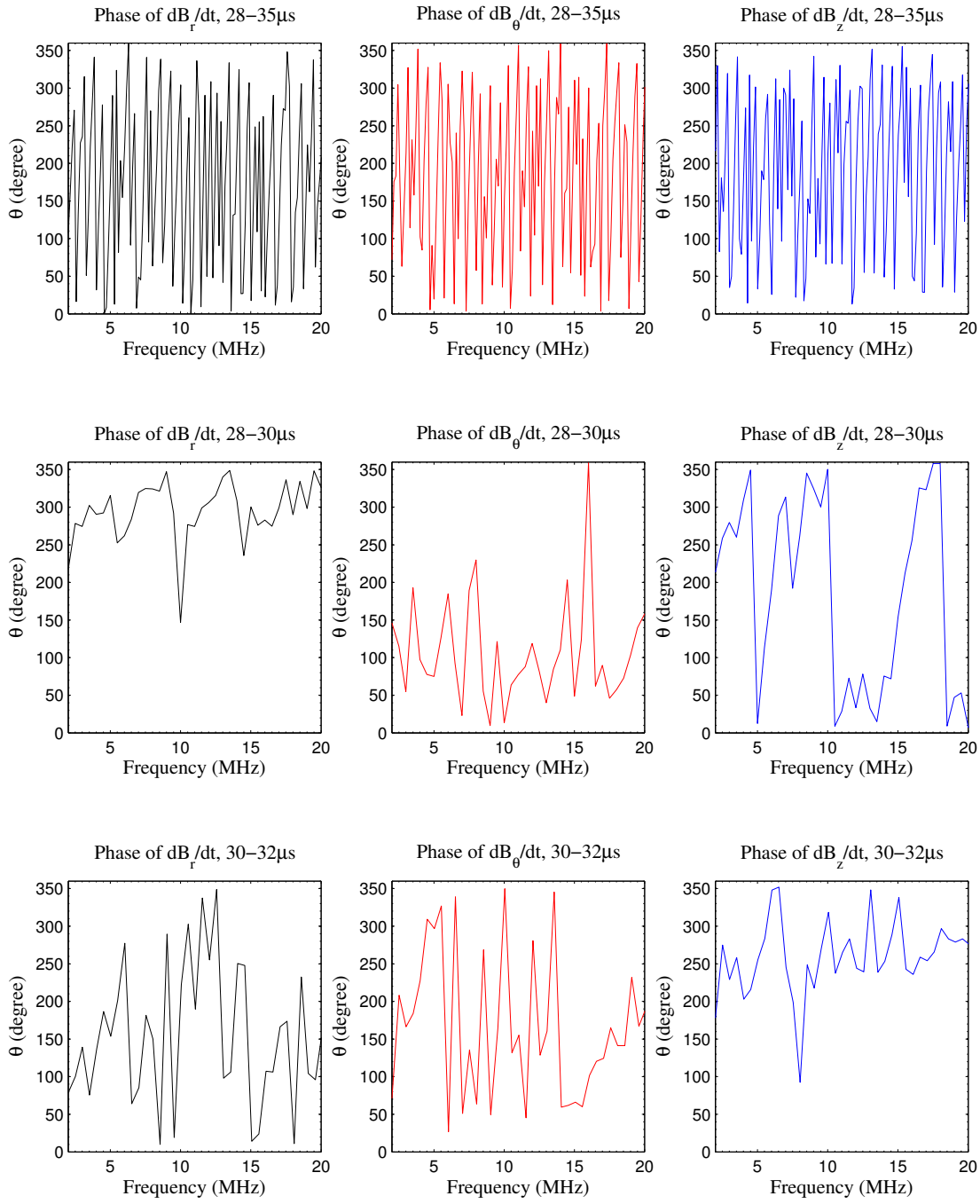

Figure 4.8: Phases of different Fourier modes obtained from Shot 17012 (probe at $z = 29$ cm, $r = 6$ cm).

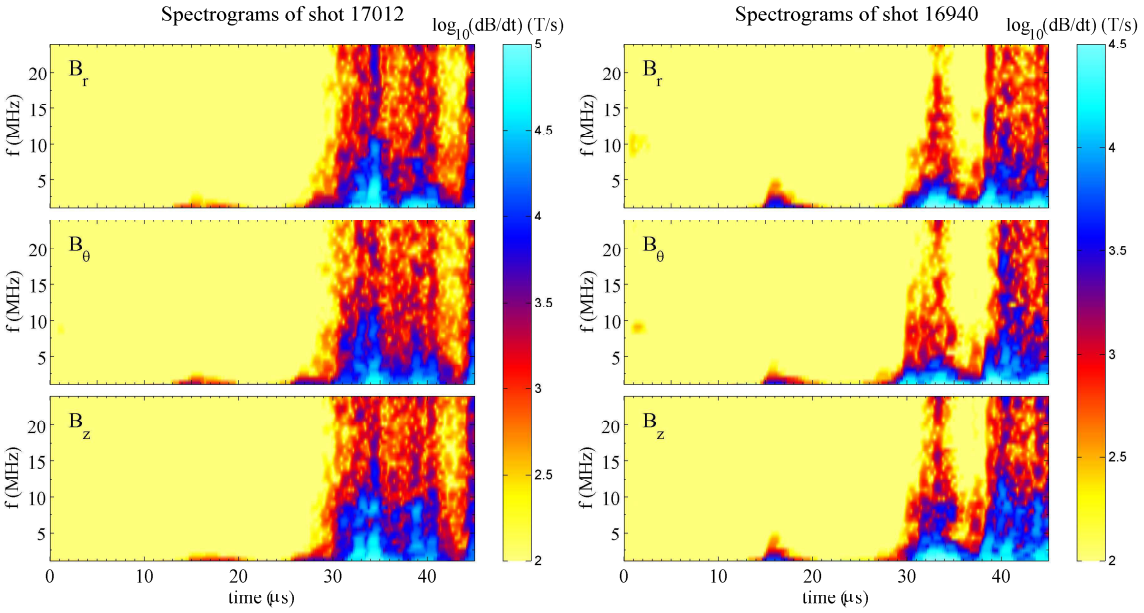

Figure 4.9: Spectrograms of the 3D magnetic fluctuations $\dot{\mathbf{B}}$ measured in shot 17012 (left) and shot 16940 (right) from $t = 0$ to 45 μs and $f = 1$ to 24 MHz. The color in all spectrograms represents the common logarithm of the amplitudes of different modes in the unit of T/sec. The sensitivity of the probe is 10^2 T/sec.

probe is located in the central dense plasma jet, different frequency modes have similar phases in the $29-36$ μs period, indicating that the different modes are coherent[2]. However, in shot 17012, where the probe is located in the low density plasma surrounding the central jet, different modes of the measured magnetic fluctuations are incoherent in the entire $28-35$ μs time period. In a short time window from 28 to 30 μs when the high frequency fluctuations were just detected, Fig. 4.8 shows that the fluctuations are somewhat coherent.

The high frequency magnetic fluctuations measured by the whistler probe are an ensemble of whistler waves of different frequencies. These whistler waves are coherent to some extent, suggesting that they might originate from the same source. The magnetic fluctuations, although with power-law spectra, are not random turbulence.

To study the time variations of the fluctuations spectra, we show the spectrograms of shot 17012 and 16940 in Fig. 4.9. The spectrograms display the fluctuation power in both the time and the frequency domain. Figure 4.9 shows that low-frequency magnetic fluctuations arise around 15 μs due to the motion of the plasma and broadband high-

[2]Note that the phase θ is periodic about 360° so α° is identical to $\alpha^\circ + n \cdot 360^\circ$ with any integer n.

frequency fluctuations arise around 30 μs when the Rayleigh-Taylor instability occurs.

4.2.3 Circularly polarized whistler wave

The whistler wave has a circularly polarized magnetic field component regardless of the angle between the direction of the wave propagation and the background magnetic field. The whistler probe can measure 3D magnetic field and therefore is in principle capable of resolving the polarization property of the fluctuations. However, the fluctuations measured by the probe at a single spatial location are an ensemble of different modes. Therefore we use 4-th order Butterworth finite impulse response (FIR) digital bandpass filters to process the measurements and select single frequency modes. The mathematical details about the FIR digital filter and Butterworth filter are given in § B.2.

Another important issue is the finite extent of the whistler probe, which spans a 6 mm by 10 mm space (see Chapter 5). In an $n_e = 10^{22}$ m^{-3} and $B = 0.3$ T plasma, the wavelength of a 5 MHz whistler wave is $\lambda = 1.4$ cm, not significantly larger than the size of the whistler probe. Therefore when the probe is immersed in the central dense jet the polarization measured by the probe is not very reliable. When the probe is at larger radius, say $r = 6$ cm, the plasma density is much lower but the magnetic field strength is similar (see the third row of Fig. 4.2). With $n_e = 10^{21}$ m^{-3} and $B = 0.2$T a 5 MHz whistler wave has a wavelength $\lambda = 3.6$ cm, much larger than the probe size. Therefore we will only study the polarization properties of the fluctuation measured in the second configuration.

In shot 17012 the probe was placed at $r = 6$ cm and $z = 29$ cm and it was in low density plasma around 30 μs. We apply a $9 - 11$ Mhz bandpass filter to the 3D measurements. The three filtered signals from 29 μs to 30 μs are presented in the left panel of Fig. 4.10 and the corresponding hodogram is shown in the right panel of the figure. The left panel shows that the three components have fixed phase differences during this 1 μs time window. The hodogram, which is the locus of the tip trajectory of the 3D fluctuating magnetic field vector, reveals that the fluctuation is circularly polarized, with an average amplitude of 710 T/sec. At 10 MHz this corresponds to an amplitude of magnetic field $\tilde{B} = 0.1$ gauss. Ten complete periods are observed. The normal vector of the wave is perpendicular to the circularly polarization but with a sign ambiguity. When assuming right-hand circular polarization the direction of the wavevector is determined. Calculation shows that the angle between the wavevector and the background magnetic field is 45.5°, so the whistler wave is

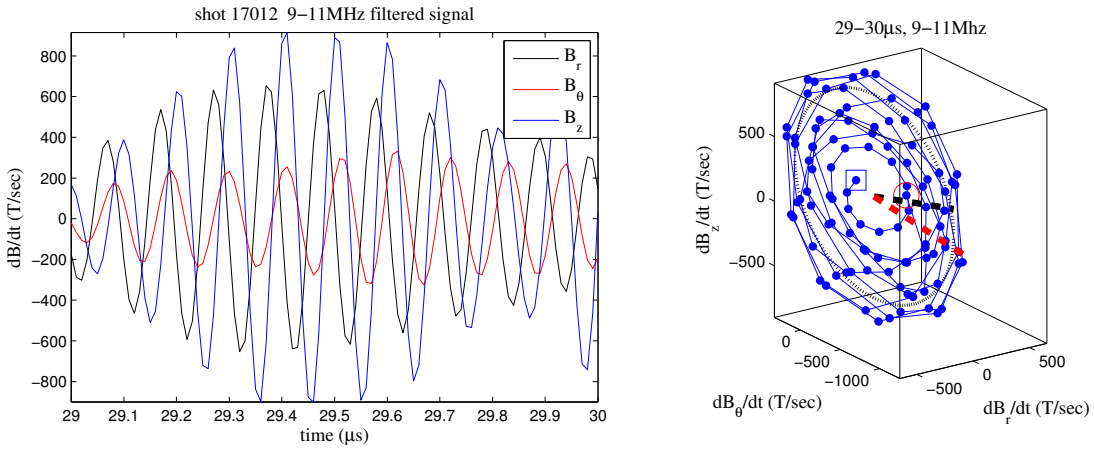

Figure 4.10: Left: 3D magnetic fluctuations $\dot{\mathbf{B}}$ measured in shot 17012 and filtered by a digital Butterworth $9-11$ MHz bandpass filter from 29 to 30 μs. Right: hodogram of the 3D filtered magnetic fluctuations (blue dots connected by the blue spiral curve). The blue square symbols marks the starting point and the red circle symbol is the ending point. The normalized wavevector (thick dashed black vector) is along $(r, \theta, z) = (0.13, 0.96, -0.24)$. The direction of background magnetic field (thick dashed red vector) is along $(r, \theta, z) = (0.35, -0.87, -0.36)$. The major and minor radii of the best fitted ellipse to the hodogram are 870 T/sec and 550 T/sec, respectively.

obliquely propagating.

When processing the hodogram, we use principal component analysis (PCA, see § B.3 for details) to find an optimal 2D plane in the 3D space so that the summation of the projection distances of the measurement points to the 2D plane is minimized. Then we project the measurement points on to the 2D plane and find a best fitted ellipse to the projected points.

Figure 4.11 show two more examples of right-hand circularly polarized magnetic fluctuation measurements at different times and frequencies.

At $B = 0.1$ T, Eq. 4.34 shows that the lower hybrid resonance frequency is $f_{lh} = \sqrt{\omega_{ci}|\omega_{ce}|}/(2\pi) = 10$ MHz, which is in the frequency range of the measured magnetic fluctuations. The detection of the circular polarization and the non-perpendicular angle between the wavevectors and the background magnetic field verify that the waves detected are not the lower hybrid resonance because the lower hybrid resonance is perpendicular to the magnetic field.

The successful identification of the circular polarization confirms that the high-frequency magnetic fluctuations are indeed whistler waves. This further verifies that the associated

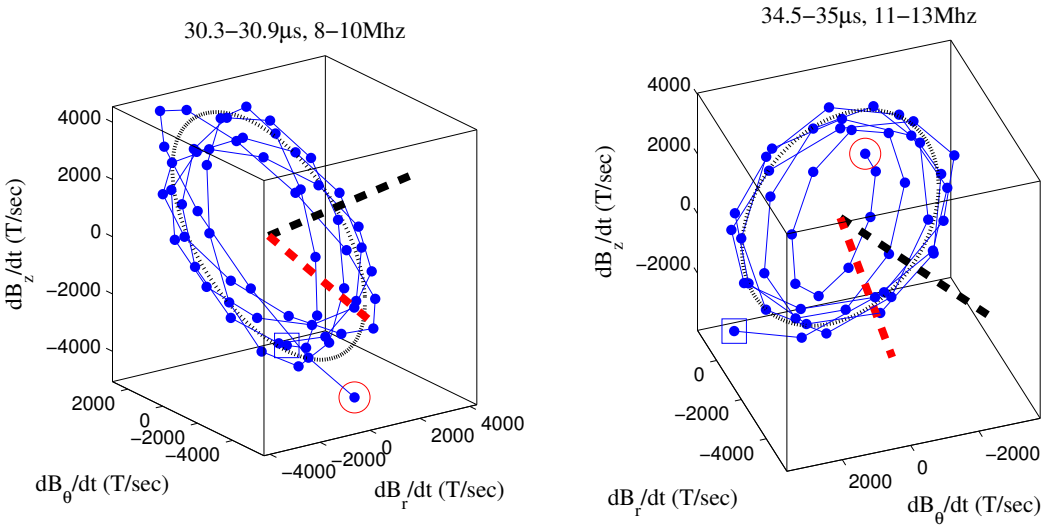

Figure 4.11: Left: hodogram of shot 17012 from 30.3 to 30.9 μs after a $8-10$ bandpass filter. A total of 5 complete periods are recorded. The angle between the direction of the wavevector $(r,\theta,z) = (0.27,-0.82,0.5)$ and the direction of the background magnetic field $(r,\theta,z) = (0.26,-0.87,-0.43)$ is 55.3°. The major and minor radii of the best fitted ellipse to the hodogram are 4710 T/sec and 3500 T/sec, respectively. Right: hodogram of shot 17012 from 34.5 to 35 μs after a $11-13$ MHz bandpass filter. A total of 6 complete periods are recorded. The angle between the direction of the wavevector $(r,\theta,z) = (-0.93,-0.39,-0.04)$ and the direction of the background magnetic field $(r,\theta,z) = (-0.60,-0.15,-0.79)$ is 50.4°. The major and minor radii of the best fitted ellipse to the hodogram are 4100 T/sec and 3240 T/sec, respectively.

magnetic reconnection is fast magnetic reconnection.

4.2.3.1 Polarization recognition algorithm

In this section we describe an automatic polarization recognition algorithm that can directly identify the existence of circular polarization in the time-frequency domain.

Consider a general single frequency signal in 3D

$$\mathbf{B}(t) = \hat{\xi} B_0 \cos\omega t + \hat{\eta} B_1 \sin\omega t, \tag{4.44}$$

where $\hat{\xi}$ and $\hat{\eta}$ are two unit vectors in 3D space and are perpendicular to each other. With $B_0 = 0$ or $B_1 = 0$, the equation can describe a linear polarized wave. With non-zero B_0 and B_1, the equation describes an elliptically polarized wave. With $B_0 = B_1 \neq 0$, the equation describes a circularly polarized wave.

The time derivative of $\mathbf{B}$ is

$$\dot{\mathbf{B}} = -\omega\hat{\xi} B_0 \sin\omega t + \omega\hat{\eta} B_1 \cos\omega t. \tag{4.45}$$

The cross product and inner product of $\mathbf{B}$ and $\dot{\mathbf{B}}$ are

$$\mathbf{B} \times \dot{\mathbf{B}} = \omega(\hat{\xi} \times \hat{\eta}) B_0 B_1, \tag{4.46}$$

$$\mathbf{B} \cdot \dot{\mathbf{B}} = \omega(B_1^2 - B_0^2)\sin\omega t \cos\omega t = (\omega/2)(B_1^2 - B_0^2)\sin 2\omega t. \tag{4.47}$$

The time average of $|\mathbf{B} \cdot \dot{\mathbf{B}}|$ within any π/ω period is

$$< |\mathbf{B} \cdot \dot{\mathbf{B}}| >_{\pi/\omega} = (\omega/2)|B_0^2 - B_1^2| \frac{\int_0^{\pi/4} \cos\theta d\theta}{\pi/4} = (2\omega/\pi)|B_0^2 - B_1^2|, \tag{4.48}$$

For linearly polarized signal, $B_0 = 0$ or $B_1 = 0$. Without loss of generality, assume $B_1 = 0$ and $B_0 \neq 0$. There are

$$\mathbf{B} \times \dot{\mathbf{B}} = 0 \qquad < |\mathbf{B} \cdot \dot{\mathbf{B}}| >_{\pi/\omega} = (2\omega/\pi) B_0^2. \tag{4.49}$$

For circularly polarized signal, $B_0 = B_1$. There are

$$\mathbf{B} \times \dot{\mathbf{B}} = \omega \hat{k} B_0^2 \qquad < |\mathbf{B} \cdot \dot{\mathbf{B}}| >_{\pi/\omega} = 0, \tag{4.50}$$

where $\hat{k} \equiv \hat{\xi} \times \hat{\eta}$ is the unit wavevector perpendicular to both $\hat{\xi}$ and $\hat{\eta}$.

Therefore $|\mathbf{B} \times \dot{\mathbf{B}}|$ is proportional to the amplitude of the circularly polarized component of a 3D signal and $< |\mathbf{B} \cdot \dot{\mathbf{B}}| >_{\pi/\omega}$ is proportional to the amplitude of the linearly polarized component of the signal. In general cases, we define the polarization factor $\alpha \equiv B_1/B_0$. Without loss of generality, we assume $|B_1| < |B_0|$ so $|\alpha| < 1$. There are

$$\frac{|\mathbf{B} \times \dot{\mathbf{B}}|}{< |\mathbf{B} \cdot \dot{\mathbf{B}}| >_{\pi/\omega}} = \frac{\pi}{2} \frac{\alpha}{1 - \alpha^2} \tag{4.51}$$

and

$$\alpha = -\frac{1}{2\beta} + \sqrt{1 + \frac{1}{4\beta^2}}, \quad \beta = \frac{2|\mathbf{B} \times \dot{\mathbf{B}}|}{\pi < |\mathbf{B} \cdot \dot{\mathbf{B}}| >_{\pi/\omega}}. \tag{4.52}$$

α is essentially the ellipticity of the polarization. Note that Eq. 4.52 guarantees $0 \leq \alpha \leq 1$. $\alpha = 1$ (or $\beta \to +\infty$) means perfectly circular polarization and $\alpha = 0$ (or $\beta \to 0$) means linear polarization.

α is a function of time and frequency. Therefore to identify circular polarization we simply need to compute α in a given time-frequency domain and look for α close to unity. The merit of this polarization recognition algorithm is that it is coordinate invariant because only cross product and inner product of 3D vectors are involved.

The direct output of the whistler probe is $\dot{\mathbf{B}}(t)$. After integration with time we obtain $\mathbf{B}(t)$. We also need to use digital bandpass filter to select single-frequency modes in order to compute $|\mathbf{B}(t,f) \times \dot{\mathbf{B}}(t,f)|$ and $|\mathbf{B}(t,f) \cdot \dot{\mathbf{B}}(t,f)|$.

We compute $\alpha(t,f)$ for shot 16940, 17012 and 17014. In shot 17014 the probe was placed at the same location as shot 17012. Figure 4.12 shows the calculation results for valid measurements (i.e., $|\dot{B}(t,f)|$ is larger than the sensitivity of the probe). It is seen that the distribution of $\alpha(t,f)$ of shot 16940 is different from 17012 or 17014, especially in the $7 - 11$ MHz range. In shot 17012 and 17014, $\alpha(t,f) \geq 0.7$ is valid at most times and frequencies, indicating that circularly polarized magnetic fluctuations are ubiquitous in these two shots.

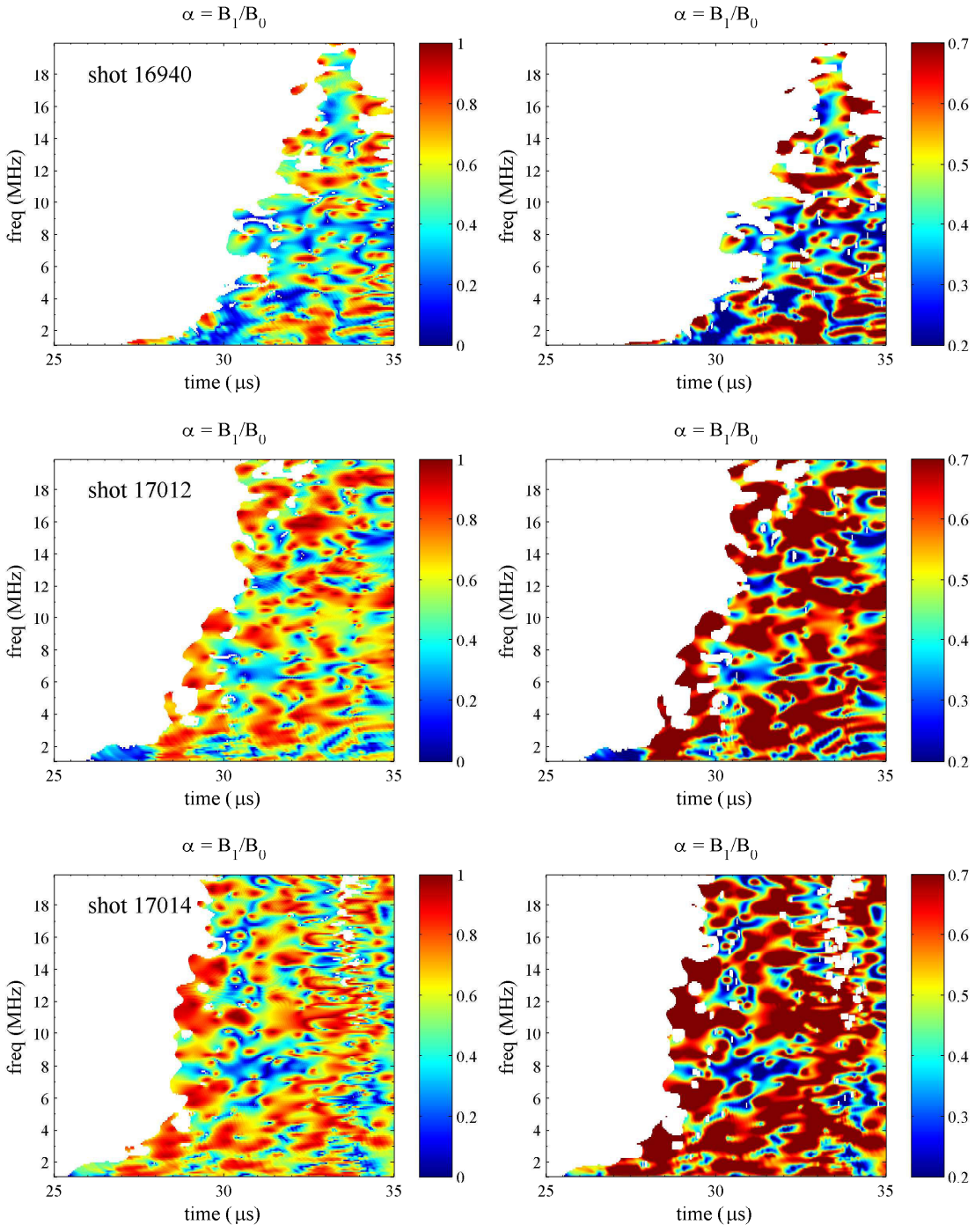

Figure 4.12: Polarization factor α in time-frequency domains for shot 16940 (top row), 17012 (middle row) and 17014 (bottom row). In each row the two colormap plots are the same except the color indexing range. We only computed $\alpha(t, f)$ for $\dot{B}(t, f) > 300$ T/sec, i.e., at least three times as large as the probe sensitivity.

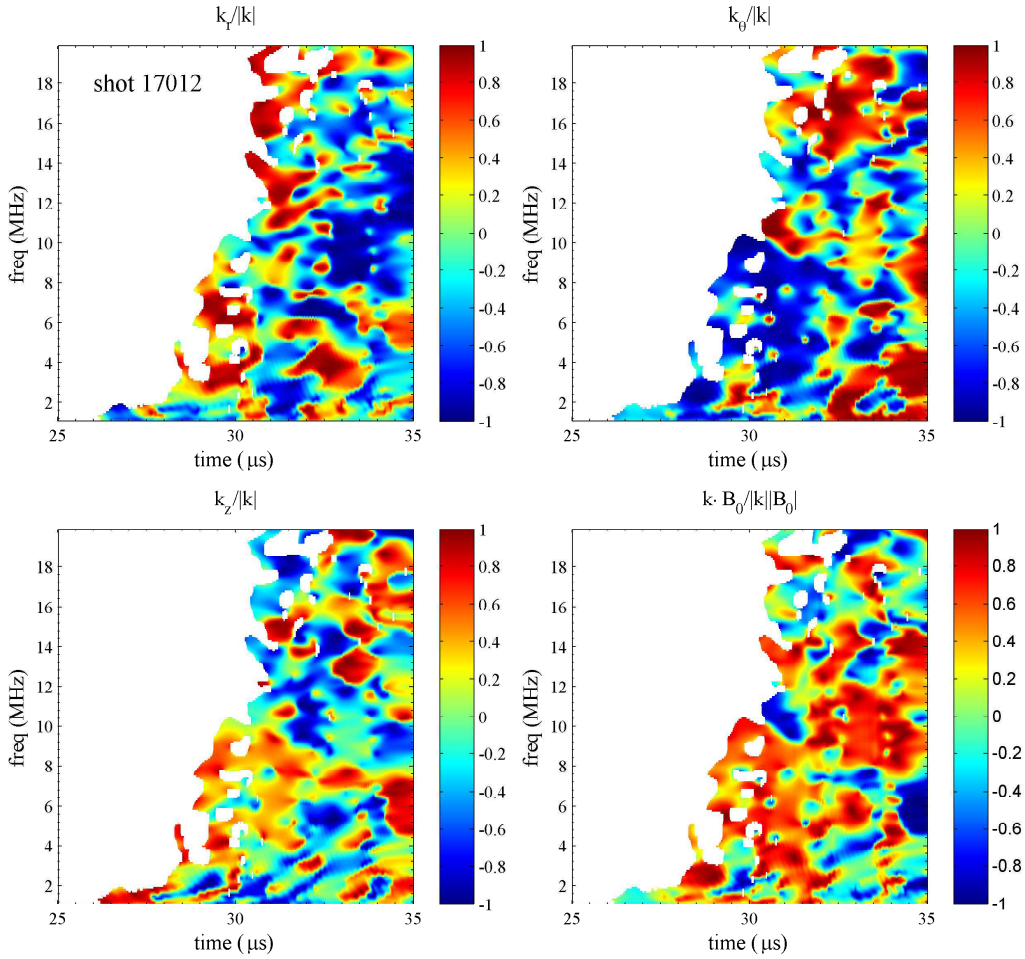

Figure 4.13: Top left, top right, bottom left panels: Three components of the normalized wavevector $\hat{k}$ of shot 17012 computed by Eq. 4.53 in the time-frequency domain. Bottom right panel: inner product of $\hat{k}$ and the direction of the background magnetic field $\hat{B}_0$. Only the valid measurements are used (i.e., $\dot{B}(t, f)$ at least three times larger than the probe sensitivity).

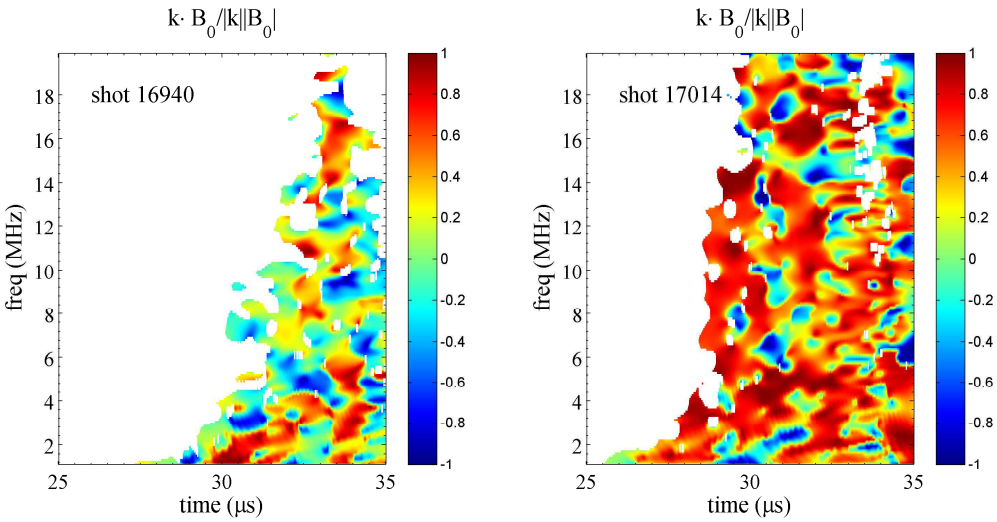

Figure 4.14: Inner product of the normalized wavevector $\hat{k}$ and the direction of the background magnetic field $\hat{B}_0$ of shot 17014 and 16940.

Equation 4.46 shows that the wavevector direction $\hat{k} \equiv \hat{\xi} \times \hat{\eta}$ can be given by

$$\hat{k} = \frac{\mathbf{B} \times \dot{\mathbf{B}}}{|\mathbf{B} \times \dot{\mathbf{B}}|}. \tag{4.53}$$

Note that Eq. 4.53 has assumed that $\mathbf{B}$ is right-hand polarized because the phase of $\dot{\mathbf{B}}$ is behind $\mathbf{B}$ by $\pi/2$ for right-hand polarized wave. Figure 4.13 shows the three components of the normalized wavevector $\hat{k} \cdot \hat{r}$, $\hat{k} \cdot \hat{\theta}$, and $\hat{k} \cdot \hat{z}$, and the inner product of $\hat{k}$ and $\hat{B}_0$ computed using Eq. 4.53. Here $\hat{B}_0$ is the direction of the background magnetic field. It is seen that most waves propagate with angles smaller than 60° (i.e., $\hat{k} \cdot \hat{B}_0 > 0.5$). Figure 4.14 gives the calculation results for shot 16940 and 17014. Measurements of shot 17014 also reveals $\hat{k} \cdot \hat{B}_0 > 0.5$ at most times and frequencies similar to shot 17012 because the two measurements are performed in the same configuration (probe at $r = 6$ cm). However, when the probe is immersed in the central dense plasma jet, shot 16940 gives a much more randomly distributed $\hat{k} \cdot \hat{B}_0$. This is because the wavelengths of the whistler waves in the central dense jet is not significantly larger than the size of the whistler probe. Hence the wave polarization inferred from shot 16940 is not very reliable.

4.3 Summary

We detected 3D high-frequency magnetic fluctuations consisting of broadband whistler waves associated with the fast magnetic reconnection in the plasma jet experiment. The 3D magnetic fluctuations have $\dot{B} \sim f^{-1}$ power-law spectra. However, detailed analysis shows that the single-frequency modes of the fluctuations are somewhat coherent especially within short time periods, suggesting that these modes may originate from a single source and the fluctuations are not random turbulence. We successfully resolve the circularly polarization of the whistler wave for obliquely propagating whistler wave. This is consistent with theoretical modes and space observations.

The detection and recognition of high-frequency whistler waves associated with the magnetic reconnection provide strong evidence that the reconnection is a fast magnetic reconnection and the dynamics is described by two-fluid theory, not MHD theory.

Chapter 5

A High-Speed 3D Magnetic Probe with Excellent Capacitive Rejection and Noise Shielding

Magnetic field is a fundamental component of current-carrying plasma and therefore magnetic diagnostics are important for magnetized plasma experiments. In-situ measurement of magnetic field uses probes such as Hall effect sensor and B-dot probe; remote detections include Zeeman splitting spectroscopic measurement and Faraday rotation measurement. The Hall effect sensor or Hall probe utilizes Hall effect to directly measure the local magnetic field perpendicular to the probe. Typically the Hall probe is used for DC or low frequency ($<$ 50 KHz) situations. B-dot probe, essentially a coil of wire, outputs voltage signal that is proportional to the flux changing rate through the coil according to Faraday's Law. B-dot probe in principle has high sensitivity at high frequency, but its output has to be integrated to obtain real magnetic field measurement. B-dot probe is more commonly seen in transient plasma experiments due to its fast time response and simple geometry [79, 95]. Remote measurements of Zeeman splitting effect or Faraday rotation have the benefit of not perturbing the plasma dynamics but require high-speed spectroscopic equipment with very fine wavelength resolution [102] or sensitive polarization detection capability.

In this chapter we present a high-speed three-dimensional (3D) magnetic probe designed to measure the magnetic component of whistler waves generated in the Caltech plasma jet experiment (Chapter 4). The frequency of the whistler wave is between the ion cyclotron frequency and the electron cyclotron frequency, which are respectively $f_{ci} \approx 60$ KHz and $f_{ce} \approx 4$ GHz in a $B = 0.15$ T magnetized argon plasma. The VME data acquisition device used in the lab has a sampling rate of 100 MHz and so is capable of measuring oscillations

up to ~ 20 MHz. The velocity of the argon plasma jet is about 10 km/s, hence the magnetic field variation due to the motion of the plasma across a 1 cm size probe has a characteristic time scale of a microsecond. With all the factors considered, the magnetic probe needs to have a good frequency response from 1 MHz to at least 20 MHz. This makes B-dot probes the only option because other types of magnetic diagnostics are too slow.

In this chapter, we will first review some basic theories about B-dot probes and an RF ground loop current diverting technique, and then show the 3D magnetic probe made out of three pairs of differential B-dot coils and finally presents measurement results.

5.1 Theories of B-dot probe

The B-dot probe is simply a small coil of wire. The probe outputs voltage (electromotive force) that is proportional to the changing rate of magnetic flux through the coil, i.e.,

$$V_{emf} = \frac{d}{dt}\int \mathbf{B}_\perp \cdot d\mathbf{S} \approx NA\frac{dB_\perp}{dt}, \tag{5.1}$$

where N is number of turns of the coil and A is the cross-section area. The subscript $_\perp$ means that the probe is only sensitive to the magnetic component perpendicular to the coil cross-section. In the following content we will assume $\mathbf{B} = \mathbf{B}_\perp$ and omit the $_\perp$ notation. If the magnetic field oscillates as $e^{i\omega t}$ then the emf voltage is

$$V_{emf} = NA\dot{B} = i\omega NAB. \tag{5.2}$$

The emf voltage applied on a finite load results in an electric current. This current, when flowing through the B-dot coil, generates a secondary magnetic field. Lenz's Law shows that this secondary magnetic field is orientated in the opposite direction of the background magnetic field, and therefore reduces the output of the coil.

An equivalent circuit of the B-dot probe is shown in Fig. 5.1. The load of the data acquisition device is $R_L = 50\ \Omega$. The output voltage of the probe is $V_p = IR_L$ where I is the current. The total impedance of the circuit is $Z = i\omega L_p + R_L$, where L_p is the

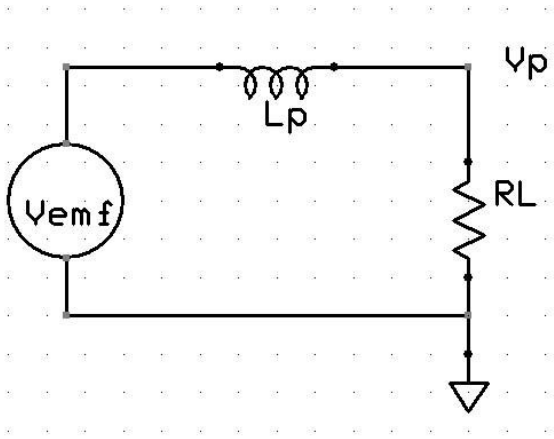

Figure 5.1: A simple equivalent circuit diagram of B-dot probe.

inductance of the B-dot probe. Hence $I = V_{emf}/Z$ and

$$\begin{aligned} V_p &= \frac{R_L}{i\omega L_p + R_L} V_{emf} = \frac{NA\dot{B}}{1 + i\omega L_p/R_L} \\ &= \frac{NA\dot{B}}{1 + \omega^2 L_p^2/R_L^2}(1 - i\omega L_p/R_L). \end{aligned} \tag{5.3}$$

Write V_p in polar form $V_p = |V_p|e^{i\Delta}$ and get

$$|V_p| = \frac{NA|\dot{B}|}{\sqrt{1 + (\omega L_p/R_L)^2}} = \frac{\omega NAB}{\sqrt{1 + (\omega L_p/R_L)^2}} \tag{5.4}$$

$$\tan\Delta = \frac{\mathrm{Im}[V_p]}{\mathrm{Re}[V_p]} = -\frac{\omega L_p}{R_L} \tag{5.5}$$

$$\text{Phase delay } -\Delta = \arctan\frac{\omega L_p}{R_L}. \tag{5.6}$$

The output of the probe has a delayed phase $|\Delta|$ compared to dB/dt. Compared the above equations with the expression of V_{emf} it is seen that the attenuation factor is

$$\text{atten} = \frac{1}{\sqrt{1 + (\omega L_p/R_L)^2}}. \tag{5.7}$$

Hence finite self-inductance of a B-dot coil attenuates the probe sensitivity, especially at high frequency. If we require no larger than 3 dB attenuation, then $\omega L_p/R_L \leq 1$ and

$$L_p \leq 0.8\mu\mathrm{H} \cdot \frac{10\mathrm{MHz}}{\omega/2\pi} \qquad f = \frac{\omega}{2\pi} \leq 8\mathrm{MHz} \cdot \frac{1\mu\mathrm{H}}{L_p}. \tag{5.8}$$

The first relation can be understood as the requirement for L_p given the frequency of interest; the second inequality gives the upper limit of the frequency the B-dot probe is sensitive to.

If the B-dot probe has N number of turns and the cross-section is a circle, the inductance of the coil can be calculated by

$$L_p = N^2 L_0 \quad , \quad L_0 = \mu_0 r \left(\ln \frac{8r}{a} - 2 + \frac{Y}{2} \right), \tag{5.9}$$

where r is the loop radius and a is the wire radius; $Y = 0$ if the current is uniformly distributed on the wire surface (skin effect) and $Y = 1/2$ if current is uniformly distributed over the cross-section of the coil wire; L_0 is the self inductance of a single turn circular coil. At $f = 10$ MHz, the skin depth of copper is 21 μm, which is much thinner than the wire we will use. Diffusion theory shows that in this case the electric current is primarily distributed on the surface of the wire, so $Y = 0$.

The probe sensitivity of a B-dot probe, defined as the ratio of output voltage to amplitude of magnetic fluctuation, is a function of number of turns, i.e.,

$$s \equiv \left| \frac{V_p}{\omega B} \right| = \frac{AN}{\sqrt{1 + (\omega L_0 / R_L)^2 N^4}} \quad \Rightarrow \quad s^2 = A^2 \frac{N^2}{1 + (\omega L_0 / R_L)^2 N^4}. \tag{5.10}$$

Maximizing s^2 by varying N^2, it is easily seen that the optimal number of turns

$$N_{best}(\omega) = \sqrt{\frac{R_L}{\omega L_0}} \tag{5.11}$$

gives the maximal sensitivity. The phase delay of N_{best} is $\Delta = \arctan 1 = 45°$.

Figure 5.2 shows the sensitivity $V_p/\omega B$ of a test B-dot probe as a function of frequency. The test probe is a $r = 1.4$ mm radius 7 turns coil made by AWG35 magnetic wire ($a = 0.14$ mm). The inductance of the probe is 0.21 μH according to Eq. 5.9, and is measured to be $L = 0.26$ μH by a RLC meter. The total cross-section area is $NA = 4.31 \times 10^{-5}$ m^2. Figure 5.2 shows that the test results are well explained by the B-dot probe theory.

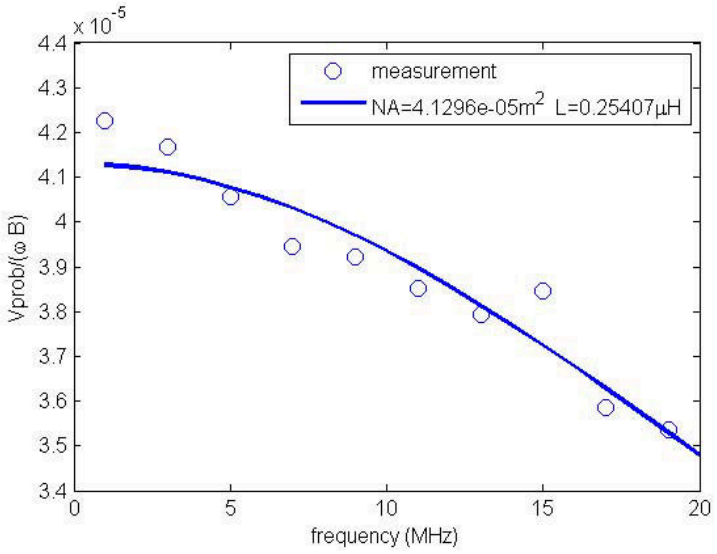

Figure 5.2: Sensitivity $V_{probe}/(\omega B)$ as a function of frequency of a test B-dot probe ($N = 7$, $r = 1.4$ mm, $a = 0.14$ mm). The experiment measurements are represented by the open-circle symbols, and the solid curve is the best fit to the measurement using Eq. 5.10 with fitted values $NA = 4.13 \times 10^{-5}$ m^2 and $L = 0.254$ μH. The best fit is obtained by performing a least-square regression of $y = a + bx$ where $y = (\omega B/V_{probe})^2$, $x = (\omega^2/R_L)^2$. The best fitted coefficients give $NA = 1/\sqrt{a}$ and $L = \sqrt{b/a}$.

5.2 Capacitive coupling and RF ground loop

Capacitive coupling can exist between any two conductive materials. For example, any probe that does not directly contact with a plasma is susceptible to capacitive coupling with the plasma. See Fig. 5.3 for a sketch of this unwanted coupling. Extra attention is required in high-speed applications because the capacitive coupling has low impedance at high frequency. This issue is extraordinarily important in the Caltech plasma jet experiment because the plasma is created via high voltage capacitive discharge.

Figure 5.3 (upper panel) illustrates the capacitive coupling between a plasma and a probe. The impedance of a capacitor C at frequency ω is

$$Z = \frac{1}{iC\omega} = \frac{1}{2\pi iCf} \qquad |Z| = 16 \text{ k}\Omega \cdot \frac{1 \text{ pF}}{C} \cdot \frac{10 \text{ MHz}}{f}. \tag{5.12}$$

With the nominal values in the above equation, even a 10 V electrostatic fluctuation at $f = 10$ MHz can introduce a current 0.625 mA through the probe, which further gives a notable 31.25 mV signal across a 50 Ω load.

Capacitive coupling at high frequency can also introduce radio frequency (RF) ground

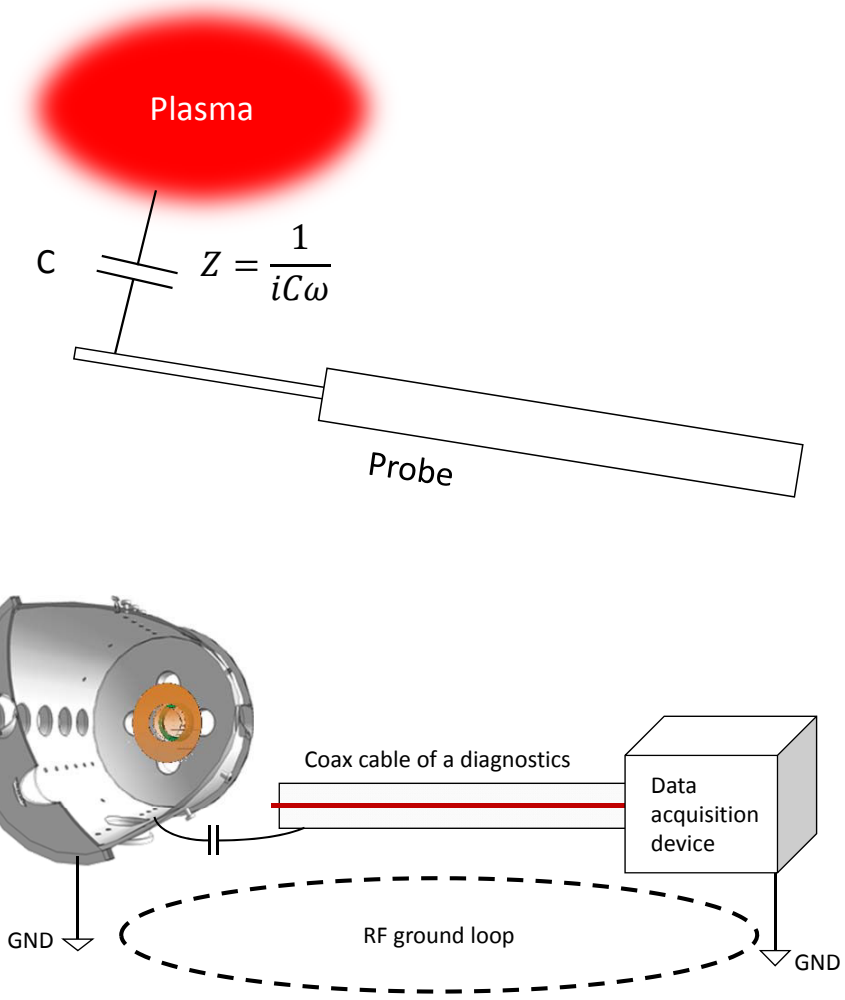

Figure 5.3: Top panel: sketch of a capacitive coupling between a probe and a plasma. Bottom panel: sketch of a RF ground loop caused by a capacitive coupling between the grounded chamber wall and outer conductor of a coax cable of a diagnostics instrument. The coax cable is connected to a data acquisition device which is also grounded.

loop. Ground loop is an unwanted electric closed loop that has two grounded points at different locations. In RF and pulsed power applications the alternating current can generate fast varying magnetic field through the ground loop and induce a large electromotive force. An RF ground loop can form even if the two grounded points are not directly connected, but are coupled via some capacitive coupling [89]. The bottom panel of Fig. 5.3 illustrates an RF ground loop. In the system shown in the figure, the vacuum chamber and the data acquisition device are grounded individually. However, if the chamber is capacitively coupled with the outer conductor of a coaxial cable that connects a diagnostic instrument to the data acquisition device, an effective ground loop that can conduct high

frequency current is formed. This RF ground loop has a large cross-section area and hence has finite inductance. Therefore this RF ground loop is a LC circuit that can cause large electromagnetic resonance at certain frequencies. An RF ground loop can also be formed through the plasma if the outer conductor of the coaxial cable is capacitive coupled with the plasma.

An electrostatic probe built by A. L. Moser is able to pick up $\sim$ 1V signal across a $R_L = 50\ \Omega$ load in the range of $5 - 15$ MHz at 8 μs and after 28 μ [80]. This corresponds to a current $I \sim 0.02$ A. If this current is caused solely by capacitive coupling between the probe and the plasma, then the electrostatic potential of the plasma should be $I/(C\omega) \approx 300$ V, assuming $C = 1$ pF. This is comparable to the electrostatic potential across the entire plasma, which is $1 \sim 2$ kV, but at a much lower frequency $f \sim 100$ kHz. A possible explanation to this anomalous large current is that the probe indeed picked up a wide-band capacitive coupling signal, but some frequencies were amplified by the large RF ground loop.

5.3 Design of 3D high-speed magnetic probe

Our goal is to build a compact magnetic probe that can measure 3D magnetic fluctuation with good frequency response in the $1 - 20$ MHz range, and have sufficient rejection to capacitive coupling signal and RF ground loop.

In order to provide sufficient electrostatic shielding to the magnetic probe, it is necessary to protect the probe with some grounded metal shield. To the author's knowledge there are primarily two methods to implement such a shielding, as listed below.

One method is to shield the entire probe by a grounded thin conductive surface. For example, Greene (1984) [39] built a compact 3D magnetic probe with small hand-wired B-dot coils using magnetic wire. The entire probe is covered by a high temperature epoxy and then a thin layer of conductive silver epoxy (Emerson & Cuming Eccobond 66C). The conductive layer is grounded and hence breaks possible capacitive coupling between the probe and the plasma. One advantage of this method is that the entire probe can be made very compact by using small diameter magnetic wire. However, the complete coverage of conductive layer (silver epoxy) can conduct loop current. When the probe is immersed in a time-dependent magnetic field, eddy currents can be induced on the silver layer, which

generates magnetic field in the opposite direction of the background magnetic field and hence attenuates the sensitivity of the probe. In an extreme case where the conductive layer is super-conducting, no magnetic field is able to diffuse through the layer. Therefore the conductive layer needs to be sufficiently thin in order to allow magnetic field to diffuse through. Detailed calculation shows that the layer should be much less than δ^2/a to have insignificant attenuation of the probe sensitivity, where a is the radius of the cross-section of the probe, and δ is the skin depth of the material of the layer. At 10 MHz, the skin depth of silver is 0.02 mm. If the radius of the probe is $a = 2$ mm, then the thickness of the silver layer d should be much less than 200 nm. Using the resistivity of silver $\rho = 1.59 \times 10^{-8}$ Ω·m, the resistance of the silver layer is

$$R = \frac{\rho l}{2\pi a d} = 3\ \Omega \cdot \frac{l}{5\ \text{cm}} \cdot \frac{20\ \text{nm}}{d}, \tag{5.13}$$

where l is the length of the conductive layer. The author built a probe similar to Greene (1984) [39] and used MG Chemical 843 Super Shield Silver Coated Copper Conductive Coating lacquer to protect the probe. The effective thickness of silver/copper of a single layer lacquer painting was tested to be 10 nm, which gives a $\approx 6\ \Omega$ resistance between the conductive layer and ground. It was found that this resistance is too big to give sufficient electrostatic shield to the probe in the Caltech jet experiment.

Another method is to construct the B-dot probe using semi-rigid coaxial cable because the center conductor of the cable is well protected by the outer jacket. A gap must be made on the outer conductor of the coaxial cable to prevent a closed loop otherwise a loop of eddy current can be induced on the outer conductor to attenuate the probe sensitivity [16, 104]. Figure 5.4 shows a sketch of a shielded loop probe constructed by a semi-rigid coaxial cable. The effective circuit of the probe is simply a single turn loop. This design minimizes the exposed area of the central conductor that can capacitively couple with the plasma. Unlike the first design where the entire probe is fully enclosed inside a conductive layer, the shielded loop probe is not completely covered by the shield (outer conductor) and so the sensitivity of the probe is not attenuated. The major disadvantage of the loop probe is that it is usually difficult to make the probe compact, because of the requirement of coaxial cable.

We choose the second method and use a 0.047 inch diameter semi-rigid coaxial cable to construct the shielded loop probes. The semi-rigid coaxial cable (part no. SR-047ST-TC,

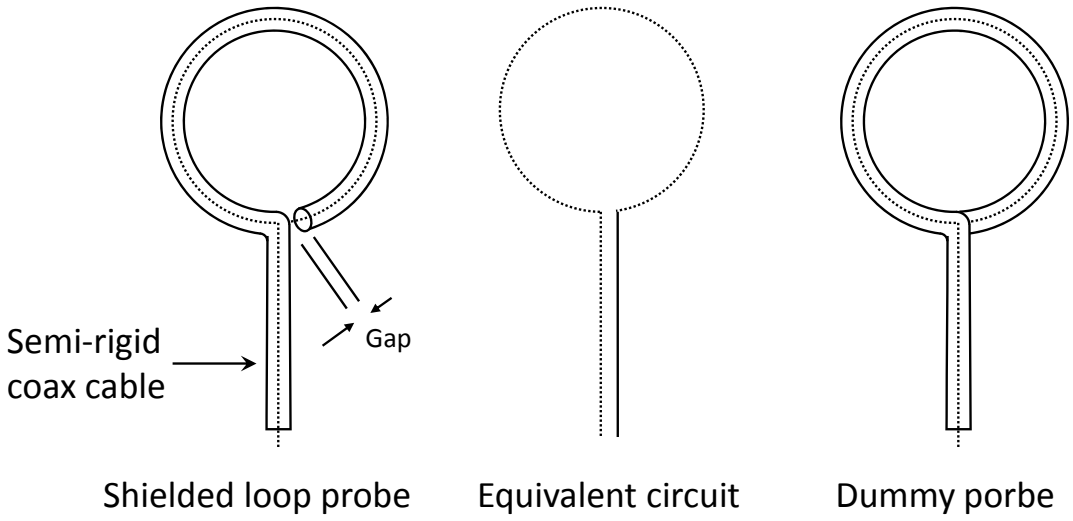

Figure 5.4: Left: Sketch of a shielded loop probe constructed using semi-rigid coaxial cable. The inner conductor connects back to the outer conductor after making a full loop. A small lateral gap is made at the end of the outer conductor. Middle: equivalent circuit of the loop probe. Right: Sketh of a dummy probe. The outer conductor is connected back to itself to form a full coverage to the inner conductor. In all sketches, the dotted curves/lines represent the inner conductor of the coaxial cable and the solid curves/lines represent the outer conductor.

crossrf.com) has 50 Ω characteristic impedance and its center conductor has a diameter of 0.287 mm. At 20 MHz, the maximum attenuation by the cable is about 5.3 dB/100 ft or 0.17 dB/m. Detailed specification can be found here http://crossrf.com/pdf/SR-047ST-TC.pdf.

5.3.1 Elimination of RF ground loop current by studying dummy probe

As previously discussed, RF ground loop is unavoidable in high-speed diagnostics. However, it is possible to reduce or even eliminate the impact from the RF ground loop. Perkins & Bellan 2011 [89] identified a large RF ground loop as the cause of radio frequency noise in a vacuum extreme ultraviolet probe array and invented a RF ground current diverting technique to prevent the RF ground current from interfering with measurement.

Figure 5.5 illustrates the principles of this RF ground current diverting technique. A capacitive coupling exists between a grounded conducting surface (e.g., chamber wall) and the outer conductor of the coaxial cable of a probe. This allows an RF ground current to flow on the outer conductor of the coax cable. A high frequency ferrite core is placed around the coaxial cable next to the data acquisition device. A short wire (low impedance

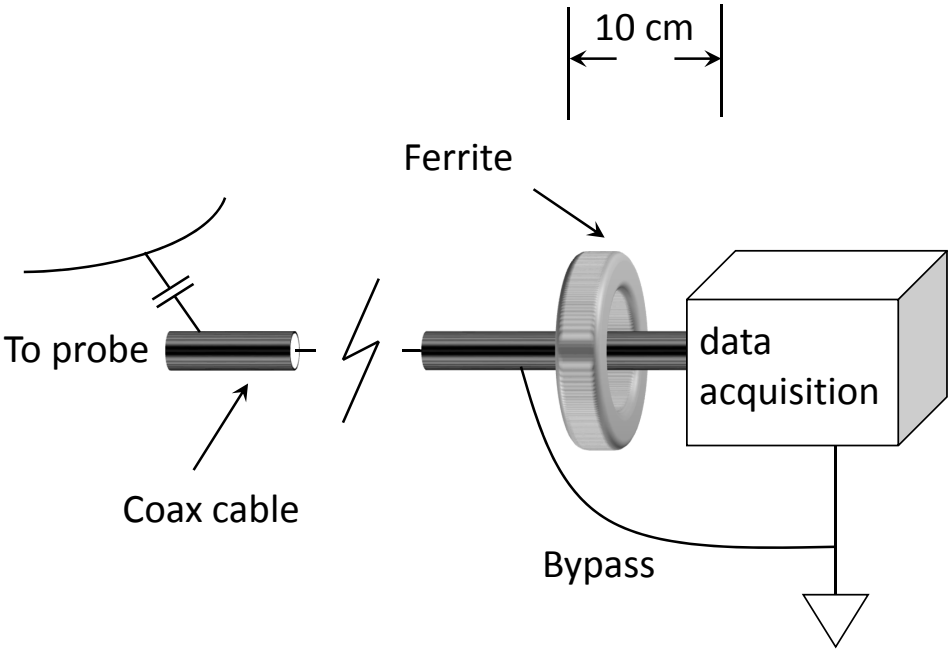

Figure 5.5: RF Ground loop diverting technique invented by Perkins & Bellan 2011 in [89].

shunt) links the ground of the data acquisition device to the outer conductor of the coax cable before the ferrite core.

The effective schematic diagrams of the configuration are plotted in Fig. 5.6. Consider a high frequency current caused by an RF ground loop. This current flows on the outer conductor of the coaxial cable and generates magnetic field around the cable. Because the ferrite has large magnetic permeability, the surface current experiences a large inductance due to the ferrite core. At high frequency large inductance gives large impedance. On the other hand, because a grounded bypass (shunt) with lower impedance is provided before the ferrite core, the surface current will be diverted to ground before the data acquisition device (Fig. 5.6B). Therefore the RF ground current does not impact the data acquisition device. The signal current, on the other hand, is equal and opposite on both the inner and outer conductor of the coaxial cable. The signal current does not generate any magnetic field outside the coaxial cable and so does not experience the external ferrite core.

The RF ground current diverting is an intelligent way to reduce the impact of RF ground loop. It is only effective to the surface current induced by the RF ground loop and has no effect on the signal being measured.

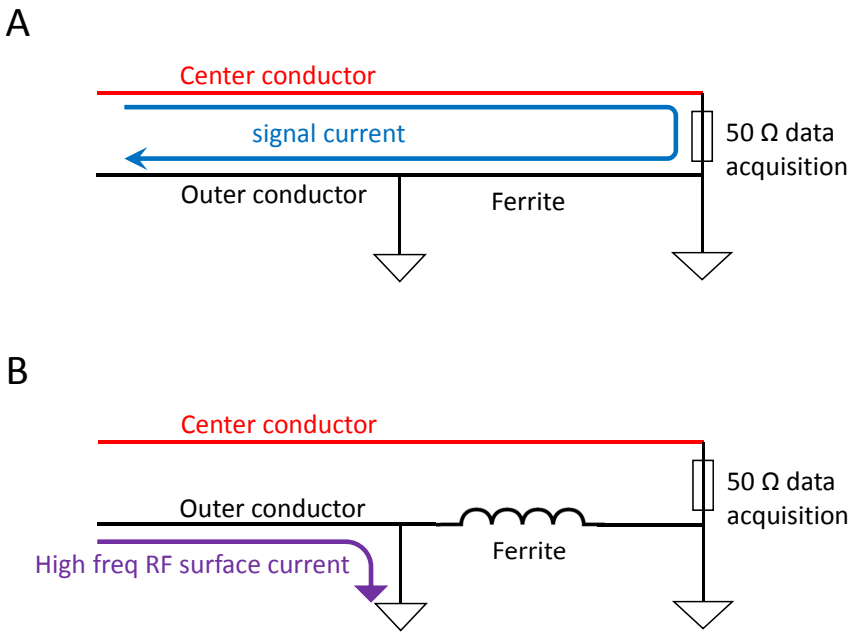

Figure 5.6: Effective schematics of the RF Ground loop diverting technique for signal current (panel A) and RF ground loop current (panel B).

We built a dummy probe to study the RF ground loop. A dummy probe is a probe that in theory should output absolute zero signal. Figure 5.4 shows a sketch of dummy probe in the right panel. The dummy probe is made of a single 1 m long 0.047 in semi-rigid coax cable. One end of the coax cable is the 6 mm diameter probe and the other end is mounted with a female SMA connector. Unlike the loop probe, the dummy probe does not have the gap between the outer conductor. Therefore the B-dot loop formed by the inner conductor is fully covered by the outer conductor. When the dummy probe is in a time-dependent magnetic field, an eddy current can be induced in the outer conductor loop. The thickness of the outer conductor of the semi-rigid coax cable is 0.125 mm, equal to the skin depth of copper at $f = 250$ KHz. Therefore magnetic fluctuation above 1 MHz is not able to diffuse through the outer conductor and be picked up by the dummy probe.

We tested the dummy probe in four different configurations to identify and solve the RF ground loop problem.

Configuration 1: flexible coax cable In this configuration, we used a 8 m long RG58 50 Ω flexible coaxial cable to connect the probe and the data acquisition device. Figure 5.7 gives the 2 MHz high-pass filtered signal from the dummy probe and the corresponding

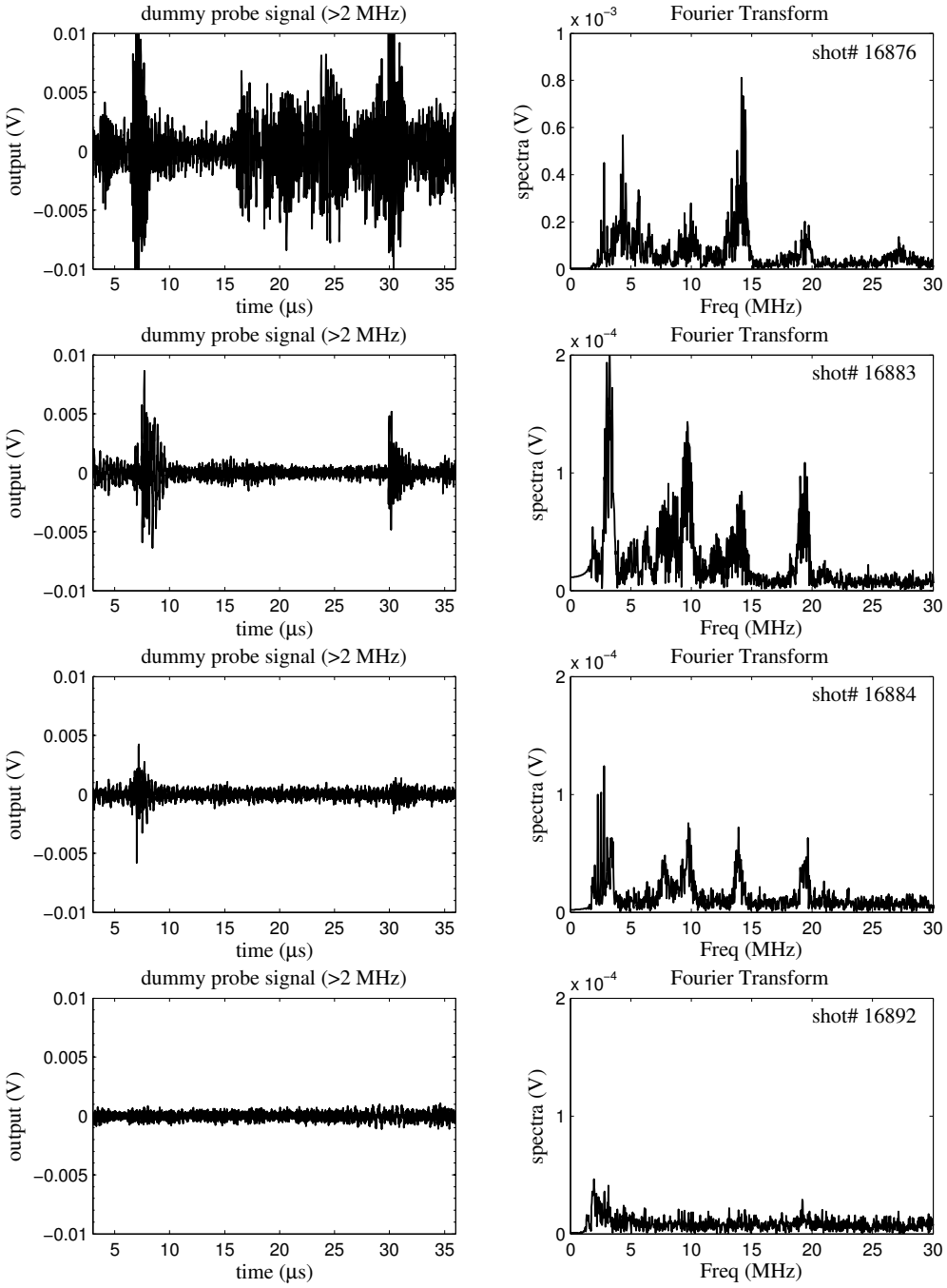

Figure 5.7: Output signals (left panels) of the dummy probe in different configurations and the corresponding power spectra (right panels). From top to bottom: (1) shot 16876, dummy probe with flexible coax cable; (2) shot 16883, dummy probe with semi-rigid coax cable; (3) shot 16884, dummy probe with semi-rigid coax cable and RF ground loop diverting (Fig. 5.5); (4) shot 16892, similar to (3) but with the semi-rigid coax cable wrapped around the ferrite core by four turns. In all four left panels, components below 2 MHz have been numerically filtered out using a 4-th order Butterworth digital filter. The y-axis of the first spectrum plot (shot 16876) is 4 times higher than other spectra plots.

spectrum (shot 16876). High frequency noises are found at 8 μs and after 17 μs, with amplitude ~ 0.01 V and frequencies primarily at 5 MHz, 10 MHz, 15 MHz, and 20 MHz. Note that without any shield the electrostatic probe picked up ~ 1 V signals at ~ 8 μs and after 28 μs in the range of $5-15$ MHz. These results suggest that there exists a RF ground loop in both the dummy probe and the electrostatic probe, with resonant frequencies at 5 MHz, 10 MHz, ... The actual capacitive signal by the electrostatic probe should be lower than $1V$, but is amplified by the RF ground loop at the resonant frequencies.

Configuration 2: semi-rigid coax cable In this configuration, we replace the 8 m long flexible coaxial cable with a 5 m long RG402 50 Ω semi-rigid coaxial cable. The second row of Fig. 5.7 shows the signal and spectrum of this configuration (shot 16882). The semi-rigid coaxial cable provides a much better EMI/RFI shield to the central conductor and gives much less noisy output. However, the RF ground loop resonances still exist.

Configuration 3: semi-rigid coax cable + RF diverting In this configuration, we apply the RF ground loop diverting technique by putting a high frequency ferrite core and a short shunt cable at the end of the semi-rigid coaxial cable, as shown in Fig. 5.12. The third row of Fig. 5.7 gives the results in this configuration (shot 16884). The high frequency MHz RF ground currents are all reduced by $\approx 50\%$ compared to shot 16883. These validates our conjecture that these high frequency components are caused by a RF ground loop. However, the RF ground current is not fully eliminated by the ferrite and the shunt.

Configuration 4: semi-rigid coax cable + RF diverting with four turns around the ferrite core The spectra of shot 16883 and 16884 shows that the shunt in shot 16884 diverts about 50% of the RF ground current, implying that the inductance of the shunt is comparable to the inductance caused by the ferrite core. In order to divert more RF ground current through the shunt, we wrap the semi-rigid coax cable around the ferrite core by four turns. The inductance due to the ferrite seen by the surface current is expected to be 16 times as large as before. The last row of Fig. 5.7 shows the dummy probe output in this configuration (shot 16892). The resonances at 5 MHz, 10 MHz, 15 MHz and 20 MHz are essentially removed. The noises at 8 μs and 30 μs are reduced to the quiescent noise level 0.0005 V. The enormous resonance at 15 MHz is reduced from 0.8×10^{-3} V in shot 16876

to 1.2×10^{-5} V in short 16892, corresponding to a 66 times reduction in noise level or 36 dB attenuation in noise power.

In this section we studied RF ground loop by testing a dummy probe in several different configurations. We show that by properly applying the RF ground current diverting technique by Perkins & Bellan 2011 [89], the RF ground current can be essentially eliminated. The quiescent level of the dummy probe is 0.5 mV, comparable to the digitization error of the data acquisition device $(1/2^{12})$ V= 0.24 mV. Recall that without any capacitive shielding or RF ground current diverting, the electrostatic probe picked up $\sim 1-2$ V signals at 8 μs and after 28 μs. Therefore a ~ 3000 times reduction in electrostatic signal is achieved by using the shielded loop and RF ground current diverting technique, corresponding to a 70 dB rejection of electrostatic noise.

5.3.2 Construction of the 3D magnetic probe

Six shielded loop probes are constructed. Each probe is made out of a 1.7 m long 0.047 inch diameter semi-rigid coaxial cable (part no. SR-047ST-TC, crossrf.com) with one end forming the 6 mm diameter shielded loop probe (left panel of Fig. 5.4) and the other end mounted by a female SMA connector. The loop probe is painted by a layer of high voltage insulating varnish (10-9002, red GLPT insulating varnish, GC electronics) and the long tail of the semi-rigid coax cable between the probe and the SMA connector are protected by fiberglass sleeving (Bentley-Harris, size 12).

The radius of the central connector of the semi-rigid coax cable is $a = 0.144$ mm. The inductance of the single loop probe is therefore $L_p = \mu_0 r \left(\ln \frac{8r}{a} - 2\right) = 6.5$ nH according to Eq. 5.9, where $r = 3$ mm is the radius of the loop. Equation 5.8 then shows that the probe is capable of measuring up to 1.2 GHz magnetic fluctuation. At 10 MHz, the attenuation factor of the probe due to finite self-inductance is 0.99997 and the phase delay is just 0.46°.

Two identical probes are placed next to each other but with the loops facing in opposite directions. As shown in Fig. 5.8, when a changing magnetic field dB/dt is perpendicular to both, the outputs of the two loop probes are

$$\begin{aligned} V_1 &= A\frac{dB}{dt} + V_c \\ V_2 &= -A\frac{dB}{dt} + V_c, \end{aligned}$$

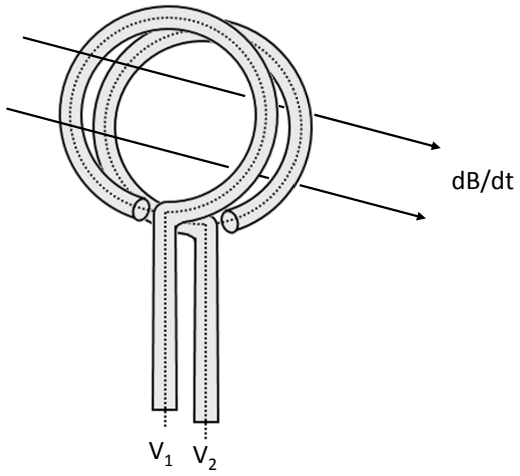

Figure 5.8: Sketch of a pair of magnetic probes facing opposite direction.

where $A = \pi r^2$ is the cross-section area of the single shielded loop and V_c are the common signal including capacitive coupling signal and RF ground loop current. The two probes are expected to have the same common signal because they are placed at the same location. The difference of the two probes' outputs is

$$V_d \equiv V_1 - V_2 = 2A\frac{dB}{dt}. \tag{5.14}$$

The common mode is thus eliminated and only the differential mode (magnetic field measurement) survives. Similar techniques can be found in other high frequency magnetic diagnostics [76]. It is important to point out that for these dual differential probes, the two sub-probes need to be placed at the same location so that the capacitive coupling between the probes and the plasma are the same.

Three pairs of the dual differential probes were made and placed orthogonal to each other as illustrated in Fig. 5.9. The overall size of the 3D probe is about 6 mm in diameter and 1 cm in length. In Fig. 5.10 we show the vacuum assembly of the high frequency 3D magnetic probe. The probe is enclosed in a 30 cm long, 8mm inner-diameter (ID), and 10mm outer-diameter (OD) quartz tube. The tails of the loop probes (semi-rigid coax cables) are wrapped around by insulating tape that contacts with the quartz tube firmly to prevent sliding. The quartz tube is glued to a 3/4 inch OD custom-made stainless steel (SS) cylindrical adapter by high vacuum Torr Seal epoxy. The 3/4 inch SS adapter is 1.5

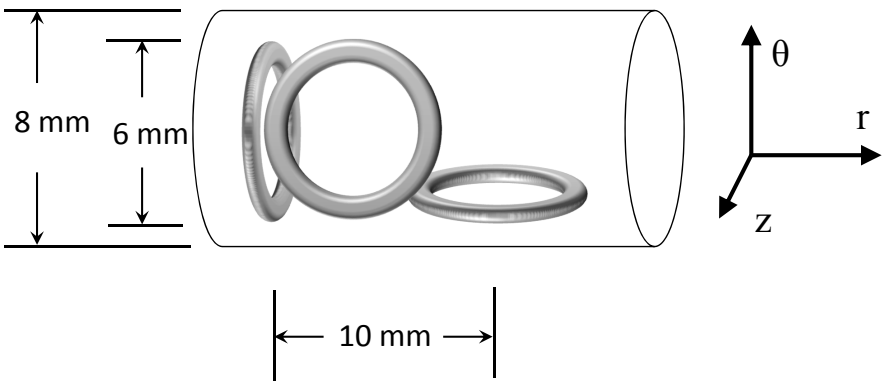

Figure 5.9: Sketch of the three pairs of dual differential probes enclosed in a 8 mm ID quartz tube.

inch (38.1 mm) long and has an 11 mm diameter 33.1 mm deep cylindrical socket from one side and an 9 mm diameter 5 mm deep cylindrical socket from the other side. The quartz tube fits inside the 11 mm diameter socket against the 9 mm diameter socket. The 3/4 inch SS adapter is welded to a Swagelok SS-12-VCO-3 O-Ring face Seal VCO fitting. This VCO fitting has a 3/4 inch diameter tube socket that well fits the 3/4 inch SS adapter. The SS-12-VCO-3 fitting is against to a Swagelok SS-12-VCO-1-12 VCO seal threaded connector, with an O-ring in between. The O-ring vacuum connection is secured by a Swagelok SS-12-VCO-4 316 SS female nut that threads on the SS-12-VCO-1-12 connector. The other end of the SS-12-VCO-1-12 connector is welded to a polished 1 m long 3/4 inch OD 304 SS tube (McMaster-Carr, part no. 1750T116). The 3/4 inch SS tube is mounted through a 2.75 inch flange on the vacuum chamber by a 0.75 inch quick-connect coupling (Kurt J. Lesker, part no. F0275XVC075). Outside the vacuum chamber, the SS tube is through a custom-made 1.5 inch OD 0.75 inch ID aluminum tube attached to the 2.75 inch flange, with two lateral $1/4-20$ set screws threaded in the aluminum tube to hold the central 3/4 inch SS tube.

Figure 5.11 gives the photos of two single shielded loop probes and the finished 3D magnetic probe in front of the coaxial electrodes. Figure 5.12 shows a photo indicating that the coaxial cables of the probe are wrapped around the ferrite cores and the short cables connect the outer conductors of the coax cables to a ground strip before the ferrite cores.

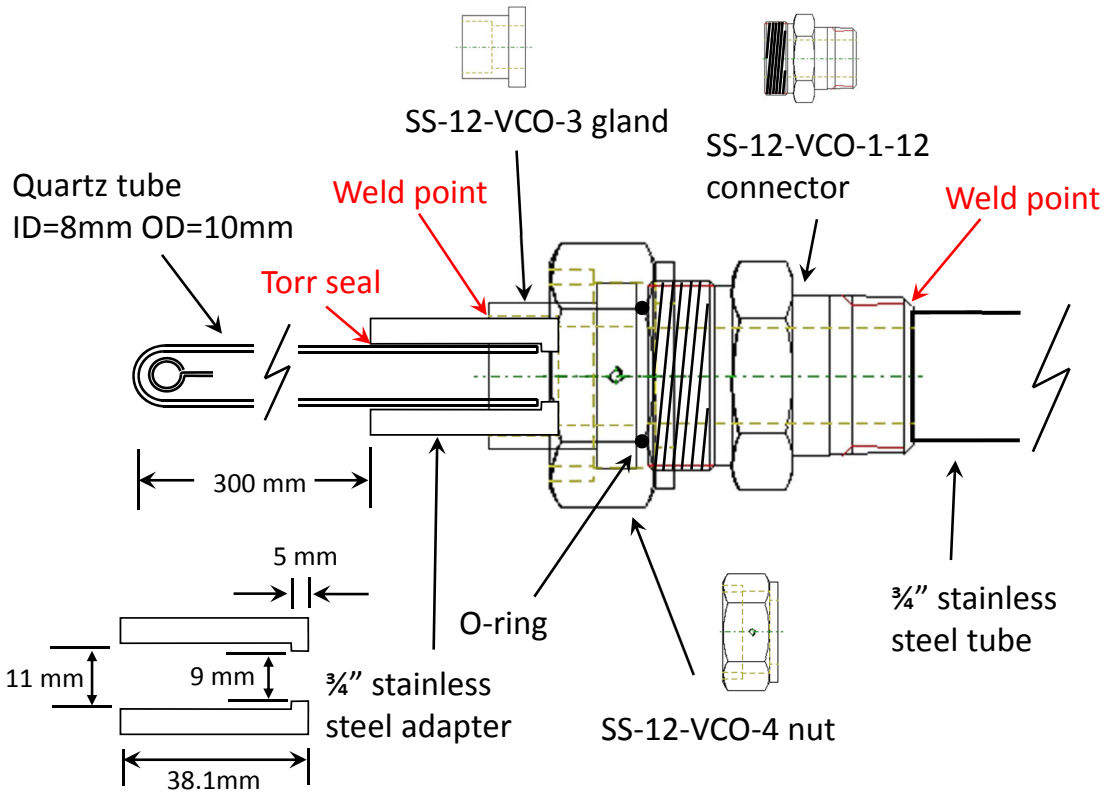

Figure 5.10: Drawing of the vacuum assembly of the 3D magnetic probe. See the text description for details.

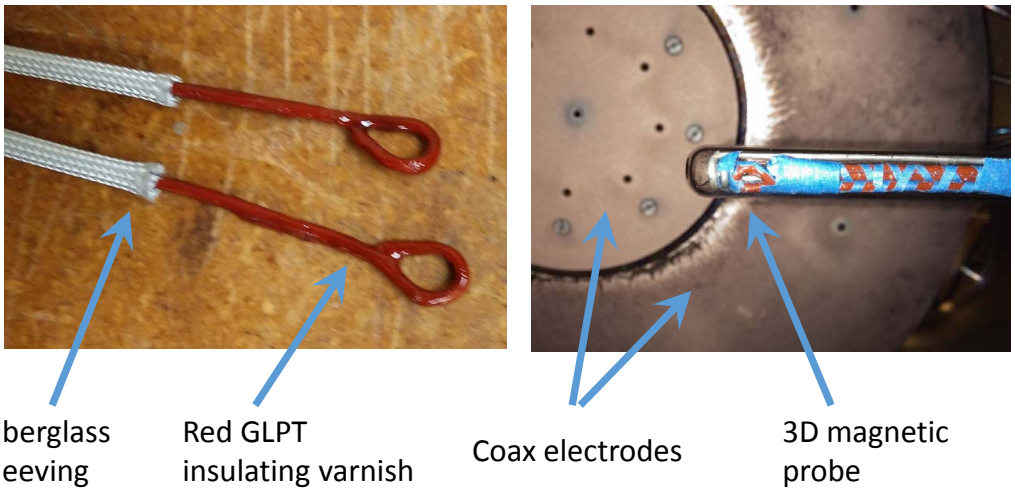

Figure 5.11: Left: photo of two single turn shielded loop with red insulating painting and fiberglass sleeving. Right: photo of the 3D magnetic probe in the vacuum chamber.

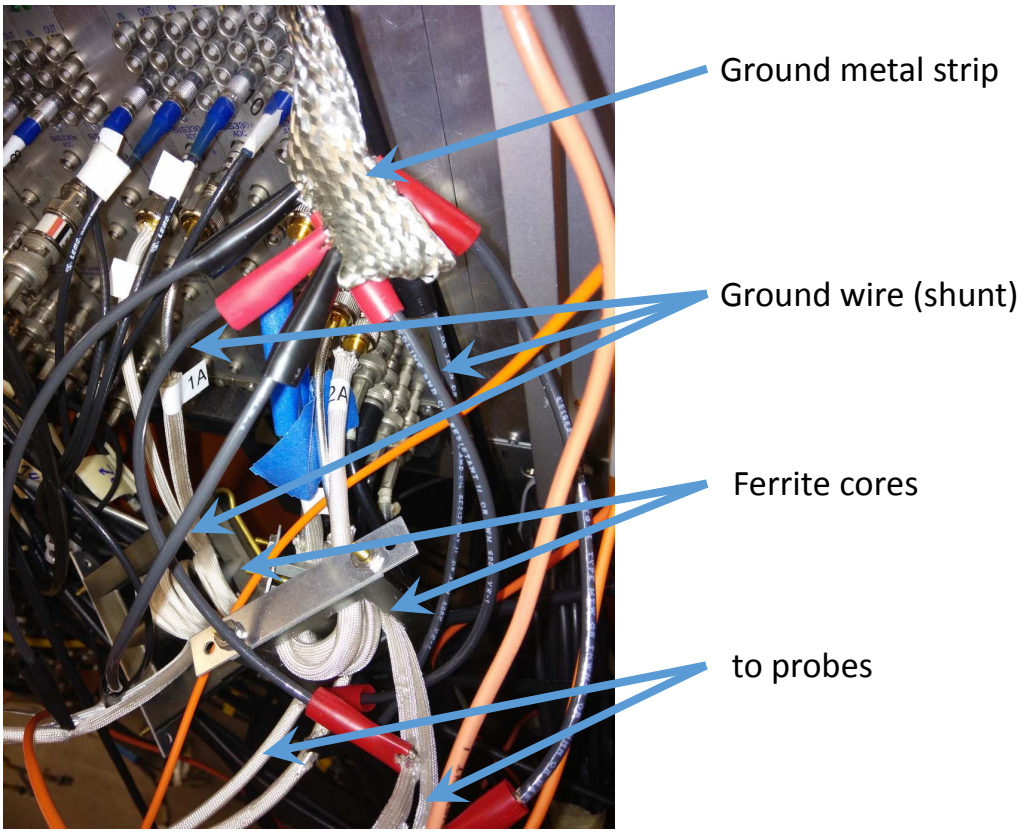

Figure 5.12: Photo of the ferrite cores and shunt cables used for diverting the RF ground current flowing on the surface of semi-rigid coaxial cables of the magnetic probe.

5.3.3 Calibration and test

A high frequency Helmholtz coil was built for calibrating the 3D magnetic probe. The Helmholtz coil contains two 2.25 cm radius 5-turn solenoids separated by 2.25 cm. When conducting same current I through each solenoids, the Helmholtz coil generates a quasi-uniform magnetic field along its axis

$$B = \left(\frac{4}{5}\right)^{3/2} \frac{\mu_0 n I}{R}, \tag{5.15}$$

where $n = 5$ is number of turns of each solenoid and R is the radius of the solenoid. The inductance of the Helmholtz coil is measured to be $L_{HC} = 1.5$ μH. The two solenoids are parallel electrically, and hence the voltage across the entire Helmholtz coil is

$$V_{HC} = 2L_{HC}\frac{dI}{dt}. \tag{5.16}$$

The time derivative of the magnetic field generated by the Helmholtz coil is

$$\dot{B} = \left(\frac{4}{5}\right)^{3/2} \frac{\mu_0 n}{2RL_{HC}} V_{HC}. \tag{5.17}$$

A B-dot probe inside the Helmholtz coil will output

$$V_{Bdot} = A_\perp \frac{dB}{dt} = A_\perp \left(\frac{4}{5}\right)^{3/2} \frac{\mu_0 n}{2L_{HC}R} V_{HC}, \tag{5.18}$$

where $A_\perp$ is the total cross-section area of the B-dot probe perpendicular to the axial direction of the Helmholtz coil.

We label the three orthogonal dual differential probes as probe 1, 2, and 3 and they are approximately aligned in the radial, azimuthal, and axial directions of the cylindrical vacuum chamber. Dual probe i contains two single loops $i+$ and $i-$. Three calibrations are performed with the Helmholtz coil placed along to the radial, azimuthal, and axial direction, respectively. In each calibration, we apply a 10 MHz sinusoidal voltage signal across the Helmholtz coil and record the output of the six loop probes and also the voltage across the Helmholtz coil.

Figure 5.13 shows the output of two single loops of each dual differential probe. Take probe 1 for example. First we plot the output of loop $1-$, denoted as V_-, versus the output of loop $1+$, denoted as V_+ (the upper left panel of Fig. 5.13). The measurement points in the diagram fall on a -1 slope straight line, implying that the two loops output equal and opposite signal. Linear regression shows that $V_- = \alpha V_+$ and $\alpha = -0.89$. In the lower left panel, we plot V_+ and V_-/α as function of time from 2 to 4 μs and verify that the two functions do coincide. We perform the same procedures for the other two dual probes and obtain similar results. We then take $(V_+ - V_-/|\alpha|)$ as the output of each dual differential probe.

We define C_{ij} as the effective area of dual probe i perpendicular to direction j, where $i = 1, 2, 3$ and $j = r, \theta, z$. For given $\dot{\mathbf{B}} = (\dot{B}_r, \dot{B}_\theta, \dot{B}_z)$, the output of the 3D probe $\mathbf{V} = (V_1, V_2, V_3)$ is

$$\mathbf{V} = \mathbb{C}\dot{\mathbf{B}} \qquad \text{or} \qquad \begin{pmatrix} V_1 \\ V_2 \\ V_3 \end{pmatrix} = \begin{pmatrix} C_{1r} & C_{1\theta} & C_{1z} \\ C_{2r} & C_{2\theta} & C_{2z} \\ C_{3r} & C_{3\theta} & C_{3z} \end{pmatrix} \begin{pmatrix} \dot{B}_r \\ \dot{B}_\theta \\ \dot{B}_z \end{pmatrix}, \tag{5.19}$$

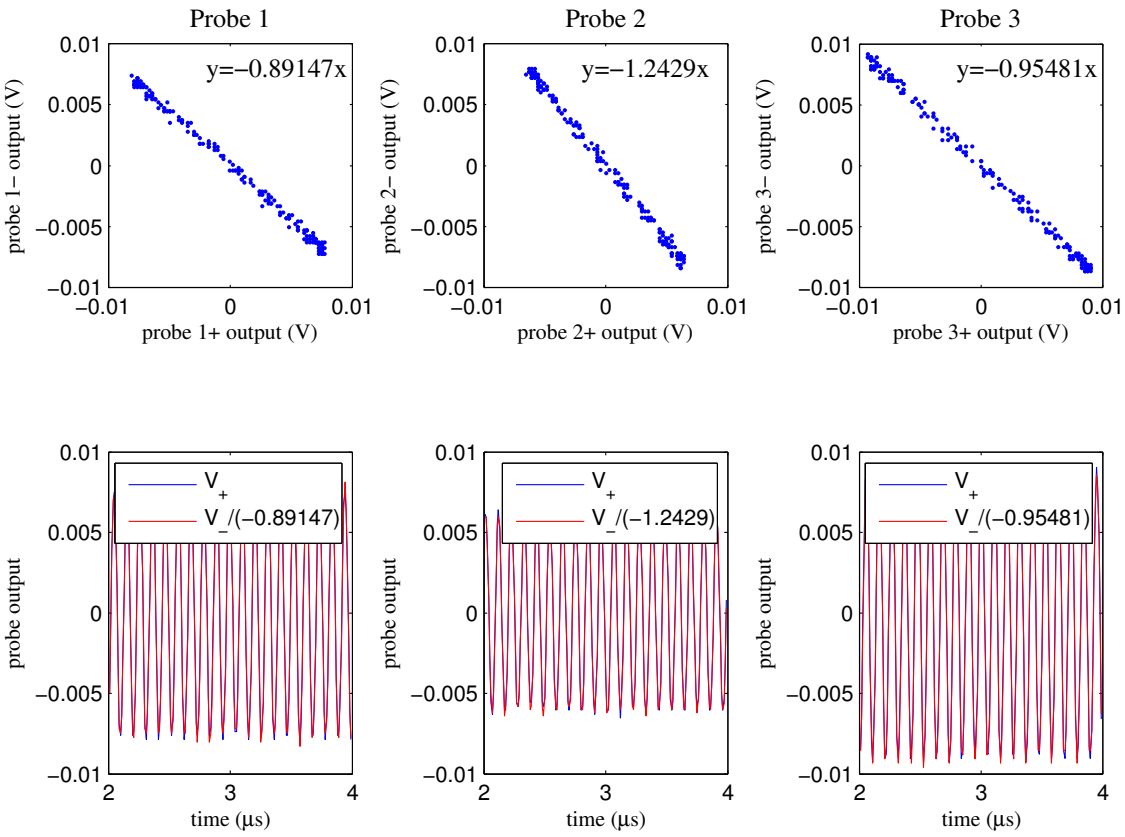

Figure 5.13: Output of the two single loops of each dual probe with the Helmholtz coil along the radial, azimuthal and axial direction, respectively. The top panels shows the output of loop $i-$ versus the output of loop $i+$ for each dual differential probe i and the linear regression results. The bottom panels show the output of loop $i+$ as function of time and also the corrected output of loop $i-$.

where $\mathbb{C} = (C_{ij})$ is the calibration matrix. When the Helmholtz coil is placed along the radial direction, $\dot{\mathbf{B}} = (\dot{B}_r, 0, 0)$ and $\dot{B}_r$ is calculated by Eq. 5.17 given the voltage across the Helmholtz coil. The first column of $\mathbb{C}$ is given by the ratio of each dual differential probe's output V_i to $\dot{B}_r$. Similarly the second and the third column of $\mathbb{C}$ can be obtained by placing the Helmholtz coil along the azimuthal and axial direction.

Figure 5.14 confirms the linear dependence of each dual probe's output on the magnetic field changing rate. The slopes of linear regressions in Fig. 5.14 give the elements of the calibration matrix $\mathbb{C}$. The latter one is found to be

$$\mathbb{C} = \begin{pmatrix} 0.4350 & 0.0516 & 0.0823 \\ -0.0016 & -0.3500 & 0.1063 \\ -0.0243 & -0.1168 & 0.5092 \end{pmatrix} \times 10^{-4}\ \mathrm{m}^2. \tag{5.20}$$

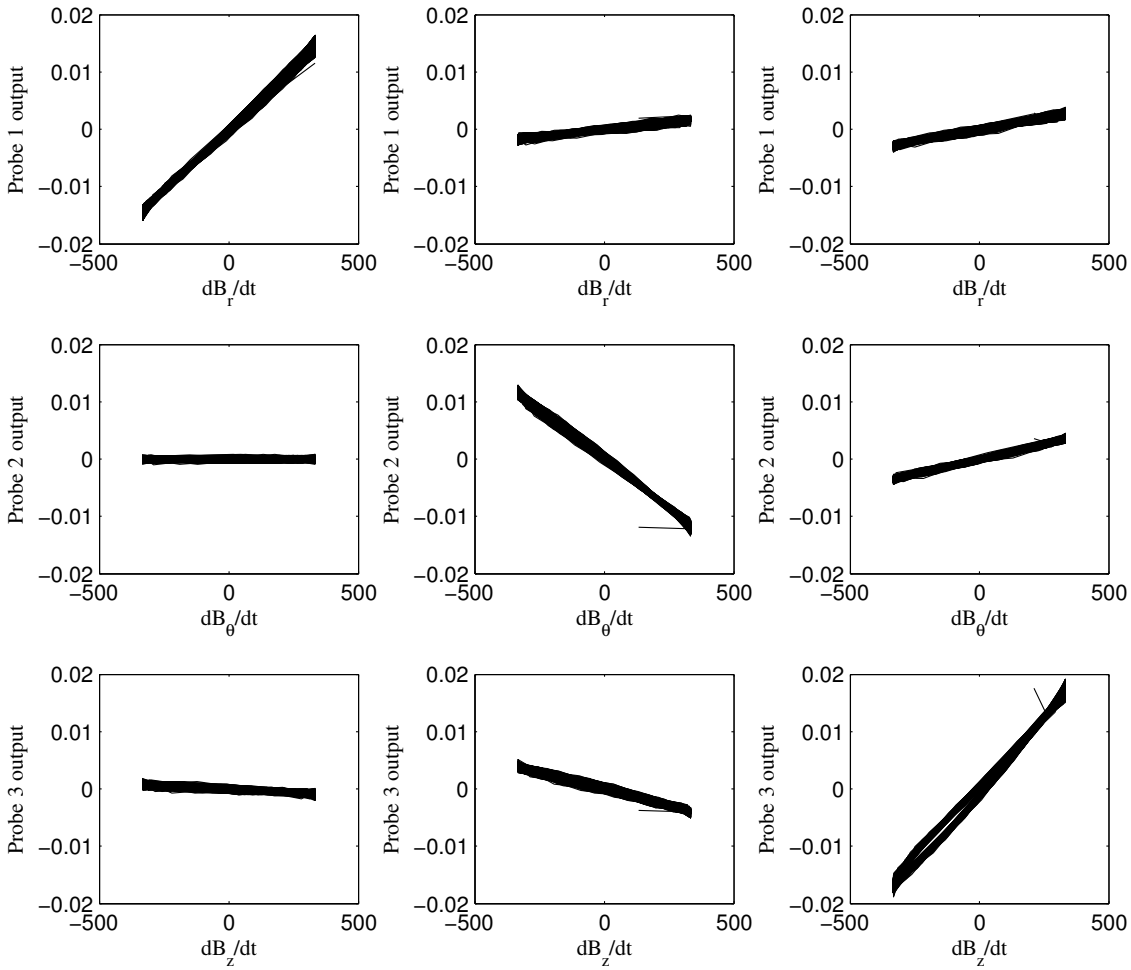

Figure 5.14: Output of each dual differential probe versus the changing rate of the magnetic field generated by the Helmholtz coil. The measurement is over a 2 μs period of time.

A 6 mm diameter single loop B-dot probe has a cross-section area 0.28×10^{-4} m^{-2}. Because each orthogonal dual probe contains two single loops, the total cross-section area of each dual probe is about 0.56×10^{-4} m^{-2}. This is consistent with the diagonal entries of the calibration matrix $\mathbb{C}$. $\mathbb{C}$ is quasi-diagonal, showing that the three dual probes are approximately along the radial, azimuthal, and axial direction, respectively.

The inverse of matrix $\mathbb{C}$ is

$$\mathbb{C}^{-1} = \begin{pmatrix} 2.2745 & 0.4926 & -0.4705 \\ 0.0246 & -3.0656 & 0.6362 \\ 0.1141 & -0.6799 & 2.0873 \end{pmatrix} \times 10^4 \text{ m}^{-2}. \tag{5.21}$$

When the probe is in an time-dependent magnetic field and the probe output is $\mathbf{V} =$

(V_1, V_2, V_3), the changing rate of the 3D magnetic field is measured to be

$$\dot{\mathbf{B}} = \mathbb{C}^{-1}\mathbf{V}. \tag{5.22}$$

5.4 Measurements

Typical measurements by the 3D magnetic probe in the plasma jet experiment are given in Fig. 5.15 (shot 17012). The probe outputs are attenuated by 50 Ω 20 dB attenuators. The inset in the first panel shows that the quiescent noise level of the probe is ±0.005 mV or $1-2$ times the data acquisition digitization error, same as the noise level of the dummy probe. Note that the data acquisition digitization error is now 2.4 mV instead of 0.24 mV because of the 20-dB attenuators. Figure. 5.15 shows that the magnetized plasma encounters the probe as early as 12 μs; however, high frequency magnetic fluctuations are not detected until 28 μs, when the Rayleigh-Taylor instability and fast magnetic reconnection occurs (See Chapter 3 and Chapter 4).

We plot the detailed measurement of shot 17012 from 29.5 μs to 30.5 μs in Fig. 5.16. The figure clearly shows that the two single loops of each dual probe give equal and opposite measurements. Therefore we have confirmed that the probe is capable of measuring high frequency magnetic fluctuation and that the noise from capacitive coupling is small compared to the magnetic measurement.

The quiescent noise level of the probe is 0.005 V with 20 dB attenuation, or 0.5 mV without attenuation. Given $C_{ii} \sim 0.5 \times 10^{-4}$ m^{-2}, the above noise levels correspond to a probe sensitivity 100 T/sec or 1 Gauss/μs with 20 dB attenuator, or 10 T/sec or 0.1 Gauss/μs without extra attenuation.

Because the sampling rate of the data acquisition device used is 100 MHz, the probe can not measure fluctuations with frequency larger than 20 MHz. However, due to the very low inductance ($L_p = 6.5$ nH) of the single turn shielded loop probe, it is expected to be capable of measuring very high frequency magnetic field. At 3 dB attenuation the B-dot probe theory shows that the probe is sensitive to 1.2 GHz with a 45° phase delay. Simple tests using USG LF44 USB function generator show that without the 20-dB attenuator the probe is sensitive to 33 T/sec time-dependent magnetic field at 150 MHz.

We have presented more detailed analyses of the measurement in Chapter 4. In Chapter

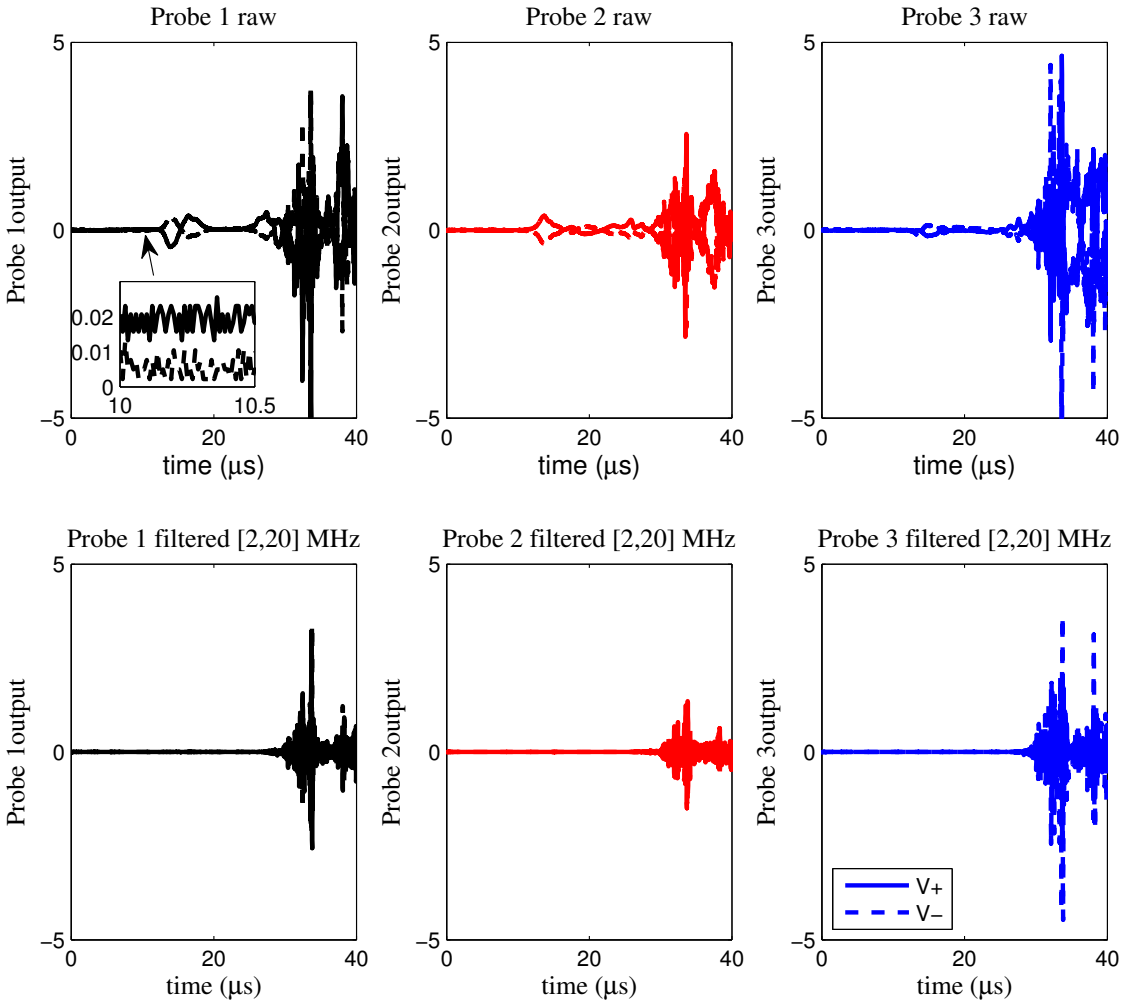

Figure 5.15: Output of the 3D magnetic probe in shot 17012. Upper panels give the raw signal output and the lower panels give the signal after filtered by a 4-th order Butterworth $[2, 20]$ MHz bandpass digital FIR filter. In each plot, the solid curve is the output by the loop probe $+$ and the dashed curve is the output by the opposite loop probe $-$ corrected by the corresponding factor α obtained from Fig. 5.13. The inset in the first panel zooms into the $10 - 10.5$ μs time window. Each probe is connected to a 12-bit VME digitizer through a 50 Ω 20-dB attenuator. The probe is located at $r = 6$ cm and $z = 29$ cm in the chamber coordinate.

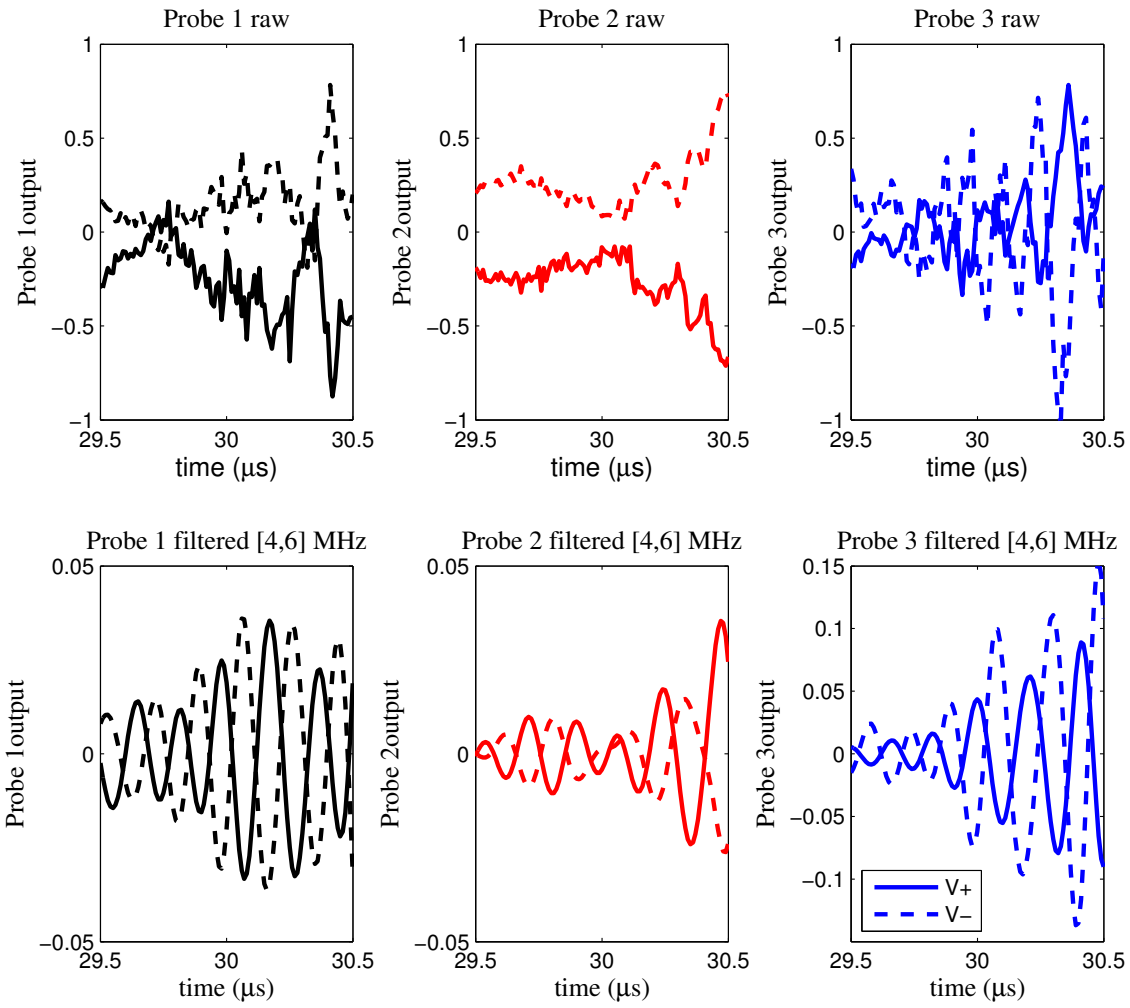

Figure 5.16: Measurement of shot 17012 from 29.5 to 30.5 μs. A 4-th order Butterworth $[4, 6]$ MHz bandpass digital filter is used to give the lower panels.

4 we utilize hodogram technique and show that the 3D magnetic probe successfully detects circularly polarized magnetic component of high frequency whistler wave generated during fast magnetic reconnection in the plasma jet experiment.

5.5 Summary

A high-speed 3D magnetic probe composed by three orthogonal pairs of oppositely orientated B-dot coils is built for the Caltech plasma jet experiment. Each B-dot coil is a single turn shielded loop probe made out of a 0.047 inch diameter semi-rigid coaxial cable and the outer jacket of the coaxial cable does not connect back to itself to avoid a closed

grounded shielding. An RF ground loop current diverting technique is implemented in the magnetic probe following Perkins and Bellan [89]: near the data acquisition device, the semi-rigid coax cable is wrapped around a high frequency ferrite core; a short grounded cable is connected to the outer conductor of the coax cable before the ferrite core. The shielded loop probe design and the RF ground current diverting technique together give a 70 dB rejection to electrostatic interference, making the magnetic probe ideal for high-speed time-dependent magnetic field detection in an extremely noisy environment.

Chapter 6

An Earth-Isolated Optically Coupled Wideband High Voltage Probe Powered by Ambient Light

An earth-isolated optically-coupled wideband high voltage probe has been developed for pulsed power applications. The probe uses a capacitive voltage divider coupled to a fast LED that converts high voltage into an amplitude-modulated optical signal, which is then conveyed to a receiver via an optical fiber. A solar cell array powered by ambient laboratory lighting charges a capacitor that, when triggered, acts as a short-duration power supply for an on-board amplifier in the probe. The entire system has a noise level ≤ 0.03 kV, a DC-5 MHz bandwidth, and a measurement range from -6 to 2 kV; this range can be conveniently adjusted.

Primary part of this chapter was published by Xiang Zhai & Paul M. Bellan, in Review of Scientific Instruments, Volume **83**, 104703, 2012 [129].

6.1 Introduction

Measuring rapidly changing high voltages in the presence of large currents is challenging because of substantial interference from ground loops, capacitive and inductive pickup, high frequency radiation, etc.

Various high voltage probes [38, 96, 97] and some commercial products (e.g., Tektronix P6015A) have been developed for measuring high voltage for different purposes. For example, a passive HV probe developed by Sarjeant and Alcock [96] uses a resistive voltage divider and can measure a < 100 ns voltage pulse with subnanosecond rise time. Another

passive HV probe developed by Gratton et al. [38] adopts a capacitive divider for measuring nanosecond HV pulses. A capacitive-RC hybrid passive probe developed by Saw et al. is designed for fast pulse discharge systems [97]. However, most of these passive HV probes, including the Tektronix P6015A, require connection to earth ground, which makes them neither convenient for long distance measurements because of ground loop susceptibility, nor suitable for real floating voltage measurements. For example, the Caltech experimental plasma group uses a Tektronix P6015A probe for pulsed power voltage measurements. To isolate the data acquisition device from the HV source, and to avoid long wires in an environment with fast changing magnetic fields, a commercial optical link is used to convert the Tektronix probe voltage signals to optical signals near the HV source and then convert back to electrical signals for recording data. However, the optical link requires a power supply that plugs into the wall. Therefore the Tektronix probe ground lead is electrically connected with mains ground through the optical link power supply, and hence cannot connect to the HV source ground. Otherwise the entire system would have multiple points connected to earth ground and form ground loops, the latter can induce huge EMFs in noisy environments, especially when a fast varying current exists close to the probe. With no ground lead connecting to the HV source, the Tektronix probe is actually measuring the voltage of one HV source terminal relative to the optical link power supply, not the ground reference voltage of the HV source. An active optically-isolated HV probe by C. A. Bleys is eligible for real floating voltage measurements since the probe uses optical fibers for conveying signal and batteries as the power supply [15]. However, the probe circuit rapidly drains the batteries so the batteries must be replaced frequently. Since the probe is placed near HV sources, battery replacement can be awkward and even an electric hazard. Also this probe is built with a fixed measurement range and requires calibration before each measurement.

We report here a fully isolated HV probe that uses both optical fibers and ordinary solar cells to isolate earth ground and avoid ground loops. The probe uses a low-capacitance lab-constructed HV capacitor and a precise 100nF low voltage capacitor to form a voltage divider. Several HV capacitors with different capacitance were built so that the probe measurement range can easily be changed by switching the HV capacitors. The probe is powered by normal laboratory ambient light and so has no batteries and no reference to earth ground. The probe is well shielded and so can be used in extremely noisy environments. The probe does not require frequent calibration thanks to its relatively low temperature

sensitivity, and the calibration can be conducted using low voltage sources.

The HV probe has a DC-5 MHz bandwidth and a ≤ 30 V noise level when measuring a fast varying HV source of -6 to 2 kV.

6.2 Probe design

The probe system consists of an RFI/EMI-shielded, solar cell-powered transmitter that converts the high voltage signal into an amplitude-modulated (AM) optical signal, two low-loss optical fibers that convey the AM signal and a trigger signal, and a battery-powered receiver that converts the AM optical signal to a low voltage signal for a data acquisition device. The use of optical fibers allows the data acquistion device to be far from the HV source so that ordinary oscilloscopes or transient digitizers can be used to record data.

6.2.1 Transmitter

The transmitter circuit diagram is shown in Fig. 6.1, and the figure caption lists the part numbers of the electronic components used in the circuit. The circuit contains four subsystems: a **capacitive voltage divider** that converts a high voltage to a low voltage, an **LED driver** that converts the low voltage signal to an AM optical signal, a **power supply**, and a **trigger system** that turns on the power supply immediately before measurements.

Except for the HV capacitor C2, the entire circuit including the solar cells is mounted on a single printed circuit board (PCB) and enclosed in a one-foot long 2" diameter aluminum pipe (Fig. 6.2). A female BNC adapter is mounted on the pipe end cap with its outer conductor connected to the pipe and the inner conductor connected to the junction point of C1 and R1 (see Fig. 6.1 for detail). In operation, the pipe is electrically connected to one electrode of the target HV source and constitutes the analog ground for the circuit. Four large apertures are milled in the pipe at the solar cell position and a steel mesh snugly covers these apertures. Light can thus shine on the solar cells inside the pipe, and yet the entire circuit is well shielded by the pipe and steel mesh.

6.2.1.1 Capacitive voltage divider

C2 is a lab-constructed cylindrical HV capacitor. Figure 6.3 gives a sketch for C2; right and left hand here refer to this sketch. C2 has two coaxial copper pipes (surface 2 and

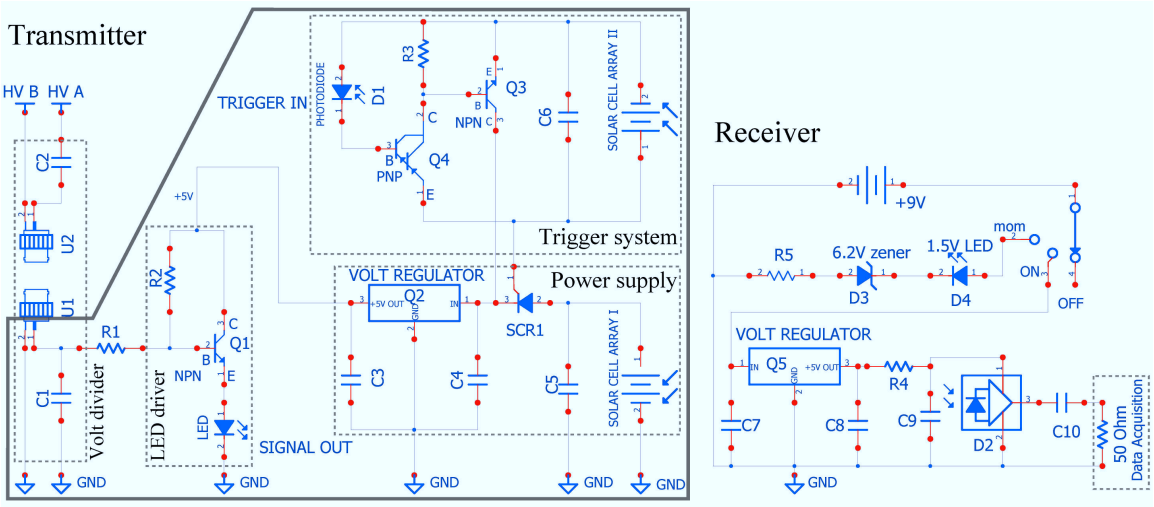

Figure 6.1: Circuit diagram of the probe transmitter (left) and receiver (right). A typical configuration for the transmitter includes: C1= 100 nF (ECH-U1H104GX9 thin film; Panasonic Electronic Components), C2= 60 pF (lab-made), R1= 20 kΩ, R2= 7.5 kΩ, Q1 NPN transistor (MMBT3904; Fairchild Semiconductor), LED (HFBR-1414 transmitter; Avago Technologies US Inc.), Q2 +5 V voltage regulator (LM340MP-5; National Semiconductor), C3= 0.1 μF (ceramic bypass), C4= 0.22 μF (ceramic bypass), SCR1 (S6X8BSRP; Littelfuse Inc.), Q3 NPN transistor (BC847CMTF; Fairchild Semiconductor), D1 PIN photodiode with ST mounting (OPF792; TT electronics/Optek Technology), Q4 PNP Darlington transistor (MMBTA64; Fairchild Semiconductor), R3= 10 kΩ, C5= 30 μF, C6= 10 μF. The solar cell array I contains four mono-crystalline 33 mm×37 mm solar cells (SCC3733-MSE; Solarbotics.com) in series; Solar cell array II contains two SCC3733 solar cells in series. Except C2, the entire circuit is enclosed in the 2" aluminum pipe (denoted by the thick solid polygon). The four dotted rectangles in the transmitter indicate the four transmitter subsystems. A typical configuration for the receiver includes: Q5 +5 V voltage regulator (LM340MP-5; National Semiconductor), C7= 0.22 μF (ceramic bypass), C8= 0.1 μF (ceramic bypass), R4= 10 Ω, C9= 33 pF (ceramic bypass), D2 analog photodiode (HFBR-2416; Avago Technologies US Inc.), C10= 47 μF (tantalum), R5= 100 Ω, D3 6.2 V zener diode (BZT52H-C6V2; NXP Semiconductors), D4 green LED (LTL-4236N; Lite-On Inc.), mom-off-on toggle switch (200MSP5T1B1M1QEH; E-Switch).

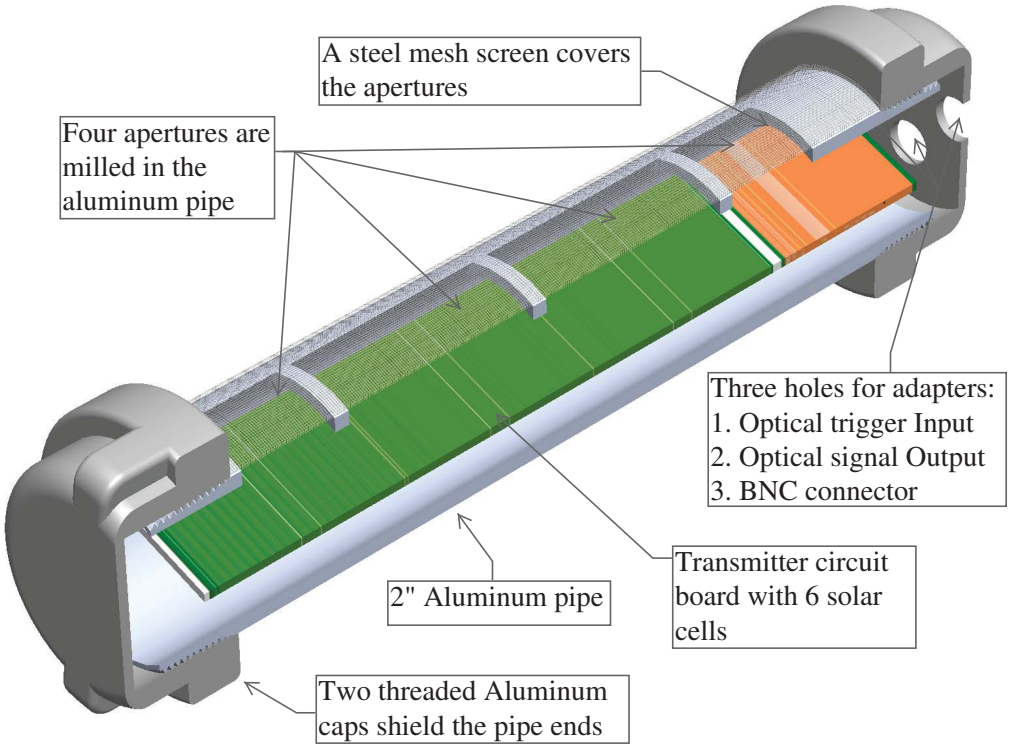

Figure 6.2: Three dimensional cross-section drawing of the transmitter without HV capacitor C2.

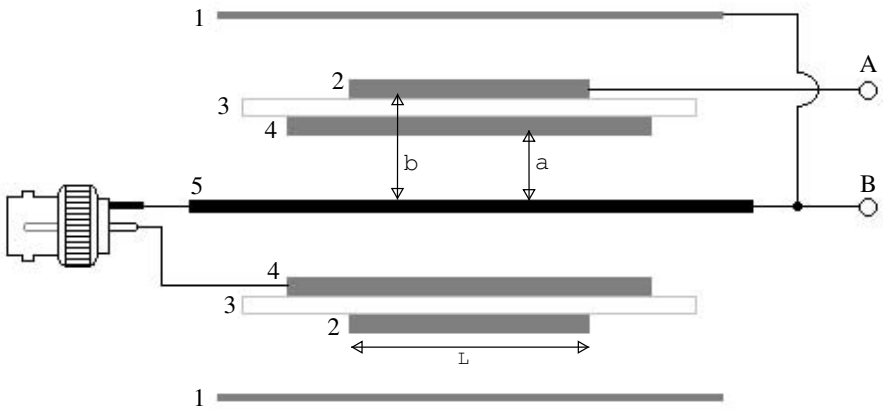

Figure 6.3: Cross-sectional sketch of the lab-constructed cylindrical HV capacitor (C2 in Fig. 6.1). Five coaxial cylindrical surfaces/object are: 1. copper sheet, 2. outer copper pipe, 3. Mylar insulation and air gap, 4. inner copper pipe, 5. central HV wire. Terminal A and B are connected with HV sources terminals. 5 and 4 are connected with a female BNC adapter's outer and inner conductors, respectively. The sketch is not to scale.

4 in Fig. 6.3) with radii a and b ($a < b$ and $|b - a| \ll a$) as two electrodes and several layers of 0.254 mm-thick Mylar sheet in between as the dielectric (surface 3 in Fig. 6.3). The capacitance of C2 is calculated by C2$\approx 2\pi a L \epsilon_0 \epsilon_{eff}/d$, where L is the overlap length of two copper pipes, $d \equiv (b - a)$ and ϵ_{eff} is the effective relative dielectric constant of air ($\epsilon_1 = 1$) and mylar sheets ($\epsilon_2 \approx 3$) [15] between the two copper pipes. ϵ_{eff} is calculated by $\epsilon_1 \epsilon_2 d/(d_1 \epsilon_2 + d_2 \epsilon_1)$, where d_1 and $d_2 = d - d_1$ are the thickness of air and mylar, respectively. A typical HV capacitor has $a = 1.44$ cm, $b = 1.75$ cm, $d = 3.1$ mm, $L = 10$ cm, and $d_2 = 2.54$ mm (10 layers mylar sheet). Hence $\epsilon_{eff} \approx 2.20$ and C2$\approx$ 60 pF. Mylar has a dielectric strength 90 kV/mm [15]. Therefore C2 can be safely charged to 10 kV or even higher. A 30 kV insulation high voltage wire (392275 WH005; Alpha Wire) is placed along the central axis of C2 (object 5 in Fig. 6.3). At the right hand end of C2, the central HV wire and the outer copper pipe connect with the two terminals A and B of the target HV source (see Fig. 6.3). At the left hand end of C2, the central HV wire and the inner copper pipe connect with the outer and inner conductor of a female BNC adapter, respectively.

To eliminate the possibility of capacitive coupling between C2 and any exterior charged surfaces, a copper sheet (surface 1 in Fig. 6.3) is wrapped around C2 and connected to the central HV wire.

A short RG58 coax cable links the HV capacitor's BNC adapter and the adapter on the aluminum pipe[1]. By doing so C2 and C1 inside the pipe form a capacitive voltage divider. Note that in this configuration the common reference of the transmitter circuit and the aluminum pipe are electrically connected with the central HV wire through C2 and the electrode of the HV source that connects to the HV wire. Therefore the entire transmitter uses the voltage of one HV source electrode as its reference voltage, and so the probe is completely floating relative to earth ground.

C1 is a fixed 100 nF thin film capacitor mounted on the PCB inside the aluminum pipe. The divided voltage by C1 and C2 equals C2/(C1+C2) times the high voltage, and is approximately C2/C1 if C1$\gg$C2. Several versions of C2 are made with capacitance 20 pF, 40 pF, 60 pF, and so on. Because C2 is external and connected to the transmitter via a coax cable, it is easy to change C2 and therefore adjust the measurement range of the transmitter.

[1]Vernon Chaplin used a shot semi-rigid coax cable because the regular RG58 flexible coax cable picked up some noise near high power RF facilities

In the following discussion, we assume C2= 60 pF and the voltage of the HV source V_H is in the range of -6 to 2 kV. Hence the voltage across C1 is V_L =C2/C1·V_H and is in the range of -3.6 to 1.2 V; the voltage across C2 is very nearly V_H.

6.2.1.2 LED driver

The divided low voltage V_L is converted into a current ΔI by resistor R1. ΔI modulates a constant bias current I_0 flowing through R2 and then to the base of NPN transistor Q1. After being amplified β times by the transistor, this amplitude-modulated current is conducted into the fast HFBR-1414 Light-Emitting Diode (LED). The LED sends an AM infrared signal into an optical fiber, which is then captured by the receiver. The resistors R1 and R2 are selected so that the LED works linearly when V_H is in the range of interest. At the same time, $\tau \equiv$R1$\times$C1 must be significantly greater than the measurement time to prevent loading of the voltage divider by the measuring circuit.

The power supply provides constant +5 V during measurements. The voltage at the transistor's base is about 2.3 V because of the forward voltage of Q1's BE junction and the LED. Typically, we choose R1= 20 kΩ and R2= 7.5 kΩ so that the amplitude-modulated current $\beta(I_0 + \Delta I)$ through the LED spans $13 - 60$ mA, given the transistor's amplification factor $\beta \approx 200$. The current range $13 - 60$ mA is located within the linear range $10 - 70$ mA of the HFBR-1414 LED. For measurement time much less than $\tau = 20$ k$\Omega \cdot 100$ nF= 2 ms, the voltage divider will not be significantly loaded by the LED driver during measurement.

6.2.1.3 Power supply

A capacitor (C5) charged by an array of solar cells (solar cell array I) with a voltage regulator (Q2) provides a constant +5 V for several milliseconds after being activated by the trigger system.

The solar cell array I shown in Fig. 6.1 contains four solar cells in series. Under normal lab ambient light, each solar cell unit can output ~ 30 μA at ~ 4 V when inside the pipe. Therefore solar cell array I can charge the 30 μF capacitor C5 to ~ 15 V in about 15 s. After the silicon controlled rectifier SCR1 is switched on by the trigger system, C5 constitutes a short duration power source for voltage regulator Q2. The latter outputs a constant +5 V to the LED driver for $\gtrsim 3$ ms (i.e., much longer than the measurement time 50 μs) until the pre-stored charge of C5 is drained. Then the SCR1 turns itself off automatically.

This power supply system allows the HV probe to perform a millisecond duration measurement every 15 s.

6.2.1.4 Trigger system

Solar cell array I cannot power the LED directly because the LED requires at least 5 mA whereas Solar cell array I is capable of only 30 μA. Therefore SCR1 located at the output lead of capacitor C5 allows C5 to become fully charged. When SCR1 is in the off state, the probe is inactive and solar cell array I charges C5 to $\sim$ 15 V. SCR1 is switched on by the trigger system just before measurements. The trigger system is powered by a separate solar cell array II.

A 175 MHz pin photodiode D1 (OPF792, see Fig. 6.1) is used to receive an externally generated optical trigger signal. D1 has a typical dark current $0.1 - 0.5$ nA and outputs current $\geq$ 20 nA when triggered by an optical signal. A PNP transistor Q4 amplifies the current by a factor of 10^4. R3 is selected to be 10 kΩ so that its voltage exceeds 0.7 V only when D1 is triggered. Since R3 is parallel to the BE junction of a NPN transistor Q3, Q3 then switches on because its BE voltage exceeds 0.7 V. Therefore the fully charged capacitor C6 is switched across the gate-cathode junction of SCR1, which turns on in $\sim$ 2 μs. The entire trigger system including SCR1 takes $\approx$ 3 μs to activate the voltage regulator Q2 after receiving the optical trigger signal. Therefore the external trigger signal must be sent to D1 at least 3 μs before measurements.

The dark current of the trigger system is only $\leq$ 0.5 nA$\cdot 10^4$ = 5 μA. Therefore, an ordinary solar cell is fully capable of serving as a power supply for the system under normal lab ambient light. To have the trigger system working reliably, the output voltage of solar cell II must be at least 1.5 V to turn on the Darlington PNP transistor Q4. In a typical configuration, two solar cell units in series form the solar cell array II (see Fig. 6.1).

6.2.2 Receiver

The receiver of the HV probe converts the AM optical signal sent by the transmitter into a voltage signal. Its circuit diagram is shown in Fig. 6.1, essentially an analog HFBR-2416 photodiode receiver. The part numbers are listed in the figure caption. HFBR-2416 outputs an analog voltage signal proportional to the AM optical signal. A voltage regulator Q5 powered by a +9 V battery provides the HFBR-2416 photodiode with constant +5 V.

A battery test can be done by switching the toggle to momentary position 2. The capacitor C10 between HFBR-2416 and 50 Ω data acquisition device adds an AC coupling to the voltage signal output. Its capacitance is 47 μF so that 47 μF$\times$50 Ω = 2.35 ms>> 50 μs, the measurement time.

With the HV source measuring the range −6 to 2 kV and the driving current in the range of 10 to 60 mA for the HFBR-1414 LED, the receiver outputs a proportional voltage signal of −0.15 to 0.05 V (see next section).

The optical fibers totally isolate the transmitter and the high voltage source, and so allow long-distance remote measurement. Meanwhile, the receiver can be safely connected to data acquisition devices directly, such as transient digitizers or oscilloscopes.

6.2.3 Calibration

Knowing the capacitance of C1 and C2, one can use a low voltage source to calibrate the probe without utilizing a high voltage source standard. The calibration to the HV probe can be conveniently done by disconnecting the HV capacitor C2 and connecting a low voltage function generator to the BNC adapter on the aluminum pipe. By doing so we are applying the low voltage directly to the junction point of the capacitive divider.

For example, we apply a 50 kHz ±10 V sine function to the junction point using a WAVETEK model 143 function generator and measure the receiver output using a Tektronix TDS1002 oscilloscope. After calculating the divided voltage in-out gain V_{junc}/V_{out}, the total gain V_{in}/V_{out} is obtained by multiplying it with $(C1 + C2)/C2$, where C1= 100 nF and C2 is measured to be 60 pF using a BK PRECISION model 885 LCR/ESR meter. Figure 6.4 shows the calibration result and verifies the linearity of the probe over the range from −6 to 2 kV.

6.3 Performance and measurement

Figure 6.5 shows a typical measurement of a pulsed power plasma experiment [42, 64, 107] that produces a magnetohydrodynamic plasma loop. The plasma is formed by charging a 60 μF capacitor to −3 kV and discharging it across a neutral Hydrogen gas for $\approx 10 - 20$ μs. The well-defined plasma loop lasts about $5 - 10$ μs and then exhibits complex dynamic behaviors. The entire voltage/current profile lasts about 50 μs during which the voltage

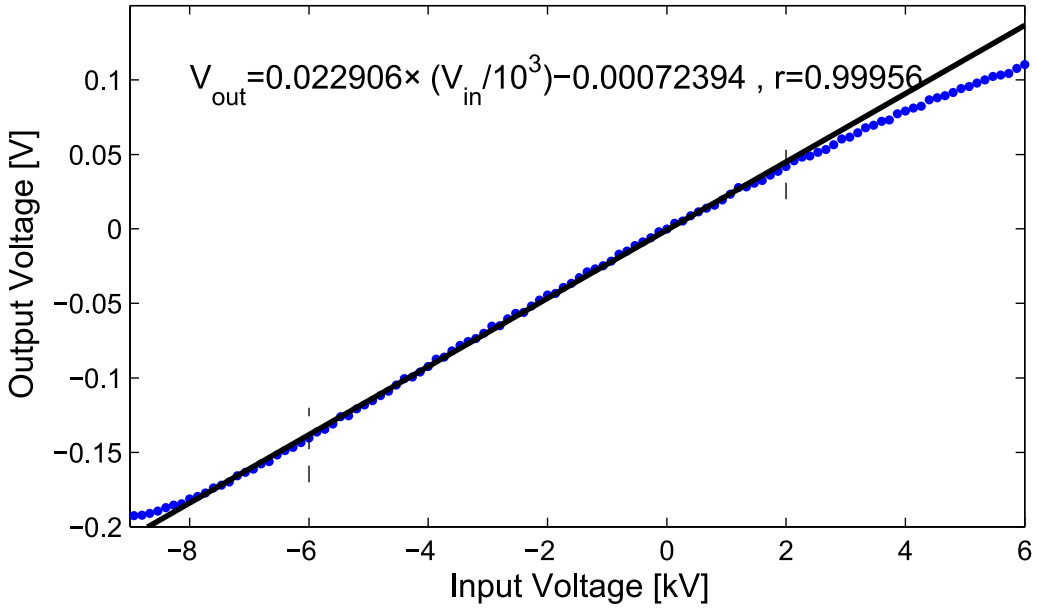

Figure 6.4: HV probe calibration result with C2= 60 pF. The solid line gives the least-square fit to the experimental data (dotted curve) in −6 to 2 kV.

across the electrodes swings between ±3 kV and the current through the electrodes oscillates over ±35 kA. The total power of the plasma can reach ≥ 100 MW. The measurement by the HV probe described by this chapter (stated as the new HV probe in the following content) is compared with the measurement by a Tektronix P6015A 75MHz probe that has been properly compensated. A DC-10MHz analog fiber optic link (732T/R; Analog Modules Inc.) is used to convey the Tektronix probe output to the data acquisition device and break the ground loop. The power supply for the optical link is isolated from earth by a transformer. The new HV probe is calibrated using the method presented in section II. The HV wire and the outer copper pipe in C2 are connected to the anode and cathode of the plasma gun, respectively. A 12-Bit 100MHz VMEbus digitizer (SIS3000, Struck Innovative Systeme) with a 0.5 V dynamic range is used for recording the data.

The detailed voltage profile from 12 to 12.5 μs in the insert in Fig. 6.5 demonstrates that the new HV probe has a white noise generally below 0.03 kV. Figure 6.5 shows that the new HV probe and the Tektronix probe agree with each other quite well over a 50 μs long measurement. The discrepancy between the two probes is generally ≤ 0.05 kV. They both capture fast voltage fluctuations as short as ∼ 0.2 μs (see insert in Fig. 6.5 from 18 to 22 μs).

The NPN transistor Q1, the HFBR-1414 LED and the HFBR-2416 photodiode used in the probe are all high-speed devices with bandwidth $\geq$ 100 MHz. The bandwidth of the probe is determined by the low-pass filter formed by R1 and the BE junction of Q1. The RC time of this low-pass filter is $\approx$ 20 k$\Omega \times$2.5 pF$\sim$ 50 ns, resulting in a $\sim$ 90 ns risetime for the entire HV probe. Although this is sufficient for the $\leq$ 50 μs long voltage measurements, the bandwidth of the probe could be improved by using a smaller R1, say, 3 kΩ (R1$\cdot$C1= 300 μs$>>$ 50 μs is still satisfied). However, this will change the probe sensitivity. Alternatively, the probe could have a wider bandwidth by replacing Q1 by a high speed transistor with sub-pF BE capacitance. A risetime as short as 15 ns should then be achievable using the same LED and photodiode.

The HFBR-2416 photodiode in the receiver is responsible for most of the noise. The unfiltered RMS output noise of the photodiode is $\leq$ 0.6 mV, corresponding to an input voltage $\leq$ 0.025 kV assuming system gain 0.0229 V/kV. The digitization rounding error of SIS3000 is $1\text{V}/2^{12} = 0.25\text{mV}$, corresponding to a 0.01kV input voltage. The combination of the two noise sources gives $\sim$ 0.03kV, consistent with Fig. 6.5. The power of the output noise is only $\leq (0.7\text{ mV})^2/50\ \Omega \sim 10$ nW, which is $\leq 10^{-16}$ times of the total power of the pulsed power plasma.

The system has a temperature dependence of $\approx 1.5\%/C^\circ$ at room temperature in V_{out}/V_{in} gain, mostly contributed by the HFBR-1414 LED in the transmitter. The heat generated by the circuit is negligible since each measurement lasts for milliseconds. However, the probe should be recalibrated if the ambient temperature has varied significantly.

In conclusion, we have reported an ambient light powered wideband optically-coupled floating-input active HV probe. Because of its excellent EMI/RFI shielding, the HV probe is useful for precise measurement of pulsed high voltages over a DC$-$5MHz bandwidth in a noisy environment. Due to the special connection design for the capacitive divider, the HV probe has an adjustable measurement range and is easy to calibrate.

6.4 HV probes in usage

The optically coupled floating HV probes are being actively used in the Cross-Flux-Tube experiment (Fig. 6.6AB), arched plasma loop experiment (Fig. 6.6C), and RF pre-ionized jet experiment (Fig. 6.6D) in the Caltech Bellan group, and are also duplicated and used

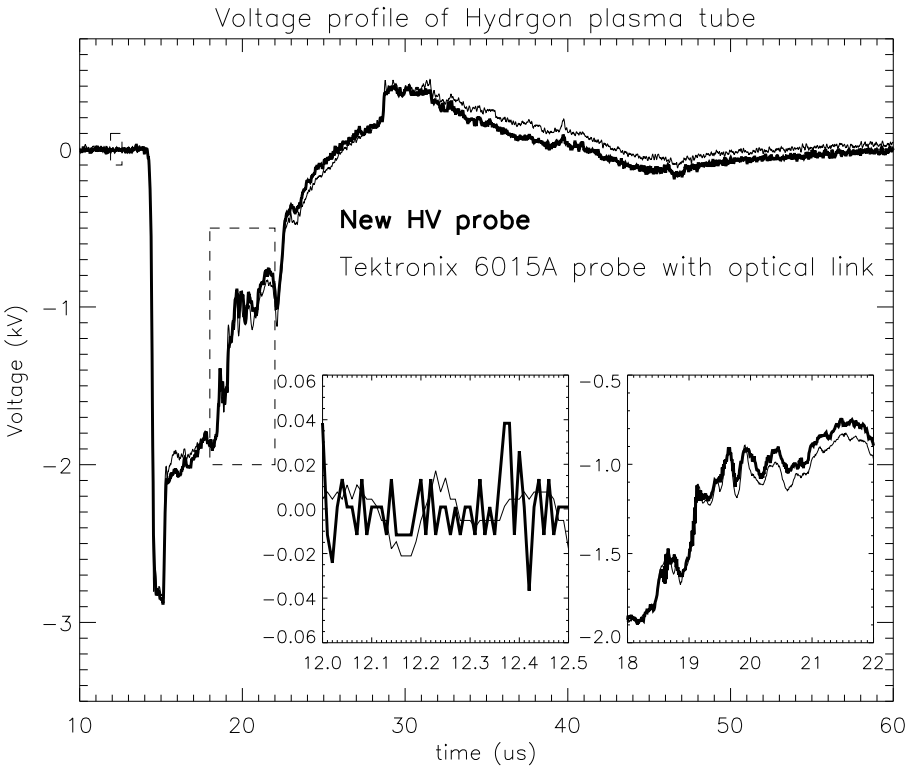

Figure 6.5: Voltage across a pulse powered Hydrogen plasma measured by the new HV probe (the heavy curve) and a Tektronix P6015A HV probe (the light curve). Two boxes at right lower corner zoom into the time interval $12 - 12.5\mu$s and $18 - 22\mu$s, showing the detailed behavior of the voltage profile. The high voltage is applied at 14.5μs. The two measurement curves are unsmoothed raw data multiplied by the corresponding calibration factors. Shot number=9950.

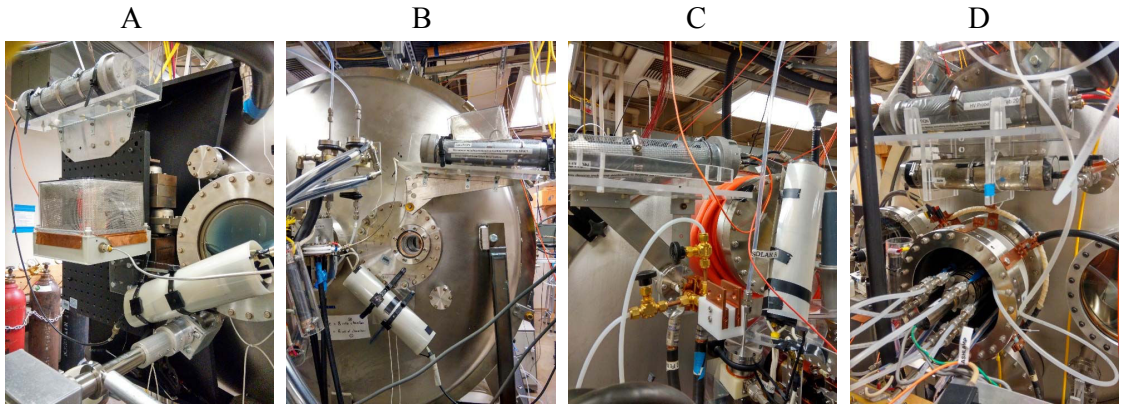

Figure 6.6: Optically coupled floating HV probes used in the cross-flux-tube experiment (A and B), arched-loop experiment (C), and RF pre-ionized plasma jet experiment (D).

by the You group at University of Washington, Seattle.

One of the greatest advantages of this HV probe is that it is totally floating on the HV source. In the cross-Flux-Tube experiment, two arched plasma tubes are created by two isolated power supplies. To measure the true voltages across each plasma tubes, we must use the floating HV probes. If we use two Tektronix probes, the two plasma tubes will be electrically connected via the ground clips. If we do not attach the ground clips of the Tektronix probes to the electrodes, then we need four probes to be able to measure the true differential voltages across the two plasma tube. Using two earth-isolated optically coupled probes solves the problem.

6.5 Some discussion about the solar cells

It has been reported that sometimes the solar cells do not work very consistently. The solar cells, despite their obvious advantages, can in fact be replaced by regular batteries to provide more reliable performance. Another benefit of using batteries is that the transmitter (not including the lab-made HV capacitor) can be made very compact since solar cells are the primary reason for the size of the transmitter. However, it is crucially important to point out that the batteries must be connected to large-value resistors in series to limit the output current from the batteries. The current-limiting resistors should be selected so that the maximum output current from the batteries is below the holding current of the SCR, which is about 5 mA. Otherwise the transmitter will work continuously and drain the batteries in hours.

Chapter 7

Summary

The Caltech experimental plasma jet is created by a magnetized coplanar coaxial electrode system and then collimated and accelerated by Magnetohydrodynamic (MHD) forces. When the current-carrying plasma jet is sufficiently long, it undergoes a current-driven ideal MHD instability, the kink instability as an attempt to relax to a lower energy state. As the kink instability grows exponentially fast, an effective lateral gravity due to the accelerating kink further induces a secondary instability called the Rayleigh-Taylor instability. The Rayleigh-Taylor instability occurs on a much smaller scale and a much faster speed and quickly evolves to a nonlinear phase. The plasma jet is pinched and compressed to a scale smaller than the ion skin depth by the Rayleigh-Taylor instability so that ions are decoupled from electrons and MHD theory fails. This further leads to a fast magnetic reconnection during which the magnetic field lines break and reconnect to form a new topology. Whistler waves are found to be associated with the reconnection event, indicating that the reconnection is in the two-fluid regime.

The plasma jet experiment is related to the launching and propagation of highly collimated astrophysical jets, plasma relaxation and spheromaks, plasma instabilities, magnetic reconnection, and plasma waves.

This thesis has described a series of experimental, numerical, and analytical studies about the Caltech plasma jet experiment.

First, the collimation and acceleration of the experimental jet is simulated numerically using an astrophysical magnetic tower model as the baseline (Chapter 2). The fundamental concept behind this work is that an ideal MHD plasma does not have any intrinsic scale.

In the simulation, we implement a purely toroidal magnetic injection localized around the central $z = 0$ plane and find that the simulation jet gains energy and helicity in a manner analogous to both the electrode-driven experimental jet and to astrophysical jets driven by accretion disks. The injected toroidal field near $z = 0$ generates a pinch force that collimates the plasma and the embedded magnetic field. A radial force balance between plasma pressure and Lorentz force is gradually established from small z to large z, resulting in a pumping mechanism that accelerates the plasma jet away from the central $z = 0$ plane. During this process, magnetic energy is converted to kinetic energy. The simulation jet agrees quantitatively with the experimental jet including the energy evolution, jet radius, velocity, and magnetic field structure.

The success of using an astrophysical model to simulate the lab experiment shows the importance of using terrestrial laboratory experiments to study astrophysical plasma phenomena. Because lab experiments share many advantages with numerical simulation such as reproducibility, freedom in parameter space, and possibility of in-situ measurement, detailed comparison between experiment and simulation can be made and then validation to the astrophysical model is deemed applicable.

The secondary instability induced by the laterally accelerating kink instability has been analytically modeled using ideal MHD (Chapter 3). We find that this instability is a new hybrid lateral Rayleigh-Taylor-Current-Driven coupled instability. The coexistence of lateral gravity and cylindrical geometry leads to a complex coupling of all azimuthal modes of the cylinder, a fundamentally different situation compared to results from a 1D or 2D Rayleigh-Taylor instabilities on planar interfaces. The coupled instability reduces to the classic current-driven instability (kink instability) in the weak gravity limit and to the conventional hydrodynamic or magnetic RT instability in the strong gravity limit. In the general cases such as Caltech argon plasma jet and type II hydrogen jet, the Rayleigh-Taylor and current-driven instabilities are coupled to result in a new hybrid instability.

We define a useful parameter $\Phi^2 = \mu_0 \rho_0 g R / b_\theta^2$ to quantify the relative importance of gravity versus toroidal magnetic field. This interesting parameter includes azimuthal magnetic field b_θ, curvature R, plasma density ρ_0, and gravity g. It is completely determined by the equilibrium state. Φ^2 can be written as $\Phi^2 = (\rho_0 g R)/(b_\theta^2/\mu_0)$, which is the ratio of gravitational energy density to toroidal magnetic energy. It can also be written as

$\Phi^2 = g/(v_{A\theta}^2/R)$, the ratio of real gravity to effective gravity due to the curvature of the azimuthal magnetic field. The real gravity g is responsible for the RT instability and $v_{A\theta}^2/R$ is responsible for the current-driven instability. Φ^2 describes whether a flux rope is more susceptible to the RT instability (if $\Phi^2 \gg 1$) or the current-driven instability (if $\Phi^2 \ll 1$), or coupled instability ($\Phi^2 \sim 1$).

The RT-CD coupled instability theory successfully explains the experimental observations. For the argon jet, the theory predicts correct instability wavelength and growth rate. For the slow-growing type I hydrogen jet the theory shows that the RT effect is not important and the instability is dominantly current-driven and for the fast-growing type II hydrogen jet, the theory gives RT-CD coupled instability. Conventional MRT instability theory that only considers axial magnetic field and axial perturbation is able to partially explain the argon jet, but fails to consider interchange mode or explain hydrogen jets.

This RT-CD coupled instability can be applied in many situations where a flux rope is presented in a lateral gravity. In those situations, there are three 'types' of gravity: real gravity due to mass attraction, effective gravity due to kinetic acceleration, and effective gravity due to magnetic curvature. I have discussed several applications of the RT-CD theory in § 3.7 including solar coronal loop, quiescent prominence, coronal mass ejection, and flux emergence.

As the Rayleigh-Taylor instability grows to a nonlinear phase, MHD becomes invalid. A fast magnetic reconnection is then induced. We detected 3D high-frequency magnetic fluctuations consisting of broadband right-hand circularly polarized whistler waves associated with the fast magnetic reconnection (Chapter 4) using a specially designed high-speed 3D magnetic probe (Chapter 5). The 3D magnetic probe is composed of orthogonal pairs of oppositely orientated shielded loop B-dot probes. An RF ground current diverting technique is implemented. The probe has an overal 70 dB rejection to capacitive interference. The magnetic fluctuations measured by the probe reveal a continuous $\dot{B} \sim f^{-1}$ power-law spectra. The fluctuations are not random turbulence because different modes are somewhat coherent, indicating that these modes may originate from a single source. We resolve the circular polarization of obliquely propagating whistler waves, consistent with theoretical modes and space observations. The oblique angles between the whistler wave propagation direction and the background magnetic field are primarily within 60°. The detection and

recognition of whistler waves associated with the magnetic reconnection shows that the reconnection is a Hall magnetic reconnection (fast magnetic reconnection) and the dynamics are in the two-fluid, not MHD, regime.

In Chapter 6 we designed and built an earth-isolated optically coupled DC-5 MHz wideband high voltage probe powered by solar cells under lab ambient light. The excellent EMI/RFI shielding and the earth-isolation property make the HV probe useful for precise measurement of pulsed floating high voltages in a noisy environment.

Appendix A

Two-color Imaging of the Plasma Jet Experiment using VariSpec Liquid Crystal Tunable Filter

A brief review of the VariSpec liquid crystal tunable filter was given in § 1.2.2.3. In this appendix we provide more details about the tunable filter and the hot mirror. Then we perform a two-color imaging of the plasma jet experiment using the tunable filter.

A.1 VariSpec liquid crystal tunable filter

The VariSpec liquid crystal tunable filter (VIS-7-35, serial No. 51892) is a compact, solid-state optical filter with the wavelengths of the light transmitted controllable electronically. The tunable filter was manufactured by Cambridge Research & Instrumentation, Inc. (CRi), which is now part of PerkinElmer Life Sciences. The filter has a 35 mm diameter working aperture and allows up to 7.5° incident angles. The tunable range of the filter spans the entire visible band, i.e., the central transmitting wavelength can be adjusted continuously from 400 nm to 720 nm with a 0.1 nm step size. When set at a fixed wavelength, the tunable filter behaves like an interference filter with the transmission curve following a Gaussian function. The peak transmission and Full-Width-Half-Maximum (FWHM) of the Gaussian transmission curve are functions of the central wavelength (Figure A.1). For example, when the filter is set at 667 nm, it has a peak transmission rate 0.51 at 667 nm and a FWHM 11 nm, meaning that at 656 nm and 678 nm the transmission rates are $0.5 \times 0.51 = 0.255$.

The tunable filter when coupled with the IMACON 200 camera gives a powerful 2D fast framing spectroscopic system. The drawbacks of the filter are the relatively low peak

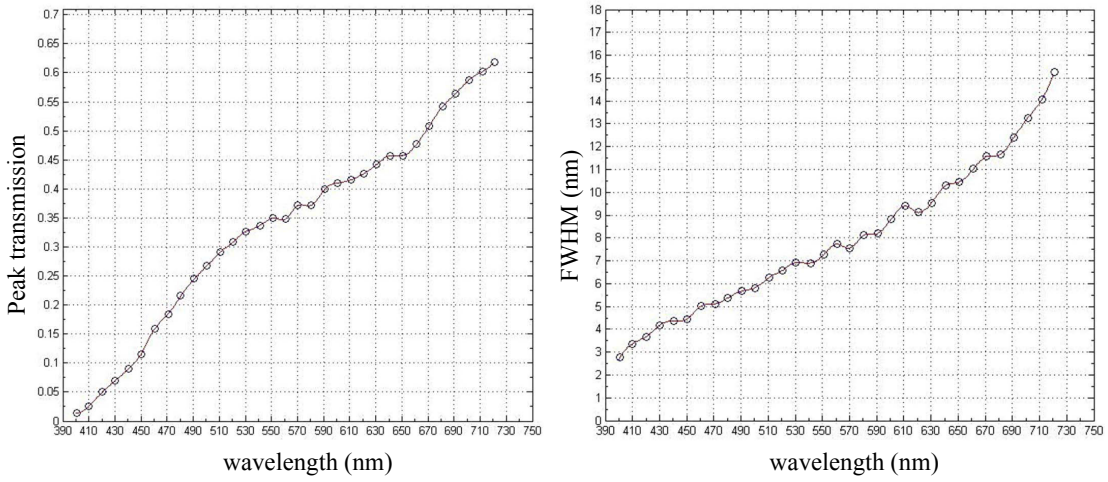

Figure A.1: Peak transmission rate and FWHM of the tunable filter as a function of central wavelength.

transmission at short wavelengths and wide FWHM at long wavelengths.

A.1.1 Hot mirrors

The VariSpec filter has a built-in hot mirror to reflect unwanted near-infrared (NIR) photons. The hot mirror, as suggested from its name, reflects infrared photons which can efficiently heat up materials when absorbed.

However, it is found that the plasma jet images taken by the IMACON 200 camera filtered by the VariSpec filter at different wavelengths are very similar, even if at the wavelengths that the plasma is not supposed to emit. The IMACON 200 camera is sensitive to visible and NIR light. On the other hand, the filter appeared to be working properly when judged by human eyes. Therefore, it is suspected that the tunable filter still allows significant amounts of NIR photons to pass through that are later recorded by the IMACON 200 camera.

We therefore mounted a 50.8 mm $\times$50.8 mm external hot mirror (Newport Optics, 20HMS-0[1]) in front of the VariSpec filter. The hot mirror reflects more than 90% NIR photons with wavelength from 720 nm to 1500 nm and allows incidence angle from 0° to $\pm$15°.

With the external hot mirror the VariSpec tunable filter works exceptionally (see Fig. A.4).

[1] see http://search.newport.com/?q=*&x2=sku&q2=20HMS-0

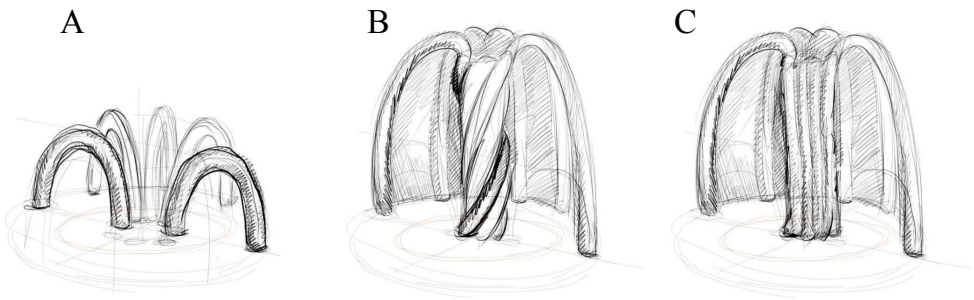

Figure A.2: Sketches of the "spider-leg" configuration as the initial state of the plasma (panel A) and two possible configurations of the plasma jet after collimated. Sketches from Setthivoine You.

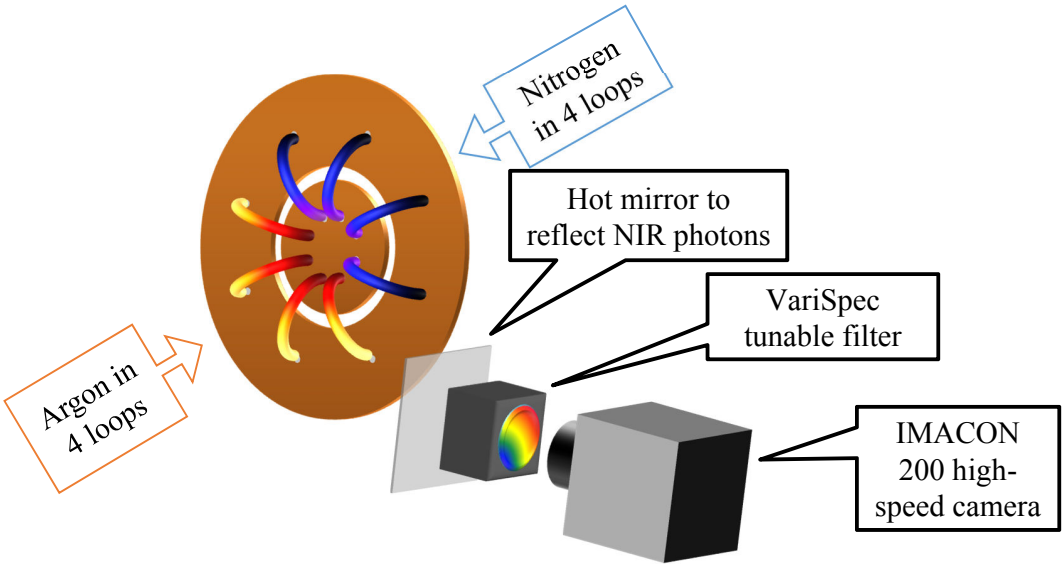

Figure A.3: Setup of the two-color imaging of the plasma jet filled by nitrogen and argon.

A.2 Two-color imaging of the plasma jet experiment

As the single collimated plasma jet forms after merging from an initial "spider-legs" configuration (Fig. A.2 panel A), two different configurations are possible. One is that the eight plasma tubes twist around each other (Fig. A.2 panel B) and the other one is that the eight plasma tubes remain parallel (Fig. A.2 panel C).

To resolve this question, we perform a two-color imaging of a dual-species plasma jet. Four the eight initial plasma tubes are filled by nitrogen and the other four are filled by argon. Figure A.3 shows the configuration of the experiment and the imaging system. Two shots are performed with the tunable filter set at 568 nm and 667 nm, respectively. At 568

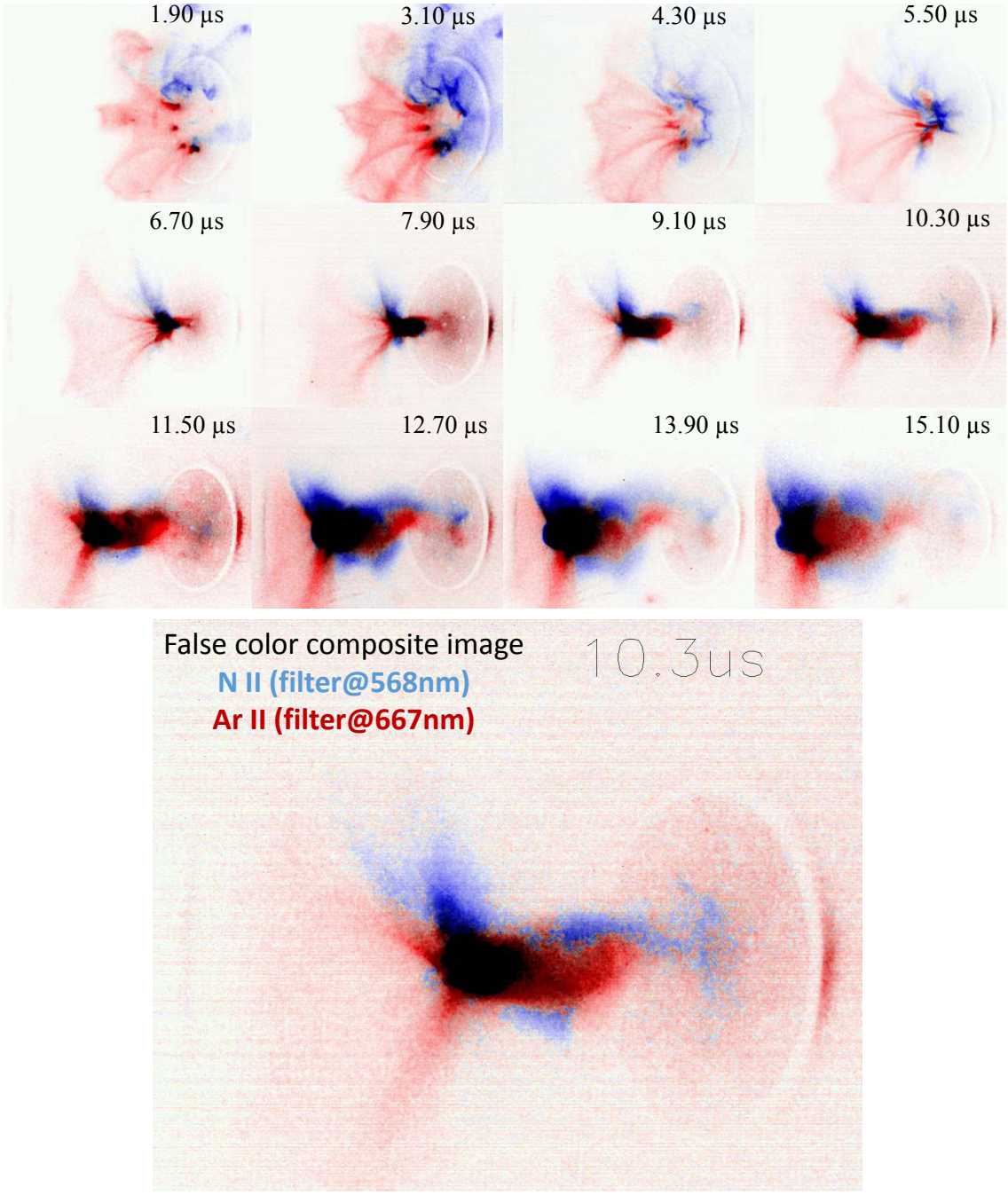

Figure A.4: Top 12 panels: time-sequence of the two-color imaging of the N-Ar dual-species plasma jet. Ar II emissions at 667 nm (shot 14365) are represented by red color and N II lines at 568 nm (shot 14366) are represented by blue color. The frame at 10.3 μs is magnified and presented as the bottom panel.

nm the tunable filter has a peak transmission = 0.37 and a FWHM = 7 nm and so transmits four major N II lines (567.6 nm, 568.0 nm, 568.6 nm and 571.1 nm) but not argon lines. At 667 nm the tunable filter transmits five Ar II lines (663.8 nm, 664.0 nm, 664.4 nm, 666.6

nm and 668.4 nm) but no important nitrogen lines.

Figure A.4 gives a time series of the two-color imaging of the nitrogen-argon dual species plasma jet using the tunable filter with the hot mirror. The figure shows that the tunable filter is fully functional as it distinguishes nitrogen plasma and argon plasma correctly and clearly. It is shown that the plasma filaments are twisted around the central axis, following a configuration shown in Fig. A.2 panel B. Magnetic reconnection is required in order to have the plasma configuration change from Fig. A.2A to Fig. A.2B.

Appendix B

Useful Signal Processing Algorithms

In this appendix chapter we will review some signal processing algorithms. These mathematical tools are very important to properly analyze wave/fluctuation measurements. In Chapter 4 we used these tools extensively.

B.1 Fourier transform and discrete Fourier transform

Fourier transform is an operation that decomposes a function of time into an ensemble of single-frequency oscillations. For a given function of time $f(t)$, its Fourier transform is given by

$$\hat{f}(\omega) = \int_{-\infty}^{+\infty} f(t) e^{-i\omega t} dt, \tag{B.1}$$

where both t and ω are real numbers. This equation is sometimes called forward Fourier transform. The inverse Fourier transform is given by

$$f(t) = \frac{1}{2\pi} \int_{-\infty}^{+\infty} \hat{f}(\omega) e^{i\omega t} d\omega. \tag{B.2}$$

This is because

$$\begin{aligned}
\frac{1}{2\pi}\int_{-\infty}^{+\infty}\hat{f}(\omega)e^{i\omega t}d\omega &= \frac{1}{2\pi}\int_{-\infty}^{+\infty}\left(\int_{-\infty}^{+\infty}f(t')e^{-i\omega t'}dt'\right)e^{i\omega t}d\omega \\
&= \frac{1}{2\pi}\int_{-\infty}^{+\infty}\int_{-\infty}^{+\infty}f(t')e^{i\omega(t-t')}d\omega dt' \\
&= \int_{-\infty}^{+\infty}\left(\frac{1}{2\pi}\int_{-\infty}^{+\infty}e^{i\omega(t-t')}d\omega\right)f(t')dt' \\
&= \int_{-\infty}^{+\infty}\delta(t-t')f(t')dt' = f(t), \qquad \text{(B.3)}
\end{aligned}$$

where the Dirac Delta function is

$$\delta(x) = \frac{1}{2\pi}\int_{-\infty}^{+\infty}e^{ixp}dp. \qquad \text{(B.4)}$$

Now consider a general function $h(t)$ assembling all $e^{i\omega t}$ modes and each mode has a different phase $\theta(\omega)$, i.e.,

$$h(t) = \int_{-\infty}^{+\infty}g(\omega)e^{i(\omega t+\theta(\omega))}d\omega, \qquad \text{(B.5)}$$

where $g(\omega)$ is the amplitude of mode $e^{i\omega t}$. Without loss of generality, we assume $g(\omega)$ is positive for all ω (if not, we can always choose $\theta(\omega)\to\theta(\omega)+\pi$ to get a positive $g(\omega)$). The Fourier transform of $h(t)$ is

$$\begin{aligned}
\hat{h}(\omega) &= \int_{-\infty}^{+\infty}h(t)e^{-i\omega t}dt \\
&= \int_{-\infty}^{+\infty}\int_{-\infty}^{+\infty}g(\omega')e^{i(\omega' t+\theta(\omega'))}e^{-i\omega t}d\omega' dt \\
&= \int_{-\infty}^{+\infty}g(\omega')e^{i\theta(\omega')}\left[\int_{-\infty}^{+\infty}e^{i(\omega'-\omega)t}dt\right]d\omega' \\
&= 2\pi\int_{-\infty}^{+\infty}g(\omega')e^{i\theta(\omega')}\delta(\omega'-\omega)d\omega' \\
&= 2\pi g(\omega)e^{i\theta(\omega)}. \qquad \text{(B.6)}
\end{aligned}$$

Therefore the absolute value of $\hat{h}(\omega)$ gives the amplitude of the corresponding mode and the argument of $\hat{h}(\omega)$ gives the initial phase of this mode, i.e.,

$$|\hat{h}(\omega)| = 2\pi g(\omega) \qquad \arg[\hat{f}(\omega)] = \theta(\omega). \qquad \text{(B.7)}$$

The definition of Fourier transform Eq. B.1 involves continuous integration in an infinitely long time period. In reality, however, we only have finite-length, discrete-time measurement. Therefore the discrete Fourier transform (DFT) is required. Assume a measurement starts at time $t_0 = 0$ and has a sampling rate F_s. Hence the sampling time interval is $\Delta t = 1/F_s$ and the n^{th} sampling time is $t_n = n\Delta t = n/F_s$. Assume the measurements are a length-N sequence $\{x_0, x_1, \cdots, x_{N-1}\}$. The DFT of $\{x_n\}$ is

$$X_k \equiv \sum_{n=0}^{N-1} x_n \cdot e^{-2\pi ikn/N} = \sum_{n=0}^{N-1} x_n \cdot e^{-i(2\pi kF_s/N)t_n}, \qquad k \in \mathbb{Z}. \tag{B.8}$$

X_k is the complex coefficient of the $\omega_k \equiv 2\pi kF_s/N = (2\pi/T)k$ sinusoidal component, where $T = N/F_s = N\Delta t$ is the total measurement period. Sometimes people use X_k/N instead of X_k to represent the amplitude of the ω_k sinusoidal component. The frequency interval is $\Delta\omega = \omega_k - \omega_{k-1} = 2\pi/T$. Hence longer measurement period gives finner Fourier spectrum.

Because the DFT is performed on discrete time, an aliasing effect exists, i.e.,

$$\begin{aligned} X_{k+N} &= \sum_{n=0}^{N-1} x_n \cdot e^{-2\pi ik(n+N)/N} \\ &= \sum_{n=0}^{N-1} x_n \cdot e^{-2\pi ikn/N} \cdot e^{-2\pi ik} \\ &= \sum_{n=0}^{N-1} x_n \cdot e^{-2\pi ikn/N} \\ &= X_k. \end{aligned} \tag{B.9}$$

In fact, it can also be shown that $X_{k+N/2} = X_k$ if k is even and $X_{k+N/2} = -X_k$ if k is odd. Hence $|X_{k+N/2}| = |X_k|$. Hence we only have to compute X_k for $k = 0, 1, \cdots, N/2-1$, corresponding to frequencies from DC to $\omega_{N/2-1} = (2\pi/T)(N/2-1) \approx \pi N/T = \pi/\Delta t = \pi F_s$. Intuitively, this is because the sampling rate F_s is finite, so the measurement is only able to capture low frequency components with $\omega < \pi F_s$ or $f = \omega/2\pi < F_s/2$.

To obtain X_k for $k = 0, 1, \cdots, N/2-1$, Eq. B.8 needs to be computed for $N/2$ times. Therefore the time complexity of the DFT is $O(N^2)$, meaning that a total number of N^2 multiplication operations need to be performed.

Fast Fourier transform (FFT) is an efficient algorithm to compute DFT, which has a time complexity of $O(N \log N)$. FFT is most efficient if N is a 2-power number, i.e., $N = 2^m$

where m is an integer.

B.2 Finite impulse response (FIR) filter

Real measurement is usually an ensemble of modes of different frequencies. To study the properties of a single frequency component, it is necessary to use bandpass filter to select some specific component of interest. Digital filters are usually preferred because they are the only option when post-measurement process is required. In this section we will have a brief review of finite impulse response (FIR) filter, a type of widely used digital filter.

In a naive attempt we might perform a Fourier transform to an input data, multiply the spectrum by a bandpass function, say, step function, and then perform an inverse Fourier transform to get a 'filtered' signal. This method is in general not working at all because it introduces significant numerical instabilities. A stable and more efficient way is to use finite impulse response (FIR) filter.

Consider an input signal $x_0, x_1, \cdots$. The output of an M^{th}-order discrete-time FIR filter is a weighted sum of M most recent input values, i.e.,

$$y_n = b_0 x_n + b_1 x_{n-1} + \cdots + b_M x_{n-M} = \sum_{i=0}^{M} b_i x_{n-i}, \tag{B.10}$$

where b_i is the coefficient of the filter. The computation is in fact a discrete convolution. The summation involves finite length of input signal and does not have any feedback. Consider a single impulse input signal (delta function) $x_n = \delta_{n0}$, i.e., $x_0 = 1$ and $x_i = 0$ for $i > 1$, the impulse response is

$$h[n] = \sum_{i=0}^{M} b_i x_{n-i} = \begin{cases} b_n & 0 \le n \le M \\ 0 & \text{otherwise} \end{cases}, \tag{B.11}$$

i.e., the coefficients of a filter are the same as the impulse response samples of the filter. Because M is finite, the filter has a finite response to an impulse. The filter's frequency response is

$$H(\omega) = \sum_{n=0}^{N-1} h[n] e^{-in\omega}, \tag{B.12}$$

here $\omega = 2\pi f$ and f is normalized to F_s, the sampling frequency. With proper selected

coefficients $h[n]$ or b_n, the FIR filter Eq. B.10 can select or stop components of certain frequencies.

There are a lot of widely used FIR filters and most of them are named after some analog electric filters, such as Butterworth filter, Chebyshev filter, and elliptical filter. These digital FIR filters are designed so that the selection of $h[n]$ gives same frequency and phase response as the corresponding analog filters. In this thesis we will use Butterworth filter, which has a flat frequency response in the favored band. Specifically, an Mth order low pass Butterworth filter has a frequency response as

$$G(\omega) = \sqrt{\frac{1}{1+\omega^{2M}}}, \tag{B.13}$$

where the cutoff frequency has been normalized to 1 rad/sec. For $\omega \gg 1$, $G(\omega) \sim \omega^{-M}$, corresponding to a power-law type cutoff. For $\omega \ll 1$, $G(\omega) \sim 1$, corresponding to a flat unit-gain response.

The following code shows how to use build-in functions in Matlab to implement Butterworth digital bandpass filter.

```
X       = ...;              %input data
Fs      = 100;              %sampling frequency
Band    = [10,20];  %frequency band
M       = 4;                %filter order

[b,a]   = butter(M,Band/(Fs/2));
%generate Butterworth filter coefficients
%Band needs to be normalized by Fs/2

Y       = filter(b,a,X); %apply Butterworth filter

[h,w]   = freqz(b,a,200);
%compute freq response h as function of angular frequency.
```

Figure B.1 demonstrates the efficiency of a 4th order Butterworth FIR digital filter. The

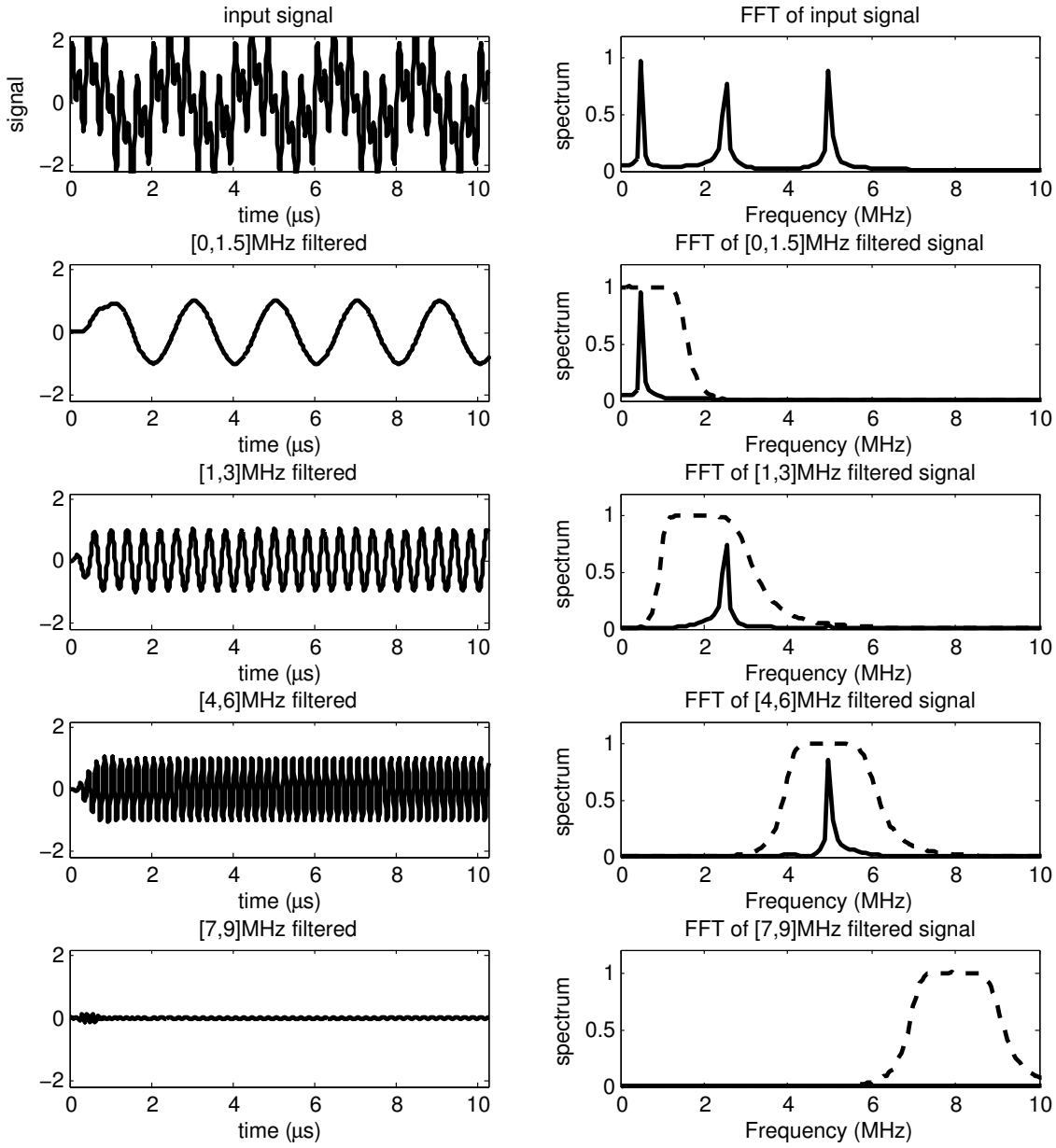

Figure B.1: Upper left panels: input signal given in Eq. B.14. Four lower left panels: signal filtered by different Butterworth bandpass filters. Right panels: spectra of the input signal and filtered signals by FFT. The dashed curves show the frequency response of the digital filters.

input signal contains three single frequency components

$$x(t) = \sin(2\pi f_1 t) + \sin(2\pi f_2 t) + \sin(2\pi f_3 t) \qquad t > 0, \tag{B.14}$$

where $f_1 = 0.5$ MHz, $f_2 = 2.5$ MHz and $f_3 = 5$ MHz. The measurement is from $t = 0$ to $t = 10.24$ μs with a sampling rate $F_s = 100$ MHz. A $[0, 1.5]$ MHz low pass filter, $[1, 3]$ MHz bandpass filter, $[4, 6]$ MHz bandpass filter and a $[7, 9]$ MHz bandpass filter are applied individually to the input signal. Fig. B.1 shows that the performance of the Butterworth FIR digital filter is very good except for the first 0.5 μs. This is because the input signal contains a step-function type impulse component at $t = 0$ and this impulse has a full spectrum. According to the definition of FIR filter, an impuse at $t = 0$ impacts filtered signal after $t = 0$ but this impact is limited to only a finite period.

B.3 Principal component analysis

Principal component analysis (PCA) is a data analysis procedure that converts a set of measurements of possibly correlated variables into a set of values of linearly uncorrelated variables called principal components. The PCA uses an orthogonal transformation to find a new orthogonal coordinate system so that after projection to the new coordinate system the variables are linearly independent from each other.

Figure B.2 shows an example of PCA that converts a coupled 2D data set into two decoupled 1D data sets. Two principal components indicated by the two arrows are obtained by PCA. The length of each arrow represents the importance of this principal components. Note that the first principal component, represented by the longer arrow along $(0.878, 0.478)$, can also be considered as a linear fit to the data. This linear fit is equivalent to finding a straight line $ax + by = c$ so that the summation of distance of each data point (x, y) to this straight line is minimized. This is different from the conventional linear regression which minimizes the summation of squared distances between y (the dependent variable of data) and $\hat{y}$ (fitted dependent variable). In PCA, variables x and y are treated equally but in linear regression x is treated as an independent variable and y is treated as a dependent variable. In statistics, independent variables are assumes to have zero uncertainties.

Measurements from the 3D Whistler probe contains three variables: $x = dB_r/dt$, $y =$

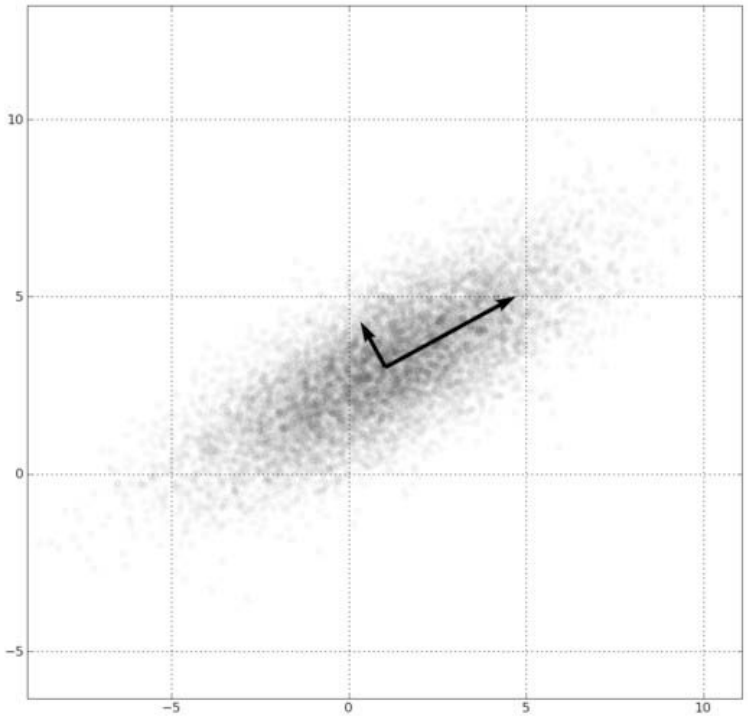

Figure B.2: An example of PCA to a 2D data set. The scattered data points are distributed according to a bivariate Gaussian distribution centered at $(1, 3)$ with a standard deviation of 3 along the $(0.878, 0.478)$ direction and of 1 in the orthogonal direction $(-0.478, 0.878)$. The two arrows gives the new coordinate system by PCA so that the data distribution along each direction is independent on the distribution along the other direction. The plot is created by Ben FrantDale under GNU Free Documentation License.

dB_θ/dt and $z = dB_z/dt$. If the magnetic fluctuations are indeed caused by whistler wave, which has a circularly polarized magnetic component, then there should exist a 2D plane in the 3D space so that the data points (x, y, z) fall on this 2D plane. By performing PCA we can obtain three orthogonal principal components (directions). The first two principal components define the 2D plane that has the minimal summation of the projected distances of the data points (x, y, z). The third principal component defines the normal vector to the 2D plane, i.e., the wave vector of the circularly polarized whistler wave, with an ambiguity of ± 1 sign.

Bibliography

[1] M. Abramowitz and I. A. Stegun. *Handbook of Mathematical Functions: With Formulas, Graphs, and Mathematical Tables*. New York: Dover Publications, 1964.

[2] D. J. Acheson. Instability by magnetic buoyancy. *Solar Phys.*, 62:23–50, 1979.

[3] P. M. Bellan. *Spheromaks: A Practical Application of Magnetohydrodynamic Dynamos and Plasma Self-Organization*. London: Imperial College Press, 2000.

[4] P. M. Bellan. Why current-carrying magnetic flux tubes gobble up plasma and become thin as a result. *Phys. Plasmas*, 10:1999–2008, 2003.

[5] P. M. Bellan. *Fundamentals of Plasma Physics*. Cambridge University Press, 2006.

[6] P. M. Bellan. Circular polarization of obliquely propagating whistler wave magnetic field. *Phys. Plasmas*, 20:082113, 2013.

[7] P. M. Bellan. Fast, purely growing collisionless reconnection as an eigenfunction problem related to but not involving linear whistler waves. *Phys. Plasmas*, 21:102108, 2014.

[8] P. M. Bellan, M. Livio, Y. Kato, S. V. Lebedev, T. P. Ray, A. Ferrari, P. Hartigan, A. Frank, J. M. Foster, and P. Nicola. Astrophysical jets: Observations, numerical simulations, and laboratory experiments. *Phys. Plasmas*, 16:041005, 2009.

[9] M. A. Berger. Introduction to magnetic helicity. *Plasma Physics and Controlled Fusion*, 41:B167–B175, 1999.

[10] T. Berger, P. Testa, A. Hillier, P. Boerner, B. C. Low, K. Shibata, C. Schrijver, T. Tarbell, and A. Title. Magneto-thermal convection in solar prominences. *Nature*, 472:197–200, 2011.

[11] R. Betti, V. N. Goncharov, R. L. McCrory, and C. P. Verdon. Growth rates of the ablative rayleightaylor instability in inertial confinement fusion. *Phys. Plasmas*, 5:1446–1454, 1998.

[12] J. Birn, J. F. Drake, M. A. Shay, B. N. Rogers, R. E. Denton, M. Hesse, M. Kuznetsova, Z. W. Ma, A. Bhattacharjee, A. Otto, and P. L. Pritchett. Geospace environmental modeling (gem) magnetic reconnection challenge. *J. Geophys. Res.: Space Phys.*, 106(A3):3715–3719, 2001.

[13] D. Biskamp. Magnetic reconnection via current sheets. *Phys. Fluids (1958-1988)*, 29(5):1520–1531, 1986.

[14] R. D. Blandford and D. G. Payne. Hydromagnetic flows from accretion discs and the production of radio jets. *Mon. Not. Roy. Astron. Soc.*, 199:883–903, 1982.

[15] C. A. Bleys. Floating input, optically isolated, high-voltage measurement probe. *Rev. Sci. Instrum.*, 47:621–623, 1976.

[16] C. F. M. Carobbi, L. M. Millanta, and L. Chiosi. The high-frequency behavior of the shield in the magnetic-field probes. In *Proc. IEEE. Int. Symp. Electromagnetic. Compatibility*, volume 1, pages 35–40, 2000.

[17] K.-B. Chai and P. M. Bellan. Extreme ultra-violet movie camera for imaging microsecond time scale magnetic reconnection. *Rev. Sci. Instrum.*, 84:123504, 2013.

[18] S. Chandrasekhar. *Hydrodynamic and Hydromagnetic Stability.* Oxford: Clarendon Press, 1961.

[19] O. Chang, S. P. Gary, and J. Wang. Whistler turbulence at variable electron beta: Three-dimensional particle-in-cell simulations. *J. Geophys. Res.: Space Phys.*, 118(6):2824–2833, 2013.

[20] A. Ciardi, S. V. Lebedev, A. F., F. Suzuki-Vidal, G. N. Hall, S. N. Bland, A. Harvey-Thompson, E. G. Blackman, and M. Camenzind. Episodic magnetic bubbles and jets: Astrophysical implications from laboratory experiments. *Astrophys. J. Lett.*, 691:L147, 2009.

[21] A. Ciardi, S. V. Lebedev, A. Frank, E. G. Blackman, J. P. Chittenden, C. J. Jennings, D. J. Ampleford, S. N. Bland, S. C. Bott, J. Rapley, G. N. Hall, F. A. Suzuki-Vidal, A. Marocchino, T. Lery, and C. Stehle. The evolution of magnetic tower jets in the laboratory. *Phys. Plasmas*, 14:056501, 2007.

[22] E. Clausen-Brown, M. Lyutikov, and P. Kharb. Signatures of large-scale magnetic fields in active galactic nuclei jets: transverse asymmetries. *Mon. Not. Roy. Astron. Soc.*, 415(3):2081–2092, 2011.

[23] S. A. Colgate, T. K. Fowler, H. Li, and J. Pino. Quasi-static model of collimated jets and radio lobes. i. accretion disk and jets. *Astrophys. J.*, 789:144, 2014.

[24] X. H. Deng and H. Matsumoto. Rapid magnetic reconnection in the Earth's magnetosphere mediated by whistler waves. *Nature*, 410:557–560, 2001.

[25] D. Dobrott, D. B. Nelson, J. M. Greene, A. H. Glasser, M. S. Chance, and E. A. Frieman. Theory of ballooning modes in tokamaks with finite shear. *Phys. Rev. Lett.*, 39:943–946, 1977.

[26] S. B. F. Dorch, V. Archontics, and A. Nordlund. 3D simulations of twisted magnetic flux ropes. *Astron. Astrophys.*, 352:L79–L82, 1999.

[27] S. B. F. Dorch and A. Nordlund. Numerical 3D simulations of buoyant magnetic flux tubes. *Astron. Astrophys.*, 338:329–339, 1998.

[28] J. F. Drake, D. Biskamp, and A. Zeiler. Breakup of the electron current layer during 3-D collisionless magnetic reconnection. *Geophys. Res. Lett.*, 24(22):2921–2924, 1997.

[29] J. F. Drake, M. A. Shay, and M. Swisdak. The Hall fields and fast magnetic reconnection. *Phys. Plasmas*, 15:042306, 2008.

[30] Attilio Ferrari. Modeling extragalactic jets. *Ann. Rev. of Astron. and Astrophys.*, 36(1):539–598, 1998.

[31] J. Finn and T. Antonsen. Magnetic helicity: what is it and what is it good for. *Comments on Plasma Physics and Controlled Fusion*, 9:111, 1985.

[32] K. Fujimoto and Richard D. S. Whistler waves associated with magnetic reconnection. *Geophys. Res. Lett.*, 35(19):L19112, 2008.

[33] H. P. Furth, J. Killeen, and M. N. Rosenbluth. Finiteresistivity instabilities of a sheet pinch. *Phys. Fluids (1958-1988)*, 6(4):459–484, 1963.

[34] C. G. R. Geddes, T. W. Kornack, and M. R. Brown. Scaling studies of Spheromak formation and equilibrium. *Phys. Plasmas*, 5(4):1027–1034, 1998.

[35] W. Gekelman and R. L. Stenzel. Magnetic field line reconnection experiments: 6. magnetic turbulence. *J. Geophys. Res.: Space Phys.*, 89(A5):2715–2733, 1984.

[36] S. E. Gibson, Y. Fan, C. Mandrini, G. Fisher, and P. Demoulin. Observational consequences of a magnetic flux rope emerging into the corona. *Astrophys. J.*, 617:600–613, 2004.

[37] M. L. Goldstein, D. A. Roberts, and W. H. Matthaeus. Magnetohydrodynamic Turbulence In The Solar Wind. *Ann. Rev. of Astron. and Astrophys.*, 33:283–326, 1995.

[38] R. Gratton, S. Mangioni, J. Niedbalski, and R. Valent. Simple capacitive probe for high-voltage nanosecond pulses. *Rev. Sci. Instrum.*, 57(10):2634–2635, 1986.

[39] G. J. Greene. *ICRF antenna coupling and wave propagation in a Tokamak plasma.* Ph.D. thesis, California Institute of Technology, 1984.

[40] X. Guan, H. Li, and S. Li. Relativistic MHD Simulations of Poynting Flux-driven Jets. *Astrophys. J.*, 781:48, 2014.

[41] E. Hameiri, P. Laurence, and M. Mond. The ballooning instability in space plasmas. *J. Geophys. Res.*, 96:1513–1526, 1991.

[42] J. F. Hansen, S. K. P. Tripathi, and P. M. Bellan. Co- and counter-helicity interaction between two adjacent laboratory prominences. *Phys. Plasmas*, 11:3177–3185, 2004.

[43] P. Hardee. Agn jets: from largest to smallest angular scales. *Journal of Physics: Conference Series*, 131:012052, 2008.

[44] E. G. Harris. Rayleigh-Taylor instabilities of a collapsing cylindrical shell in a magnetic field. *Phys. Fluids (1958-1988)*, 5:1057–1062, 1962.

[45] P. Hartigan and L. Hillenbrand. Adaptive Optics Echelle Spectroscopy of [Fe II] 1.644 μm in the RW Aur Jet: A Narrow Slice Down the Axis of the Flow. *Astrophys. J.*, 705:1388–1394, 2009.

[46] P. Hennebelle and S. Fromang. Magnetic processes in a collapsing dense core. I. Accretion and ejection. *Astron. and Astrophys.*, 477:9–24, 2008.

[47] A. Hillier, H. Isobe, K. Shibata, and T. Berger. Numerical simulations of the magnetic Rayleigh-Taylor instability in the Kippenhahn-Schluter prominence model. *Astrophys. J. Lett.*, 736:L1, 2011.

[48] S. C. Hsu and P. M. Bellan. A laboratory plasma experiment for studying magnetic dynamics of accretion discs and jets. *Mon. Not. Roy. Astron. Soc.*, 334(2):257–261, 2002.

[49] S. C. Hsu and P. M. Bellan. Experimental identification of the kink instability as a poloidal flux amplification mechanism for coaxial gun spheromak formation. *Phys. Rev. Lett.*, 90:215002, 2003.

[50] S. C. Hsu and P. M. Bellan. On the jets, kinks, and spheromaks formed by a planar magnetized coaxial gun. *Phys. Plasmas*, 12:032103, 2005.

[51] D. W. Hughes and F. Cattaneo. A new look at the instability of a stratified horizontal magnetic field. *Geophys. Astrophys. Fluid Dynamics*, 39:65–81, 1987.

[52] H. Isobe, T. Miyagoshi, K. Shibata, and T. Yokoyama. Filamentary structure on the sun from the magnetic Rayleigh-Taylor instability. *Nature*, 434:478–481, 2005.

[53] H. Isobe, T. Miyagoshi, K. Shibata, and T. Yokoyama. Three-dimensional simulation of Solar emerging flux using the earth simulator i. magnetic Rayleigh-Taylor instability at the top of the emerging flux as the origin of filamentary structure. *Publ. Astron. Soc. Japan*, 58:423–438, 2006.

[54] H. Ji, S. Terry, M. Yamada, R. Kulsrud, A. Kuritsyn, and Y. Ren. Electromagnetic fluctuations during fast reconnection in a laboratory plasma. *Phys. Rev. Lett.*, 92:115001, 2004.

[55] H. Ji, M. Yamada, S. Hsu, R. Kulsrud, T. Carter, and S. Zaharia. Magnetic reconnection with Sweet-Parker characteristics in two-dimensional laboratory plasmas. *Phys. Plasmas*, 6:1743–1750, 1999.

[56] W. Junor, J. A. Biretta, and M. Livio. Formation of the radio jet in M87 at 100 Schwarzschild radii from the central black hole. *Nature*, 401:891–892, 1999.

[57] R. C. Kerr and J. R. Lister. Island arc and mid-ocean ridge volcanism, modelled by diapirism from linear source regions. *Earth Planet. Sci. Lett.*, 88:143–152, 1988.

[58] B. Kliem and T. Török. Torus instability. *Phys. Rev. Lett.*, 96:255002, 2006.

[59] M. D. Kruskal and M. Schwarzschild. Some instabilities of a completely ionized plasma. *Proc. R. Soc. Lon. Ser. A*, 223:348–360, 1958.

[60] R. M. Kulsrud. *Plasma Physics for Astrophysics.* Princeton series in astrophysics. Princeton, N.J. Princeton University Press, 2005.

[61] D. Kumar. *Experimental investigations of magnetohydrodynamic plasma jets.* Ph.D. thesis, California Institute of Technology, 2009.

[62] D. Kumar and P. M. Bellan. Heterodyne interferometer with unequal path lengths. *Rev. Sci. Instrum.*, 77:083503, 2006.

[63] D. Kumar and P. M. Bellan. Nonequilibrium Alfvénic plasma jets associated with Spheromak formation. *Phys. Rev. Lett.*, 103:105003, 2009.

[64] D. Kumar, A. L. Moser, and P. M. Bellan. Energy efficiency analysis of the discharge circuit of caltech spheromak experiment. *Plasma Science, IEEE Transactions on*, 38:47–52, 2010.

[65] P. Kumar, K.-S. Cho, S.-C. Bong, S.-H. Park, and Y. H. Kim. Initiation of coronal mass ejection and associated flare caused by helical kink instability observed by SDO/AIA. *Astrophys. J.*, 746:67, 2012.

[66] A. Kuritsyn, M. Yamada, S. Gerhardt, H. Ji, R. Kulsrud, and Y. Ren. Measurements of the parallel and transverse Spitzer resistivities during collisional magnetic reconnection. *Phys. Plasmas*, 13:055703, 2006.

[67] S. V. Lebedev, A. Ciardi, D. J. Ampleford, S. N. Bland, S. C. Bott, J. P. Chittenden, G. N. Hall, J. Rapley, C. A. Jennings, A. Frank, E. G. Blackman, and T. Lery. Magnetic tower outflows from a radial wire array Z-pinch. *Mon. Not. Roy. Astron. Soc.*, 361:97–108, 2005.

[68] H. Li, G. Lapenta, J. M. Finn, S. Li, and S. A. Colgate. Modeling the Large-Scale Structures of Astrophysical Jets in the Magnetically Dominated Limit. *Astrophys. J.*, 643:92–100, 2006.

[69] H. Li, R. V. E. Lovelace, J. M. Finn, and S. A. Colgate. Magnetic Helix Formation Driven by Keplerian Disk Rotation in an External Plasma Pressure: The Initial Expansion Stage. *Astrophys. J.*, 561:915–923, 2001.

[70] S. Li and H. Li. LA-UR-03-8935. Technical report, Los Alamos National Lab, 2003.

[71] J. R. Lister and R. C. Kerr. The effect of geometry on the gravitational instability of a buoyant region of viscous fluid. *J. Fluid Mech.*, 202:577–594, 1989.

[72] J. R. Lister, R. C. Kerr, N. J. Russell, and A. Crosby. Rayleigh-Taylor instability of an inclined buoyant viscous cylinder. *J. Fluid Mech.*, 671:313–338, 2011.

[73] R. V. E. Lovelace, H. Li, A. V. Koldoba, G. V. Ustyugova, and M. M. Romanova. Poynting Jets from Accretion Disks. *Astrophys. J.*, 572:445–455, 2002.

[74] D. Lynden-Bell. Magnetic collimation by accretion discs of quasars and stars. *Mon. Not. Roy. Astron. Soc.*, 279:389–401, 1996.

[75] D. Lynden-Bell. On why discs generate magnetic towers and collimate jets. *Mon. Not. Roy. Astron. Soc.*, 341:1360–1372, 2003.

[76] W. Lewis M. P. Reilly and G. H. Miley. Magnetic field probes for use in radio frequency plasma. *Rev. Sci. Instrum*, 80:053508, 2009.

[77] M. E. Mandt, R. E. Denton, and J. F. Drake. Transition to whistler mediated magnetic reconnection. *Geophys. Res. Lett.*, 21:73–76, 1994.

[78] M. K. Matzen. Z pinches as intense x-ray sources for high-energy density physics applications. *Phys. Plasmas*, 4:1519–1527, 1997.

[79] A. L. Moser. *Dynamics of magnetically driven plasma jets : an instability of an instability, gas cloud impacts, shocks, and other deformations*. Ph.D. thesis, California Institute of Technology, 2012.

[80] A. L. Moser and P. M. Bellan. Magnetic reconnection from a multiscale instability cascade. *Nature*, 482:379–381, 2012.

[81] A. L. Moser and P. M. Bellan. Observations of magnetic flux compression in jet impact experiments. *Astrophys. Space Sci.*, 337(2):593–596, 2012.

[82] M. Nakamura, H. Li, and S. Li. Structure of magnetic tower jets in stratified atmospheres. *Astrophys. J.*, 652:1059–1067, 2006.

[83] M. Nakamura, H. Li, and S. Li. Stability properties of magnetic tower jets. *Astrophys. J.*, 656:721–732, 2007.

[84] M. Nakamura, I. L. Tregillis, H. Li, and S. Li. A numerical model of herculesa by magnetic tower: Jet/lobe transition, wiggling, and the magnetic field distribution. *Astrophys. J.*, 686:843–850, 2008.

[85] S. Noschese, L. Pasquini, and L. Reichel. Tridiagonal toeplitz matrices: Properties and novel applications. *Numer. Linear Algebra Appl.*, 20:302–326, 2013.

[86] M. Oieroset, T. D. Phan, M. Fujimoto, R. P. Lin, and R. P. Lepping. In situ detection of collisionless reconnection in the earth's magnetotail. *Nature*, 412(6845):414, 2001.

[87] E. N. Parker. Sweet's mechanism for merging magnetic fields in conducting fluids. *J. Geophys. Res.*, 62(4):509–520, 1957.

[88] E. N. Parker. The dynamical state of the interstellar gas and field. *Astrophys. J.*, 145:811–833, 1966.

[89] R. J. Perkins and P. M. Bellan. Elimination of Radio-Frequency noise by identifying and diverting large RF ground currents. *AIP Conference Proceedings*, 1406:531–534, 2011.

[90] D. L. Peterson, R. L. Bowers, J. H. Brownell, A. E. Greene, K. D. McLenithan, T. A. Oliphant, N. F. Roderick, and A. J. Scannapieco. Two-dimensional modeling of magnetically driven Rayleigh-Taylor instabilities in cylindrical Z pinches. *Phys. Plasmas*, 3:368–381, 1996.

[91] L. A. Pustil'nik. Instability of quiescent prominences and the origin of Solar flares. *Soviet Astronomy*, 17:763–767, 1973.

[92] X. M. Qiu, L. Huang, and G. D. Jian. Synergistic mitigation of the Rayleigh-Taylor instability in Z-pinch implosions by sheared axial flow and finite Larmor radius effect. *Phys. Plasmas*, 10:2956–2961, 2003.

[93] T. P. Ray, T. W. B. Muxlow, D. J. Axon, A. Brown, D. Corcoran, J. Dyson, and R. Mundt. Large-scale magnetic fields in the outflow from the young stellar object T Tauri S. *Nature*, 385:415–417, 1997.

[94] B. N. Rogers, R. E. Denton, J. F. Drake, and M. A. Shay. Role of dispersive waves in collisionless magnetic reconnection. *Phys. Rev. Lett.*, 87:195004, 2001.

[95] C. A. Romero Talamás, P. M. Bellan, and S. C. Hsu. Multielement magnetic probe using commercial chip inductors. *Rev. Sci. Instrum.*, 75:2664–2667, 2004.

[96] W. J. Sarjeant and A. J. Alcock. High-voltage probe system with subnanosecond rise time. *Rev. Sci. Instrum.*, 47(10):1283–1287, 1976.

[97] S. H. Saw, C. S. Wong, and S. Lee. A fast capacitive-RC hybrid probe for high power voltage pulse measurement. *Rev. Sci. Instrum.*, 62:532–533, 1991.

[98] H. Shang, A. Allen, Z.-Y. Li, C.-F. Liu, M.-Y. Chou, and J. Anderson. A unified model for bipolar outflows from young stars. *Astrophys. J.*, 649:845, 2006.

[99] D. H. Sharp. An overview of Rayleigh-Taylor instability. *Physica D: Nonlinear Phenomena*, 12:3–18, 1984.

[100] B. D. Sherwin and D. Lynden-Bell. Electromagnetic fields in jets. *Mon. Not. Roy. Astron. Soc.*, 378(2):409–415, 2007.

[101] K. Shibasaki. High-beta disruption in the Solar atmosphere. *Astrophys. J.*, 557:326–331, 2001.

[102] T. Shikama and P. M. Bellan. Development of a polarization resolved spectroscopic diagnostic for measurements of the vector magnetic field in the caltech coaxial magnetized plasma jet experiment. *Rev. Sci. Instrum.*, 84:023507, 2013.

[103] F. H. Shu, J. Najita, E. C. Ostriker, and H. Shang. Magnetocentrifugally driven flows from young stars and disks. v. asymptotic collimation into jets. *Astrophys. J. Lett.*, 455:L155–L158, 1995.

[104] D.C. Smith. Signal and noise measurement techniques using magnetic field probes. In *Proc. IEEE. Int. Symp. Electromagnetic. Compatibility*, volume 1, pages 559–563, 1999.

[105] L. Spitzer. *Physics of Fully Ionized Gases.* Interscience, New York, 1956.

[106] H. C. Spruit. Theory of Magnetically Powered Jets. In T. Belloni, editor, *Lecture Notes in Physics, Berlin Springer Verlag*, volume 794 of *Lecture Notes in Physics, Berlin Springer Verlag*, pages 233–263, March 2010.

[107] E. V. Stenson and P. M. Bellan. Magnetically driven flows in arched plasma structures. *Phys. Rev. Lett.*, 109:075001, 2012.

[108] R. L. Stenzel. Whistler waves in space and laboratory plasmas. *J. Geophys. Res.: Space Phys.*, 104(A7):14379–14395, 1999.

[109] R. L. Stenzel and J. M. Urrutia. Magnetic antenna excitation of whistler modes. ii. antenna arrays. *Phys. Plasmas*, 21(12):122108, 2014.

[110] J. M. Stone and T. Gardiner. The magnetic Rayleight-Taylor instability in three dimensions. *Astrophys. J.*, 671:1726–1735, 2007.

[111] P. A. Sweet. The Neutral Point Theory of Solar Flares. In B. Lehnert, editor, *Electromagnetic Phenomena in Cosmical Physics*, volume 6 of *IAU Symposium*, page 123, 1958.

[112] H. Takabe, K. Mima, L. Montierth, and R. L. Morse. Selfconsistent growth rate of the Rayleigh-Taylor instability in an ablatively accelerating plasma. *Phys. Fluids (1958-1988)*, 28:3676–3682, 1985.

[113] C. A. Romero Talamás. *Investigations of Spheromak plasma dynamics: High-speed imaging at the Sustained Spheromak Physics Experiment and magnetic diagnostics at the Caltech Spheromak experiment.* Ph.D. thesis, California Institute of Technology, 2005.

[114] J. B. Taylor. Relaxation of toroidal plasma and generation of reverse magnetic fields. *Phys. Rev. Lett.*, 33:1139, 1974.

[115] F. Trintchouk, M. Yamada, H. Ji, R. M. Kulsrud, and T. A. Carter. Measurement of the transverse Spitzer resistivity during collisional magnetic reconnection. *Phys. Plasmas*, 10:319–322, 2003.

[116] B. T. Tsurutani, E. J. Smith, R. R. Anderson, K. W. Ogilvie, J. D. Scudder, D. N. Baker, and S. J. Bame. Lion roars and nonoscillatory drift mirror waves in the magnetosheath. *J. Geophys. Res.: Space Phys.*, 87(A8):6060–6072, 1982.

[117] B. T. Tsurutani, O. P. Verkhoglyadova, G. S. Lakhina, and S. Yagitani. Properties of dayside outer zone chorus during hildcaa events: Loss of energetic electrons. *J. Geophys. Res.: Space Phys.*, 114:A03207, 2009.

[118] D. A. Uzdensky and A. I. MacFadyen. Magnetar-Driven Magnetic Tower as a Model for Gamma-Ray Bursts and Asymmetric Supernovae. *Astrophys. J.*, 669:546–560, 2007.

[119] O. P. Verkhoglyadova, B. T. Tsurutani, and G. S. Lakhina. Properties of obliquely propagating chorus. *J. Geophys. Res.: Space Phys.*, 115:A00F19, 2010.

[120] J. Wesson. *Tokamak*. Oxford University Press, 1987.

[121] L. Woltjer. A theorem on force-free magnetic fields. *P. Natl. Acd. Sci.*, 44:489, 1958.

[122] H. Xu, H. Li, D. Collins, S. Li, and M. L. Norman. Formation of X-Ray Cavities by the Magnetically Dominated Jet-Lobe System in a Galaxy Cluster. *Astrophys. J. Lett.*, 681:L61–L64, 2008.

[123] M. Yamada, R. Kulsrud, and H. Ji. Magnetic reconnection. *Rev. Mod. Phys.*, 82:603–664, 2010.

[124] M. Yamada, J. You, J. Jara-Almonte, H. Ji, R. M. Kulsrud, and C. E Myers. Conversion of magnetic energy in the magnetic reconnection layer of a laboratory plasma. *Nature communications*, 5:4774, 2014.

[125] J. Yoo, M. Yamada, H. Ji, J. Jara-Almonte, and C. E. Myers. Bulk ion acceleration and particle heating during magnetic reconnection in a laboratory plasma. *Phys. Plasmas*, 21:055706, 2014.

[126] G. S. Yun and P. M. Bellan. Plasma tubes becoming collimated as a result of magnetohydrodynamic pumping. *Phys. Plasmas*, 17:062108, 2010.

[127] G. S. Yun, S. You, and P. M. Bellan. Large density amplification measured on jets ejected from a magnetized plasma gun. *Nuclear Fusion*, 47:181–188, 2007.

[128] R. T. Zavala and G. B. Taylor. Faraday Rotation Measure Gradients from a Helical Magnetic Field in 3C 273. *Astrophys. J. Lett.*, 626:L73–L76, 2005.

[129] X. Zhai and P. M. Bellan. An earth-isolated optically coupled wideband high voltage probe powered by ambient light. *Rev. Sci. Instrum.*, 83:104703, 2012.

[130] X. Zhai, H. Li, P. M. Bellan, and S. Li. Three-Dimensional MHD simulation of the Caltech plasma jet experiment: First results. *Astrophys. J.*, 791:40, 2014.